MODEL CALCULATIONS OF RADIATIVE TRANSFER AND TROPOSPHERIC CHEMISTRY

Yu Lu
B.S., Nanjing University, 1983
M.S., Oregon Graduate Institute of Science and Technology, 1990

A dissertation submitted to the faculty of
the Oregon Graduate Institute
of
Science & Technology
in partial fulfillment of the
requirements for the degree
Doctor of Philosophy
in
Environmental Science and Engineering

April, 1993

The dissertation "Model Calculations of Radiative Transfer and Tropospheric Chemistry" by Yu Lu has been examined and approved by the following Examination Committee:

Dr. M. A. K. Khalil, Thesis Advisor
Professor, Oregon Graduate Institute

Dr. R. A. Rasmussen, Professor
Oregon Graduate Institute

Dr. J. J. Huntzicker, Professor
Oregon Graduate Institute

Dr. J. P. Pinto, Research Scientist
U.S. Environmental Protection Agency

Dr. T. M. Hard, Research Fellow
Portland State University

DEDICATION

This Dissertation is dedicated to my wife, Wenjun, for her love, understanding, and support.

ACKNOWLEDGEMENTS

I would like to acknowledge and thank many people. In particular, I am very grateful to Dr. M. A. K. Khalil for his guidance, encouragement, support, and all kinds of help. Without his advice, help, and support, this dissertation would not have been possible.

I thank the other members of my thesis committee, Dr. R. A. Rasmussen, Dr. J. J. Huntzicker, Dr. J. P. Pinto, Dr. T. M. Hard for taking time out of their busy schedule to read this manuscript as well as for their valuable comments.

I would like to express my appreciation to Dr. A. Thompson at NASA and Dr. Fish at this department for help and valuable discussions. I am grateful to Ms. M. J. Shearer for her technical help with many computer problems I have encountered as well as for helpful discussion. I am indebted to Mrs. E. Taylor for her very effective secretarial help. I thank R. Mackay, F. Moraes, W. Zhao, and T. Ye, my classmates, for their friendships and helpful discussions. I would also like to thank all of the library staffs and department secretaries, Pam and Judi, for their helps.

Finally I am extremely grateful to my family, especially to my grandmother, my parents, my parents-in-law, and my dear wife, Wenjun Bao. Without their love and support, this work could not have succeeded.

The financial support for this work was provided by grants from the National Science Foundation (ATM-8811059, DPP-8820632), the Department of Energy (DE-FG06-85ER60313), Resources of Andarz Co., and Oregon Graduate Institute of Science and Technology, which are gratefully acknowledged.

TABLE OF CONTENTS

ABBREVIATIONS

ma6	Vertically non-uniform cloud, whose maximum water liquid content is equal to the mean liquid water content of the uniform cloud *uni* and is located at 60% of the whole cloud thickness from the cloud bottom
ma8	Vertically non-uniform cloud, whose maximum water liquid content is equal to the mean liquid water content of the *uni* and is located at 80% of the whole cloud thickness from the cloud bottom
uni	Vertically uniform cloud with uniform liquid water content everywhere inside the cloud
va6	Vertically non-uniform cloud whose maximum liquid water content is located at the same height as the *ma6* and whose vertically averaged liquid water content is equal to that of the *uni*
va8	Vertically non-uniform cloud whose maximum liquid water content is located at the same height as the *ma8* and whose vertically averaged liquid water content is equal to that of the *uni*
AE	Normal optical thickness of the aerosol extinction
AS	Normal optical thickness of the aerosol scattering
AT	Urban air with an altostratus cloud at 5.5 ~ 6.5 km
AREAL	Atmospheric Research and Exposure Assessment Laboratory
CA	Clean and clear atmosphere
DCH_4	Loss rate of OH due to the direct reaction of OH with CH_4 (Direct Effect)

DCO	Loss rate of OH due to the direct reaction of OH with CO (Direct Effect)
$FBCH_4$	Changing rate of OH due to the effects from the HO_2 and H_2O_2 created by the cycles initiated by the reaction between OH and CH_4 (Buffer Effect)
FBCO	Changing rate of OH due to the effects from the resulting HO_2 and H_2O_2 created by the cycles initiated by the reaction between OH and CO (Buffer Effect)
$FCCH_4$	Changing rate of OH due to the effect from a series of resulting organic compounds created by the cycles initiated by the reaction between OH and CH_4 (Buffer Effect)
FCH_4	Changing rate of OH due to all the three feedbacks of the direct effect of CH_4 (Total Feedback)
FCO	Changing rate of OH due to both the buffer feedback and the oxygen feedback of the direct effect of CH_4 (Total Feedback)
$FOCH_4$	Changing rate of OH due to the effect from a series of resulting oxidants (NO_2, O_3, etc) created by the cycles initiated by the reaction between OH and CH_4 (Oxygen Effect)
FOCO	Changing rate of OH due to the effect from a series of resulting oxidants (NO_2, O_3, etc) created by the cycles initiated by the reaction between OH and CO (Oxygen Effect)
GSFC	Goddard Space Flight Center
IA	Ice ages
LGM	Last glacial maximum
LET	Vertical profiles of CO recommended by Logan et al. (1981).

LWC	Liquid water content
M1DPCM	Multiple one-dimensional photochemical model
MD	Mode radius, corresponding to the maximum number of droplets.
MT	Modern times
ND	Number density of the droplet in a cloud
NH	Northern hemisphere
OA	Normal optical thickness of the ozone absorption
PE	Pre-industrial Era
RS	Normal optical thickness of Rayleigh scattering
SH	Southern hemisphere
ST	Urban air with a stratus cloud at 1.5 ~ 2.5 km
TCH_4	Changing rate of OH due to both the direct effect of CH_4 and all its feedbacks (Total Effect)
TCO	Changing rate of OH due to both the direct effect of CO and all its feedbacks (Total Effect)
UA	Urban air

SYMBOLS

a_n	Mie coefficient
b_b	Fraction of the backward scattering energy
b_f	Fraction of the forward scattering energy
b_n	Mie coefficient
ds	A finite distance for radiation traverses
e	Water vapor pressure
f_p	Fractional-volume of the species *p*
g	Asymmetry factor
g(z)	Atmospheric asymmetry factor at height z
$\overline{g}$	Averaged atmospheric asymmetry factor between heights z and $z+\Delta z$
g_a	Asymmetry factor of aerosols
g_c	Asymmetry factor of cloud droplets
g_i	Atmospheric asymmetry factor at height z_i
$\overline{g_i}$	Averaged atmospheric asymmetry factor between heights z_i and $z_i+\Delta z$
g_p	Asymmetry factor for N_p particles
h	Hour angle

i	Solar inclination
j	Actinic flux (photon $cm^{-2} s^{-1}$)
k_m	Photolysis (photodissociation) rate of the species *m* (s^{-1})
l	Latitude
m	a) Non-dimensional refractive index of molecules; b) Complex refractive index ($m=m_1+i \cdot m_2$; the real part, m_1, related to scattering, and the imaginary part, m_2, related to absorption); c) air mass
n	Number density of a certain matter (cm^{-3})
n_a	Size distribution function of aerosols ($\mu m^{-1} cm^{-3}$)
n_c	Size distribution function of cloud droplets ($\mu m^{-1} cm^{-3}$)
$n_p(r)$	Size distribution function of a certain type of particles ($\mu m^{-1} cm^{-3}$)
n_w	Number density of water molecules
r	a) Distance between the tiny particle (or the molecule); b) Spherical radius of a single particle
r_k	Relative contribution of the seasonally and vertically averaged nighttime OH at the *k*th latitude
r_{ki}	Relative contribution of the vertically averaged nighttime OH at the *k*th latitude in the *i*th season
r_{kij}	Relative contribution of the nighttime OH at the *j*th altitude and the *k*th latitude in the *i*th season
r_{kj}	Relative contribution of the seasonally averaged nighttime OH at the *j*th altitude in the *i*th season

t	Time (hour)
t_{ki}	Time from sunset to sunrise in the *i*th season at the *k*th latitude (hour)
x	Mie size parameter ($=2\pi r/\lambda$)
y	Mie size parameter ($=mx$)
A	Pre-exponential factor of a bimolecular reaction rate (cm^3 $molecule^{-1}$ s^{-1})
C_n	Number density of the *n*th species ($molecules/cm^3$)
$C_{nj}^{\ i}$	Number density of the *n*th species at the *j*th grid point and the *i*th time step ($molecules/cm^3$)
C_p	Number density of the species *p* ($molecules/cm^3$)
D_{1n}	Loss rate of the *n*th species by the first order process (s^{-1})
D_{2n}	Loss rate of the *n*th species by the second order process (cm^3 $molecule^{-1}$ s^{-1})
D_n	Loss rate of the *n*th species (s^{-1})
$D_{nj}^{\ i}$	Loss rate of the *n*th species at the *j*th grid point and the *i*th time step (s^{-1})
D_x	Loss rate of the species *X*
E	Activation energy for a bimolecular reaction (J/mole)
E_0	Saturation water vapor pressure at 273°K (=6.11 mbar)
F^+	Upward diffuse flux
F^-	Downward diffuse flux
F_d	Direct radiative flux
F_{net}	Irradiance (net radiative flux)

$[HO_2]_{S0}$	HO_2 concentration at the Earth's surface in summer (molecules/cm^3)
$[HO_2]_{S6}$	HO_2 concentration at 6 km above the Earth's surface in summer (molecules/cm^3)
$[HO_2]_{W0}$	HO_2 concentration at the Earth's surface in winter (molecules/cm^3)
$[HO_2]_{W6}$	HO_2 concentration at 6 km above the Earth's surface in winter (molecules/cm^3)
I_0	monochromatic intensity (or radiance) of incident radiation
I	Scattering intensity
I_λ	monochromatic intensity (or radiance) at wavelength λ
I_λ^{ns}	Net scattering intensity in the forward direction
I_λ^{ts}	Total intensity due to Mie scattering
J	Actinic Flux
J_m	Photolysis (photodissociation) rate of the species *m* (s^{-1})
K	Eddy diffusivity (m_2/s)
K_0	a) Low-pressure limiting rate (cm^{-6} molecule^{-2} s^{-1}); b) pre-exponential factor of the heterogeneous rate (s^{-1})
K_∞	High-pressure limiting rate (cm^{-3} molecule^{-1} s^{-1})
K_{bim}	Bimolecular reaction rate (cm^{-3} molecule^{-1} s^{-1})
K_{het}	Heterogeneous loss rate (s^{-1})
$K_{r,s}$	Rate of the reaction between the *r*th and *s*th species
K_{ter}	Termolecular reaction rate (cm^{-3} molecule^{-1} s^{-1})
$K_{u,n}$	Rate of the reaction between the *u*th and *n*th species

K_z	Vertical eddy diffusivity (m_2/s)
$K_{zj+½}$	Mean vertical eddy diffusivity between the vertical grids j and $j+1$ (m_2/s)
L	Latent heat of the vaporization
L_n	Chemical removal rate of the nth species (molecule cm^{-3} s^{-1})
[M]	Number density of the atmosphere (molecules/cm^3)
N	Total number of molecules per unit volume
N_0	Arogadro's number ($=6.02297\times10^{23}$ molecules/cm^3)
N_a	Number density of atmospheric aerosols at the altitude z
N_c	Number density of cloud droplets
N_m	Number density of air molecules at the altitude z
N_p	Number of a certain spherical particles with different sizes and the same refractive index
$N_O(z)$	Number density of O_3 at height z above the earth's surface
$[OH]_{S0}$	OH concentration at the Earth's surface in summer (molecules/cm^3)
$[OH]_{S6}$	OH concentration at 6 km above the Earth's surface in summer (molecules/cm^3)
$[OH]_{W0}$	OH concentration at the Earth's surface in winter (molecules/cm^3)
$[OH]_{W6}$	OH concentration at 6 km above the Earth's surface in winter (molecules/cm^3)
P	Pressure (N/m_2)
$P(\cos\Theta)$	Phase function
$P(r,\Theta)$	Phase function

P_n Chemical production rate of the *n*th species (molecule cm^{-3} s^{-1})

$P_n^1(\cos\Theta)$ Associated Legendre polynomial function

P_{nj}^i Chemical production rate of the *n*th species at the *j*th grid point and the *i*th time step (molecule cm^{-3} s^{-1})

P_x^y Chemical production rate of the species *X* in the cycles initiated by the direct reaction between OH and *Y* (*Y* is CO or CH_4) (molecule cm^{-3} s^{-1})

Q_e Extinction efficiency

Q_s Scattering efficiency

R Universal gas constant (=8.31432 J $mole^{-1}$ $°K^{-1}$)

R_w Gas constant for water vapor (=0.461 J g^{-1} $°K^{-1}$)

$S_{r,s}$ Stoichiometric coefficient of the reaction between the *r*th and *s*th species

T Temperature

$\vec{v}$ Wind velocity vector (m/s)

[X] Number density of the species *X* (molecules/cm^3), where *X* is the molecular formula of a species

$[X]_k$ Number density of the species *X* at the *k*th time step (molecules/cm^3)

$[X]^Y$ Number of the species *X* in a unit volume, which is generated in the cycles initiated by the direct reaction between OH and *Y* (*Y* is CO or CH_4) (molecules/cm^3)

$[\overline{X}]_{kji}$ Diurnally averaged concentration of the species *X* at the *j*th altitude and the *k*th latitude in the *i*th season (molecules/cm^3)

$[X]_{ki}$ Diurnally and vertically averaged concentration of the species X at the kth latitude in the ith season (molecules/cm^3)

$\overline{[X^n]}_{kji}$ Averaged nighttime concentration of the species X at the jth altitude and the kth latitude in the ith season (molecules/cm^3)

$\overline{[X^n]}_{ki}$ Vertically averaged nighttime concentration of the species X at the kth latitude in the ith season (molecules/cm^3)

Z Altitude z (km)

α Polarizability of the small particle, or molecule

ϵ Relative error

η a) Relative difference; b) Relative error

θ Zenith angle

λ Wavelength (nm); 1 nm = 10^{-9} m

μ a) $\cos\Theta$; b) $\cos\theta$

μ_0 $\cos\theta_0$

μ_1 Weighted factor

πF_0 Extraterrestrial flux

σ Cross section (cm^2)

σ_a^O Absorption cross section of O_3 (cm^2)

σ_e Extinction cross section (cm^2)

σ_m Absorption cross section of the species m (cm^2)

σ_s	Scattering cross section (cm^2)
σ_s^a	Cross section for aerosol scattering (cm^2)
σ_s^c	Cross section for the scattering of cloud droplets (cm^2)
σ_s^m	Cross section for Rayleigh (or molecular) scattering (cm^2)
σ_s^p	Scattering cross section for a certain type of particles
σ_λ	Cross section at wavelength λ
τ	Normal optical depth (thickness)
$\tau_{a,i}^a$	Optical depths in the *i*th layer due to the absorption of the atmospheric aerosols
$\tau_{a,i}^O$	Optical depths in the *i*th layer due to the ozone absorption
τ_a^O	Normal optical depth (thickness) for O_3 absorption
τ_i	Total optical depths in the *i*th layer due to all kinds of scattering and absorption
$\tau_{s,i}$	Total optical depths in the *i*th layer due to all the atmospheric scattering processes
$\tau_{s,i}^a$	Optical depths in the *i*th layer due to the scattering of the atmospheric aerosols
$\tau_{s,i}^c$	Optical depths in the *i*th layer due to the scattering of droplets in clouds
$\tau_{s,i}^m$	Optical depths in the *i*th layer due to the scattering of the atmospheric molecules
τ_s^m	Normal optical depth for Rayleigh scattering
Θ	Scattering angle
ω_0	Single-scattering albedo
ϕ	Azimuthal angle

ϕ_m Quantum yield of the photolysis of the species m

Δt_i Difference between the $i+1$th and ith time steps ($\Delta t_i = t_{i+1} - t_i$)

ΔZ (or Δz) Vertical spacing (resolution) (km)

$\Delta \tau_s^m$ Optical depth for Rayleigh scattering at the altitudinal range form z to $z+\Delta z$

$\Delta \tau_a^O$ Optical depth for O_3 absorption at the altitudinal range form z to $z+\Delta z$

LIST OF FIGURES

LIST OF TABLES

PUBLICATIONS AND CONFERENCE PROCEEDINGS*

[1] Lu, Y. and M. A. K. Khalil, 1993, Methane and carbon monoxide in OH chemistry: The effects of feedbacks and reservoirs generated by the reactive products, *Chemosphere 26*, 641-655.

[2] Lu, Y. and M. A. K. Khalil, 1993, Theoretical simulation of the asymmetry factor for various atmospheric conditions, *J. Atmos. Sci. (to be submitted), pp52.*

[3] Lu, Y. and M. A. K. Khalil, 1993, Effects of cloud on tropospheric OH, *J. Geophys. Res. (to be submitted).*

[4] Lu, Y. and M. A. K. Khalil, 1992, Model calculations of nighttime OH, *Tellus 44B*, 106-113.

[5] Lu, Y. and M. A. K. Khalil, 1992, Radiative and actinic fluxes for atmospheric chemistry: Calculations for various atmospheric conditions, *J. Geophys. Res. (submitted), pp49.*

[6] Lu, Y. and M. A. K. Khalil, 1992, Temporal and spatial variation of actinic flux and tropospheric OH, *EOS, Transactions 73 (43),* 92.

[7] Lu, Y. and M. A. K. Khalil, 1992, Radiative transfer and tropospheric chemistry, *EOS, Transactions 73 (25),* 26.

[8] Lu, Y. and M. A. K. Khalil, 1992, Effects of aerosols and clouds on solar radiative transfer and tropospheric chemistry, *EOS, Transactions 73 (14),* 67.

[9] Lu, Y. and M. A. K. Khalil, 1991, Tropospheric OH: Model calculations of spatial, temporal, and secular variations, *Chemosphere 23, No. 3*, 397-444.

[10] Lu, Y. and M. A. K. Khalil, 1991, The real roles of CO and CH_4 in OH chemistry, EOS, *Transactions 72 (44),* 100.

[11] Lu, Y. and M. A. K. Khalil, 1991, Methane: the key sink of OH, Presented at NATO Advanced Research Workshop, *The Global Cycle of Atmospheric Methane,* Timberline Lodge, Portland, Oregon, Oct. 6-11, 1991.

[12] Lu, Y. and M. A. K. Khalil, 1990 , Model calculations of nighttime OH, *EOS Transactions 71,* 1232-1233.

[13] Lu, Y. and M. A. K. Khalil, 1990, Model calculations of nighttime OH, Presented at 7th annual PNWIS/A&WMA conference, Portland, Oregon, November 14th-16th, 1990.

[14] Lu, Y., 1990, *Modeling tropospheric OH chemistry,* M.S. Thesis, *pp245,* (OGI/ESE/CAS, Beaverton, Oregon).

---

* The entire dissertation was written based on the above listed materials that have been or will be published. Each chapter associated with the above publications are shown below (Publication number):

Chapter 2 [4], [9], [12], [13], [14]
Chapter 3 [1], [9], [10], [11], [14]
Chapter 4 [2], [5], [6]
Chapter 5 [5], [6], [7], [8]
Chapter 6 [3], [6], [7], [8]

ABSTRACT

MODEL CALCULATIONS OF RADIATIVE TRANSFER AND TROPOSPHERIC CHEMISTRY

Yu Lu, Ph.D.

Oregon Graduate Institute of Science and Technology, 1993

Supervising Professor: M. A. K. Khalil

The tropospheric chemistry of HO_x, NO_y, O_x, and CH_iO_j were studied with our time-dependent multiple one-dimensional photochemical model. Besides its diurnal, vertical, seasonal, and latitudinal variations, the globally averaged OH level may decrease by about 40% from ices ages to the present and about 10% from the pre-industrial era to the present. However, the averaged nighttime OH in ice ages is about three times as large as the current nighttime OH, 1.3×10^4 molecules/cm^3, which is about two orders of magnitude smaller than the averaged daytime OH, 1.6×10^6 molecules/cm^3, at present.

By tracing the reactions, which are initiated by the direct reactions of OH with CO and CH_4, the total effects of CH_4 and CO were calculated. Atmospheric methane, along with its feedbacks, may remove as much as or more atmospheric OH than carbon monoxide,

although CO is widely accepted as the largest sink of the atmospheric OH.

A detailed radiative transfer model was developed for various atmospheric conditions by including the optical properties and other physical features of various types of clouds and aerosols. The model results indicates the variations of the synoptic and environmental conditions in the lower atmosphere affect not only the actinic fluxes locally but also the radiation field in the upper atmosphere.

Finally coupling the radiative transfer model with the photochemical model shows the effect of aerosols on OH chemistry becomes important only in the atmospheric boundary layer. The OH concentrations could drop significantly below a cloud but increase above the cloud compared to the OH levels in a clear atmosphere. The averaged OH level for the whole troposphere could be increased by low clouds but decreased by high clouds. More importantly, the increase of tropospheric OH by low clouds could be larger than that due to stratospheric O_3 depletion.

CHAPTER 1 INTRODUCTION

The earth's atmosphere is necessary for most lives as we understand. It is a huge reservoir of various gases. More than 99% of the atmosphere is N_2 (78.08%), O_2 (20.98%), and noble gases such as Ar (0.93%) (see for example, Levine, 1985). These major gases in the atmosphere are chemically relatively inert and thus are of secondary importance for atmospheric chemistry. In contrast, many of minor remaining components in the atmosphere, or trace gases, are very reactive and create most of the chemical reactions in the atmosphere. Most of trace gases exist in the troposphere, which is the lowest layer of the atmosphere, from the earth's surface up to 12 km above the surface, and which contains about 80~85% of the total mass of the atmosphere.

The distributions of trace gases in the troposphere depend not only on the emissions and removals occurring at the two boundaries of the troposphere, the earth's surface and the tropopause, due to the natural and anthropogenic processes, but also on the chemical transformations as well as all kinds of mixing, physical production, and dry and wet removal processes in the troposphere. In addition, the chemical processes are greatly affected by the radiation field and other physical characteristics of the atmosphere since almost all chemical reactions in the atmosphere are initiated by the solar radiation. The physical features of the atmosphere control not only the physical processes such as mixing, emissions, and removals of trace gases but also the state of chemical transformations. These physical and chemical

processes are inextricably tied together, making the tropospheric chemistry very complicated. Another complexity of atmospheric chemistry is that reactive trace gases and free radicals in the troposphere are continuously held in reservoirs, from which they can be regenerated.

In tropospheric chemistry, the hydroxyl radical, OH, plays a central role. Most of the photochemistry in the troposphere is initiated by reactions of the hydroxyl radical (OH) with other species. Nearly all tracers and free radicals in the troposphere react with OH. The chemical cycles in the troposphere such as the HO_x cycle, the NO_x cycle, and the hydrocarbon cycles, are all associated with OH. The concentrations of many trace gases and free radicals in the troposphere are also determined by the OH level since reactions of OH with these species are their major removal processes.

Although tropospheric chemistry is very complicated and covers a wide range of fields in addition to chemical transformation, such as the physics and dynamics of atmospheric processes, our knowledge of tropospheric chemistry has been advanced tremendously as a result of observations and monitoring, laboratory measurements of chemical kinetics and photochemical data, and numerical modeling with the rapid development of computer facilities. Nevertheless, tropospheric OH chemistry remain an active area of research not only because of its extreme importance and complexity but also because some aspects of OH chemistry remains uncertain or unknown. Thus the first purpose of this study was to develop a multiple one-dimensional photochemical model (M1DPCM) to evaluate the temporal, spatial, and secular variations of the tropospheric OH.

Although OH reacts with almost all trace gases and free radicals, not all the species and reactions are equally important in determining tropospheric OH concentration. Thus the second purpose of this study was to investigate the chemical mechanism of tropospheric OH to find the important reactions that control tropospheric OH. In addition, the evaluation of the total contributions to OH from two most important direct sinks of OH, CH_4 and CO, is also one of the main interests in this study.

Radiation from the sun is the main source of energy for the atmosphere, the earth, and the life on the earth. It is also the main driving force for photolysis processes. The strengths of photolysis and concentrations of reactive species are very sensitive to the variation of the radiation field. Thus to better understand tropospheric chemistry it is essential to have a comprehensive knowledge of radiation fields and to understand the variation of the radiation fields in terms of the diurnal, seasonal, and latitudinal changes due to the relative position between the sun and the observational point on the earth's atmosphere, as well as the variations of optical properties and other physical characteristics of various atmospheric components such as O_3, air molecules, atmospheric aerosols, and various types of clouds. Thus the final purpose of this study is to model and calculate the various radiation fields and to evaluate the feedbacks of variations of radiation field on tropospheric chemistry.

This dissertation is divided into seven chapter based on the purposes and results in this study. Chapter 2 focuses on the multiple one-dimensional photochemical model (M1DPCM) developed in this study and the model results. The formulation and numerical

method of the M1DPCM will be described in detail for readers to modify the model or reproduce the results. The model results including the temporal (diurnal and seasonal), spatial (altitudinal and latitudinal), and secular (from ice ages to the present) are fully illustrated and discussed. The chemical mechanisms of tropospheric OH are discussed in the next chapter. All the chemical reactions are compared to find the most important reactions affecting tropospheric OH. As one highlight of this dissertation, the numerical model to calculate the total contributions of CO and CH_4 is presented. Chapter 4 deals with optical properties of various atmospheric components including O_3, air molecules, aerosol particles, and cloud droplets. The numerical scheme to calculate the absorption and scattering cross sections and the asymmetry factors of various atmospheric components are described in detail. On important feature of this chapter is the derivation and illustration of the distinction between the atmospheric asymmetry factor and the asymmetry factor of a certain atmospheric component. In the following chapter, the radiative transfer model is described in detail, and the variations of the radiation fields for various atmospheric conditions including the clear and clean sky, urban air, and various cloudy atmospheres, calculated with the radiative transfer model, are demonstrated and discussed. As one of important pieces of this dissertation, the sensitivity of the macro structures of clouds are explored in this chapter. Chapter 6 deals with the variations of the tropospheric OH in response to the variations of various atmospheric scenarios and tests the impacts of clouds and aerosols particles on the tropospheric chemistry. The final chapter summarizes the important results in this study and give some thoughts for future research.

CHAPTER 2 MODEL CALCULATIONS OF TROPOSPHERIC OH CHEMISTRY

2.1 Introduction

A possible role of the highly reactive hydroxyl radical in the chemistry of the atmosphere was suggested by Leighton (1961). The significance of the radical for the chemical cycles of most trace gases in the troposphere was first recognized by Weinstock (1969) and Levy (1971) about two decades ago. Since then a great deal of research has been done to try to determine the distribution and chemical cycles of OH. Over the last two decades comprehensive and relatively consistent models to estimate atmospheric OH concentrations have been developed. (e.g., Fishman and Crutzen, 1978; Wofsy, 1978; Logan et al., 1981; Volz et al., 1981; Chameides and Tan, 1981; Thompson and Cicerone, 1982; Crutzen and Gidel, 1983; Chameides, 1984; Kasting and Singh, 1986; Jacob, 1986; Liu and Trainer, 1987; Lelieveld and Crutzen, 1990; Donahue and Prinn, 1990; Spivakovsky et al., 1990; Thompson et al., 1990; Hough 1991; Lu and Khalil, 1991a; Crutzen and Zimmermann, 1991; Pinto and Khalil, 1991; Lu and Khalil, 1992a). The estimated OH values during the daytime have also been confirmed by measurements with various techniques (e.g., Wang et al., 1981; Campbell et al., 1982, 1986; Watanabe et al., 1982; Davis et al., 1982; Hübler et al., 1984; Rodgers et al., 1985; Hard et al., 1986, 1992; Perner et al., 1987; Shirinzadeh et al., 1987; Felton et al., 1988; Platt et al., 1988; Chan et al., 1990; Eisele and Tanner, 1991). In addition to the photochemical model computations and the direct measurements of OH, OH concentrations can be derived independently from measurements of methyl chloroform (e.g., Singh, 1977a, b; Khalil and Rasmussen, 1984a;

Prinn et al, 1987 and 1992; Prather and Spivakovsky, 1990) and CO (Pinto et al, 1983). For an overview of measurements and model calculations of OH concentrations, see Altshuller (1989) and Thompson (1992).

Atmospheric OH remains an active area of research because of its extreme importance and complex chemistry. Most of the photochemistry in the troposphere is initiated by reactions of the hydroxyl radical with other species in the troposphere. Many environmentally important trace gases and free radicals in the troposphere react with OH. The tropospheric chemical cycles of HO_x, NO_x, and hydrocarbons are all affected and controlled by OH. Environmentally important trace gases such as CO, CH_4, nonmethane hydrocarbons, and CH_3CCl_3 and many other hydrogen-containing halocarbons that can cause global warming or destroy stratospheric O_3 are removed principally by reacting with OH.

Based on the time dependent photochemical model developed during the study for my M.S. degree (Lu, 1990), a detailed time-dependent multiple one-dimensional photochemical model (M1DPCM) has been developed to calculate the temporal (both diurnal and seasonal), spatial (altitudinal and latitudinal), and secular (from ice ages to the present) variations of a number of reactive species including OH and other reactive species in CH_iO_j, HO_x, NO_x, and O_x families. In the following sections in this chapter, tropospheric OH chemistry will first be briefly reviewed. Then the governing equations and the numerical method of the M1DPCM will be described in detail. Finally the temporal, spatial, and secular variations of a series reactive species, especially OH, will be shown and discussed.

2.2 Tropospheric OH Chemistry

To obtain the distribution of OH in the troposphere, it is essential to understand the mechanisms of its production and destruction. Figure 2.1 shows the major reactions affecting OH as well as the entire HO_x family. The HO_x family, or the odd hydrogen family, is usually defined to be the hydroxyl radical (OH), the hydroperoxyl radical (HO_2), hydrogen peroxide (H_2O_2), and the hydrogen atom (H). The primary production of OH, or the HO_x family, is the reaction between $O(^1D)$ and water vapor:

$$O(^1D) + H_2O \rightarrow OH + OH \qquad (R3)$$

where the excited oxygen atom, $O(^1D)$, comes from the photodissociation of O_3 at the wavelength less than 320 nm:

$$O_3 + h\nu \quad (\lambda \leq 320nm) \rightarrow O_2 + O(^1D) \qquad (R36)$$

Once OH is produced, it reacts with a variety of trace gases and free radicals, among which carbon monoxide and methane are two important species which significantly affect the OH distribution:

$$OH + CO \rightarrow H + CO_2 \qquad (R17)$$

$$CH_4 + OH \rightarrow CH_3 + H_2O \qquad (R18)$$

The resulting H atoms from the reaction (R17) mostly re-combine with molecular oxygen in the atmosphere to form hydroperoxyl radicals, HO_2,

$$H + O_2 + M \rightarrow HO_2 + M \qquad (R26)$$

which cycle themselves back to OH through the reactions with NO and with O_3:

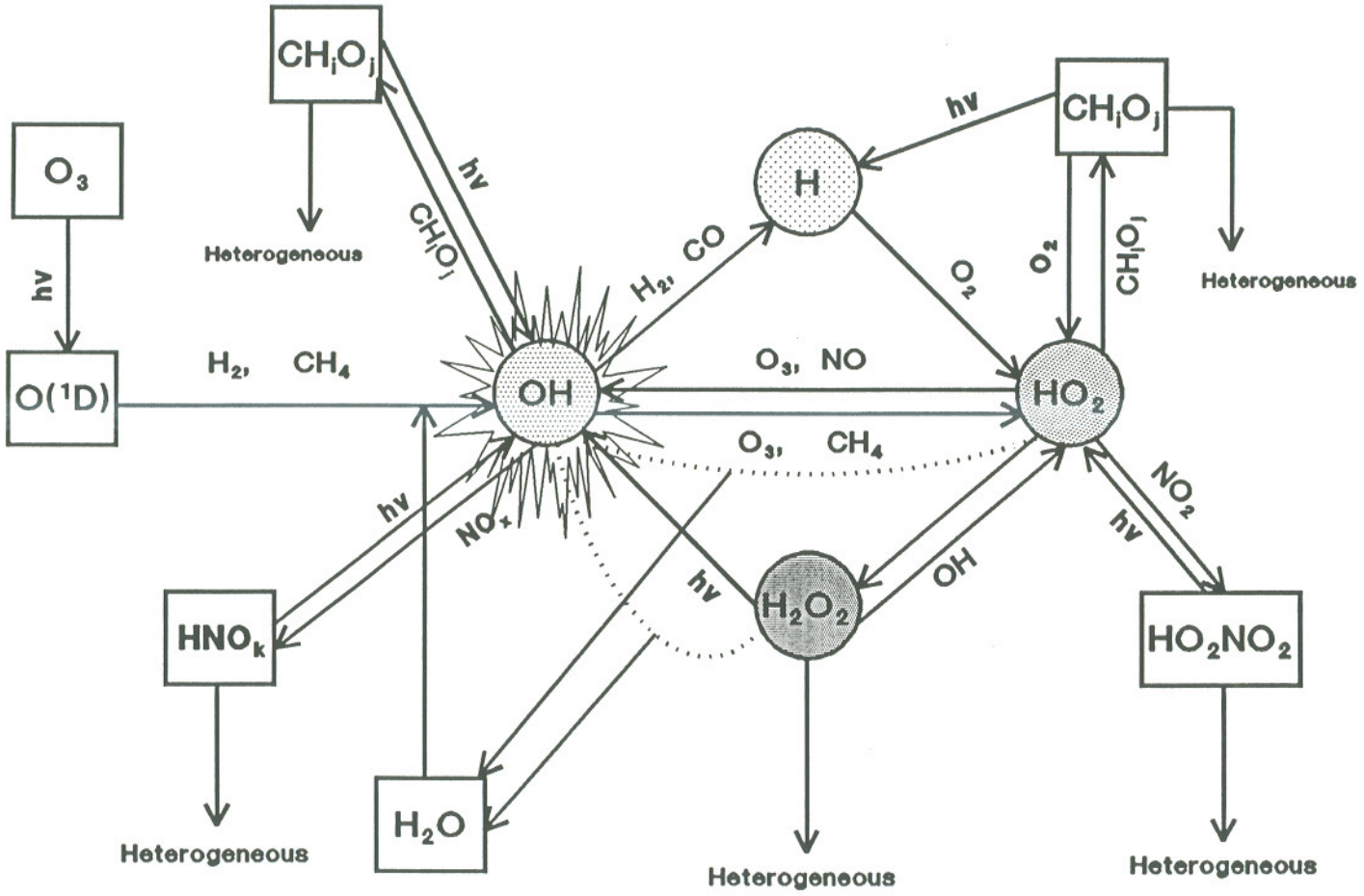

Fig. 2.1 The major reactions within the HO_x family and the main interactions of the HO_x family members with the other species and the other species families, modified from Logan et al. (1981).

$$HO_2 + NO \rightarrow OH + NO_2 \qquad (R13)$$

$$HO_2 + O_3 \rightarrow OH + O_2 + O_2 \qquad (R9)$$

It should be emphasized that reaction (R9) is the only significant source of nighttime OH since all photolysis stops and the NO concentration decreases very rapidly after sunset. Unlike daytime HO_2, nighttime HO_2, which is prevailing source of nighttime OH, mainly comes from the thermal dissociation of HO_2NO_2.

Hydroperoxyl radicals also react among themselves to generate hydrogen peroxide, H_2O_2, which may decompose to OH under sunlight:

$$HO_2 + HO_2 \rightarrow H_2O_2 + O_2 \qquad (R11)$$

$$H_2O_2 + h\nu \rightarrow OH + OH \qquad (R37)$$

The reaction between CH_4 and OH initiates a complicated sequence of reactions (for example, see Logan et al., 1981), which eventually transfer some OH to HO_2, and creates a series of organic compounds, each of which consists of only one carbon atom. It is convenient to define these compounds as a family, CH_iO_j, consisting of H_2CO, CH_3, CH_3O, CH_3O_2, CH_3OOH, and HCO. These organics also affect OH directly or indirectly.

The heterogeneous loss of H_2O_2 is a direct loss process for HO_x family. The heterogeneous removal processes of the nitrogen-containing acids such as HNO_2, HNO_3, and HO_2NO_2 are important indirect losses of HO_x family since the major sources of these acids in the troposphere are the reactions between HO_x species and NO_x species:

$$OH + NO + M \rightarrow HNO_2 + M \qquad (R29)$$

$$HO_2 + NO_2 + M \rightarrow HO_2NO_2 + M \qquad (R31)$$

$$OH + NO_2 + M \rightarrow HNO_3 + M \qquad (R30)$$

The reaction between two members of odd hydrogen family always removes at least one molecule of HO_x, creating an important loss process. Reaction (R11) is such an example. Others considered are:

$$OH + HO_2 \rightarrow H_2O + O_2 \qquad (R10)$$

$$OH + H_2O_2 \rightarrow H_2O + HO_2 \qquad (R12)$$

2.3 Equations and Numerical Solution

The mass continuity equation is a fundamental method to describe the temporal and the spatial distribution of an atmospheric trace gas:

$$\frac{\partial C_n}{\partial t} + \nabla \cdot (\vec{V} \cdot C_n) = \nabla \cdot (\vec{K} \cdot \nabla C_n) + P_n - L_n \qquad n = 1, \ 2, \ \cdots, \ N \qquad (2.1)$$

where C_n is the concentration of the nth species, $\vec{V}$ is the vector of the wind velocity, and $\vec{K}$ is the eddy diffusivity (for a review see Khalil and Rasmussen, 1984b). P_n and L_n are the chemical production and loss terms, which, according to the definition, can be expressed respectively as:

$$P_n = \sum_{r=1}^{N} \sum_{s=1}^{N} S_{r,s} K_{r,s} (C_r)^{L_r} C_s \qquad r, s \neq n \qquad (2.2)$$

$$L_n = \sum_{u=1}^{N} K_{u,n} (C_u)^{L_u} C_n \qquad (2.3)$$

where $S_{r,s}$ is the stoichiometric coefficient (proportion); $K_{r,s}$ and $K_{u,n}$ are the rate coefficients of the chemical reactions between the *r*th species and the *s*th species and between the *u*th species and the *n*th species; $K_{u,n}$ and $K_{r,s}$ are considered as zero if the related reactions are very weak or the concentrations of the corresponding reactants are not large enough to be significant. Since the reactions, which the *n*th species takes part in, result only in the losses of the *n*th species, the reactions are not sources but sinks of the *n*th species. Therefore, C_n appears only in the chemical loss terms, eq. 2.3. L_r and L_u are identification coefficients; they equal zero when the related reactions are photodissociations or a heterogeneous removal processes; otherwise they are equal to one and the corresponding reaction is a bimolecular reaction or a termolecular reaction.

For many applications, such as the species from the HO_x, NO_y, and CH_iO_j families, the terms of the transports due to the mean motion and due to the horizontal turbulent mixing can be neglected compared to other terms:

$$\frac{\partial C_n}{\partial t} = P_n - L_n + \frac{\partial}{\partial Z} K_z \frac{\partial C_n}{\partial Z} \tag{2.4}$$

Referring to eqs. 2.2 ~ 2.4, eq. 2.4 can be rewritten into two types as follows:

$$\frac{\partial C_n}{\partial t} = P_n - D_n C_n + \frac{\partial}{\partial Z} K_z \frac{\partial C_n}{\partial Z} \tag{2.5}$$

$$\frac{\partial C_n}{\partial t} = P_n - D_{1n} C_n - D_{2n} C_n^2 + \frac{\partial}{\partial Z} K_z \frac{\partial C_n}{\partial Z} \tag{2.6}$$

By comparing eqs. 2.5 and 2.6 with eqs. 2.4 and 2.3, it is clear that D_n and D_{1n} are functions of time, location, and the concentrations of other species, and D_{2n} is a function of altitude.

We have included eighteen reactive species or free radicals, which we consider most important for tropospheric OH budget. Each of them should satisfy the mass continuity equation, eq. 2.4. Specifically the equations to be solved are as follows:

$$\frac{\partial[O(^1D)]}{\partial t} = -\{K_1[N_2]+K_2[O_2]+K_3[H_2O]+K_4[H_2]+(K_{5a}+K_{5b})[CH_4] + K_6[N_2O]\}[O(^1D)]+J_{36}[O_3]+\frac{\partial}{\partial Z}K_z\frac{\partial[O(^1D)]}{\partial Z} \quad (2.7)$$

$$\frac{\partial[O]}{\partial t} = -K_{27}[O_2][O]+J_{38}[NO_2]+J_{39b}[NO_3]+(K_1[N_2]+K_2[O_2])[O(^1D)] + \frac{\partial}{\partial Z}K_z\frac{\partial[O]}{\partial Z} \quad (2.8)$$

$$\frac{\partial[OH]}{\partial t} = -\{K_{29}[NO]+K_{30}[NO_2]+K_7[H_2]+K_8[O_3]+(K_{10a}+K_{10b})[HO_2]+K_{12}[H_2O_2] + K_{17}[CO]+K_{18}[CH_4]+K_{19}[H_2CO]+K_{20}[CH_3OOH]\}[OH]+2J_{37}[H_2O_2]+J_{43}[HNO_3] + J_{40}[HNO_2]+J_{44}[HO_2NO_2]+J_{42}[CH_3OOH]+2K_3[O(^1D)][H_2O]+K_4[O(^1D)][H_2] + K_{5a}[O(^1D)][CH_4]+K_9[HO_2][O_3]+K_{13}[NO][HO_2]+\frac{\partial}{\partial Z}K_z\frac{\partial[OH]}{\partial Z} \quad (2.9)$$

$$\frac{\partial[HO_2]}{\partial t} = -\{K_9[O_3]+(K_{10a}+K_{10b})[OH]+K_{13}[NO]+K_{24}[CH_3O_2]+K_{31}[NO_2]\}[HO_2] - (K_{11a}+K_{11b})[HO_2]^2+K_8[OH][O_3]+K_{12}[OH][H_2O_2]+K_{21}[CH_3O][O_2] + K_{22}[HCO][O_2]+K_{26}[H][O_2]+K_{35}[HO_2NO_2]+\frac{\partial}{\partial Z}K_z\frac{\partial[HO_2]}{\partial Z} \quad (2.10)$$

$$\frac{\partial[H_2O_2]}{\partial t} = -\{K_{12}[OH]+K_{46}+J_{37}\}[H_2O_2]+(K_{11a}+K_{11b})[HO_2]^2 + \frac{\partial}{\partial Z}K_z\frac{\partial[H_2O_2]}{\partial Z} \quad (2.11)$$

$$\frac{\partial[H]}{\partial t} = -K_{26}[O_2][H] + J_{41a}[H_2CO] + K_4[O(^1D)][H_2] + K_7[OH][H_2]$$

$$+ K_{17}[OH][CO] + \frac{\partial}{\partial Z}K_z\frac{\partial[H]}{\partial Z} \qquad (2.12)$$

$$\frac{\partial[NO]}{\partial t} = -\{K_{25}[CH_3O_2] + K_{13}[HO_2] + K_{14}[O_3] + K_{15}[NO_3] + K_{29}[OH]\}[NO]$$

$$+ 2K_6[O(^1D)][N_2O] + J_{38}[NO_2] + J_{40}[HNO_2] + J_{39a}[NO_3] + \frac{\partial}{\partial Z}K_z\frac{\partial[NO]}{\partial Z} \qquad (2.13a)$$

By substituting $[NO]=[NO_x]-[NO_2]$ into the above equation, we get

$$\frac{\partial[NO]}{\partial t} = -\{K_{25}[CH_3O_2] + K_{13}[HO_2] + K_{14}[O_3] + K_{15}[NO_3] + K_{29}[OH] + J_{38}\}[NO]$$

$$+ 2K_6[O(^1D)][N_2O] + J_{38}[NO_x] + J_{40}[HNO_2] + J_{39a}[NO_3] + \frac{\partial}{\partial Z}K_z\frac{\partial[NO]}{\partial Z} \qquad (2.13b)$$

$$\frac{\partial[NO_2]}{\partial t} = -\{K_{30}[OH] + K_{31}[HO_2] + K_{32}[NO_3] + K_{33}[CH_3O_2] + J_{38} + K_{16}[O_3]\}[NO_2]$$

$$+ K_{34}[N_2O_5] + K_{35}[HO_2NO_2] + J_{39b}[NO_3] + J_{45}[N_2O_5] + J_{43}[HNO_3] + K_{13}[NO][HO_2]$$

$$+ K_{14}[NO][O_3] + 2K_{15}[NO][NO_3] + K_{25}[CH_3O_2][NO] + \frac{\partial}{\partial Z}K_z\frac{\partial[NO_2]}{\partial Z} \qquad (2.14a)$$

By substituting $[NO_2]=[NO_x]-[NO]$ into the above equation, we obtain

$$\frac{\partial[NO_2]}{\partial t} = -\{K_{30}[OH] + K_{31}[HO_2] + K_{32}[NO_3] + K_{33}[CH_3O_2] + J_{38} + K_{16}[O_3] + (K_{13}[HO_2]$$

$$+ K_{14}[O_3] + 2K_{15}[NO_3] + K_{25}[CH_3O_2])\}[NO_2] + K_{34}[N_2O_5] + K_{35}[HO_2NO_2] + J_{39b}[NO_3]$$

$$+ J_{45}[N_2O_5] + J_{43}[HNO_3] + (K_{13}[HO_2] + K_{14}[O_3] + 2K_{15}[NO_3] + K_{25}[CH_3O_2])[NO_x]$$

$$+ K_{25}[CH_3O_2])[NO_x] + \frac{\partial}{\partial Z}K_z\frac{\partial[NO_2]}{\partial Z} \qquad (2.14b)$$

$$\frac{\partial[NO_3]}{\partial t} = -\{K_{32}[NO_2]+(J_{39a}+J_{39b})+K_{15}[NO]\}[NO_3]+K_{34}[N_2O_5]+J_{45}[N_2O_5]$$

$$+J_{44}[HO_2NO_2]+K_{16}[NO_2][O_3]+\frac{\partial}{\partial Z}K_z\frac{\partial[NO_3]}{\partial Z} \qquad (2.15)$$

$$\frac{\partial[N_2O_5]}{\partial t} = -(K_{34}+J_{45})[N_2O_5]+K_{32}[NO_2][NO_3]+\frac{\partial}{\partial Z}K_z\frac{\partial[N_2O_5]}{\partial Z} \qquad (2.16)$$

$$\frac{\partial[HNO_2]}{\partial t} = -(K_{46}+J_{40})[HNO_2]+K_{29}[OH][NO]+\frac{\partial}{\partial Z}K_z\frac{\partial[HNO_2]}{\partial Z} \qquad (2.17)$$

$$\frac{\partial[HO_2NO_2]}{\partial t} = -(K_{46}+K_{35}+J_{44})[HO_2NO_2]+K_{31}[HO_2][NO_2]$$

$$+\frac{\partial}{\partial Z}K_z\frac{\partial[HO_2NO_2]}{\partial Z} \qquad (2.18)$$

$$\frac{\partial[CH_3]}{\partial t} = -K_{28}[O_2][CH_3]+K_{5a}[O(^1D)][CH_4]+K_{18}[OH][CH_4]+\frac{\partial}{\partial Z}K_z\frac{\partial[CH_3]}{\partial Z} \qquad (2.19)$$

$$\frac{\partial[H_2CO]}{\partial t} = -\{K_{46}+J_{41a}+J_{41b}+K_{19}[OH]\}[H_2CO]+K_{5b}[O(^1D)][CH_4]$$

$$+K_{21}[CH_3O][O_2]+K_{23b}[CH_3O_2]^2+\frac{\partial}{\partial Z}K_z\frac{\partial[H_2CO]}{\partial Z} \qquad (2.20)$$

$$\frac{\partial[CH_3O]}{\partial t} = -K_{21}[O_2][CH_3O]+J_{42}[CH_3OOH]+K_{25}[CH_3O_2][NO]$$

$$+2K_{23a}[CH_3O_2]^2+\frac{\partial}{\partial Z}K_z\frac{\partial[CH_3O]}{\partial Z} \qquad (2.21)$$

$$\frac{\partial[CH_3O_2]}{\partial t} = -\{K_{33}[NO_2]+K_{24}[HO_2]+K_{25}[NO]\}[CH_3O_2]-(K_{23a}+K_{23b}$$

$$+K_{23c})[CH_3O_2]^2+K_{28}[O_2][CH_3]+K_{20}[OH][CH_3OOH]+\frac{\partial}{\partial Z}K_z\frac{\partial[CH_3O_2]}{\partial Z} \qquad (2.22)$$

$$\frac{\partial[CH_3OOH]}{\partial t} = -\{K_{46} + J_{42} + K_{20}[OH]\}[CH_3OOH] + K_{24}[CH_3O_2][HO_2] + \frac{\partial}{\partial Z}K_z\frac{\partial[CH_3OOH]}{\partial Z} \quad (2.23)$$

$$\frac{\partial[HCO]}{\partial t} = -K_{22}[O_2][HCO] + J_{41a}[H_2CO] + K_{19}[OH][H_2CO] + \frac{\partial}{\partial Z}K_z\frac{\partial[HCO]}{\partial Z} \quad (2.24)$$

where a species with the brackets, [ ], represents the concentration of the species at time t. Among eqs. 2.7 ~ 2.24, only eqs. 2.10 and 2.22 are like eq. 2.6. The other equations are like eq. 2.5. In our calculations, the distribution of NO_x was taken from Logan et al. (1981).

Consequently, the eqs. 2.7 ~ 2.24 are coupled together, defining the variation of tropospheric OH and other reactive species. Unfortunately, there are no analytical solutions to such high order partial differential equations. Therefore the numerical method for such a highly nonlinear equation set is required in order to obtain the concentrations of OH and other reactive species.

In this study, Eulerian-backward implicit finite difference approximation was used to numerically solve the above set of partial differential equations. Specifically, the finite difference approximations to eqs. 2.5 and 2.6 are expressed as:

$$\frac{C_{n_j}^{i+1} - C_{n_j}^{i}}{\Delta t_i} = P_{n_j}^{i+1} - D_{n_j}^{i+1}\cdot C_{n_j}^{i+1} + \frac{K_{z_{j+\frac{1}{2}}}\cdot C_{n_{j+1}}^{i+1} + K_{z_{j-\frac{1}{2}}}\cdot C_{n_{j-1}}^{i+1}}{\Delta Z^2} - \frac{\left(K_{z_{j+\frac{1}{2}}} + K_{z_{j-\frac{1}{2}}}\right)\cdot C_{n_j}^{i+1}}{\Delta Z^2} \quad (2.25)$$

$$\frac{C_{n_j}^{i+1} - C_{n_j}^{i}}{\Delta t_i} = P_{n_j}^{i+1} - D_{1n_j}^{i+1} \cdot C_{n_j}^{i+1} - D_{2n_j} \cdot \left(C_{n_j}^{i+1}\right)^2 + \frac{K_{z_{j+\frac{1}{2}}} \cdot C_{n\,j+1}^{i+1} + K_{z_{j-\frac{1}{2}}} \cdot C_{n\,j-1}^{i+1}}{\Delta Z^2} - \frac{\left(K_{z_{j+\frac{1}{2}}} + K_{z_{j-\frac{1}{2}}}\right) \cdot C_{n_j}^{i+1}}{\Delta Z^2} \qquad (2.26)$$

where subscript n stands for the *n*th species, subscript j represents the *j*th grid point, superscript i denotes the *i*th time step. It should be noted that $\Delta t_i = t_{i+1} - t_i$ and $K_{j+1/2}$ is the mean value of eddy diffusivity between the vertical grids of j and j+1.

One might notice that eqs. 2.25 and 2.26 contain the concentrations of the *n*th species, which are located at the *(j-1)*th, *j*th, and *(j+1)*th vertical grids, and depend on time at stages *i* and *i+1*. In addition, in these two equations, P_n, D_n, and D_{1n} include concentrations of other species and free radicals, which are at the *j*th vertical grid and also depend on time at stage i+1. However, eq. 2.25 can be seen as a normal linear equation of $C_{n_j}^{i+1}$ and eq. 2.26 can be seen a normal quadratic equation of $C_{n_j}^{i+1}$. Thus solving the differential equations is the same as solving a system of normal algebraic equations, which only contains linear and quadratic equations like eqs. 2.25 and 2.26. The solution of the linear equation, eq. 2.25, is:

$$C_{n_j}^{i+1} = \frac{C_{n_j}^{i} + P_{n_j}^{i+1} \cdot \Delta t_i + \left(K_{z_{j+\frac{1}{2}}} \cdot C_{n\,j+1}^{i+1} + K_{z_{j-\frac{1}{2}}} \cdot C_{n\,j-1}^{i+1}\right) \cdot \Delta t_i / \Delta Z^2}{1 + D_{n_j}^{i+1} \cdot \Delta t_i + \left(K_{z_{j+\frac{1}{2}}} + K_{z_{j-\frac{1}{2}}}\right) \cdot \Delta t_i / \Delta Z^2} \qquad (2.27)$$

Using the quadratic formula, the solution of the quadratic equation, eq. 2.26, can be found:

$$C_{n_j}^{i+1} = \frac{-b + \sqrt{b^2 + 4 \cdot a \cdot c}}{2 \cdot a} = \frac{2 \cdot c}{b + \sqrt{b^2 + 4 \cdot a \cdot c}} \qquad (2.28)$$

where $a = \Delta t_i \cdot D_{2n_j}$

$$b = 1 + \Delta t_i \cdot D_{1n_j}^{i+1} + (K_{z_{j+\frac{1}{2}}} + K_{z_{j-\frac{1}{2}}}) \cdot \Delta t_i / \Delta Z^2$$

$$c = C_{n_j}^{i} + P_{n_j}^{i+1} \cdot \Delta t_i + \left(K_{z_{j+\frac{1}{2}}} \cdot C_{n_{j+1}}^{i+1} + K_{z_{j-\frac{1}{2}}} \cdot C_{n_{j-1}}^{i+1} \right) \cdot \Delta t_i / \Delta Z^2$$

It should be noted that the right sides of eqs. 2.27 and 2.28 also contain terms which depend on time at stage i+1. There are no exact solutions for such kinds of highly nonlinear algebraic equations. The iterative process is thus used here to solve the equations. The iterative process we used contains three aspects: a number of initial values to begin an iterative process, a series of iterative formulas in forms of eqs. 2.27 and 2.28 to do successive approximations, and a periodic condition to test the validity, convergence, and accuracy of the model computations. Considering the reactive natures of the species, the photo-steady state is assumed to estimate the initial values. In addition, only a few reactions, which are supposed to most significantly affect the *i*th species, are taken into account in the computation of the initial estimate of the *i*th species. For example, only the effects caused by CO, CH_4, $O(^1D)$, and H_2O, are considered to determine the initial concentration of OH. For the detailed description of the technique to determine the initial concentrations of the reactive species, see Lu (1990). The periodic condition is based on the fact that the difference of the concentrations of a reactive species at the same time but in the two adjacent days is very small and can be neglected, i.e.:

$$C_n(t+24, Z) \doteq C_n(t, Z) \qquad 0 \le t < 24 \text{ Hours} \qquad (2.29)$$

where the subscript n designates the *n*th reactive species. In the model to calculate the concentration of the hydroxyl radical, the above equation can be further expressed as:

$$\frac{|C_n(t_i+24, Z)-C_n(t_i, Z)|}{C_n(t_i, Z)} \le 10^{-6} \qquad 0 \le t_i < 24 \ \text{Hours} \qquad (2.30)$$

where subscript i represents the *i*th time state and Z is altitude.

2.4 Input

In order to calculate the concentrations of OH and other reactive species, the distributions of H_2O, CO, CH_4, NO_x, O_3, and the rates of a series of atmospheric chemical reactions are required before the numerical method described in the previous section is used.

2.4.1 Chemical Reactions and Rates

Table 2.1a to table 2.1d list all chemical reactions included in our photochemical model. These reactions greatly affect tropospheric OH directly or indirectly. There are three categories of chemical reactions that are taken into account in this study: bimolecular reactions, termolecular reactions, and photodissociations. Photodissociations are stimulated by the radiative energy, and they initiate the whole atmospheric chemical reactions. The rate of the photolysis of a molecule or free radical (*species m)* can be quantitatively expressed as:

$$J_m = \int_{\lambda_1}^{\lambda_2} \Phi_m(\lambda, T)\sigma_m(\lambda, T)j(\lambda, \theta)d\lambda \qquad (2.31a)$$

where $\Phi_m(\lambda, T)$ is the quantum yield of the photodissociation that the species *m* experiences on absorbing radiation of wavelength λ at temperature T. Here the quantum yield denotes the probability for the occurrences of the dissociation after the

Table 2.1a. Binary Reactions and Rate Expressions.

No.	Reaction			Rate Expression
1	$O(^1D) + N_2$	→	$O + N_2$	1.8(-11) exp (107/T)
2	$O(^1D) + O_2$	→	$O + O_2$	3.2(-11) exp (67/T)
3	$O(^1D) + H_2O$	→	$OH + OH$	2.2(-10)
4	$O(^1D) + H_2$	→	$H + OH$	1.0(-10)
5a	$O(^1D) + CH_4$	→	$OH + CH_3$	1.4(-10)
5b	$O(^1D) + CH_4$	→	$H_2 + H_2CO$	1.4(-11)
6	$O(^1D) + N_2O$	→	$NO + NO$	6.7(-11)
7	$OH + H_2$	→	$H_2O + H$	6.1(-12) exp (-2030/T)
8	$OH + O_3$	→	$HO_2 + O_2$	1.6(-12) exp (-940/T)
9	$HO_2 + O_3$	→	$2O_2 + OH$	1.4(-14) exp (-580/T)
10a	$OH + HO_2$	→	$H_2O + O_2$	1.7(-11) exp (416/T)
10b	$OH + HO_2 + M$	→	$H_2O + O_2 + M$	3.0(-31) [M] exp (500/T)
11a	$HO_2 + HO_2$	→	$H_2O_2 + O_2$	2.3(-13) exp (590/T)
11b	$2HO_2 + M$	→	$H_2O_2 + O_2 + M$	1.7(-33) [M] exp (1000/T)
12	$OH + H_2O_2$	→	$H_2O + HO_2$	3.1(-12) exp (-187/T)
13	$NO + HO_2$	→	$NO_2 + OH$	3.7(-12) exp (240/T)
14	$NO + O_3$	→	$NO_2 + O_2$	1.8(-12) exp (-1370/T)
15	$NO + NO_3$	→	$2NO_2$	1.3(-11) exp (250/T)
16	$NO_2 + O_3$	→	$NO_3 + O_2$	1.2(-13) exp (-2450/T)
17	$OH + CO$	→	$CO_2 + H$	1.5(-13) $(1 + 0.6\ P_{atm})$
18	$OH + CH_4$	→	$CH_3 + H_2O$	2.4(-12) exp (-1710/T)
19	$OH + H_2CO$	→	$H_2O + HCO$	1.0(-11)
20	$OH + CH_3OOH$	→	$CH_3O_2 + H_2O$	1.0(-11)
21	$CH_3O + O_2$	→	$H_2CO + HO_2$	8.4(-14) exp (-1200/T)
22	$HCO + O_2$	→	$CO + HO_2$	3.5(-12) exp (140/T)
23a	$CH_3O_2 + CH_3O_2$	→	$2CH_3O + O_2$	
23b		→	$H_2CO + CH_3OH + O_2$	1.6(-13) exp (220/T)
23c		→	$CH_3OOCH_3 + O_2$	
24	$CH_3O_2 + HO_2$	→	$CH_3OOH + O_2$	7.7(-14) exp (1300/T)
25	$CH_3O_2 + NO$	→	$CH_3O + NO_2$	4.2(-12) exp (180/T)

Table 2.1b. Termolecular Reactions

No.	Reaction	k_0^{300}	n	k_∞^{300}	m
26	$H + O_2 + M \rightarrow HO_2 + M$	5.5(-32)	1.6	7.5(-11)	0.
27	$O + O_2 + M \rightarrow O_3 + M$	6.0(-34)	2.3	-	-
28	$CH_3 + O_2 + M \rightarrow CH_3O_2 + M$	4.5(-31)	2.0	1.8(-12)	1.7
29	$OH + NO + M \rightarrow HNO_2 + M$	7.0(-31)	2.6	1.5(-11)	0.5
30	$OH + NO_2 + M \rightarrow HNO_3 + M$	2.6(-30)	3.2	2.4(-11)	1.3
31	$HO_2 + NO_2 + M \rightarrow HO_2NO_2 + M$	2.0(-31)	2.7	4.2(-12)	2.0
32	$NO_2 + NO_3 + M \rightarrow N_2O_5 + M$	2.2(-30)	4.3	1.5(-12)	0.5
33	$NO_2 + CH_3O_2 + M \rightarrow CH_3O_2NO_2 + M$	1.5(-30)	4.0	6.5(-12)	2.0
34	$N_2O_5 + M \rightarrow NO_2 + NO_3 + M$	$K_{32} \times 5.65(+26) \exp(-11001/T)$			
35	$HO_2NO_2 + M \rightarrow HO_2 + NO_2 + M$	$1.3(+14) \exp(-10418/T)$			

Table 2.1c. Photodissociation Processes

No.	Reaction
36	$O_3 + h\nu \rightarrow O(^1D) + O_2$
37	$H_2O_2 + h\nu \rightarrow OH + OH$
38	$NO_2 + h\nu \rightarrow NO + O$
39a	$NO_3 + h\nu \rightarrow NO + O_2$
39b	$NO_3 + h\nu \rightarrow NO_2 + O$
40	$HNO_2 + h\nu \rightarrow OH + NO$
41a	$H_2CO + h\nu \rightarrow HCO + H$
41b	$H_2CO + h\nu \rightarrow H_2 + CO$
42	$CH_3OOH + h\nu \rightarrow CH_3O + OH$
43	$HNO_3 + h\nu \rightarrow NO_2 + OH$
44	$HO_2NO_2 + h\nu \rightarrow NO_3 + OH$
45	$N_2O_5 + h\nu \rightarrow NO_3 + NO_2$

Table 2.1d. Heterogeneous Processes

No.	Species	Rate Expression	
46	HNO_2 HNO_3 HO_2NO_2 H_2O_2 H_2CO CH_3OOH	K_0	$Z \leq Z_0$
		$K_0 \exp[-A(Z-Z_0)]$	$Z > Z_0$

Note: 1. The notation 1.8(-11) represents 1.8×10^{-11}.

2. Apart from reactions 34, 35, 39, 45, and 46, the chemical kinetic and photochemical data in the above tables are taken from NASA (1985).

3. Apart from reactions 34 and 35, the rate expression for the termolecular reactions is expressed as:

$$K_{ter}(T,M) = \frac{K_0(T)[M]}{1+K_0(T)[M]/K_\infty(T)} 0.6^{\left\{1+[Log_{10}\frac{K_0(T)[M]}{K_\infty(T)}]^2\right\}^{-1}}$$

where [M] is the number density of the atmosphere; $K_0=K_0^{300}(300/T)^n$ is low-pressure limiting rate; $K_\infty=K_\infty^{300}(300/T)^m$ is high-pressure limiting rate.

4. The rate expressions of reactions 34 and 35 are from Atkinson and Lloyd (1984). The cross sections and quantum yields of NO_3 are taken or derived from Atkinson and Lloyd (1984). The cross section of N_2O_5 is taken from table 3.32 from Finlayson-Pitts and Pitts (1986) by using the temperature-dependent expression recommended by Yao et al. (1984).

5. The rate heterogeneous loss is taken from Logan et al. (1981) and Z_0=4 (km) in the formula is the height of the layer, under which the heterogeneous loss rate, $K_0=2.31\times10^{-6}$, is uniform. Above the layer in the troposphere the rate decreases exponentially with height, and $A=1.6\times10^{-4}$.

species m is excited by the solar insolation. $\sigma_m(\lambda, T)$ is the absorption cross section at wavelength λ and temperature T, which is analogous to the geometrical area of the molecule, denoting the amount of energy absorbed by the molecule; $j(\lambda, \theta)$ is the actinic flux (the integrated radiation from all directions to a sphere) at wavelength λ and the solar zenith angle, θ, which can be expressed as a function of known angles (Liou, 1980):

$$\cos\theta = \sin i \sin l + \cos i \cos l \cos h \qquad (2.32)$$

where i is the solar inclination; l is the latitude; h is the hour angle.

The inclination i, which is the angular distance of the sun north (positive) or south (negative) of the equator, is a function only of the day of year and is independent of location. It varies from 23°27' on June 21 to -23°27' on December 22. The hour angle h is zero at solar noon, and increases by 15° for every hour before or after solar noon. Given a certain latitude and a particular day of a year, the particular time of the day at the latitude can be expressed as:

$$t = 12 - \cos^{-1}\left(\frac{\cos\theta - \sin i \sin l}{\cos i \cos l}\right) / 15^\circ \ (\text{Hour}) \qquad \text{When } t \le 12 \text{ Hour} \qquad (2.33a)$$

$$t = 12 + \cos^{-1}\left(\frac{\cos\theta - \sin i \sin l}{\cos i \cos l}\right) / 15^\circ \ (\text{Hour}) \qquad \text{When } t > 12 \text{ Hour} \qquad (2.33b)$$

Upon substituting values of a specific latitude, the specific solar inclination corresponding the particular day of a year, and various values of solar zeniths from 0° to 86°, we can obtain the corresponding time of the day at the particular location. In order to compute the photodissociation rate constants by using the intensity of the solar radiation at each time step during the daytime, we choose the time values calculated by eqs. 2.33a and 2.33b as daytime grids. There is no photodissociation

during the night; therefore, the time grids at night are simply chosen at equal intervals between each of two adjacent time nodes. There are twenty-seven time nodes a day, varying with seasons and latitudes.

In practice, the integral in eq. 2.31a is usually approximated by a summation over a wavelength interval of 5~10 nm and the actinic flux is seen as the function of time t instead of the zenith angle θ:

$$J_M = \sum_j \bar{\Phi}(\lambda_j, T)\bar{\sigma}(\lambda_j, T)\bar{j}(\lambda_j, t)\Delta\lambda \qquad (2.31b)$$

where the overbar denotes an average over a wavelength interval $\Delta\lambda$ centered at λ_j, and t denotes the time of day.

All the photolysis processes included in this study are listed in table 2.1d. Most of the absorption cross sections and quantum yield data are also taken from DeMore et al. (1985). The cross section for photolysis of N_2O_5 is taken from table 3.32 from Finlayson-Pitts and Pitts (1986) by using the temperature-dependent expression recommended by Yao et al. (1984). The cross section and quantum yield of NO_3 are taken from Atkinson et al. (1984). The solar radiation intensity is taken from Seinfeld (1986), derived from the results of Demerjian et al. (1980) in this study. Later, the actinic fluxes directly calculated from our detailed radiative transfer model will be also used to test the effects of variation of radiation fields on troposphere chemistry (see chapters 4 and 6 for more detail).

Though chemical reactions in the atmosphere are initiated mainly by solar radiation, most common reactions in the troposphere take place by molecular collision processes. Bimolecular reactions and termolecular reactions belong to this category. There are only two reactants involved in a bimolecular reaction, and the rates of

bimolecular reactions are generally independent of atmospheric pressure except the reaction between OH and CO, which has a linear relation with atmospheric pressure, as shown in table 2.1a. The rate for a bimolecular reaction is usually given in Arrhenius form:

$$K_{bim}(T) = A\exp\{-\left(\frac{E}{R}\right)/T\} \tag{2.34}$$

where T is the absolute temperature, and R is the gas constant. The pre-exponential factor A is related to the collision frequency between reactants. The constant E is referred to as the activation energy, following the proposal first made by S. Arrhenius in 1889.

Although three different molecules or free radicals participate in a termolecular reaction, the third participants, N_2 or O_2, usually acts as a "catalyst". Termolecular reactions exhibit a pressure dependence. The formula for the rate of a termolecular reaction is expressed as:

$$K_{ter}(T,M) = \frac{K_0(T)[M]}{1+K_0(T)[M]/K_\infty(T)}\,0.6^{\left\{1+[\mathrm{Log}_{10}(K_0(T)[M]/K_\infty(T))]^2\right\}^{-1}} \tag{2.35}$$

where [M] is the number density of the atmosphere; $K_0(T) = K_0^{300}\left(\frac{T}{300}\right)^{-n}$ is low-pressure limiting rate; and $K_\infty(T) = K_\infty^{300}\left(\frac{T}{300}\right)^{-m}$ is high-pressure limiting rate.

The kinetic data to calculate bimolecular and termolecular reaction rates are listed in table 2.1a and table 2.1b. Apart from reaction 34 and reaction 35, the kinetic data are adopted from DeMore et al. (1985). The kinetic data relevant to reaction 34 and reaction 35 are taken from Atkinson and Lloyd (1984).

Though a chemical reaction in the atmosphere changes the concentration of a certain species, in chemistry the integrity of the atom is preserved. In fact, chemical reactions only rearrange the atoms among the molecules. Molecules and free radicals are ultimately removed from the atmosphere through the processes of heterogeneous removal of big molecules and big radicals, which are generated by small radicals and small molecules. The major heterogeneous loss process is the absorption of big molecules by droplets followed by the removal of droplets by precipitation (precipitation scavenging process). The following formula for the rate of the loss process was first suggested by Fishman and Crutzen (1977) and used by a number of authors later on (Fishman and Crutzen, 1978; Logan et al., 1981; Lu and Khalil, 1991; Tie et al., 1991):

$$K_{het}(Z) = K_0 \exp[-A(Z-Z_0)] \qquad \text{where} \qquad Z > Z_0 \qquad (2.36a)$$

$$K_{het}(Z) = K_0 \qquad \text{where} \qquad Z \le Z_0 \qquad (2.36b)$$

where Z_0 (km) is the height of the layer, in which heterogeneous loss rate, K_0 is uniform. The heterogeneous loss rate expression and the related data are from Logan et al. (1981), as shown in table 2.1c.

Capture and absorption by soil, vegetation, buildings, and other surfaces, and collision with particulates or aerosols are not important removal process for molecules and free radicals, especially above the surface layer. These processes are neglected in this study.

2.4.2 Physical Characteristics of the Model Atmosphere:

The model atmosphere adopted in this study is the U. S. Standard Atmosphere (U. S. Standard Atmosphere, 1976), which is an idealized, steady-state representation of the earth's atmosphere. The fractional-volume compositions are 0.78084 for N_2, 0.209476 for O_2, and 5×10^{-7} for H_2. The profiles of temperature and pressure, shown in figure 2.2, are expressed as follows:

$$T = 288.15 - 0.656500Z \quad (°K) \qquad 0 \le Z < 11 \,(km) \qquad (3.37a)$$

$$T = 216.650 \quad (°K) \qquad 11 \le Z < 20 \,(km) \qquad (3.37b)$$

$$P = 101325\left(\frac{288.15}{T}\right)^{-5.255877} \quad (N/m^2) \qquad 0 \le Z < 11 \,(km) \qquad (3.38a)$$

$$P = 22632\, e^{-0.156768832(Z-11)} \,(N/m^2) \qquad 11 \le Z < 20 \,(km) \qquad (3.38b)$$

The number density of the atmosphere, [M], can be expressed by using the ideal gas law as follows:

$$[M] = 10^{-6} \cdot \frac{P \cdot N_0}{R \cdot T} \quad (molecule/cm^3) \qquad (3.39)$$

where R=8.31432 J $mole^{-1}$ $°K^{-1}$, is the universal gas constant and $N_0 = 6.02297\times10^{23}$ molecules/mole, is Arogadro's number. The vertical profile of the number density of the atmosphere is displayed in fig. 2.3. Thus the number densities of species such as N_2, O_2, and H_2 is equal to its fractional-volume, f_p, times the number density of the atmosphere.

$$C_p = f_p \cdot [M] \qquad (3.40)$$

where C_p represents the number density of the species p such as N_2, O_2, N_2O, H_2,

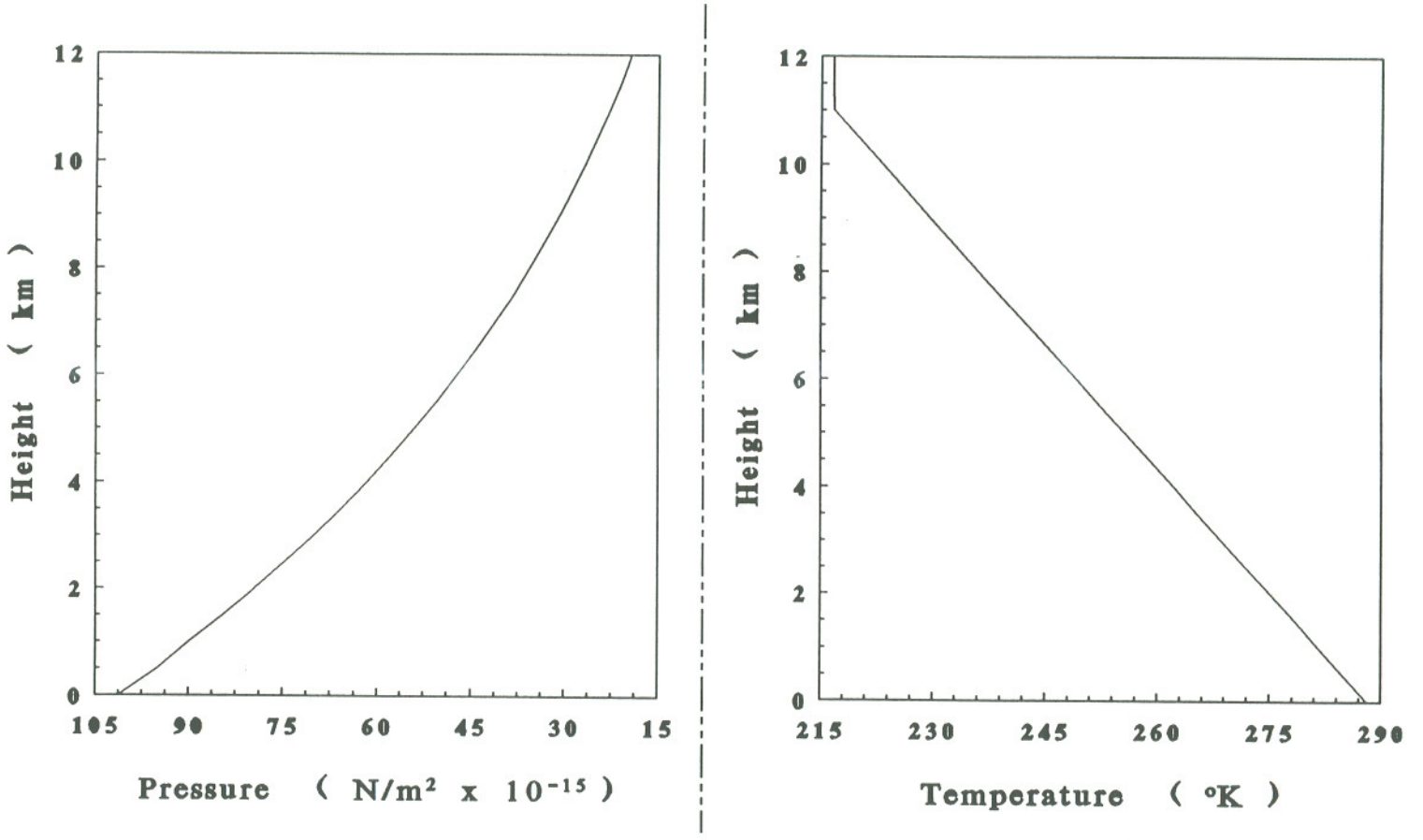

Fig. 2.2 The vertical profiles of pressure and temperature in the troposphere, adapted from U.S. Standard Atmosphere (1976).

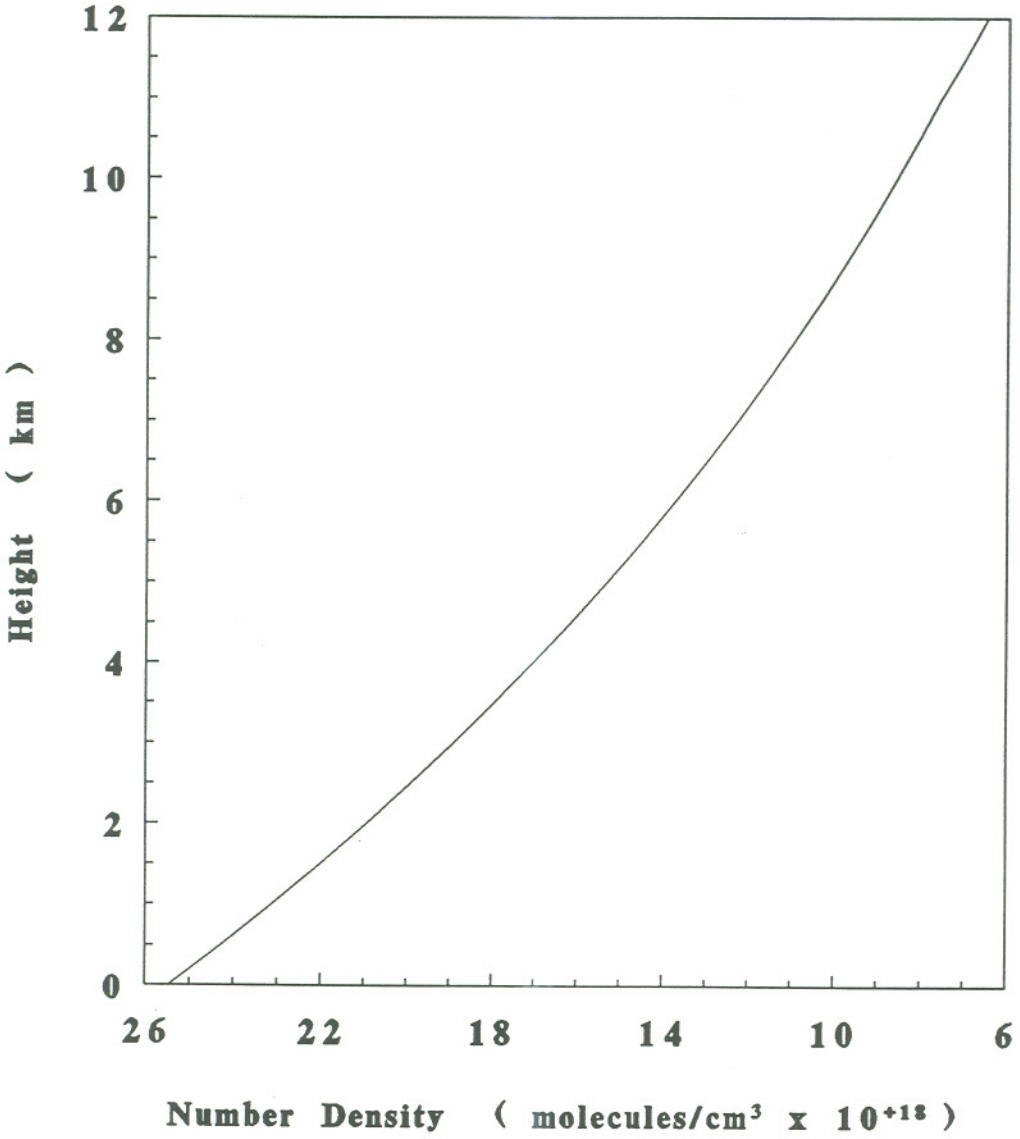

Fig. 2.3 The vertical profiles of the number density of the air molecules in the troposphere (U. S. Standard Atmosphere, 1976).

CO, CH_4, etc, and f_p represents the fractional-volume of the species p.

The distribution of water vapor is adapted from Logan et al. (1981), as shown in fig. 2.4. Generally the number densities of water vapor are higher in tropics than in the middle latitudes corresponding to larger area of ocean in the tropics than in the middle latitudes. The seasonal variations with maximum values in summer and minimum values in winter are more significant in the middle latitudes than in the tropics resulting from a bigger seasonal variation of temperature in the middle latitudes than in the tropics. This feature of water vapor is easily understood since the atmosphere with higher temperature holds more water vapor than that with lower temperature.

The vertical profiles of CO are shown in fig. 2.5. This distribution was obtained by simply adapting the surface CO measurements (Khalil and Rasmussen, 1984c and 1990) and by assuming that the ratio of CO concentration obtained by Khalil and Rasmussen (1984c and 1990) to that used by Logan et al. (1981) is a constant at all heights in the troposphere for a given season and latitude (also see Lu and Khalil, 1991a).

The vertical distributions of NO_x ($NO+NO_2$) and nitric acid are taken from Logan et al. (1981). Figs 2.6 and 2.7. show their distributions in the northern hemisphere. The higher NO_x level at 45 °N than at 15 °N, resulting from larger anthropogenic sources in the middle latitudes than in the tropics in the northern hemisphere. The seasonal cycle of NO_x with its maximum in winter and its minimum in summer results from the seasonal variations of its sink, OH, which has a maximum concentration in summer and minimum value in winter.

The vertical profiles of O_3 were derived from O_3 measurements by Logan et al.

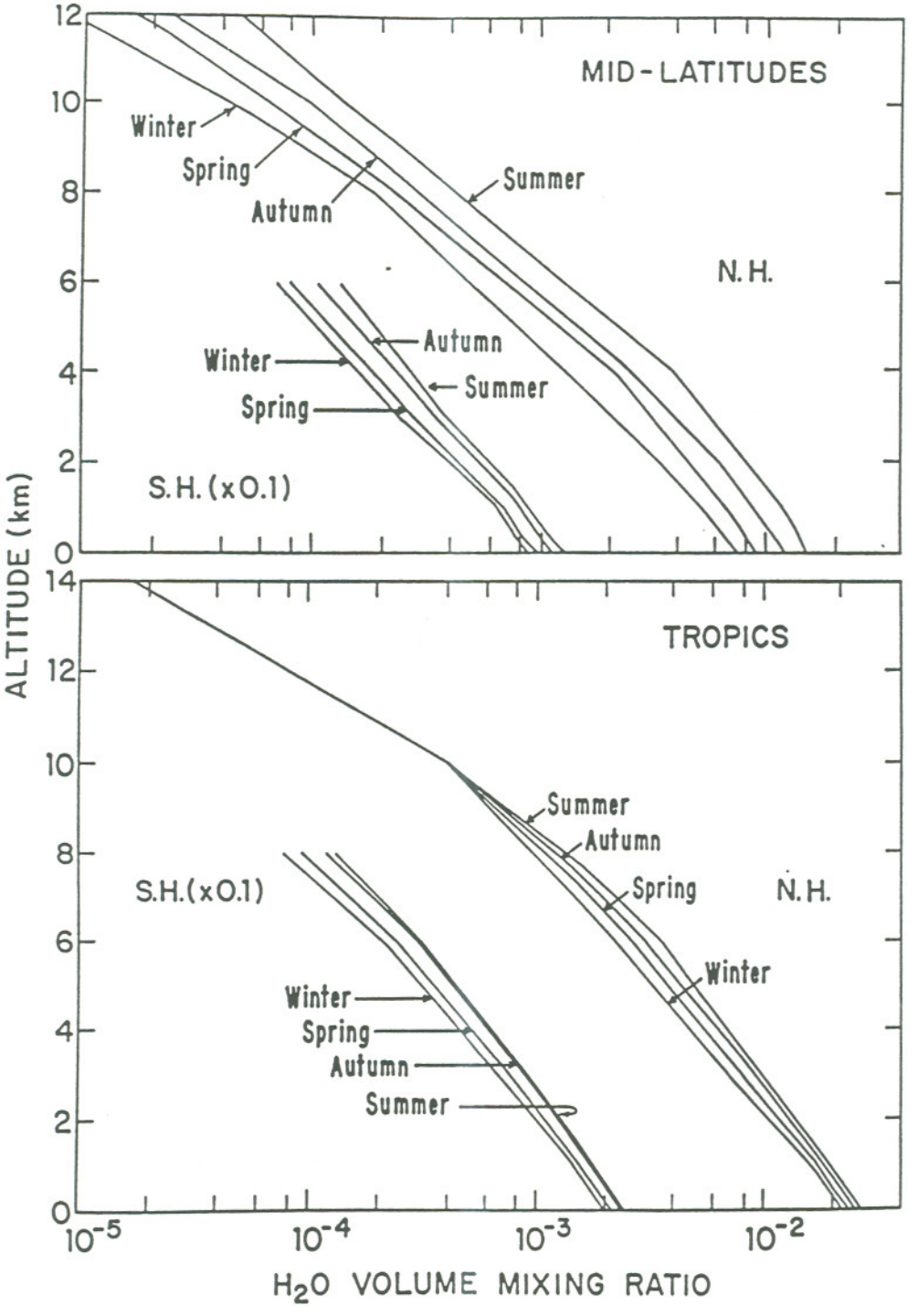

Fig. 2.4 The distribution of water vapor in the troposphere, taken from Logan et al. (1981).

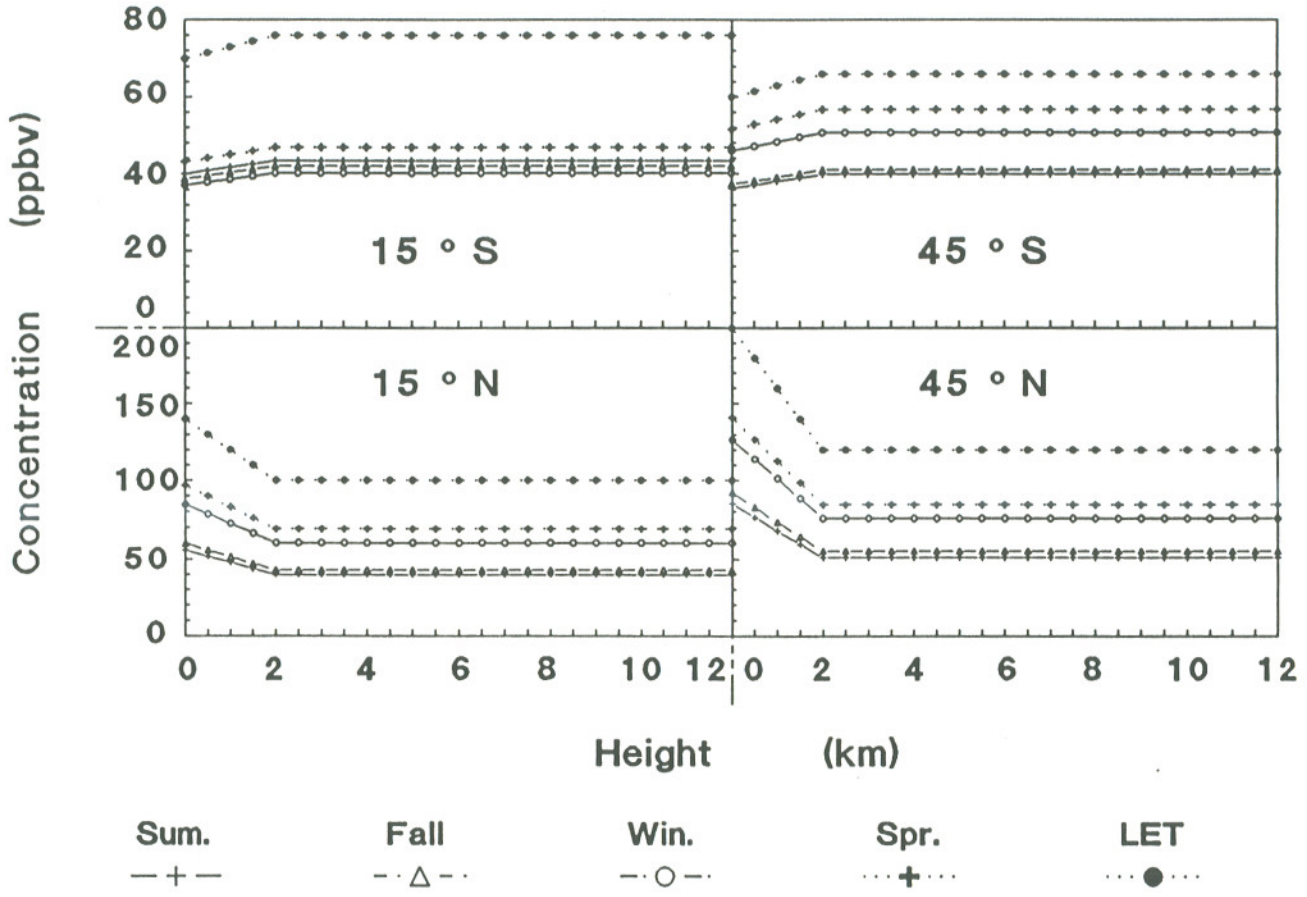

Fig. 2.5 The vertical profiles of CO, adapted from Lu and Khalil (1991). "LET" represents the vertical profiles of CO recommended by Logan et al. (1981). The distribution of CO was obtained by simply adapting the surface CO measurements (Khalil and Rasmussen, 1984c and 1990b) and by assuming that the ratio of CO concentration obtained by Khalil and Rasmussen (1984c and 1990b) to that used by Logan et al. (1981) is a constant at all heights in the troposphere for a given season and latitude.

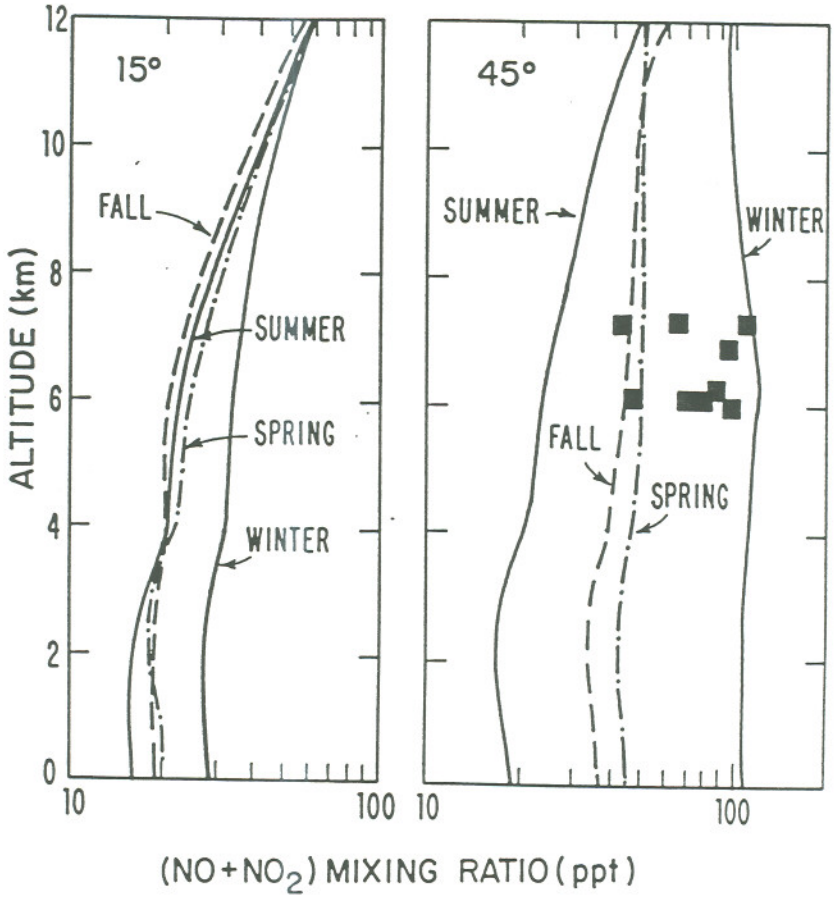

Fig. 2.6 The distribution of NO_x in the northern hemisphere, adapted from Logan et al. (1981).

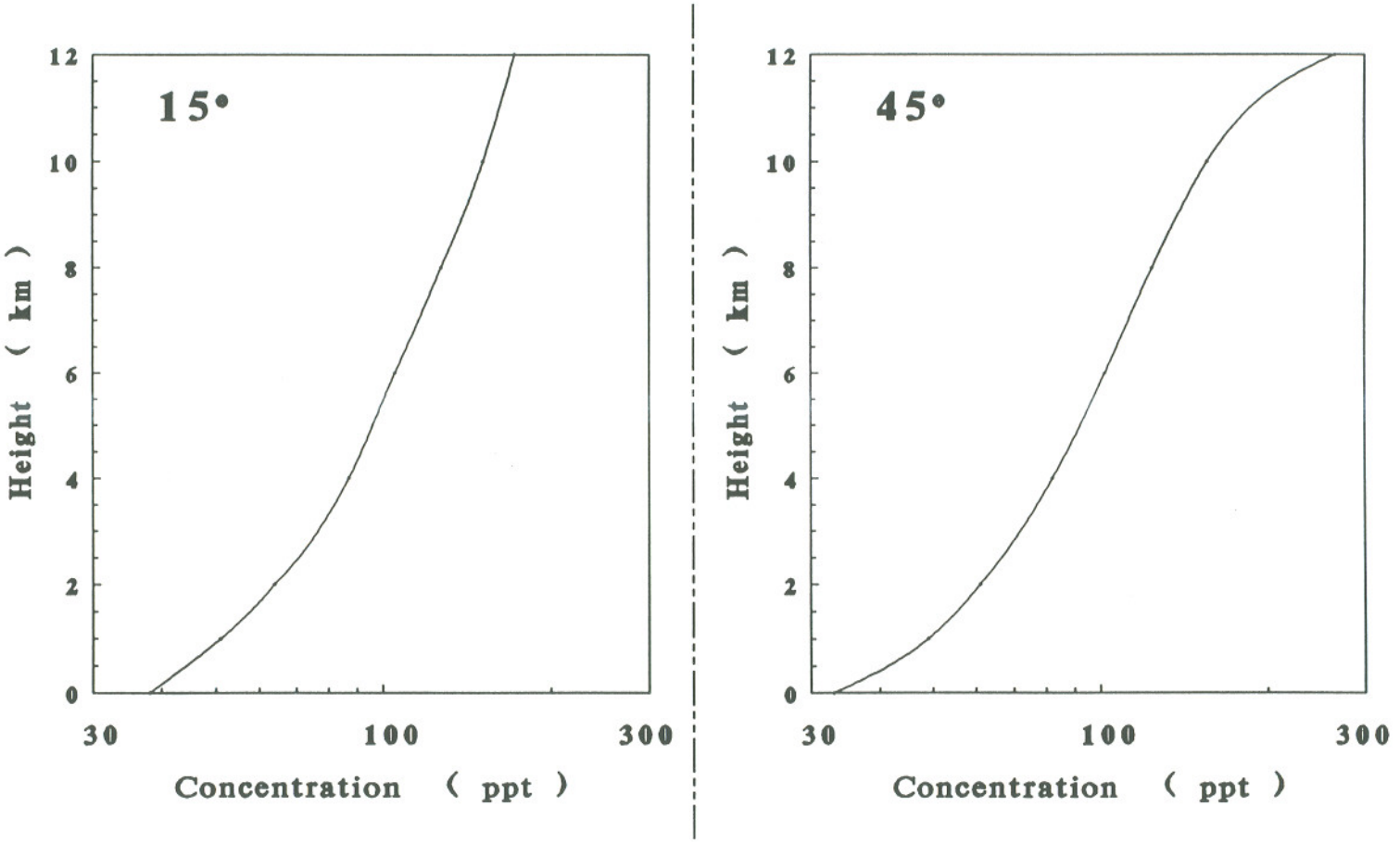

Fig. 2.7 The distribution of HNO_3 in the northern hemisphere, adapted from Logan et al. (1981).

(1981; and references therein), as shown in fig. 2.8. Methane data are taken from Khalil and Rasmussen (1983b). The concentration of N_2O are taken from Khalil and Rasmussen (1983a) and Weiss (1981).

The distribution of the vertical eddy diffusivity is adapted from the results derived from the Radon 222 measurements by Liu et al. (1984), as shown in fig. 2.9.

In summary, a time-dependent multiple one-dimensional photochemical model (M1DPCM) was developed in this study to calculate the concentrations of OH and a series of other reactive species at different times of a day in different seasons and at different locations. The model contains information on the physical features of the atmosphere such as temperature, pressure, turbulent diffusion, and solar intensity, as well as on chemical kinetic and photochemical data. The model consists of 28 species, among which the distributions of 10 species are specified to calculate the concentrations of another 18 species including OH and HO_2. The concentrations of the 18 reactive species are calculated for different times of day, four seasons, and different latitudes and altitudes. The summary of the model including the adopted input data set to calculate the current distribution of OH is shown in fig. 2.10.

2.5 Diurnal, Seasonal, Altitudinal, and Latitudinal Variations at Present

Using M1DPCM, the concentrations of OH and other reactive species were obtained for different times of day, seasons, latitudes, and altitudes. In this section, the diurnal, seasonal, altitudinal, and latitudinal variations of OH and other reactive species will be illustrated and discussed.

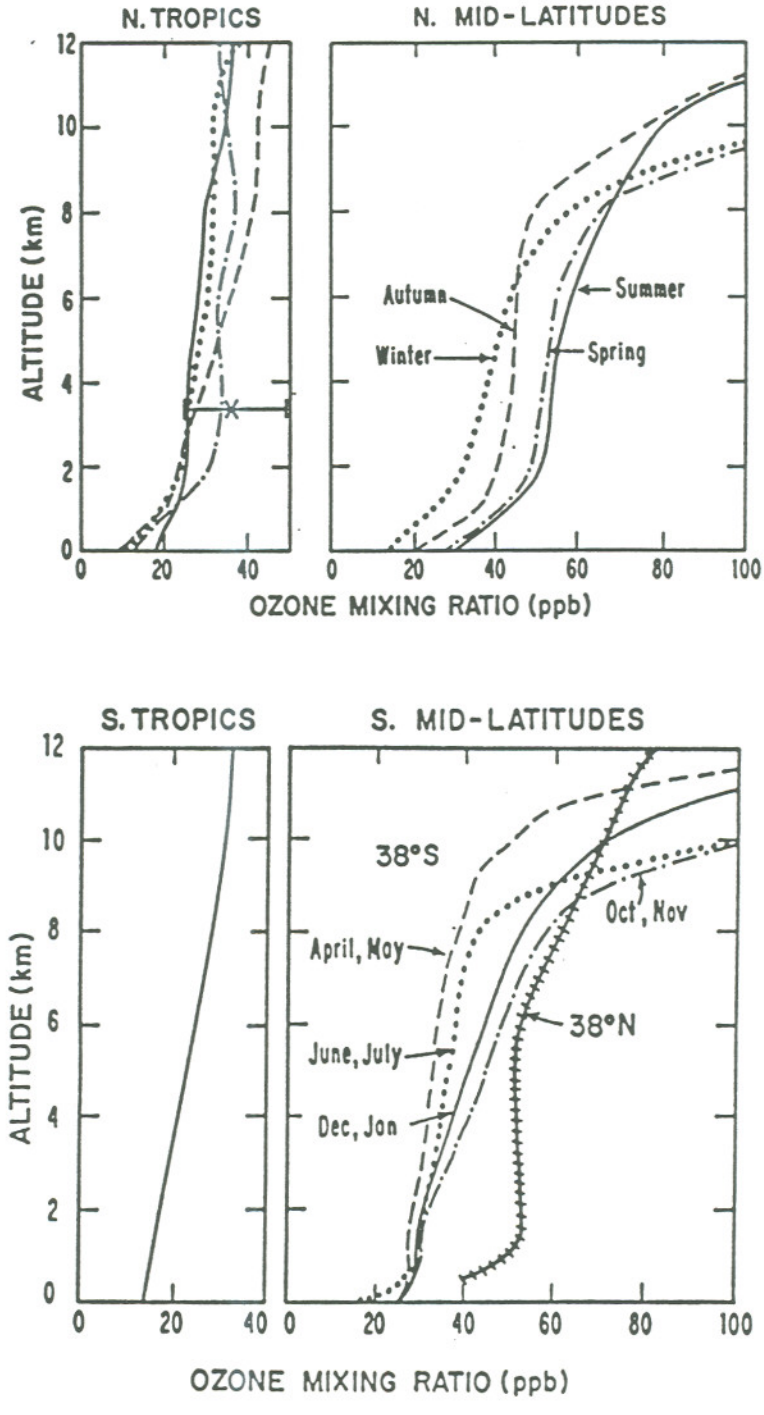

Fig. 2.8 The distribution of O_3 in the troposphere, adapted from Logan et al. (1981).

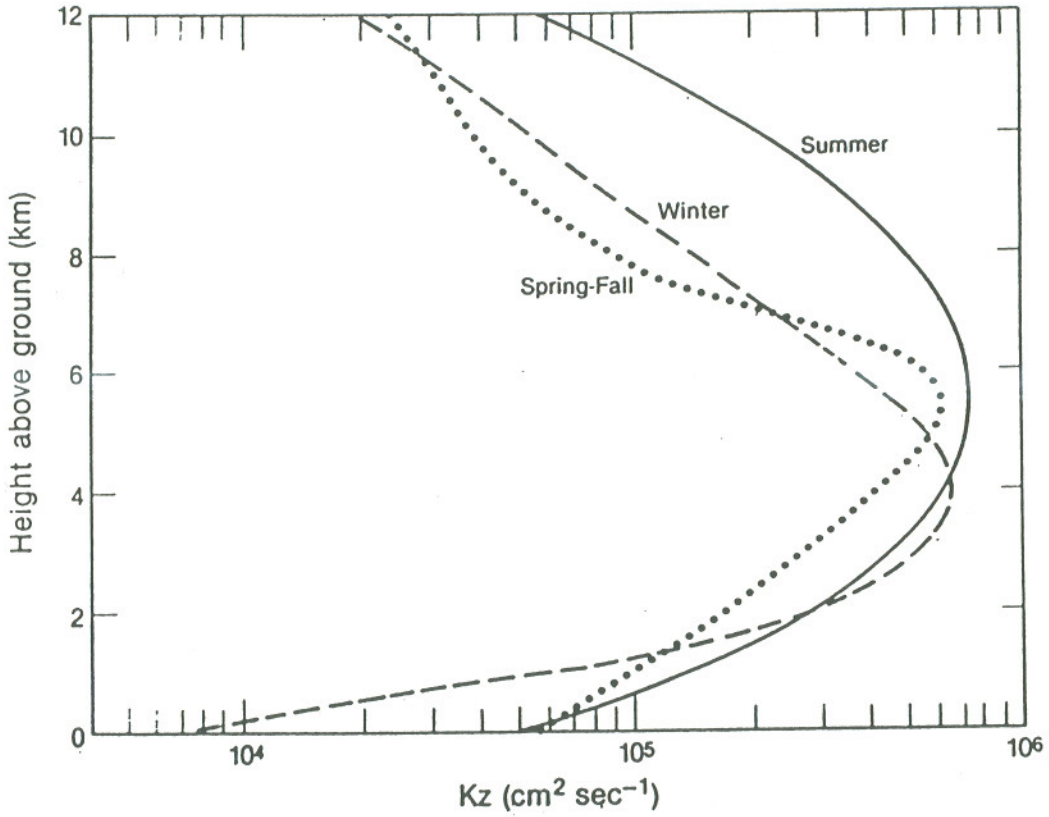

Fig. 2.9 The distribution of the vertical eddy diffusivity, adapted from by Liu et al. (1984).

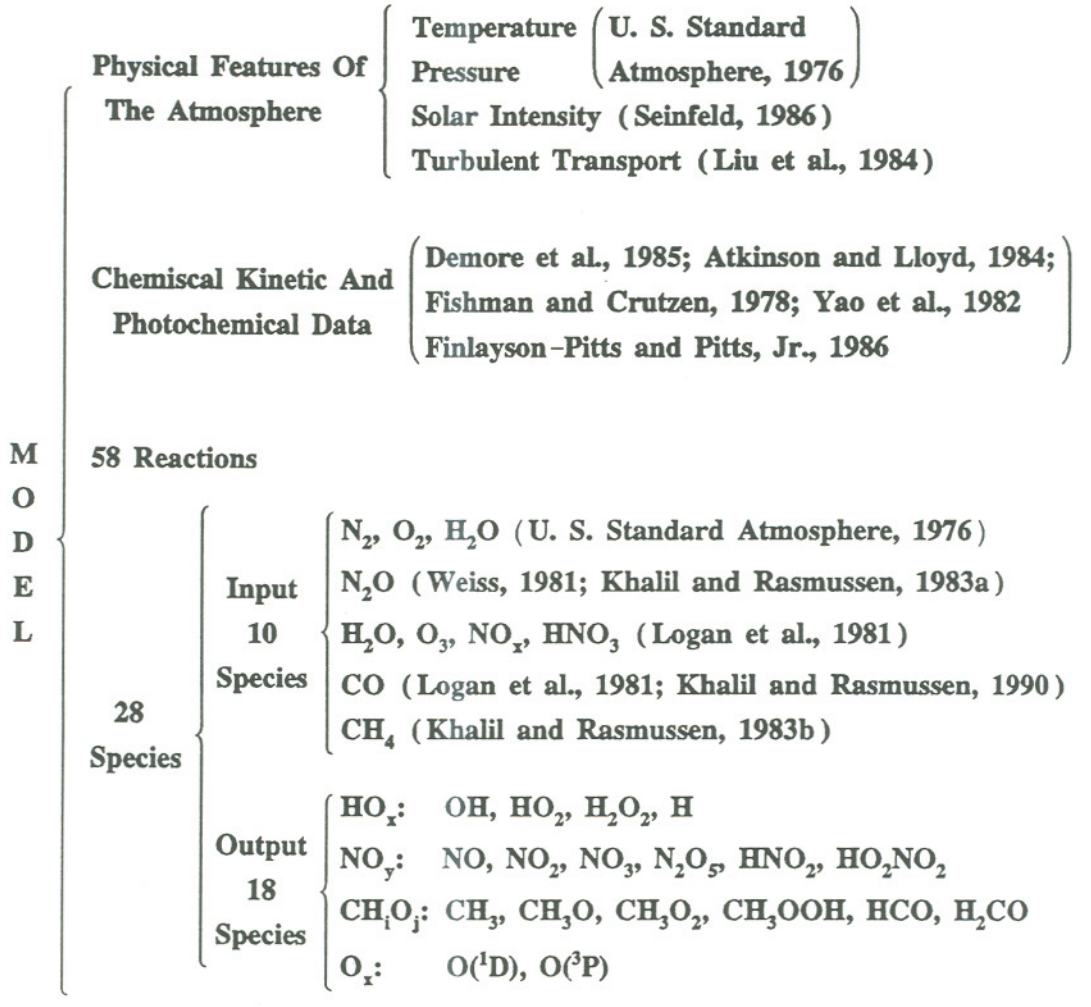

Fig. 2.10 Summary of the multiple one-dimensional photochemical model (M1DPCM).

2.5.1 Diurnal Variations

Fig. 2.11 shows the diurnal variations of OH in summer and winter, at the surface of the earth and 6 km above the surface, and at four latitudes (45 °S, 15 °S, 15 °N, and 45 °N). The related data are tabulated in appendix 2 of Lu and Khalil (1991). The significantly diurnal variations of OH concentration with maximum values at noon and minimum values at dawn, as shown in this figure, result mainly from the diurnal cycle of the solar insolation, since the reaction between $O(^1D)$ and H_2O is a dominant source of OH during the daytime and the solar insolation is the energy to dissociate O_3 to $O(^1D)$.

The diurnal variations of OH concentration change with latitude and season corresponding to the diurnal variations of solar insolation for different latitudes and seasons. For example, the intensity of solar radiation at noon is stronger and the daytime is longer in summer than in winter for any given latitude and height. Accordingly, the peak OH concentration of OH are higher and wider in summer than in winter at that location. As another evident example, the peak OH concentrations are lower and narrower in winter in the middle latitudes than in the tropics since the noontime solar radiation is weaker and the daytime is shorter in winter in the middle latitudes than in the tropics. It is worthwhile to note that the seasonal and latitudinal variations of some key species such as CO, H_2O, and O_3 also strongly affect the corresponding variations of OH. The clear differences between nighttime OH concentrations at the same latitudes in two hemispheres are such an example.

The magnitude of diurnal variations also changes with height. At any latitude in any season, during noontime the OH concentration is always higher at the surface of the earth than at 6 km above the earth's surface. In contrast, at night the concentration of OH at 6 km is higher than that at the earth's surface. Consequently, the

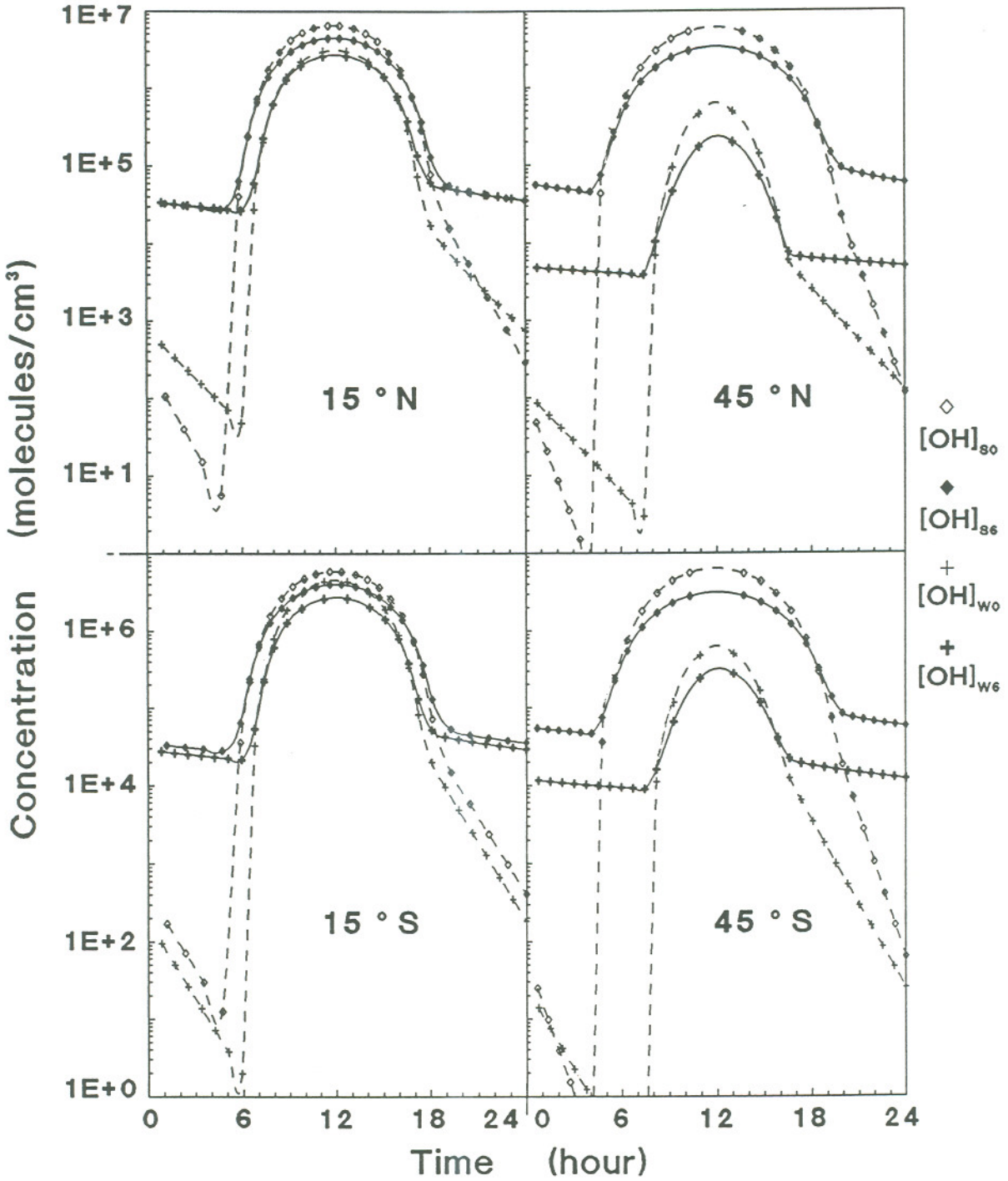

Fig. 2.11 Diurnal variations of OH at four latitudes, where $[OH]_{S0}$ and $[OH]_{S6}$ correspond to the OH concentrations at the earth's surface and at 6 km above the surface in summer, and $[OH]_{W0}$ and $[OH]_{W6}$ are the analogous concentrations in winter.

difference between the maximum concentration of OH at noon and the minimum at dawn at the earth's surface is about a 10^{+6} molecules/cm^3, which is much larger than the difference of about 10^{+2} molecules/cm^3 at 6 km. According to our calculations, the characteristics of the changes of the diurnal variations of OH concentrations with height are mainly affected by the vertical profiles of key species such as CO, H_2O, O_3, and NO_x.

The hydroperoxyl radical, HO_2, is also of another major interest in this study, not only because it is a highly reactive species, but also because it acts as a major buffer of OH, especially at night when the reaction between water vapor and $O(^1D)$ does not take place since there is no $O(^1D)$ without the photodissociation of O_3. The diurnal variations of HO_2 concentrations in summer and winter at two altitudes and at four latitudes are shown in figure 2.12. Similar to OH, the concentration of HO_2 exhibits a strong diurnal variation because HO_2 is mainly generated by the reaction between O_2 and atomic hydrogen, H, which is mostly produced by the reaction between OH and CO. In addition, the magnitude of the variation of the HO_2 concentrations, coupling with OH, changes with season, latitude, and height.

For comparison, the diurnal variations of the concentrations of all the reactive species at the earth's surface as well as at 6 km in the northern hemisphere in spring are shown in figs 2.13 - 2.15. The results are very close to previous publications (e.g., Logan et al., 1981; Thompson and Cicerone, 1982). Generally the diurnal variation of each reactive species is stronger at the surface than in the middle troposphere, and in the northern midlatitudes than in the northern tropics, resulting from the latitudinal variations of solar radiation and the concentrations of the key species such as CO, O_3, and H_2O. By averaging the concentrations of a reactive species at all vertical nodes at each time grid at a given latitude in a certain season, the diurnal variation of the vertically averaged concentration of the species in the troposphere for the given

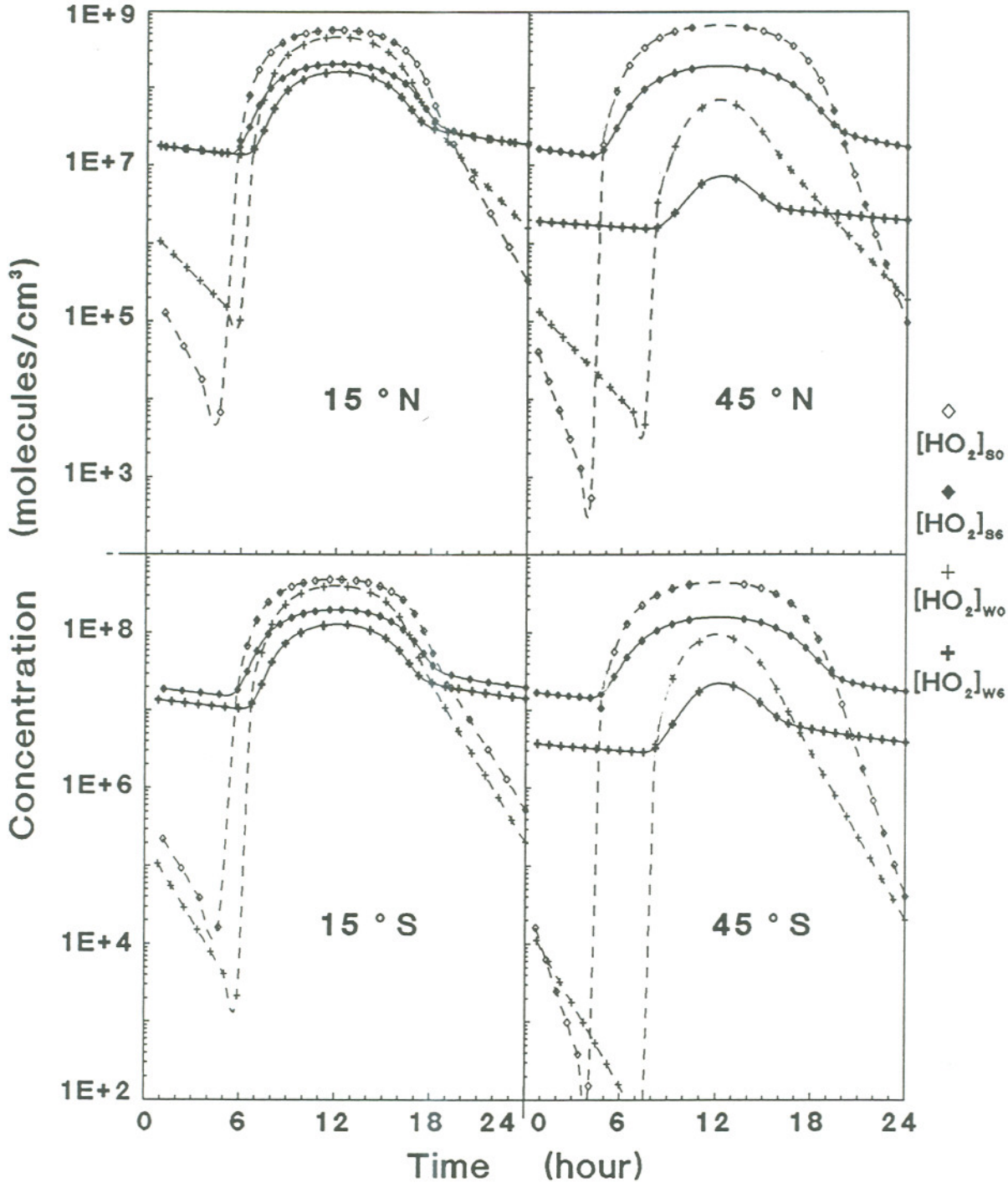

Fig. 2.12 Diurnal variations of HO_2 at four latitudes (45°S, 15°S, 15°N, and 45°), where $[HO_2]_{S0}$ and $[HO_2]_{S6}$ correspond to the HO_2 concentrations at the earth's surface and at 6 km above the surface in summer, and $[HO_2]_{W0}$ and $[HO_2]_{W6}$ are the analogous concentrations in winter.

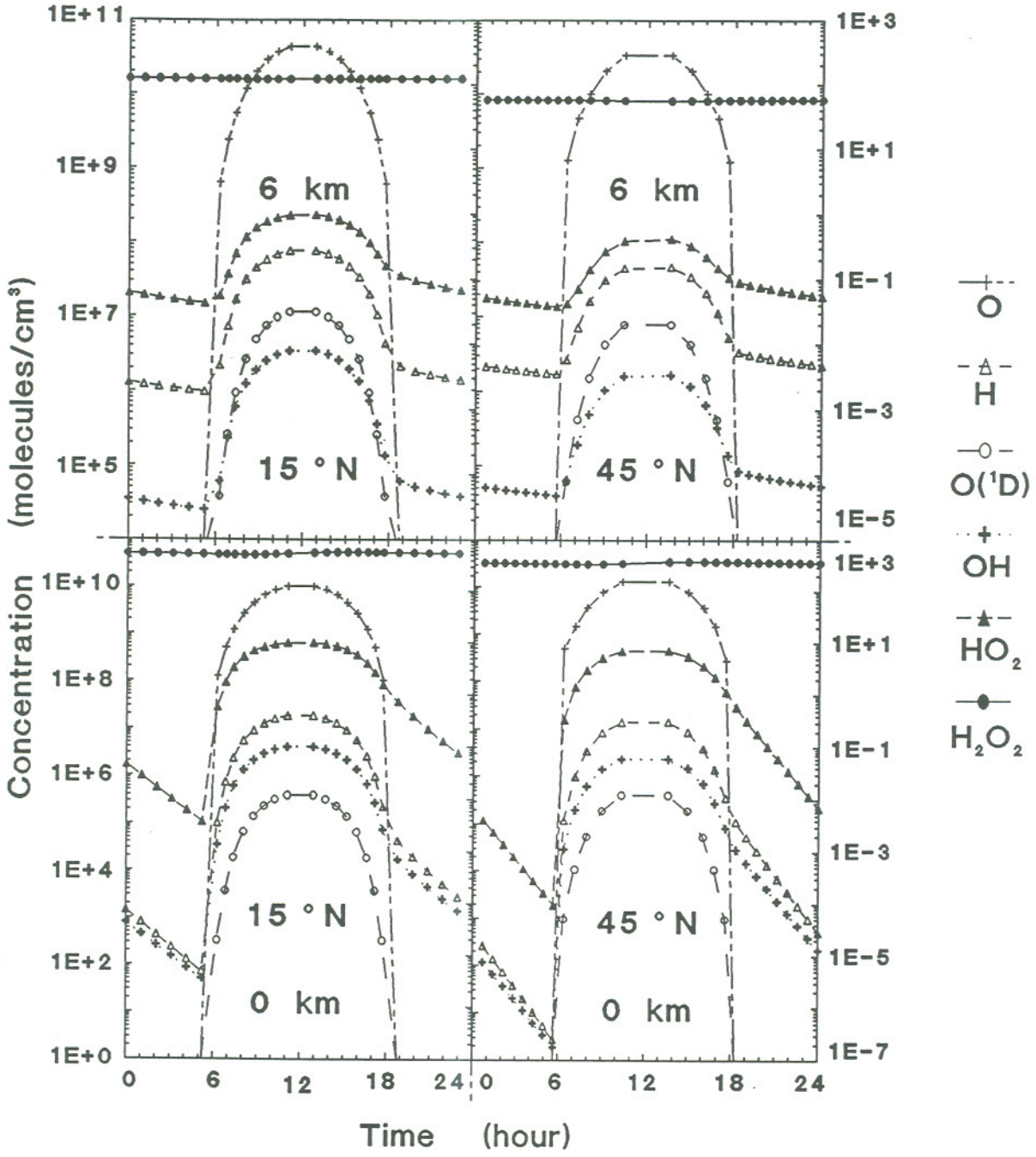

Fig. 2.13 Diurnal variations of the concentrations of O, H, $O(^1D)$, OH, HO_2, and H_2O_2 at two different altitudes in the northern hemisphere in spring. The diurnal variations of the concentrations of O, H, $O(^1D)$ are plotted against the top-right coordinate system and those of OH, HO_2, and H_2O_2 are drawn against the bottom-left coordinate system.

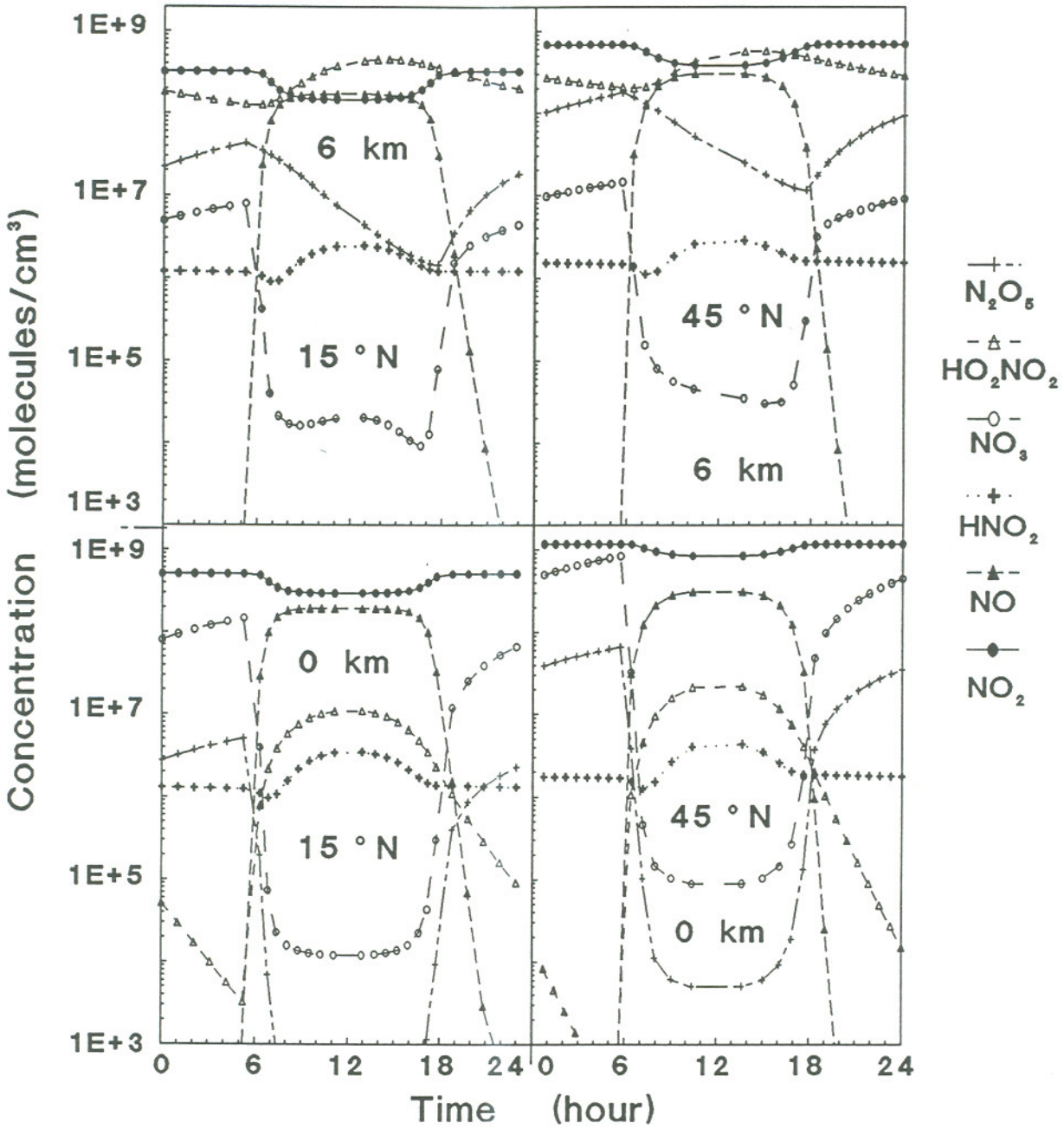

Fig. 2.14 Diurnal variations of the concentrations of NO, NO_2, NO_3, HNO_2, HNO_3, and HO_2NO_2 at the earth's surface as well as at 6 km in the northern hemisphere in spring.

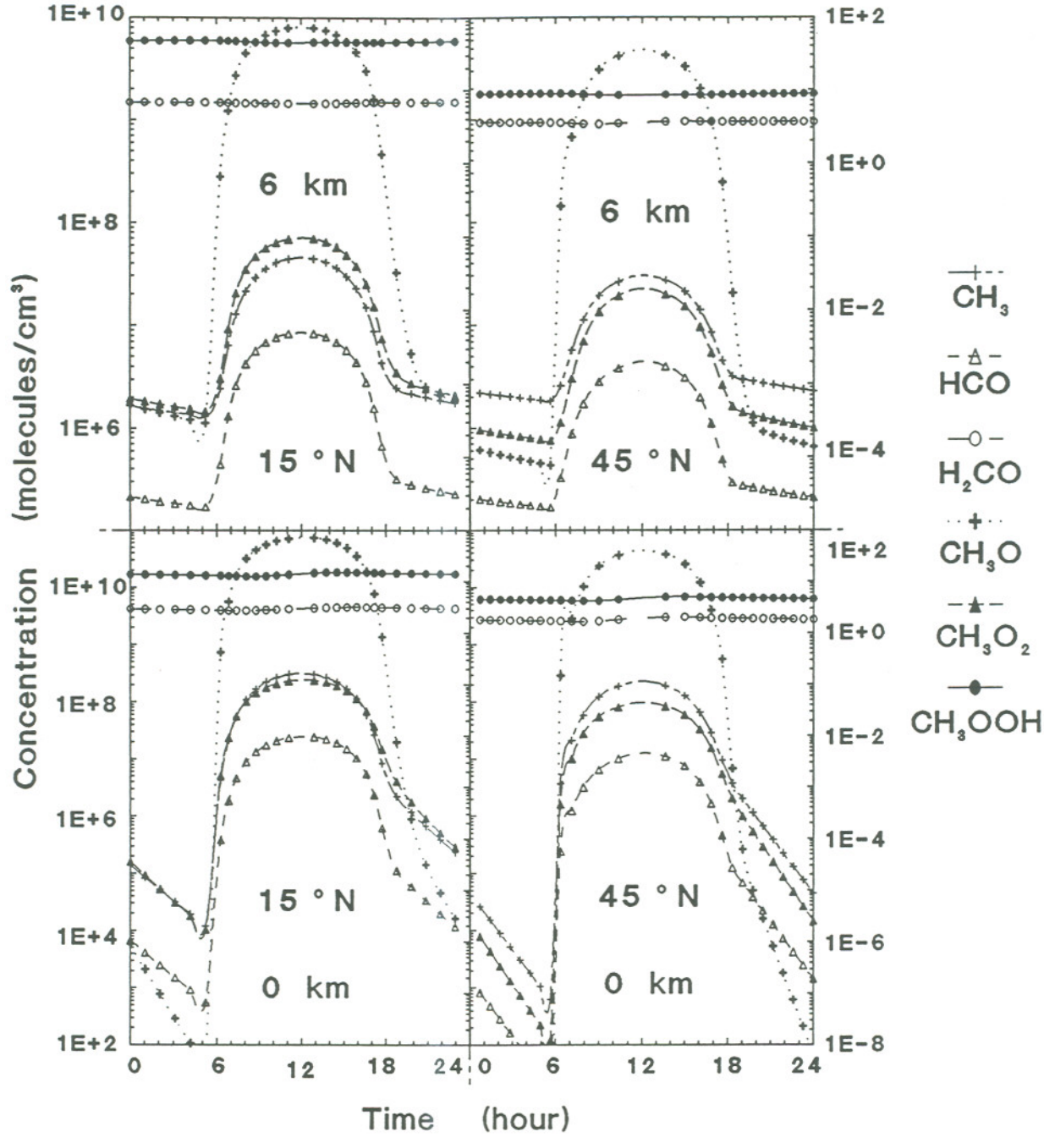

Fig. 2.15 Diurnal variations of the concentrations of CH_3, HCO, H_2CO, CH_3O, CH_3O_2, and CH_3OOH at two altitudes in the northern hemisphere in spring. The diurnal variations of the concentrations of CH_3, HCO, and CH_3O, are plotted against the top-right coordinate system and those of H_2CO, CH_3O_2, and CH_3OOH are drawn against the bottom-left coordinate system.

latitude and season was obtained. The diurnal variations of the vertically averaged concentrations of the eighteen reactive species in spring at four latitudes are shown in figs 2.16 - 2.18. In general the patterns of the diurnal variations in the southern tropics are similar to those in the northern tropics, and the patterns of the diurnal variations in the southern midlatitudes are also like those in the northern midlatitudes; however, there is a significant difference between the patterns of the diurnal variations at middle latitudes and those at the tropics. This is understandable since solar radiation is the main force driving photochemical reactions and the total radiation at any latitude in the southern hemisphere is the same as that at the same latitude in the northern hemisphere. The insolation, however, is different in the midlatitudes compared to the tropics. In addition, the diurnal variations of a species are usually stronger in the northern hemisphere than in the southern hemisphere since CO, CH_4, and NO_x are more abundant in the northern hemisphere than in the southern hemisphere. Logically, since each reactive species chosen in the model computation has an effect, either directly or indirectly, on OH, the variation of OH, in turn, influences these species; therefore, the diurnal variation of a reactive species is more or less linked with the diurnal variation of OH.

2.5.2 Daytime Concentrations

Most of the chemical production and destruction processes in the atmosphere take place during the daytime; for example, the concentration of OH is much higher during daytime than at night, as clearly shown in the previous section, leading to most removal processes of species or free radicals due to the reactions with OH during daytime. Thus daytime atmospheric chemistry is very important for the estimates of the concentrations of trace gases and free radicals.

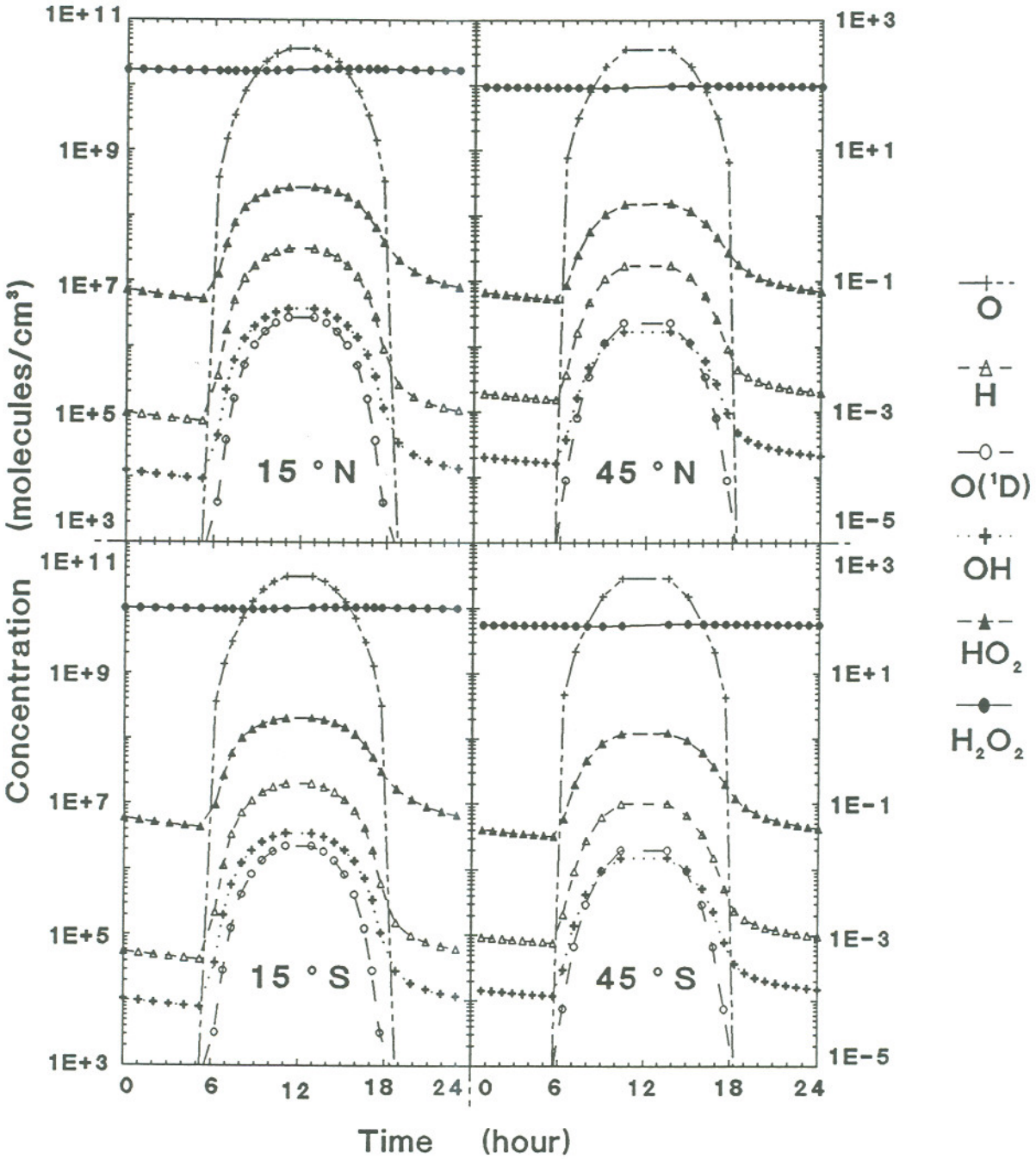

Fig. 2.16 Diurnal variations of the vertically averaged concentrations of O, H, $O(^1D)$, OH, HO_2, and H_2O_2 at four latitudes in spring. The diurnal variations of O, H, $O(^1D)$ are plotted against the top-right coordinate system and those of OH, HO_2, and H_2O_2 are drawn against the bottom-left coordinate system.

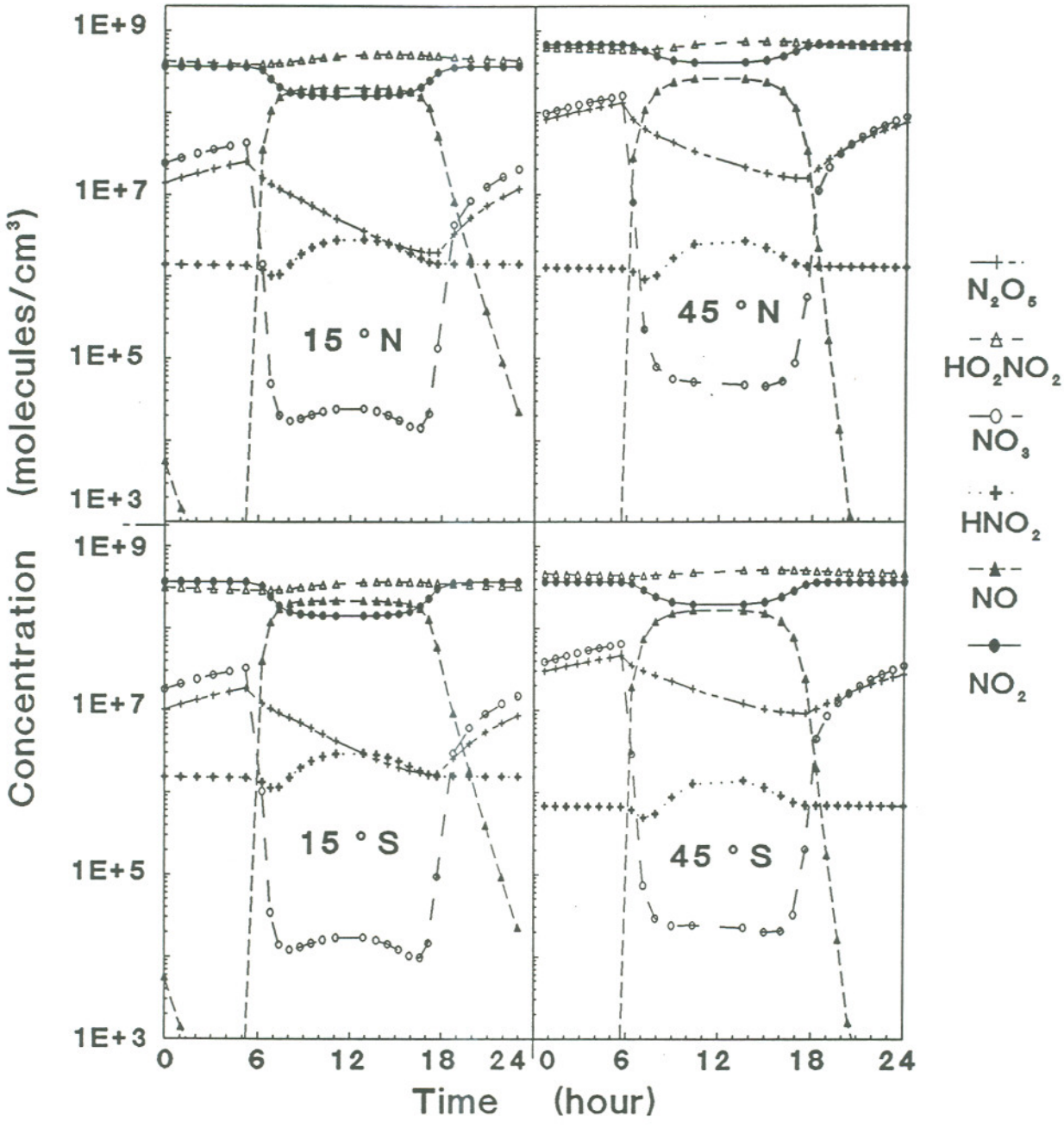

Fig. 2.17 Diurnal variations of the vertically averaged concentrations of NO, NO_2, NO_3, HNO_2, HNO_3, and HO_2NO_2 at four latitudes in spring.

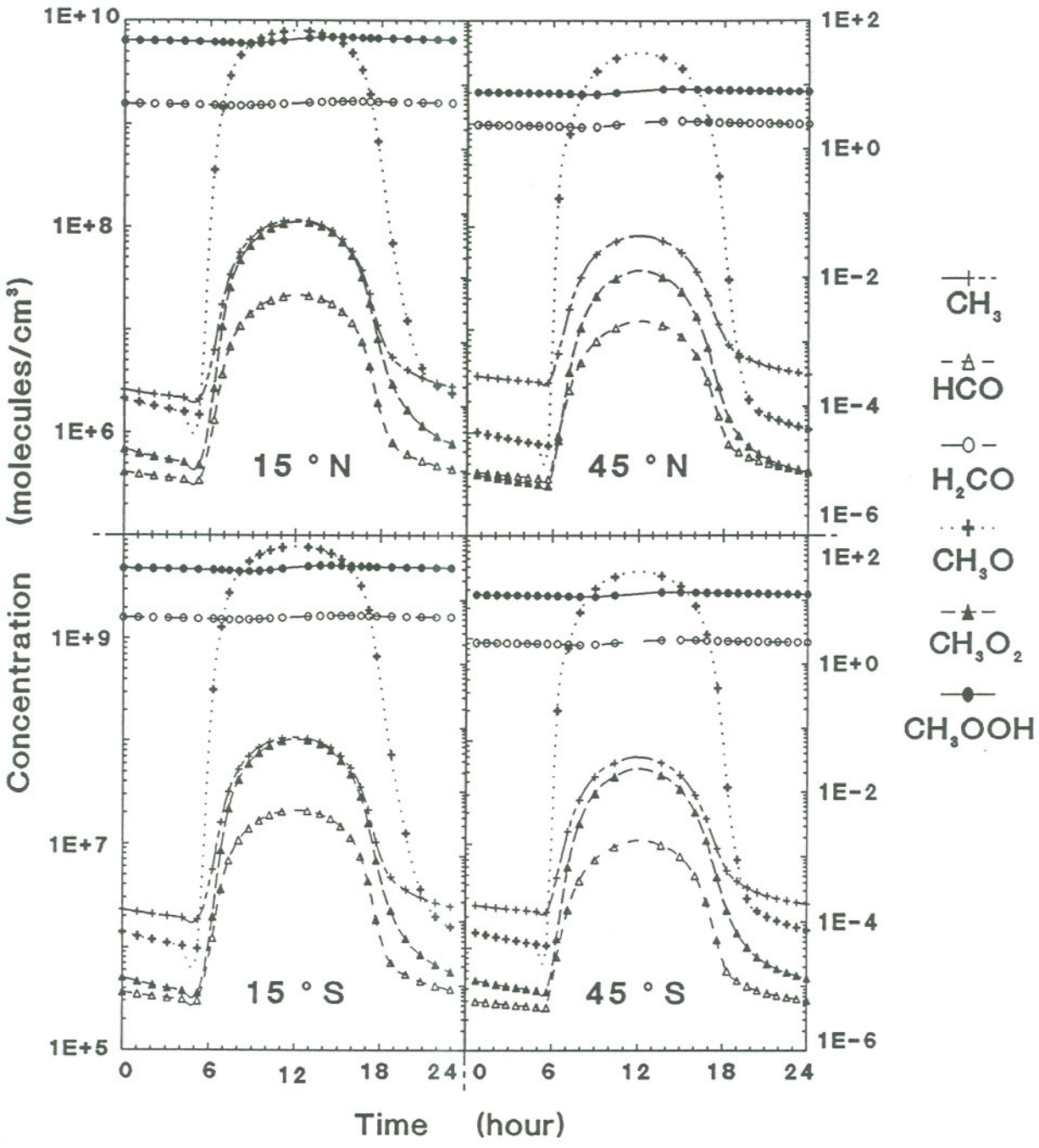

Fig. 2.18 Diurnal variations of the vertically averaged concentrations of CH_3, HCO, H_2CO, CH_3O, CH_3O_2, and CH_3OOH at four latitudes in spring. The diurnal variations of CH_3, HCO, and CH_3O, are plotted against the top-right coordinate system and those of H_2CO, CH_3O_2, and CH_3OOH are drawn against the bottom-left coordinate system.

By taking an average of the concentrations of OH during daytime, from sunrise to sunset, at a specific location in a season, the averaged daytime concentration of OH for that season and location was obtained. The vertical profiles of the averaged daytime OH concentrations are shown in fig. 2.19. The averaged daytime OH concentration generally decreases with height for all heights except in the lower troposphere (<2 km) in the northern hemispheres, while the daytime OH concentration simply decreases with height in the southern hemisphere. The decrease of the OH concentration with height results mainly from the rapid decrease of water vapor with height, as shown in fig. 2.4, since the reaction between water vapor and $O(^1D)$ is the dominant source of OH during the daytime. As shown in fig. 2.5, CO concentration decreases with height within the lowest two kilometers in the troposphere in the northern hemisphere due to human activities. The decrease of CO implies an increase of OH. Therefore, the effect of the sharp decrease of CO with height within the lowest 2 km leads to the increase of OH with height within the lowest 2 km in the northern hemisphere. In contrast, the transport of CO from the northern hemisphere to the southern hemisphere leads to a increase of CO with height in the lowest 2 km in the southern hemisphere, resulting in the decrease of the daytime OH concentration with height within the lowest 2 km in the southern hemisphere.

As another result shown in fig. 2.19, the seasonal variations of the averaged daytime OH concentration are much larger in the midlatitudes than in the tropics corresponding to the considerably larger seasonal variations of the total solar flux in the midlatitudes than in the tropics, since the reaction between H_2O and the immediate product from the photodissociation of O_3, $O(^1D)$, is the primary source of the daytime OH.

The vertical profiles of the averaged daytime HO_2 concentrations are also

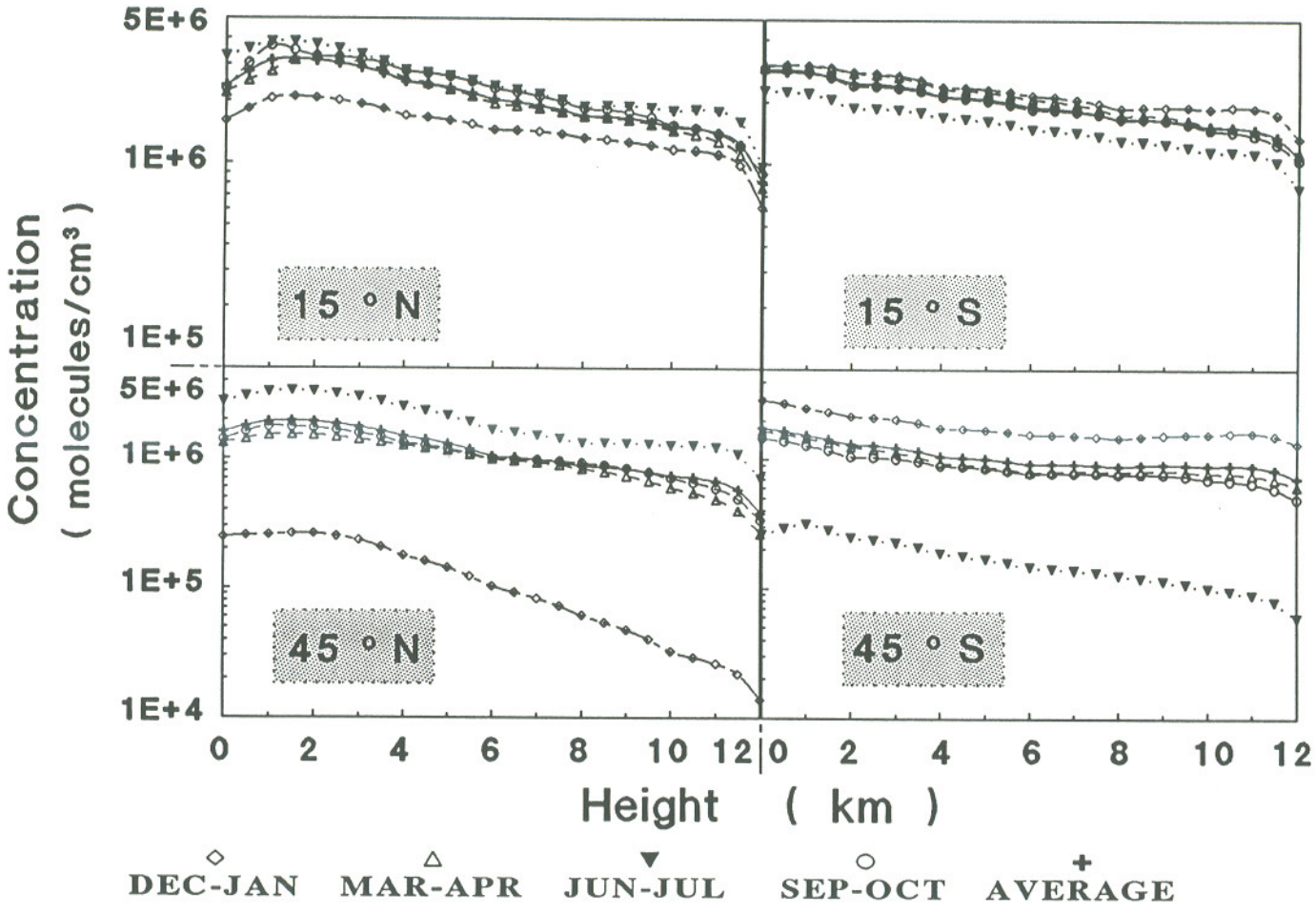

Fig. 2.19 Vertical profiles of the averaged daytime OH concentrations for four seasons and four latitudes.

shown in fig. 2.20. Similar to the averaged daytime OH concentrations, the seasonal variations of the averaged daytime HO_2 concentrations at the middle latitudes are much larger than those in the tropics since the major source of HO_2 during daytime is the reaction between O_2 and H, most of which is produced from the reaction between OH and CO. In other words, the seasonal variations of the averaged daytime HO_2 concentrations are mainly caused by the seasonal variations of the averaged daytime OH concentrations.

One particular noteworthy feature of HO_2 is that the averaged daytime HO_2 concentration, unlike the averaged daytime OH concentration, decreases monotonically in the low troposphere in both hemispheres. As described before, the difference of the vertical structures of CO in the lower troposphere in the two hemispheres causes the main difference between the shapes of the vertical profiles of the averaged daytime OH concentrations in the northern and southern hemispheres. The major daytime source of HO_2, however, is the reaction between O_2 and H which is mostly produced by the reaction between OH and CO. On the one hand, CO is an indirect source of HO_2, as described above; on the other hand, CO is an indirect sink of HO_2 since CO is a key sink of OH. Consequently, the effect of CO on HO_2 is attenuated, leading to the decreases of HO_2 with height in response to the vertical structure of the decrease of HO_2 with height at all latitudes.

By taking an average over altitude and latitude, we obtained the globally averaged daytime OH concentration of 1.6×10^6 molecules/cm^3, with about 9% more daytime OH in the northern hemisphere than in the southern hemisphere, corresponding to the greater concentrations of O_3 and NO_x in the northern hemisphere than in the southern hemisphere.

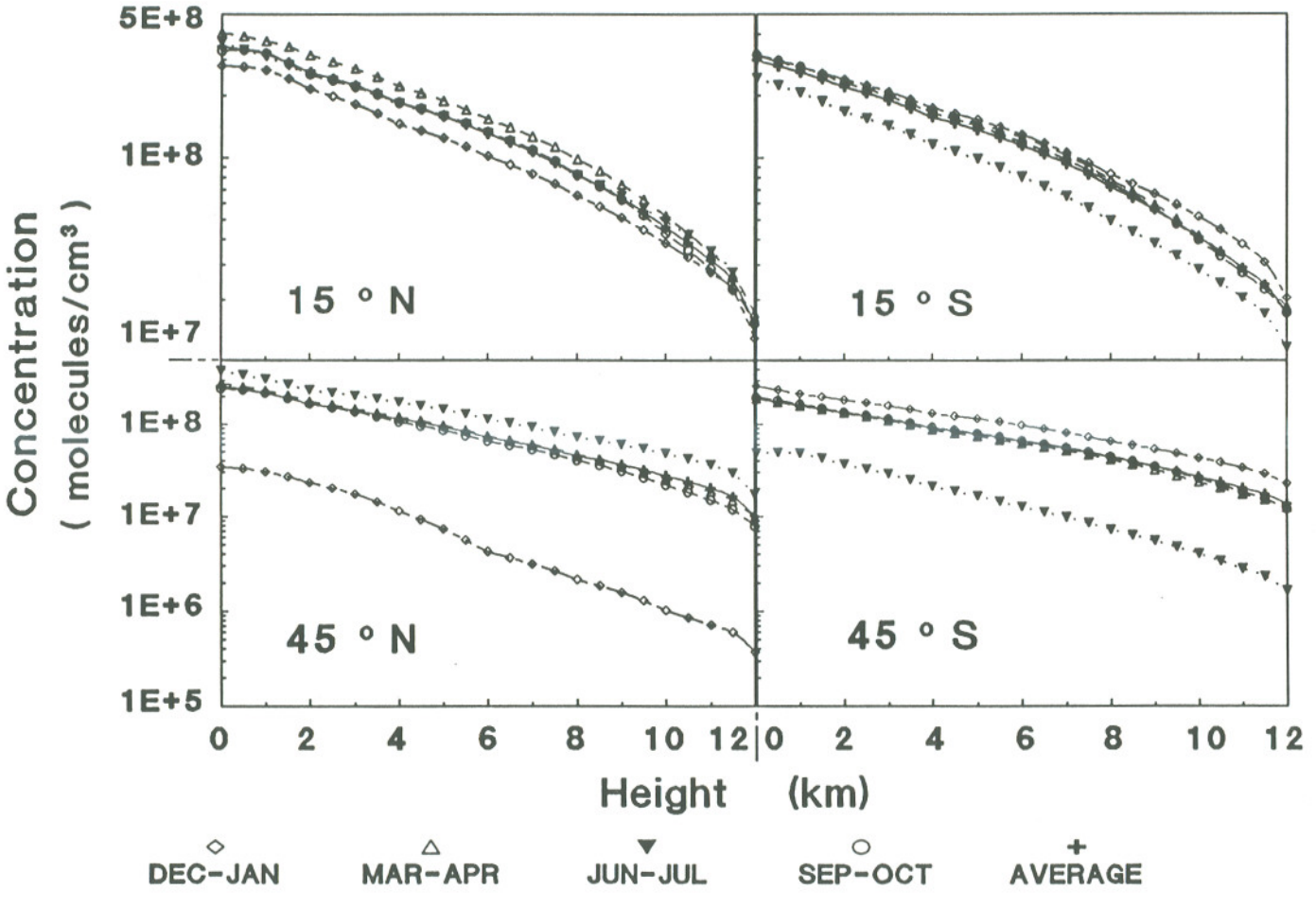

Fig. 2.20 Vertical profiles of the averaged daytime HO_2 concentrations for four seasons and four latitudes.

2.5.3 Nighttime Concentrations

As shown in section 2.5.2, the nighttime OH concentration is much smaller than daytime OH concentration. Probably because the concentrations of OH at night is too small to detect, or perhaps, because it makes a small contribution to global atmospheric chemistry, nighttime OH has rarely been reported (Hard, et al., 1986, 1992; Shirinzadeh et al., 1987, Donahue and Prinn, 1990, Chan et al., 1990). Nevertheless, OH exists at night and continues to react with many species and radicals in the atmosphere. With the M1DPCM and its predecessor model, a time-dependent photochemical model (Lu, 1990), the nighttime OH have been studied (Lu, 1990; Lu and Khalil, 1990, 1991a, and 1992a).

By taking a time average of the concentrations of OH for the whole night, from sunset to sunrise, the averaged nighttime OH concentration at a specific location in a season can be obtained. As shown in figure 2.21, the vertical profiles of the averaged nighttime OH concentrations at different latitudes in different seasons have a common feature: the averaged nighttime value first increases with height in the lower troposphere, reaches a maximum at around the middle troposphere, then decreases with height until it reaches a minimum at 10 or 11 km, and finally changes slightly with height at the top of the troposphere. This vertical structure of the averaged nighttime OH concentration is mainly controlled by the vertical structures of the concentrations of O_3, HO_2NO_2, NO_2, CO, and CH_4. According to our calculation, more than 95% of the total nighttime OH is produced by the reaction between O_3 and HO_2 and more than 60% of nighttime HO_2 is generated by the thermal dissociation of HO_2NO_2, while CO and CH_4 consume large fractions of nighttime OH (about 50% for CO and about 20% for CH_4) and O_3 and NO_2 remove almost all the nighttime HO_2 (about 50% for O_3 and 45% for NO_2) (see the next section for more

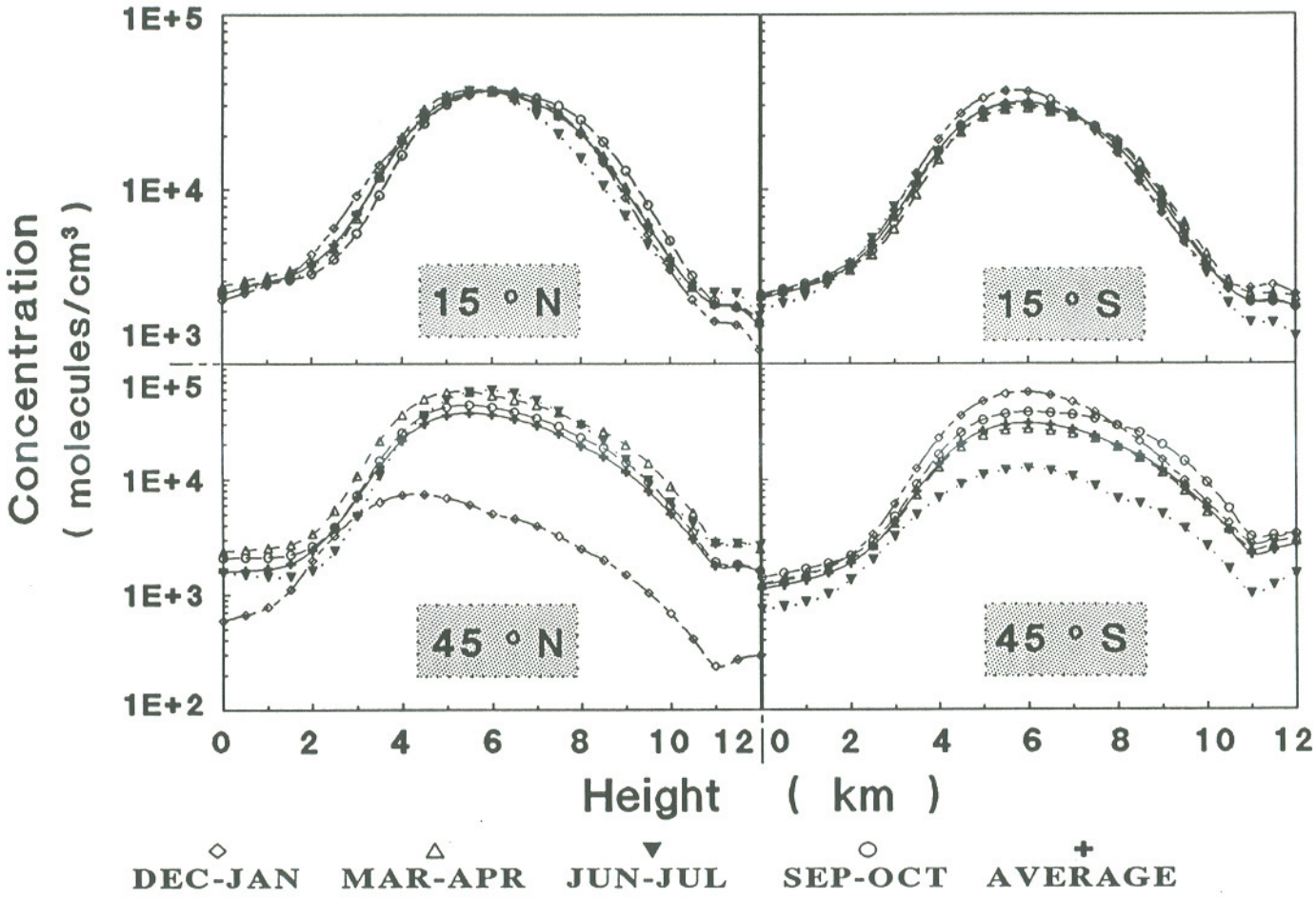

Fig. 2.21 Vertical profiles of the averaged nighttime OH concentrations for four seasons and four latitudes.

detail, and also see Lu and Khalil, 1991a). This figure also indicates that on average the nighttime OH concentration at the earth's surface is much lower than 10^5 molecules/cm^3, consistent with the conclusion that OH level is lower than 0.9×10^5 molecules/cm^3 (their detection limit) at night given by Shirinzadeh (1987) from their OH measurements in ambient air.

By taking an average over altitude and latitude, we obtained the globally averaged nighttime OH concentration of 1.3×10^4 molecules/cm^3, with a about 15% more abundance of nighttime OH in the northern hemisphere than in the southern hemisphere, corresponding to the greater concentrations of O_3 and HO_2NO_2 in the northern hemisphere. On the whole, the averaged nighttime OH concentration is about two orders of magnitude smaller than the averaged daytime OH concentration, 1.6×10^6 molecules/cm^3.

On the global scale, the effect of nighttime OH on the atmospheric chemistry is vary small compared to the daytime OH. However, the difference changes with season, altitude, and latitude, as we compare the diurnal variations of OH in the section 2.5.1. To find out the potential importance of OH, we define the relative contribution of the nighttime OH at the *j*th altitude in the *i*th season at the *k*th latitude, r_{kij}:

$$r_{kij} = \frac{\overline{[OH^n]}_{kij} \cdot t_{ki}}{\overline{[OH]}_{kij} \cdot 24} \qquad (2.41a)$$

where t_{ki} is the time from sunset to sunrise in hours in the *i*th season at the *k*th latitude; $\overline{[OH^n]}_{kij}$ is the averaged OH nighttime concentration and $\overline{[OH]}_{kij}$ is the diurnally averaged OH concentration. Similarly, the relative contributions of seasonally averaged nighttime OH at the *j*th altitude and the *k*th latitude (r_{kj}), those of the

vertically averaged nighttime OH in the *i*th season (r_{ki}), and those of the seasonally and vertically averaged nighttime OH at the *k*th latitude, r_k, were also defined by the following formulas:

$$r_{kj} = \frac{\sum_{i=1}^{4} \overline{[OH^n]}_{kij} \cdot t_{ki}}{\sum_{i=1}^{4} \overline{[OH]}_{kij} \cdot 24} \qquad (2.41b)$$

$$r_{ki} = \frac{\overline{[OH^n]}_{ki} \cdot t_{ki}}{\overline{[OH]}_{ki} \cdot 24} \qquad (2.41c)$$

$$r_{k} = \frac{\sum_{i=1}^{4} \overline{[OH^n]}_{ki} \cdot t_{ki}}{\sum_{i=1}^{4} \overline{[OH]}_{ki} \cdot 24} \qquad (2.41d)$$

where $\overline{[OH^n]}_{ki}$ is the vertically averaged nighttime concentration of OH in the *i*th season at the *k*th latitude and $\overline{[OH]}_{ki}$ is the vertically and diurnally averaged concentration of OH in the same season at the same latitude.

Fig. 2.22 shows the vertical profiles of the relative contributions of nighttime OH in four seasons at four latitudes and those of seasonally averaged nighttime OH at four latitudes. Generally, the values of the relative contributions of the averaged nighttime OH, r_{kj}, are less than 0.5% in the lower and the upper troposphere, indicating that the nighttime OH there contributes little to the chemical cycles of most trace gases in the troposphere. In contrast, because of the relatively larger values, (for r_{kj}, about 3% in the middle latitudes and 2% in the tropics in the middle troposphere), the nighttime OH in the middle troposphere is more important, especially at the midlatitudes in winter in which r_{kij} is 13% at 45°S and 8% at 45°N, indicating that about 10% of removal process resulting from reacting with OH

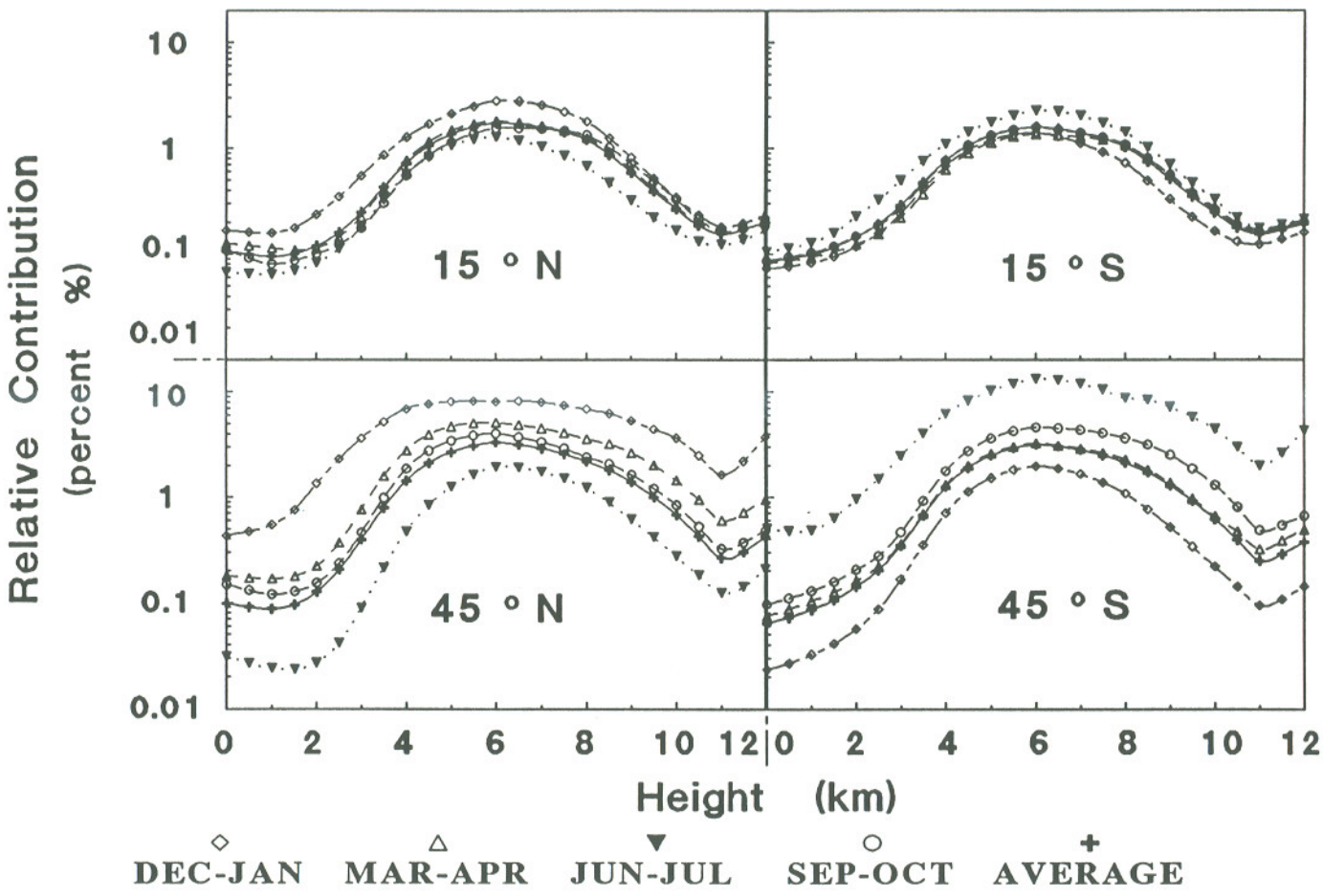

Fig. 2.22 Vertical profiles of the relative contributions of nighttime OH in four seasons at four latitudes and those of seasonally averaged nighttime OH at four latitudes.

occurs at night. The large values of r_{kij} not only results from the weak intensity of the solar radiation and the short daytime, but also because of more O_3 and HO_2NO_2 in these regions. On average, only about 1% of the total daily OH is produced at night in the whole troposphere.

As shown in fig. 2.23, the seasonal variations of the averaged nighttime HO_2, similar to the corresponding seasonal variations of the averaged nighttime OH, are larger at the middle latitudes than at the tropics since OH is a significant source of HO_2. In addition, there is a significant hemispheric difference in the vertical profiles of the averaged nighttime HO_2 concentrations within the lowest 2 km: the averaged nighttime HO_2 concentration decreases with height in the northern hemisphere in contrast to the slight change with height in the southern hemisphere. This difference is mainly due to the difference of the vertical distributions of CO in two hemispheres (the sharp decrease of CO with height in the northern hemisphere and the slight increase of CO with height in the southern hemisphere in the lower troposphere) since CO is indirectly a dominant source of HO_2.

The relative contribution of nighttime HO_2 is also calculated for different heights, altitudes, and latitudes. Similar to that of nighttime OH, the relative contribution of nighttime HO_2 appears significant in the middle troposphere at the middle latitudes in winter, as shown in fig. 2.24.

2.5.4 Diurnal Concentrations

The diurnally averaged OH concentration is calculated from photochemical models for two purposes. First the diurnally averaged OH concentrations calculated from a photochemical model is commonly compared with those directly derived from

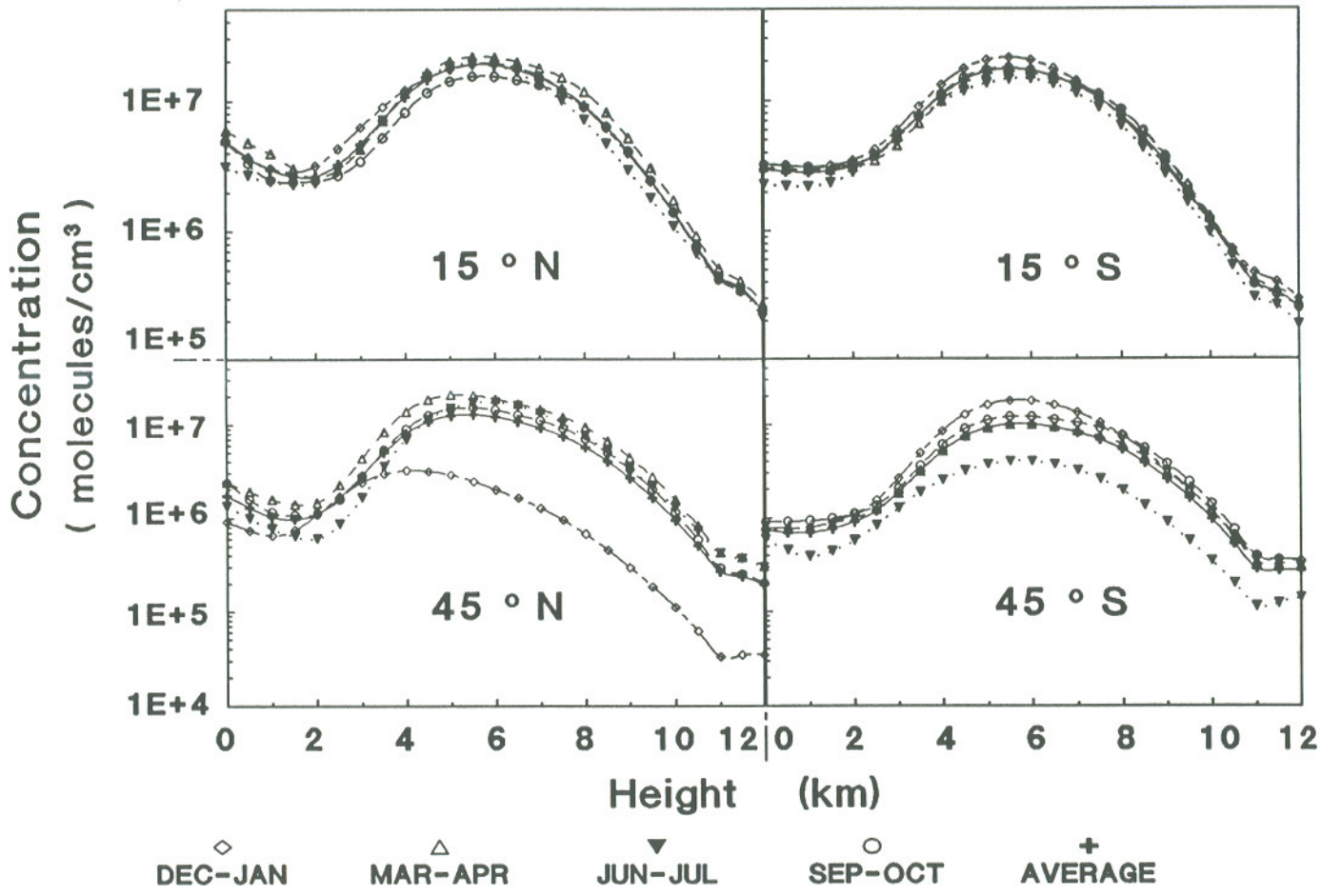

Fig. 2.23 Vertical profiles of the averaged nighttime HO_2 concentrations for four seasons and four latitudes.

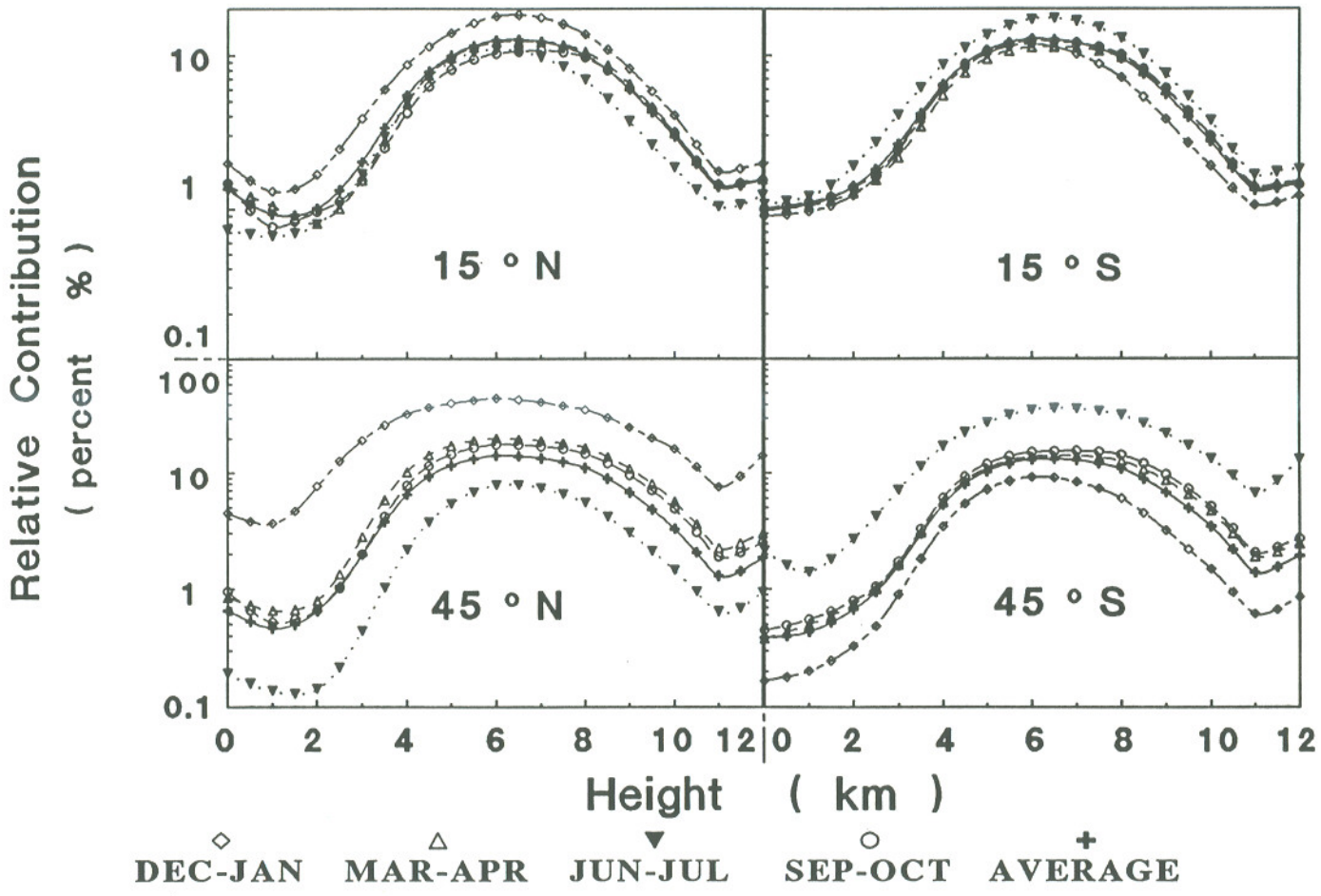

Fig. 2.24 Vertical profiles of the relative contributions of nighttime HO_2 in four seasons at four latitudes and those of seasonally averaged nighttime HO_2 at four latitudes.

the methy chloroform (CH_3CCl_3) measurements to make sure the photochemical model obtain the right OH level. Second the calculated OH value can be used to calculate the lifetimes of a number of species which are mainly removed by OH.

The vertical profiles of the diurnally averaged OH concentrations in four different seasons at four different latitudes, and the vertical profiles of the seasonally and diurnally averaged OH concentrations at the four latitudes are shown in fig. 2.25. Comparing fig. 2.25 with fig. 2.19, the pattern of the vertical profiles of the diurnally averaged OH is very similar to that of the averaged daytime OH since daytime OH is dominant over nighttime OH, as shown in previous sections. The diurnally averaged OH has all the features of the vertical structure of the averaged daytime OH, discussed in section 2.5.2. By taking the diurnally averaged OH concentrations over seasons, altitudes, and latitudes, a globally, seasonally, and diurnally averaged OH concentration of $8.2 \times 10^{+5}$ molecules/cm^3 with about 9% more OH in the northern hemisphere than in the southern hemisphere is obtained. The abundance of OH in the northern hemisphere compared to OH level in the southern hemisphere results from more O_3 and NO_x in the northern hemisphere than southern hemisphere. By comparing the OH concentrations calculated in this study with the OH levels reported in the literature, our model results generally agree with others, as shown in fig. 2.26.

Similarly, the vertical profiles of the diurnally averaged HO_2 concentrations, shown in fig. 2.27, have almost the same patterns as those of the averaged daytime HO_2 concentrations, shown in fig. 2.20 because the averaged daytime HO_2 concentrations are generally much larger than the averaged nighttime OH concentrations, as discussed in the previous sections. By further taking an average of the diurnally averaged HO_2 concentrations for all seasons, latitudes, and altitudes, a $5.9 \times 10^{+7}$ molecules/cm^3 of the globally, seasonally, and diurnally averaged HO_2 concentration

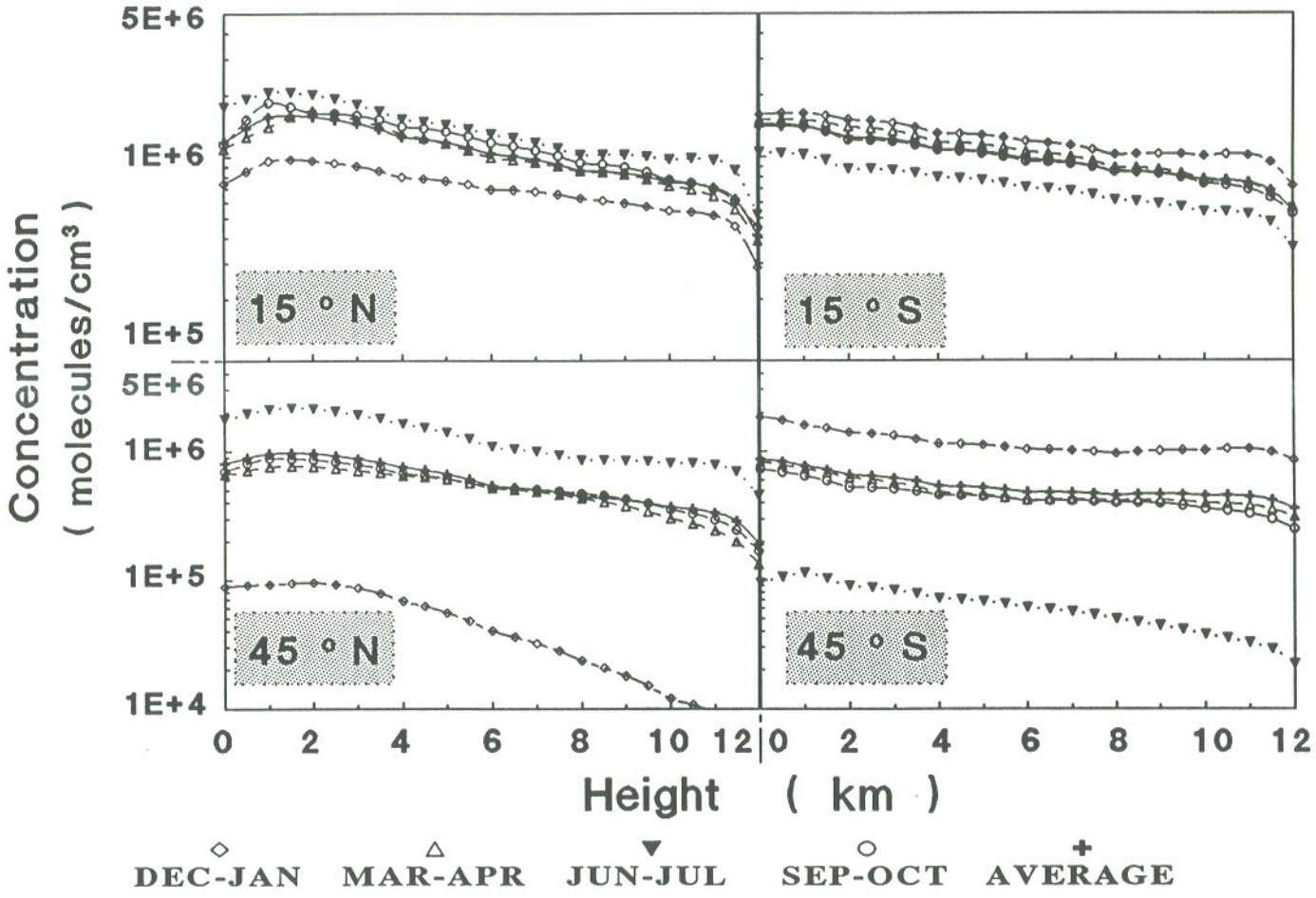

Fig. 2.25 Vertical profiles of the diurnally averaged OH concentrations for four seasons and four latitudes.

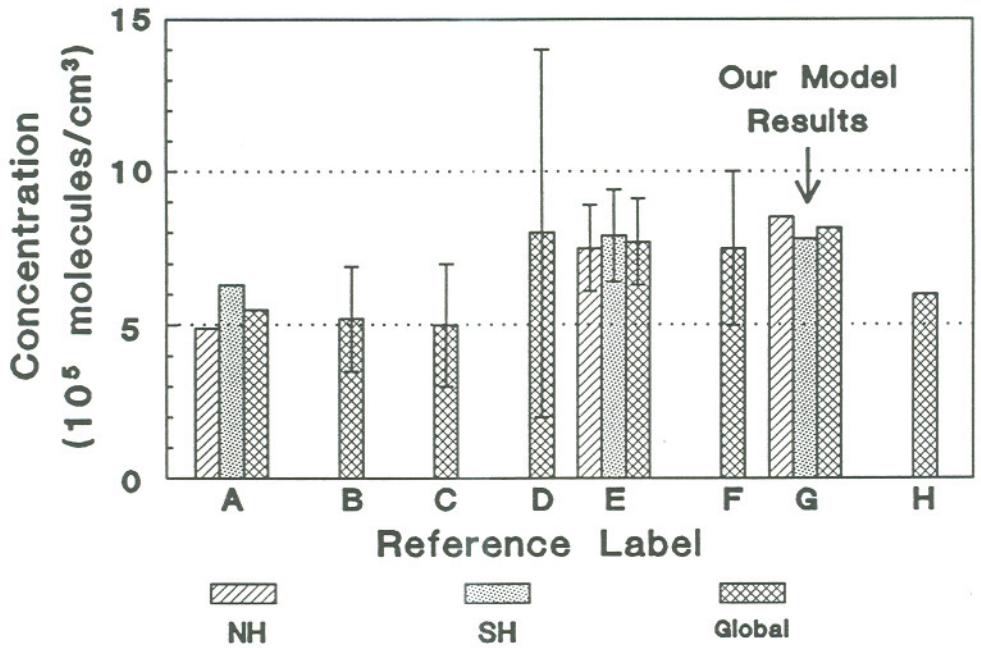

Reference	NH	SH	Global
A) Crutzen and Gidel (1983)	4.9	6.3	5.5
B) Singh et al. (1983)	-	-	5.2 ± 1.7
C) Prinn et al. (1983)	-	-	5 ± 2
D) Khalil and Rasmussen (1984)	-	-	8 ± 6
E) Prinn et al. (1987)	7.5 ± 1.4	7.9 ± 1.5	7.7 ± 1.4
G) Spivakovsky (1990)			7.5 ± 2.5
F) Lu and Khalil (1991)	8.5	7.8	8.2
H) Pinto and Khalil (1991)	-	-	6

Fig. 2.26 Comparison of the diurnally and seasonally averaged OH concentrations (in units of 10^5 molecules/cm^3) in the northern troposphere (NH), the southern troposphere (SH), and the entire troposphere (global).

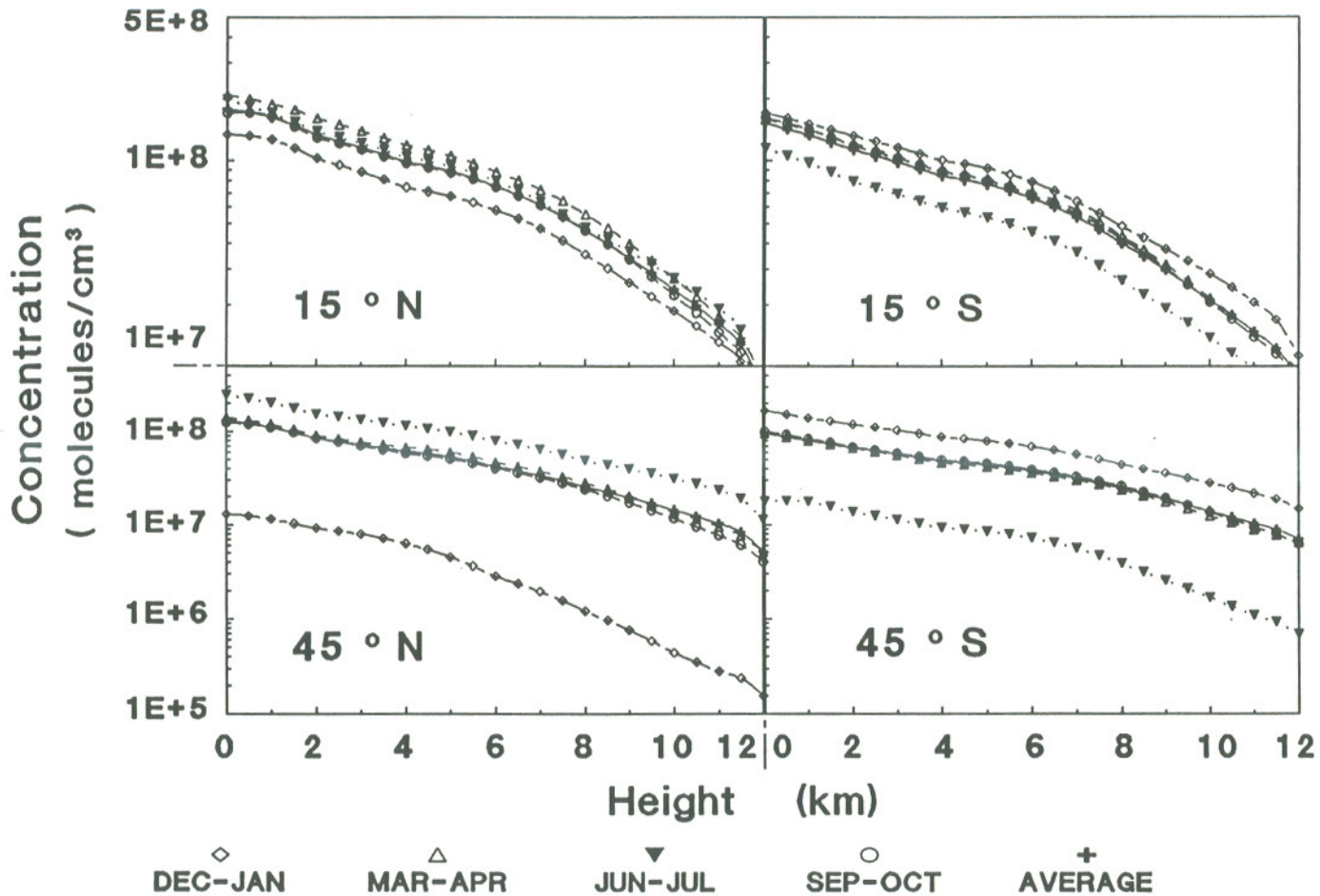

Fig. 2.27 Vertical profiles of the diurnally averaged HO_2 concentrations for four seasons and four latitudes.

was obtained with about 20% more HO_2 in the northern hemisphere, resulting from the greater amount of CO in the northern hemisphere than in the southern hemisphere.

The globally, seasonally, and diurnally averaged concentrations of the other sixteen reactive species are also computed in this study, as summarized in table 2.2 for further study.

2.6 Secular Variations

As we know, OH is a major species cleansing CO, CH_4, NMHC, NO_x, and other pollutants in the atmosphere. In turn, the atmospheric OH level is greatly affected by these species. There is growing concern regarding the decrease of the atmospheric OH concentration, resulting from the increases of trace gases and air pollutants due to increasing human activities (e.g. Levine et al, 1985; Thompson and Cicerone, 1986; McElory, 1989; Valentine, 1990; Crutzen and Zimmermann, 1991; Law and Pyle, 1991; Lu and Khalil, 1991a; Pinto and Khalil, 1991; Thompson, 1992).

The OH trend over a wide range of climatic conditions, from the last ice age (about 18,000 years ago), to the pre-industrial era (about 200 years ago), to the present modern times is one of major interests in this study since the past trend always give us a hint about the future change. Clearly for past conditions, there is no way to obtain OH concentration except for using photochemical models. With our photochemical model, we calculated the OH levels in different climatic conditions. The input data set for the three climatic periods is shown in table 2.3 (also see Lu and Khalil, 1991a), taken from Pinto and Khalil (1991), which derived from the ice core measurements.

Table 2.2. Globally, Seasonally, and Diurnally Averaged Concentrations of Some Reactive Species.

Species	Concentration[a] (molecules/cm^3)		
	SH	NH	Global
$O(^1D)$	5.0×10^{-3}	6.3×10^{-3}	5.7×10^{-3}
O	73	91	82
H	4.2×10^{-2}	5.7×10^{-2}	5.0×10^{-2}
H_2O_2	$6.8\times10^{+9}$	$1.0\times^{+10}$	$8.4\times10^{+9}$
NO	$8.0\times10^{+7}$	$9.4\times10^{+7}$	$8.7\times10^{+8}$
NO_2	$3.0\times10^{+8}$	$4.9\times10^{+8}$	$4.0\times10^{+8}$
NO_3	$1.4\times10^{+7}$	$2.7\times10^{+7}$	$2.0\times10^{+7}$
N_2O_5	$1.9\times10^{+7}$	$5.5\times10^{+7}$	$3.7\times10^{+8}$
HNO_2	$1.4\times10^{+6}$	$1.6\times10^{+6}$	$1.5\times10^{+6}$
HO_2NO_2	$3.3\times10^{+8}$	$3.9\times10^{+8}$	$3.6\times10^{+8}$
CH_3	1.5×10^{-2}	1.7×10^{-2}	1.6×10^{-2}
HCO	1.0×10^{-4}	1.2×10^{-4}	1.1×10^{-4}
H_2CO	$1.3\times10^{+8}$	$1.3\times10^{+8}$	$1.3\times10^{+8}$
CH_3O	15	16	15
CH_3O_2	$2.5\times10^{+7}$	$2.8\times10^{+7}$	$2.6\times10^{+7}$
CH_3OOH	$3.7\times10^{+8}$	$4.3\times10^{+9}$	$4.0\times10^{+9}$

[a] Each value inside the inner box surrounded with double lines corresponds to the seasonally and diurnally averaged concentration of one of the sixteen reactive species in the northern troposphere (NH), or in southern hemisphere (SH), and in the whole troposphere (Global).

Table 2.3. Concentrations of Tracers, Number Density of Water Vapor, and Temperature at the Surface of the Earth for Three Climatic Conditions[a], from Ice ages (IA) to the Pre-industrial Era (PE), to Modern Times (MT).

Period		MT	PE	IA
CH_4 (ppbv)		1650	750	350
CO (ppbv)		110	57	28
H_2 (ppbv)		500	230	150
O_3 (ppbv)	Upper Limit	17.2	11.5	10.0
	Average	22.0	14.0	12.0
	Lower Limit	28.6	17.2	14.5
NO_y[b] (ppbv)		0.1	0.05	0.05
N_2O (ppbv)		305	285	240
H_2O (molecule/cm^3)		3.32×10^{17}	3.32×10^{17}	2.44×10^{17}
Temperature (°K)		288.15	288.15	283.15

[a] The data listed in the table are all taken from Pinto and Khalil (1991) except the number density of water vapor, computed by the formula for relative humidity given by Manabe and Wetherald (1967) and Clausius-Clapeyron equation. The levels of O_3 in the above table were calculated with a one dimensional photochemical model (Pinto and Khalil, 1991). The levels of the other species were obtained based on ice core measurements and current understanding of these species (for more details, see Pinto and Khalil, 1991).

[b] $NO_y = NO + NO_2 + NO_3 + 2 \cdot N_2O_5 + HNO_2 + HNO_3 + HO_2NO_2$

Fig. 2.28 shows the averaged concentrations of the daytime OH, the nighttime OH, and the daily OH at the earth's surface. As shown in fig. 2.28a (and fig. 2.28b), the OH levels, on average, decline but only slightly although the concentrations of CO and CH_4 doubled from ice ages to the pre-industrial era and doubled again from the pre-industrial era to the modern times. The stability of OH results from the compensation between the effects of the increases of the source species of OH such as O_3 and NO_x and the increases of the sink species such as CO and CH_4. This result is consistent with that given by Pinto and Khalil (1991), in which a different photochemical model was used.

Unlike the daytime OH, the nighttime OH concentrations decreased significantly from ice ages to the present; as shown in figure 2.28c (and fig. 2.28d), the averaged nighttime OH concentration in ice ages is about three times as large as that at present. The mechanism of the consumption of OH during the daytime is about the same as that at night; CO and CH_4 deplete most of the hydroxyl radicals both during the daytime and at night (Lu and Khalil, 1991a; also see the next chapter). However, the sources of OH are significantly different during the daytime and nighttime. It should be emphasized that the level of nighttime HO_2 is inversely proportional to O_3 since the reaction between HO_2 and O_3 consumes a large fraction of nighttime HO_2. Thus increasing O_3 level, on the one hand, tends to increase OH level directly through the reaction between O_3 and HO_2; on the other hand, the trend of decreasing HO_2 level due to increasing O_3 tends to decrease OH. Consequently the effect of increasing O_3 on OH is significantly reduced at night. Therefore, the significant decrease of nighttime OH arises mainly from the significant increase of CO and CH_4 from ice ages to the pre-industrial era and from the pre-industrial era to the modern times.

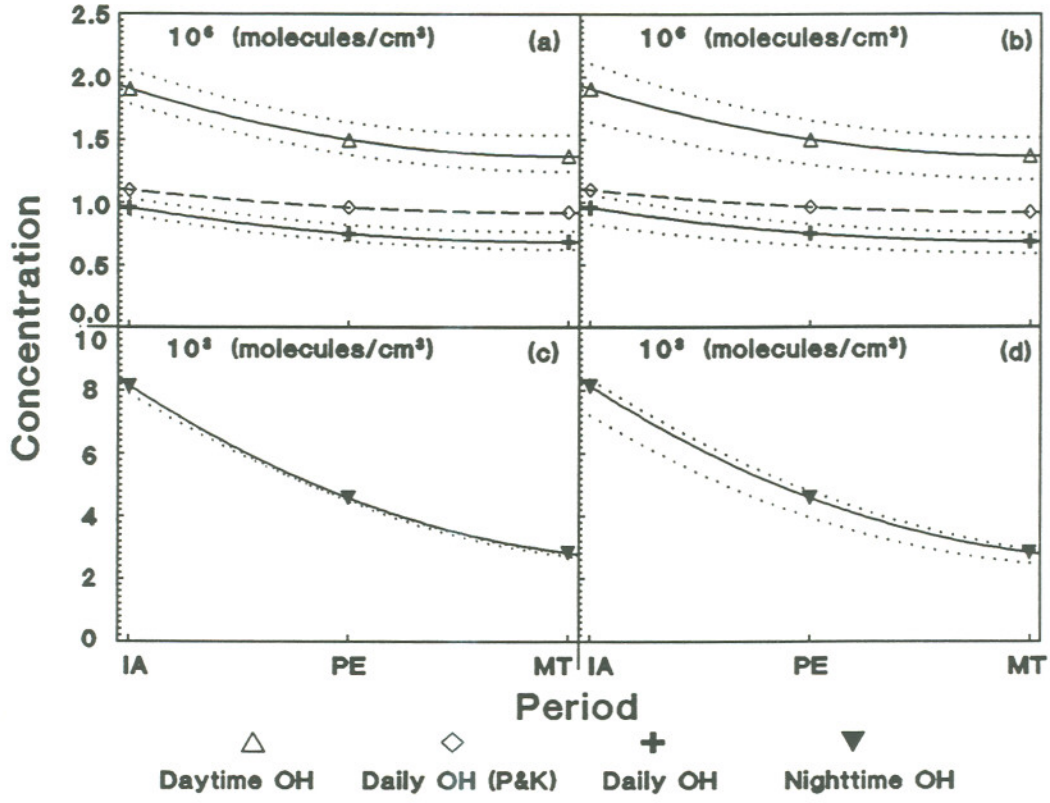

Fig. 2.28 The seasonally averaged concentrations of the daytime OH and the daily OH (*figs. 2.28a and 2.28b*), and the nighttime OH (*figs. 2.28c and 2.28d*) at the earth's surface over a wide range of climatic conditions, from ice ages (IA) to the pre-industrial era (PE), to modern times (MT). "Daily OH", "Daytime OH", and "Nighttime OH" represent the seasonally averaged concentrations of the daily OH, the daytime OH, and the nighttime OH, calculated by our photochemical model in this study, while "Daily OH (P&K)" corresponds to the seasonally averaged daily OH concentration calculated by Pinto and Khalil with a different photochemical model (1991).

Note: 1. The dotted lines in figs. 2.28a and 2.28c represent the variations of OH due to the variations of O_3; the dotted lines were obtained by substituting the upper and lower limits of O_3 data, which are listed in table 2.3, into our photochemical model.

2. The dotted lines in figs. 2.28b and 2.28d represent the variations of OH due to the variations of NO_x; the dotted lines were obtained by increasing and decreasing 50% of NO_x standard level in each climatic conditions.

The possible changes of OH levels in the three climatic conditions (the dotted lines in fig. 2.28a and fig. 2.28c) due to the variations of ozone were also calculated by substituting the upper and lower limits of O_3 levels, as listed in table 2.3. During the daytime more O_3 produces more OH under all climatic conditions, since more O_3 produces more $O(^1D)$ by the photodissociation, and thus more OH through the reaction between the resulting $O(^1D)$ and H_2O. In contrast, at night the difference of OH levels due to increasing and decreasing O_3 in any climatic condition is very small because of the two opposite effects of O_3 on nighttime OH, as described above.

NO_y also plays a important role in OH chemistry. During daytime NO_x produces 20% - 25% of the total daytime OH by reaction between NO and HO_2. At night, the thermal dissociation of HO_2NO_2 generates more than 60% of HO_2, which is the major source of nighttime OH by reacting with O_3. Consequently, NO_y, like O_3, is a significant source of OH, and errors of the estimates of OH levels might be attributed to the uncertainty of NO_y levels. To see the response of OH to NO_y, we increased and reduced the standard NO_y levels by 50% for each climatic condition and calculated the corresponding OH concentrations, which are shown in figure 2.28b and figure 2.28d (dotted lines). During the daytime a 50% increase (or decrease) in NO_y in each climatic condition results in a little more than 10% increase (or decrease) in the OH level. In contrast, at night a 50% increases in NO_y levels causes less than 5% increase in the nighttime OH levels for all three climatic conditions, while a 50% decrease in NO_y results in more than 10% decrease in OH. Since NO_y produces nighttime OH through the thermal dissociation of HO_2NO_2 followed by the reaction between the resulting HO_2 and O_3, it is of interest to look into the sources and sinks of nighttime HO_2. As to be discussed in the next chapter, the major nighttime HO_2 source is the dissociation of HO_2NO_2, producing more than 60% of the total nighttime HO_2. The almost equally important sinks are the reactions of HO_2

with NO_2 and with O_3, consuming more than 90% of the total nighttime HO_2 at standard NO_y level. Increasing NO_y level increases the relative importance of NO_2. The trend of increasing HO_2 due to increasing HO_2NO_2 is compensated by the trend of decreasing HO_2 due to increasing NO_2. Reducing NO_y makes NO_2 a relatively weak sink for HO_2 compared to O_3; therefore, the trend of decreasing HO_2 is largely due to decreasing HO_2NO_2.

2.7 Summary

Based on the mass continuity theory, a detailed time-dependent multiple one dimensional photochemical model (M1DPCM[a]) has been developed to calculate the global distribution of the hydroxyl radicals (OH) and other reactive species in the troposphere. In order to calculate the distribution of OH with this model, the physical characteristics of the atmosphere such as temperature, pressure, solar intensity, and turbulent transfer, and the distributions of several trace gases, and chemical kinetic and photochemical data are prescribed.

---

[a] M1DPCM is a one dimensional photochemical model, which can be used to calculate the seasonal, latitudinal, and even longitudinal variations of a number of reactive species with different input data sets for various seasons, latitudes, and longitudes. For short-lived species, the results of M1DPCM are similar to those of two dimensional or even three dimensional photochemical models, while M1DPCM avoids long computational time. However, when the effects of horizontal transport are comparable to or even larger than those of vertical turbulent mixing and chemical production and removal processes, the M1DPCM is no longer effective. The technique of M1DPCM has been widely used in dealing with photochemistry (e.g., Logan et al., 1981, Thompson et al., 1990; Lu and Khalil, 1991a)

The OH concentrations calculated with this model are consistent with various measurements and model predictions (For comparison, see Altshuller, 1989 and Thompson, 1992). Generally the concentration of OH in the troposphere changes with times of day as well as with altitude, season, and latitude. On the whole, the globally, seasonally, and diurnally averaged OH concentration is about $8.2 \times 10^{+5}$ molecules/cm^3 with about 10% greater abundance of OH in the northern hemisphere than in the southern hemisphere, corresponding to more O_3 and NO_x in the northern hemisphere.

There are two major differences between daytime OH and nighttime OH. First there is, on average, about two orders of magnitude greater concentration of OH during the day than at night (the globally averaged daytime OH concentration is $1.6 \times 10^{+6}$ molecules/cm^3 compared to the averaged nighttime OH of $1.3 \times 10^{+4}$ molecules/cm^3). Second the maximum nighttime OH concentrations occur in the midlatitudes and mid-troposphere, while the greatest daytime OH concentrations are in the lowest part of the troposphere.

Besides OH, the hydroperoxyl radical, HO_2, is another species discussed fully in this dissertation since it acts as a buffer of OH. Similar to OH, the diurnal variation of HO_2 is also very large, and vertically the maximum daytime HO_2 concentration appears at the surface of the earth or in the lower troposphere but the maximum nighttime OH is in the middle troposphere.

The concentrations of sixteen other reactive species were also calculated and illustrated in this study, and our model results agree well with other model results (e.g. Logan et al., 1980; Thompson and Cicerone, 1982). Generally, the features of these species are linked with the features of OH since each of these species influences OH, directly or indirectly.

Finally the surface concentrations of OH over a wide range of climatic conditions, from ice ages to the present were studied. The OH concentration decreases very little from ice ages to the present despite the large changes of the key species that remove OH. The stability of OH is caused by concurrent increases of the sources and sinks of OH. However, the decrease of nighttime OH is significant from ice ages to the present. The current nighttime OH level is only about 30% of that in ice ages, arising mainly from the significant increase of CO and CH_4, the two major sinks of OH. We also tested the sensitivities of OH to O_3 and NO_y. Our results show that during the daytime OH level is sensitive to both O_3 and NO_y; however, OH is insensitive to O_3 at night since increasing O_3 tends to decrease HO_2, which cancels out the directly increasing trend of OH due to the reaction between O_3 and HO_2. The changes of the nighttime OH concentrations are smaller due to increasing NO_x than due to decreasing NO_x because of the compensation between the trend of increasing HO_2 due to increasing HO_2NO_2 and the trend of decreasing HO_2 due to increasing NO_2.

In summary, table 2.4 compares several model evaluations of the current global OH level and possible past OH levels over a long climatic period, adapted from Thompson (1992). Generally the current global OH level calculated with various photochemical models are converged to $0.5\sim1.0\times10^{+6}$ molecules/cm^3. However, the deviation of the past OH levels calculated with various models is substantially large, mainly resulting from the input data sets used by different models. This indicates that more work is needed to before we have a better estimate of OH trends. Deriving past OH levels from ice-core measurements of some "ideal" gases which are removed directly by OH yet are uncoupled from CH_4-CO-NO_x-OH-NMHC-O_3 cycle is a desirable alternative (Thompson, 1992).

Table 2.4. Comparisons of several Model-calculated Changes in Global OH[a]

Model and type	Reference	Current global OH (10^6 cm^{-3})*	OH change since preindustrial time	OH change since LGM
Harvard University (1D)	(*56*)	n.a.	60% loss	150% loss†
Cambridge University (2D)	(*30*)	0.95	NH: 50% loss SH: 20% gain	
Max Planck (2D)	(*82*)	0.91	NH: 50% gain to 40% loss SH: 20–40% loss	30–40% loss
Max Planck (3D)	(*83*)	0.6–0.80	NH: 10–20% gain SH: 10–20% loss	
USEPA/AREAL (1D)	(*55*)	0.6	4% loss	20% loss
OGI (multi-1D)	(*25*)	0.8	11% loss	40% loss
GSFC (multi-1D)	(*53*)	0.6	20% loss	32% loss

*Global average refers to volume average over model domain. †LGM calculation neglected temperature effect on H_2O vapor.

[a] The above table is taken from table 1 of Thompson (1992). For Harvard University (1D), see McElroy (1989); For Cambridge University (2D), see Law and Pyle (1991); See Valentin (1990) for Max Planck (2D) and Crutzen and Zimmenman (1991) for Max Planck (3D); See Pinto and Khalil (1991) for USEPA/AREAL (1D), where AREAL is Atmospheric Research and Exposure Assessment Laboratory; See Lu and Khalil (1991a) for their multi-1D's results, where OGI is Oregon Graduate Institute; See Thompson et al. (1992) for their multi-1D results, where GSFC is the Goddard Space Flight Center. NH is northern hemisphere and SH is southern hemisphere. n.a. is not available.

CHAPTER 3 CHEMICAL MECHANISMS OF THE HYDROXYL RADICAL AND FEEDBACK EFFECTS OF CO AND CH_4

As addressed previously, OH controls the atmospheric levels of many trace gases and free radicals by directly reacting with them. In turn the concentration of OH is affected by these trace gases and free radicals; a change of the concentration of any species, with which OH reacts, will change the levels of OH. The latitudinal and altitudinal variations of OH are greatly affected by the distributions of a number of trace gases and free radicals. Thus the first purpose of this chapter is to find the most important direct sources and sinks of the tropospheric OH. The reactions directly affecting HO_2 are also studied to derive the species and reactions most controlling HO_2 concentration, since HO_2 is the most important buffer of OH.

Carbon monoxide and methane are the two largest direct sinks of atmospheric OH. Globally the reaction between OH and CO provides the largest direct sink of OH, which is about twice as large as the reaction between OH and CH_4. However, neither CO nor CH_4 affects OH only by direct reactions. In fact, the direct reaction of OH with either CO or CH_4 initiates a series of reactions and products, which also affect the atmospheric OH and can thus be considered as feedbacks. A numerical method has been developed to calculate the total effects of either CO or CH_4 to OH by tracing a series of reactions and products, which are initiated by the direct reaction of OH with either CO or CH_4. The second purpose of this chapter is to discuss the total effects of CO and CH_4 to tropospheric OH by using this method.

3.1 Direct Sources and Sinks of OH and HO_2

In this study, ten reactions, considered as direct sources of OH, and another ten reactions, chosen as direct sinks of OH, were included in the model computations, as shown in table 3.1a. Considering the significant difference between daytime and nighttime OH concentrations, it is appropriate to study the sources and sinks both during daytime and at night.

The vertical averages of the direct sources of daytime OH for the four seasons and four latitudes are shown in fig. 3.1. The source strength of each source changes with latitude and season, resulting from the seasonal and latitudinal variations of solar insolation and a number of related trace gases and free radicals. Four of the ten sources are apparently much larger than the remaining six, as shown in this figure. The fraction of each of the four sources, or the ratio of each of the seasonal and vertical averages of the four direct sources of daytime OH to the sum of the seasonal and vertical averages of all the ten sources of daytime OH, was computed and is listed in percentage units immediately at the top of the appropriate black bar in the figure. On average, more than 97% of OH in the unpolluted troposphere is produced by the four reactions, among which the reaction between $O(^1D)$ and H_2O generates about 50% of the OH, being the largest direct source. The reactions of HO_2 with NO and O_3 contribute about 25% and around 15% respectively, or together about 40% of the total OH in the troposphere. The above three reactions, therefore, create about 90% of the all OH in the troposphere. The photodissociation of H_2O_2 generates about 10% of daytime OH in the troposphere, while the remaining six reactions together only produce less than 3% of the total OH.

At night all photolysis stops; therefore, the photodissociations as well as the reactions immediately linked with photolysis are no longer sources of OH. As shown

Table 3.1a The Expressions of all the Direct Sources and the Direct Sinks of OH, Included in This Study.

Index (i)	1	2	3	4	5
source (P_i)	$2J_{37}[H_2O]$	$J_{43}[HNO_3]$	$J_{40}[HNO_2]$	$J_{44}[HO_2NO_2]$	$J_{42}[CH_3OOH]$
sink (L_i)	$K_{29}[NO][OH]$	$K_{30}[NO_2][OH]$	$(K_{10a}+K_{10b})[HO_2][OH]$	$K_8[O_3][OH]$	$K_{12}[H_2O_2][OH]$
Index (i)	6	7	8	9	10
source (P_i)	$2K_3[O(^1D)][H_2O]$	$K_4[O(^1D)][H_2]$	$K_{5a}[O(^1D)][CH_4]$	$K_9[O_3][HO_2]$	$K_{13}[NO][HO_2]$
sink (L_i)	$K_7[H_2][OH]$	$K_{17}[CO][OH]$	$K_{18}[CH_4][OH]$	$K_{19}[H_2CO][OH]$	$K_{20}[CH_3OOH][OH]$

Table 3.1b The Expressions of all the Direct Sources and the Direct Sinks of HO_2, Included in This Study.

Index (i)	1	2	3
source (P_i)	$K_8[O_3][OH]$	$K_{12}[H_2O_2][OH]$	$K_{21}[CH_3O][O_2]$
sink (L_i)	$(K_{10a}+K_{10b})[OH][HO_2]$	$K_9[O_3][HO_2]$	$K_{13}[NO][HO_2]$
Index (i)	4	5	6
source (P_i)	$K_{22}[O_2][HCO]$	$K_{26}[O_2][H]$	$K_{35}[HO_2NO_2]$
sink (L_i)	$K_{24}[CH_3O_2][HO_2]$	$K_{31}[NO_2][HO_2]$	$(K_{11a}+K_{11b})[HO_2][HO_2]$

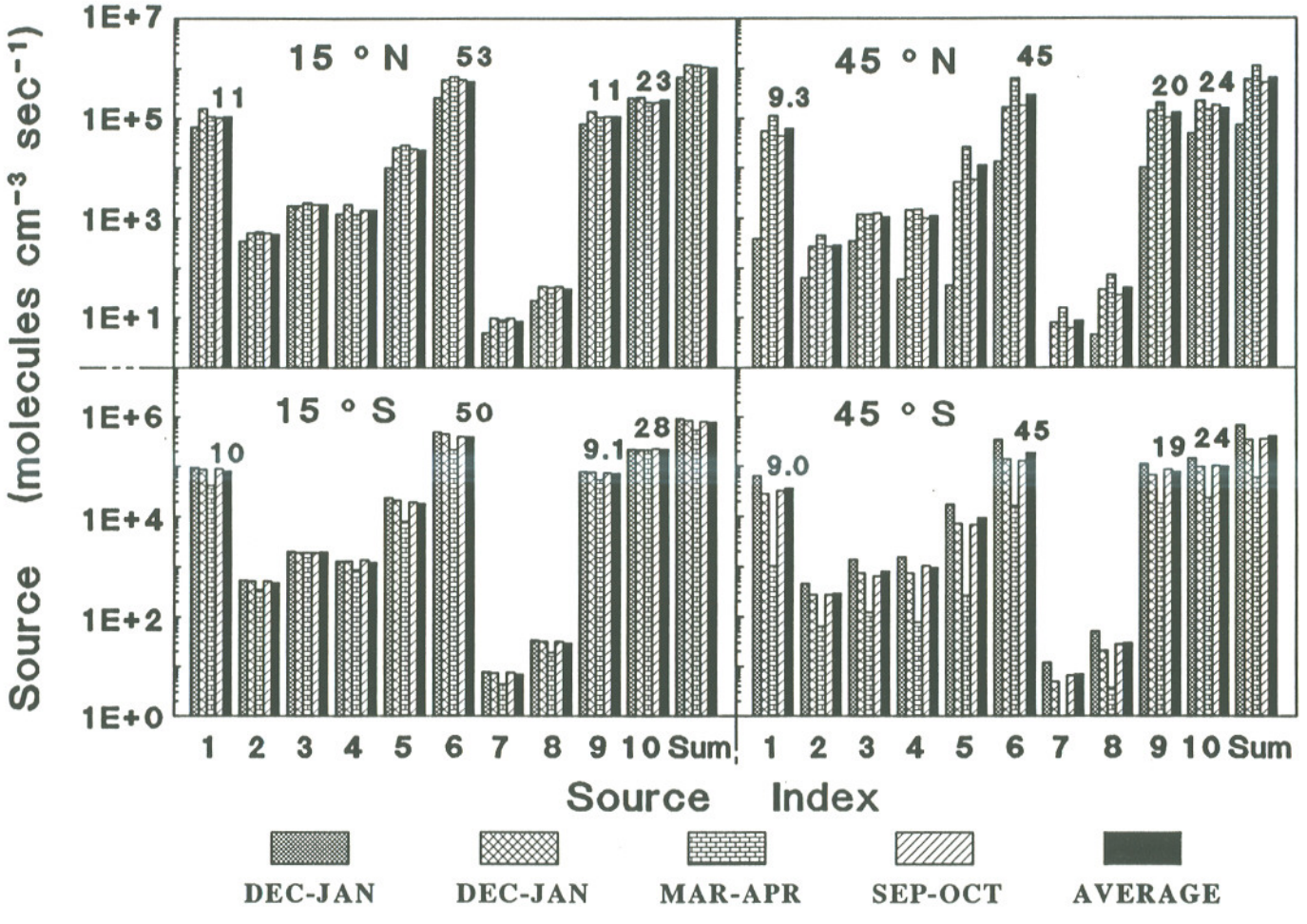

Fig. 3.1 The vertical averages of the direct sources of daytime OH. A black bar above shows a seasonal average and the notation 1E+5 represents 10_5. The data immediately at the top of a black bar is the ratio (in percentage) of the seasonal and vertical average of the direct source of OH (the black bar) to the sum of the seasonal and vertical averages of the all the direct sources of OH (the black bar corresponding to "Sum" label in x-axis). See table 3.1 for more information about expressions of the rates for production (or sources) of OH corresponding to all the source indexes.

in fig. 3.2, the reactions of HO_2 with O_3 and with NO are the only two sources to produce OH at night, but the source strengths, or the rates of production of OH, are much smaller at night than during daytime. The reaction between HO_2 and O_3 produces more than 99% of the total nighttime OH at the middle latitudes and more than 95% of the total nighttime OH at the tropics. Due to the rapid decrease of the concentration of NO after sunset, the reaction between NO and HO_2 contributes little OH at night.

The vertical averages of the direct daytime sinks and the direct nighttime sinks of OH are shown in figs. 3.3 and 3.4. Although the strengths of the sinks, or the rates of the consumption of OH, are much larger during daytime than at night, the patterns of the sinks of OH are similar: CO and CH_4 deplete most of OH during both day and night. In addition, the reaction between OH and CH_3OOH directly consumes about 15% tropospheric OH, being the third most important direct sink of OH.

As shown figs. 3.1 and 3.2, the reactions of HO_2 with NO and with O_3 produce a large amount of OH, especially at night when the reaction between HO_2 and O_3 becomes the only significant source of OH. On the other hand, HO_2 can directly reacts with OH although the amount of OH directly removed by HO_2 is rather small compared to other direct sinks, as shown in figs. 3.3 and 3.4. Thus in order to better understand OH chemistry, we need to have a good knowledge of the chemical cycle of HO_2. Six reactions are considered as direct sinks of HO_2, and another six reactions are chosen as direct sources of HO_2 for our model computations in this study.

Fig. 3.5 shows the vertical averages of all these six direct daytime sources of HO_2. The most significant daytime source is the reaction between O_2 and H, which produces about 60% of the total daytime HO_2 in the troposphere. The remaining

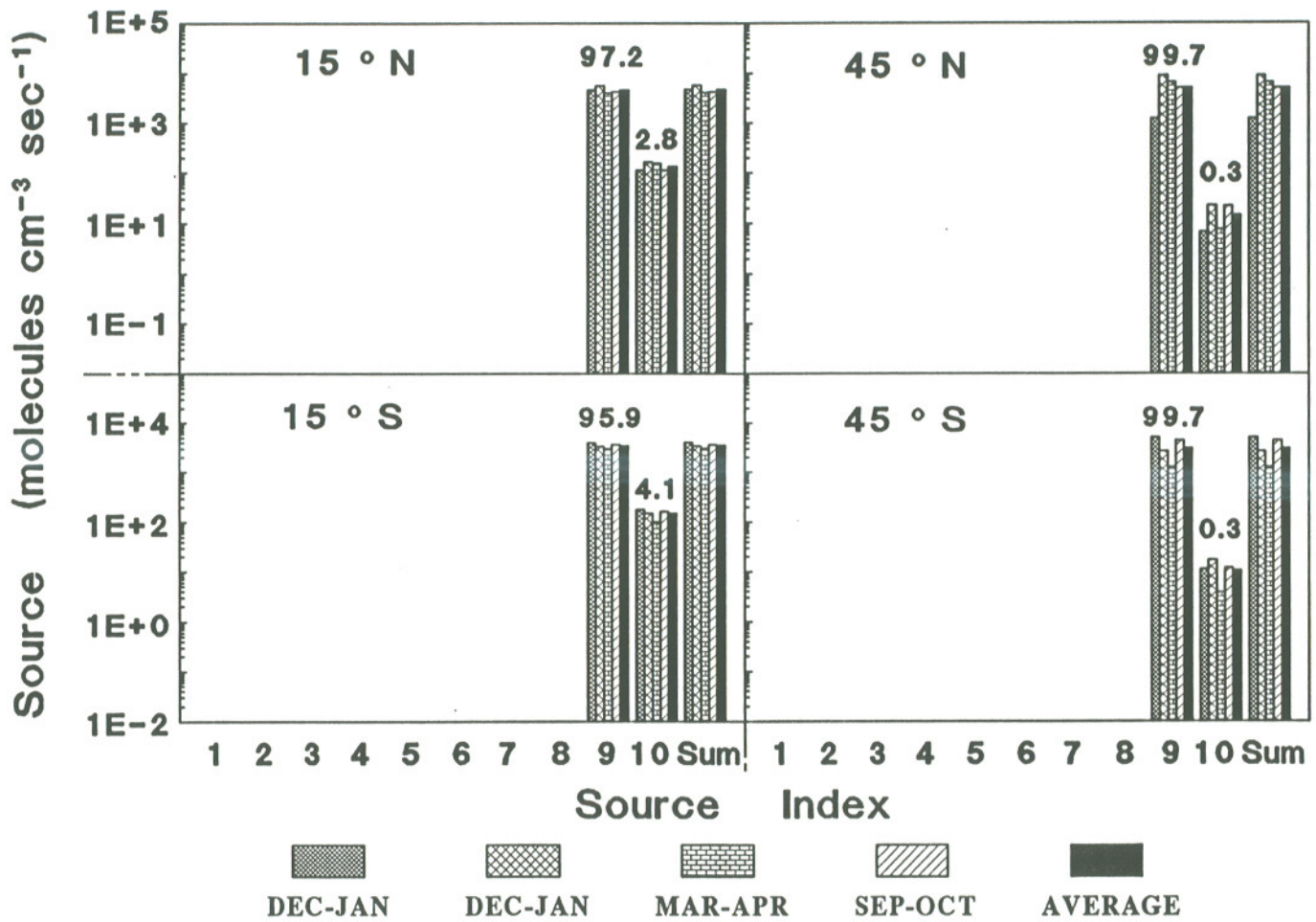

Fig. 3.2 The vertical averages of the direct sources of nighttime OH. A black bar above shows a seasonal average and the notation 1E+5 represents 10_5. The data immediately at the top of a black bar is the ratio (in percentage) of the seasonal and vertical average of the direct source of OH (the black bar) to the sum of the seasonal and vertical averages of the all the direct sources of OH (the black bar corresponding to "Sum" label in x-axis). See table 3.1 for more information about expressions of the rates for production (or sources) of OH corresponding to all the source indexes.

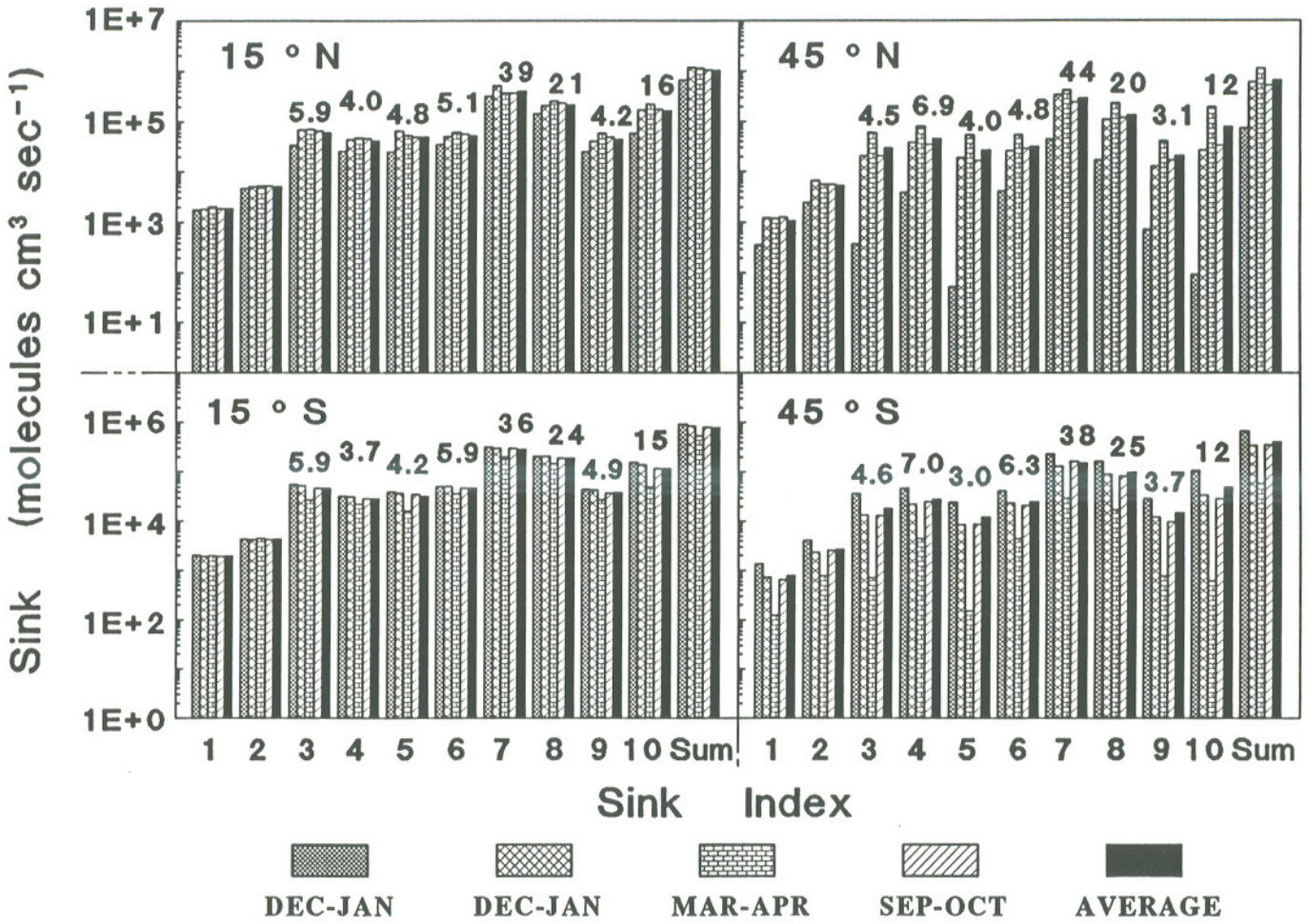

Fig. 3.3 The vertical averages of the direct sinks of daytime OH. A black bar above shows a seasonal average and the notation 1E+5 represents 10_5. The data immediately at the top of a black bar is the ratio (in percentage) of the seasonal and vertical average of the direct sink of OH (the black bar) to the sum of the seasonal and vertical averages of the all the direct sinks of OH (the black bar corresponding to "Sum" label in x-axis). See table 3.1 for more information about expressions of the rates for destruction (or sinks) of OH corresponding to all the sink indexes.

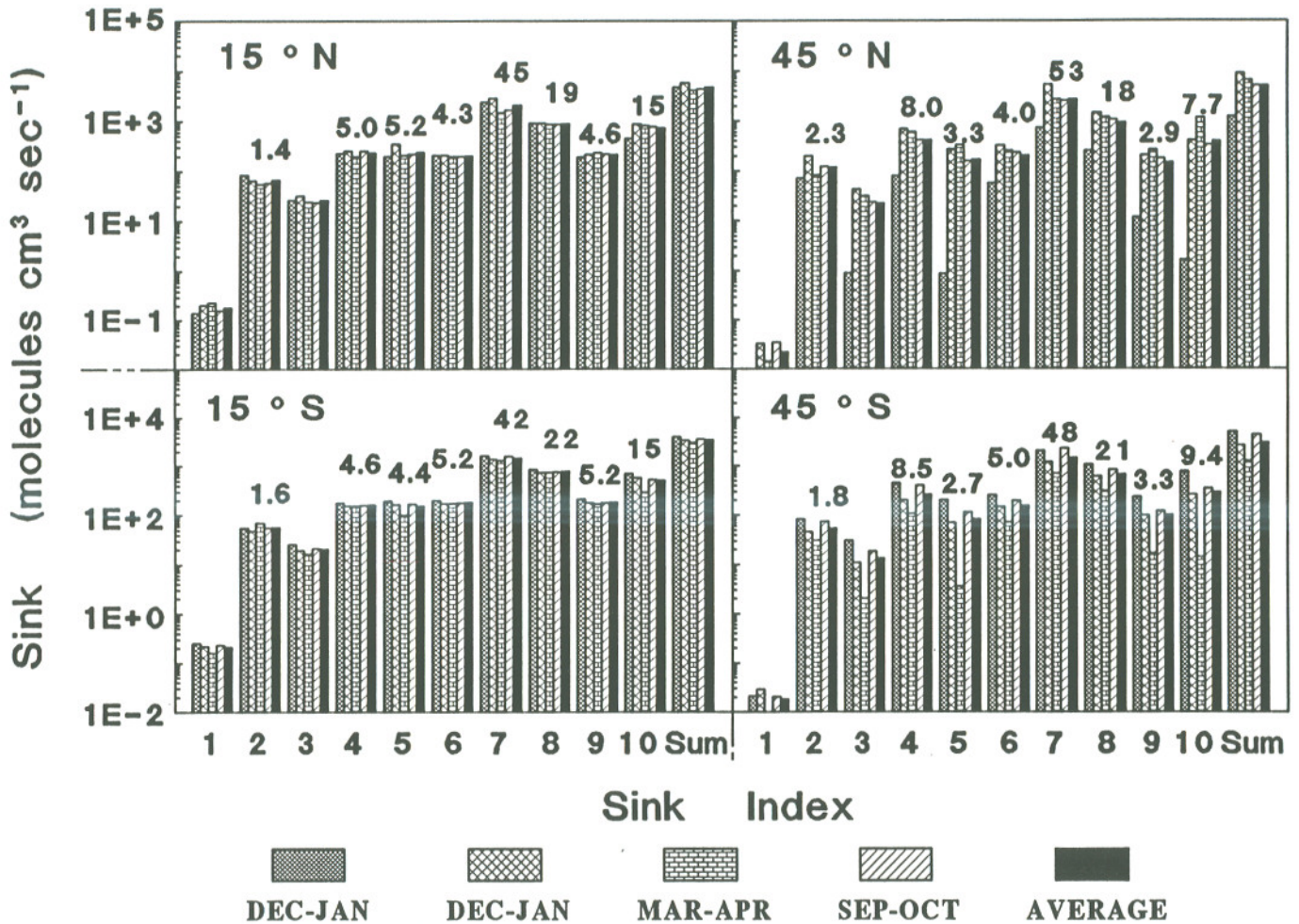

Fig. 3.4 The vertical averages of the direct sinks of nighttime OH. A black bar above shows a seasonal average and the notation 1E+5 represents 10_5. The data immediately at the top of a black bar is the ratio (in percentage) of the seasonal and vertical average of the direct sink of OH (the black bar) to the sum of the seasonal and vertical averages of the all the direct sinks of OH (the black bar corresponding to "Sum" label in x-axis). See table 3.1 for more information about expressions of the rates for destruction (or sinks) of OH corresponding to all the sink indexes.

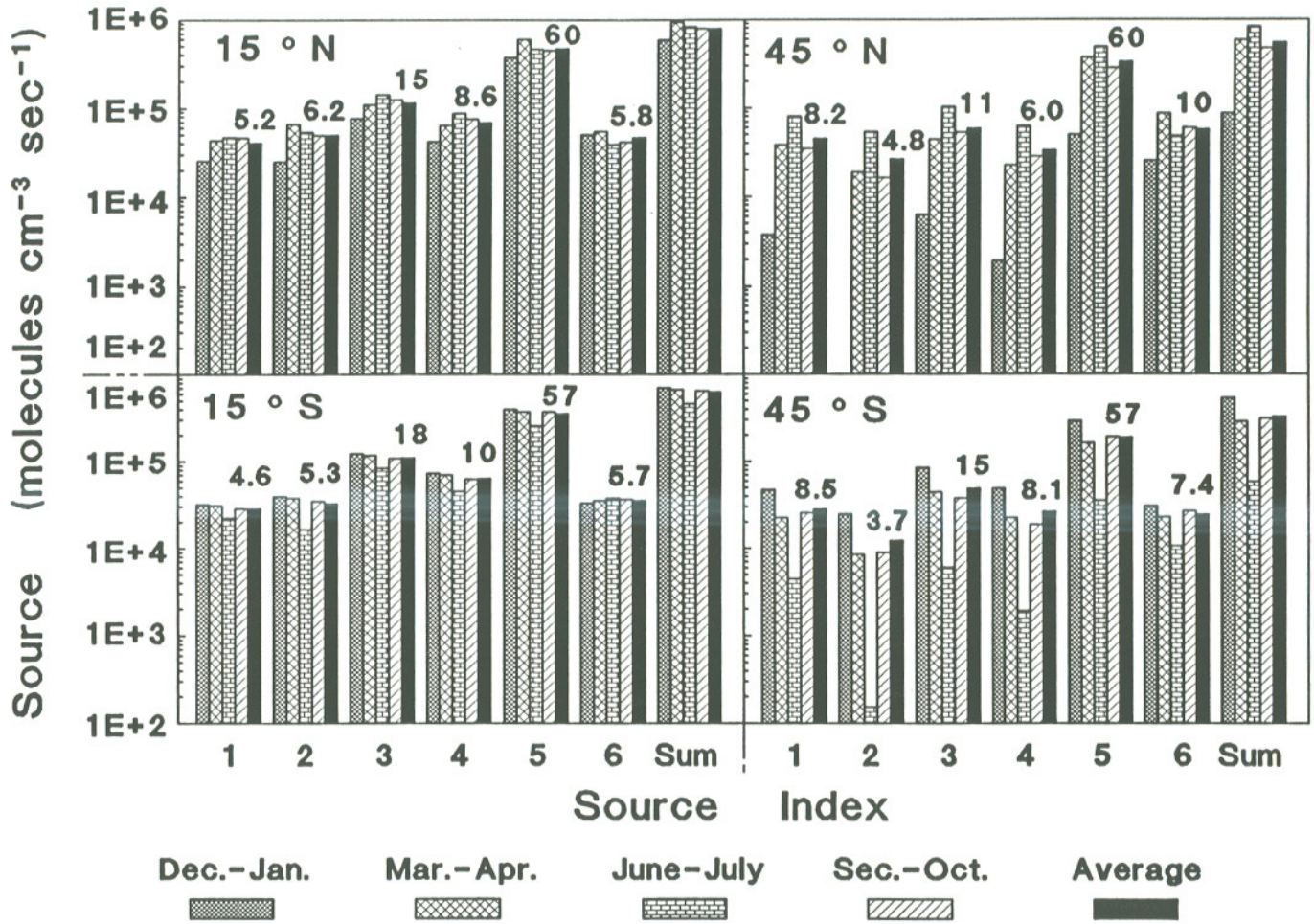

Fig. 3.5 The vertical averages of the direct sources of daytime HO_2. A black bar above shows a seasonal average and the notation 1E+5 represents 10_5. The data immediately at the top of a black bar is the ratio (in percentage) of the seasonal and vertical average of the direct source of HO_2 (the black bar) to the sum of the seasonal and vertical averages of the all the direct sources of HO_2 (the black bar corresponding to "Sum" label in x-axis). See table 3.1 for more information about expressions of the rates for production (or sources) of HO_2 corresponding to all the source indexes.

daytime HO_2 is generated by the other five reactions, among which the reaction between CH_3O and O_2, on the whole, is a little more important than the other four reactions. Unlike the direct daytime sources of OH, during daytime none of the six direct sources of HO_2 produce less than 1% of the total daytime HO_2 in the troposphere.

At night, due to the lower concentrations of most short lived species, the strengths of the six sources become weaker, as shown in fig. 3.6. Taking the place of the reaction between O_2 and H, the dissociation of HO_2NO_2 becomes the most important nighttime source of HO_2 by producing more than 60% of the total nighttime HO_2 in the troposphere, since the difference between the concentrations of the daytime HO_2NO_2 and the nighttime HO_2NO_2 is smaller than that between the concentrations of the daytime H and the nighttime H. The reaction between O_2 and H generates about 30% of the nighttime HO_2, being the second most important source at night. The above two reactions create more than 90% of the total nighttime HO_2.

Unlike the sinks of the daytime OH, the differences among sinks of HO_2 are not very large during daytime, as shown in fig. 3.7. The relatively large sink is the reaction between NO and HO_2, but the other five reactions are also important sinks during daytime.

At night, the concentrations of NO, CH_3O_2, and OH rapidly drop, while the concentration of NO_2 increases and the concentration of O_3 does not change. Therefore, the reactions of HO_2 with O_3 and with NO_2 at night become two dominant sinks of HO_2, together consuming more than 90% of HO_2 at night, as shown in fig. 3.8.

In summary, among all the reactions included in this model calculation, only

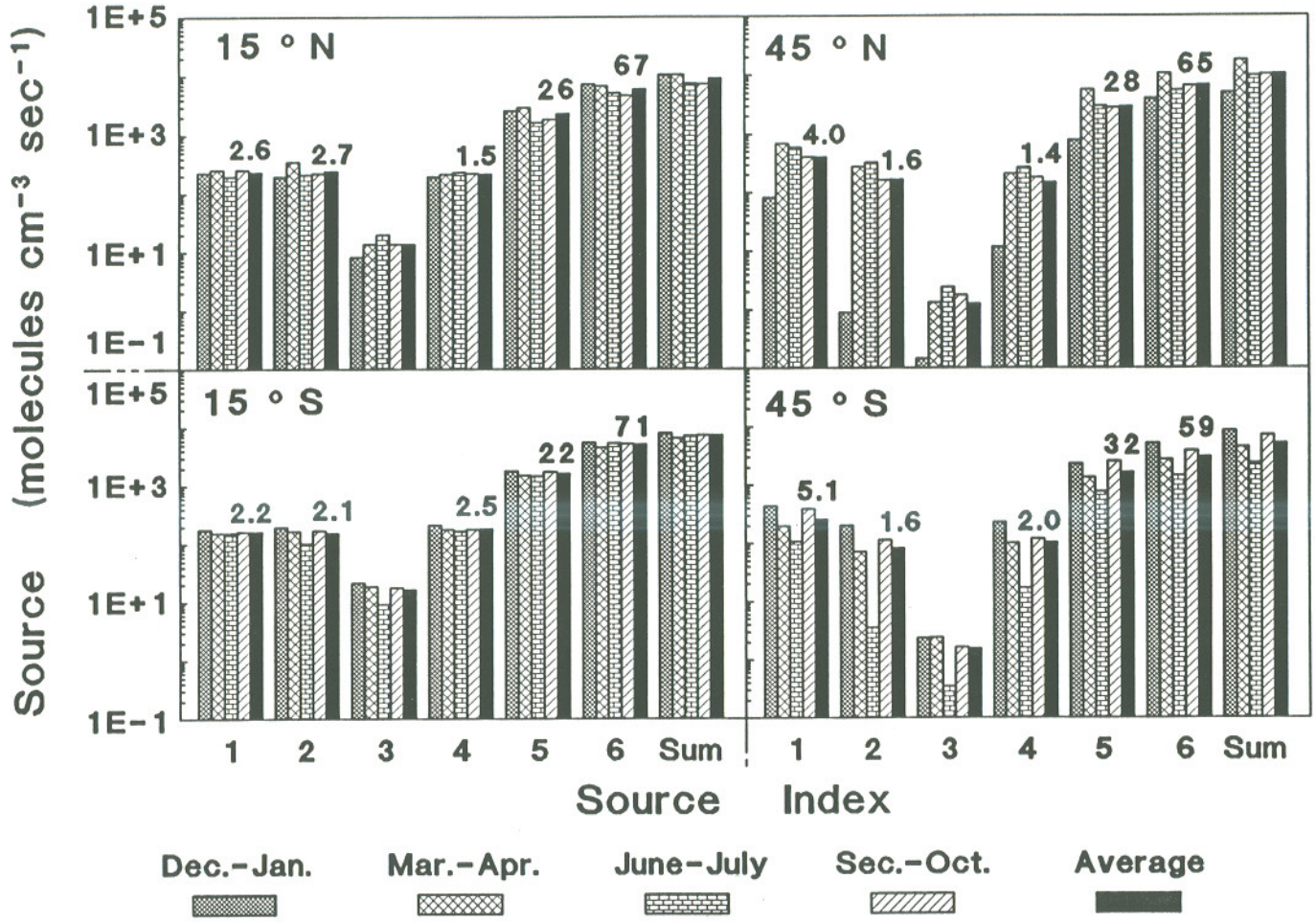

Fig. 3.6 The vertical averages of the direct sources of nighttime HO_2. A black bar above shows a seasonal average and the notation 1E+5 represents 10_5. The data immediately at the top of a black bar is the ratio (in percentage) of the seasonal and vertical average of the direct source of HO_2 (the black bar) to the sum of the seasonal and vertical averages of the all the direct sources of HO_2 (the black bar corresponding to "Sum" label in x-axis). See table 3.1 for more information about expressions of the rates for production (or sources) of HO_2 corresponding to all the source indexes.

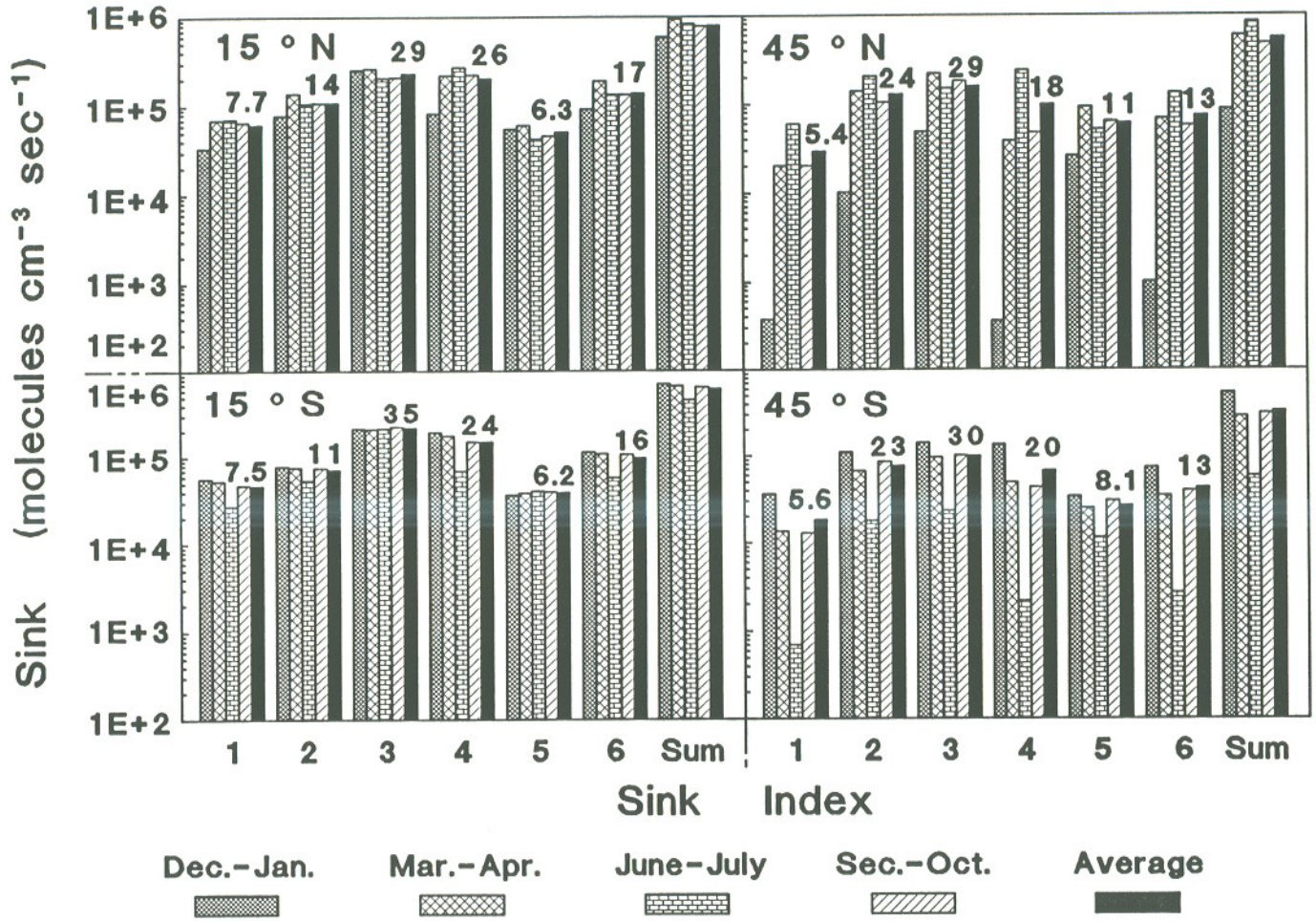

Fig. 3.7 The vertical averages of the direct sinks of daytime HO_2. A black bar above shows a seasonal average and the notation 1E+5 represents 105. The data immediately at the top of a black bar is the ratio (in percentage) of the seasonal and vertical average of the direct sink of HO_2 (the black bar) to the sum of the seasonal and vertical averages of the all the direct sinks of HO_2 (the black bar corresponding to "Sum" label in x-axis). See table 3.1 for more information about expressions of the rates for destruction (or sinks) of HO_2 corresponding to all the sink indexes.

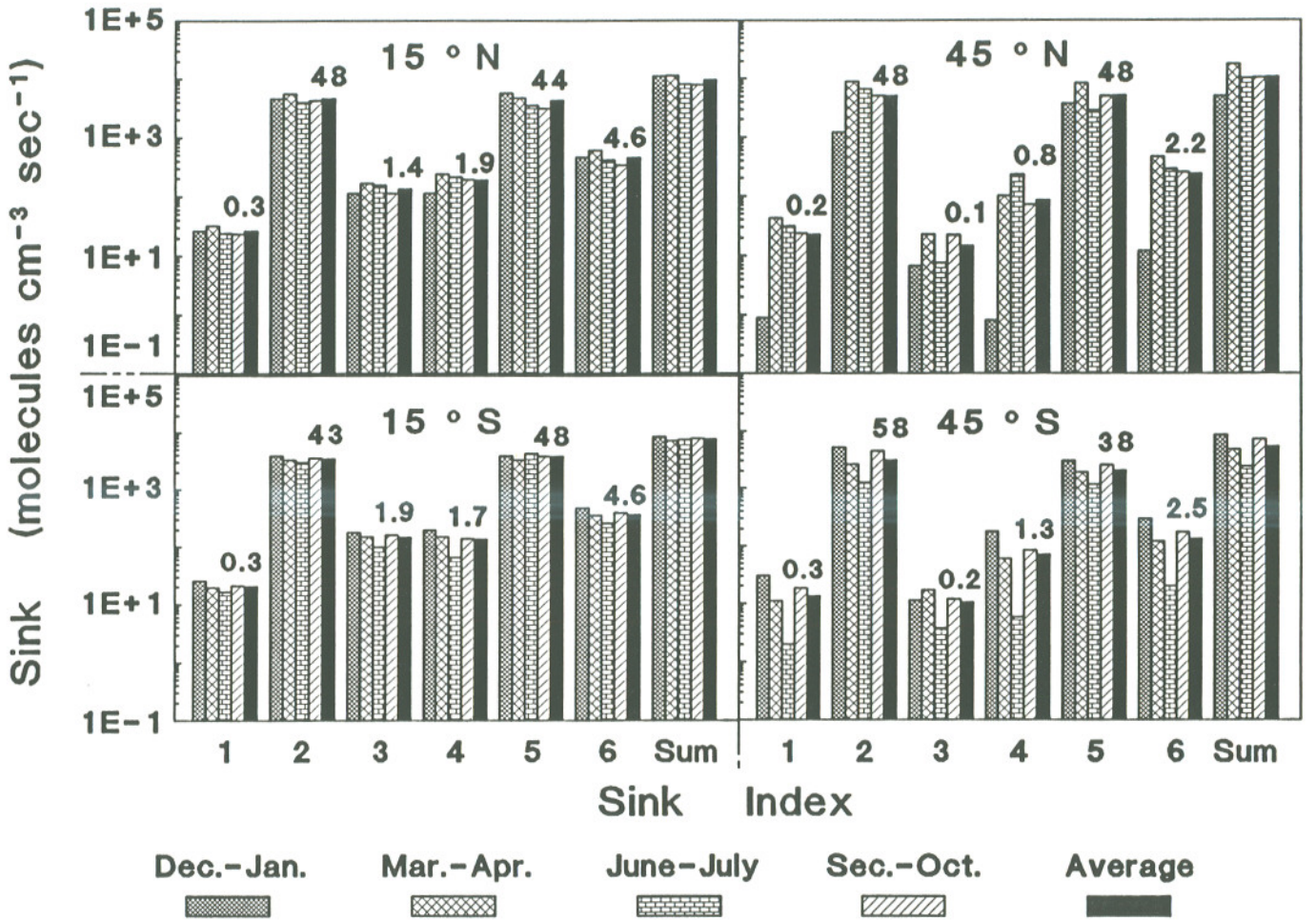

Fig. 3.8 The vertical averages of the direct sinks of nighttime HO_2. A black bar above shows a seasonal average and the notation 1E+5 represents 10_5. The data immediately at the top of a black bar is the ratio (in percentage) of the seasonal and vertical average of the direct sink of HO_2 (the black bar) to the sum of the seasonal and vertical averages of the all the direct sinks of HO_2 (the black bar corresponding to "Sum" label in x-axis). See table 3.1 for more information about expressions of the rates for destruction (or sinks) of HO_2 corresponding to all the sink indexes.

five reactions directly control the distribution of OH: the reaction of $O(^1D)$ with H_2O and the reactions of HO_2 with NO and with O_3 produce most of OH in the troposphere, while CO and CH_4 consume most of the OH. In contrast, all the six reactions, considered as direct sinks of HO_2 in this study, are important during daytime although the reaction between NO and HO_2 is a little more significant than the others. At night only two sinks of HO_2, the reactions of HO_2 with O_3 and with NO_2, are important. The most dominant direct source of HO_2 is the reaction between H and O_2, which on an average provides for more than 60% of HO_2 during the day. The dissociation of HO_2NO_2 is also an important source of HO_2, especially at night when it generates more than 60% of nighttime HO_2. Since the reaction between O_3 and HO_2 is the only significant source of nighttime OH, it can be further inferred that atmospheric HO_2NO_2 is a dominant source for the nighttime OH.

3.2 Actual contributions of CO and CH_4 to OH

As shown in figs. 3.3 and 3.4, among all the species reacting with OH, CO and CH_4 consume directly most of OH in troposphere. An increasing level of either CO or methane implies a decrease of OH, resulting in longer lifetimes and higher concentrations of other gases and free radicals whose sinks are controlled by OH. Although the reaction of OH with CO and with CH_4 provide the two largest direct sinks of OH, these reactions are not the only contributions to OH from CO and CH_4. As the matter of fact, the direct reactions initiate a series of reactions and generate a number of products, which further affect OH and can thus be seen as feedbacks of the direct contributions. The total contribution to OH from either CO or CH_4 is the sum of the direct contribution and all its feedbacks.

Model calculations of OH have been reviewed by Altshuller (1989) and Thompson (1992). As the two largest OH consumers, the current atmospheric levels of both CO and CH_4, their budgets, and their increasing trends are of considerable current interest (e.g., Khalil and Rasmussen, 1983, 1990a,b; Pinto et al., 1983; Cicerone and Oremland, 1989; Crutzen, 1991; Fung et al., 1991; Tie et al., 1991). The direct relationships between OH and CO and between OH and CH_4 have been studied extensively (e.g., Logan et al., 1981; Crutzen and Gidel, 1983; Lu and Khalil, 1991a). The variations of atmospheric OH concentrations responding to the changing levels of atmospheric CO and CH_4 have been reported in several recent papers (e.g., Khalil and Rasmussen, 1985, Levine et al., 1985; Thompson and Cicerone, 1986; Rotmans et al., 1990; Thompson et al., 1990 and 1991; Pinto and Khalil, 1991; Lu and Khalil, 1991a; Thompson, 1992). However, the chemical mechanisms of CO, CH_4, and OH have rarely been studied in such a way as to show the total contribution of either CO or CH_4 by taking into account not only the direct contribution but also all the feedbacks initiated by the direct reactions.

Based on chemical mechanisms and mass conservation law, we first studied the total contributions of CO and CH_4 to OH by tracing a series of reactions and products, which are initiated by the direct reaction of OH with CO or CH_4 (Lu, 1990). Based on this tracing technique, we further developed a more general method to calculate the total contribution to OH from either CO or CH_4 (Lu and Khalil, 1993a). All the contributions to OH, including the direct contributions and their feedbacks are taken into account by this method. In this section, based on our recent paper, the method are presented in sufficient detail, and then the model results are then discussed.

3.2.1 Chemical Mechanisms

As shown in fig. 3.9, the reaction between carbon monoxide and OH does not remove OH permanently from the atmosphere. Instead, it transfers OH to H,

$$OH + CO \rightarrow H + CO_2 \qquad (R17)$$

The resulting H atoms from the reaction (R17) mostly re-combine with molecular oxygen in the atmosphere to form hydroperoxyl radicals, HO_2,

$$H + O_2 + M \rightarrow HO_2 + M \qquad (R26)$$

and a large fraction of the resulting HO_2 radicals cycle themselves back to OH through the reactions with NO and with O_3:

$$HO_2 + NO \rightarrow OH + NO_2 \qquad (R13)$$

$$HO_2 + O_3 \rightarrow OH + O_2 + O_2 \qquad (R9)$$

The self-reaction of hydroperoxyl radicals also transfer themselves to hydrogen peroxide, H_2O_2, and some of the resulting H_2O_2 decomposes back to OH by photodissociation:

$$HO_2 + HO_2 \rightarrow H_2O_2 + O_2 \qquad (R11)$$

$$H_2O_2 + h\nu \rightarrow OH + OH \qquad (R37)$$

Noticing that the lifetimes of HO_2 and H_2O_2 are much longer than that of OH, and that both HO_2 and H_2O_2 cycle themselves back to OH as just described, HO_2 and H_2O_2 can be seen as buffers of OH, and the processes of the transferring HO_2 and H_2O_2 back to OH is defined as the buffer feedback of the direct contribution (Lu, 1990).

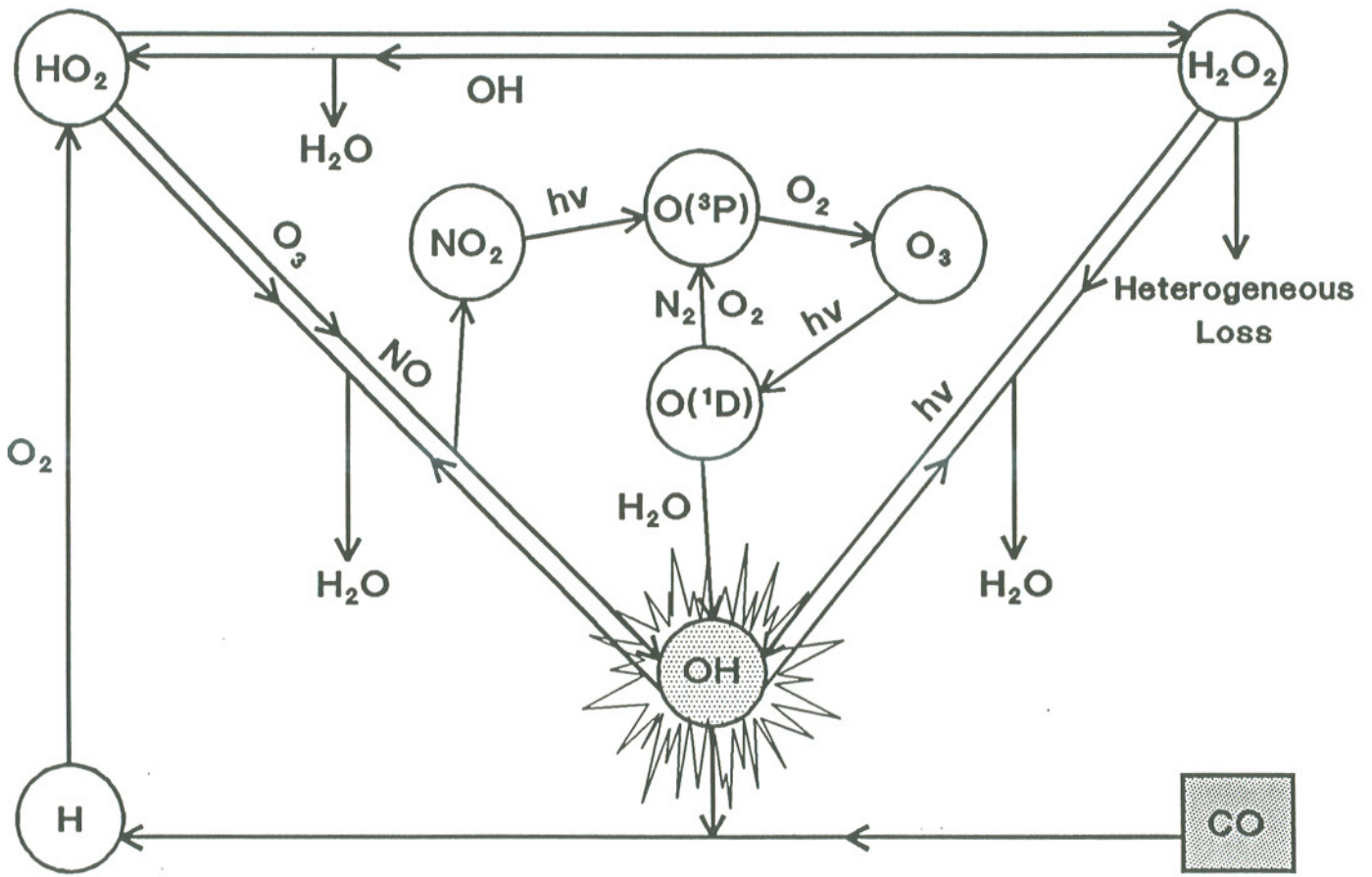

Fig. 3.9 The major reactions and species affecting OH, initialized by CO.

It should be emphasized here that the OH radicals would not be lost through the cycle initiated by the reaction between OH and CO, if there were not other removal processes for HO_x family. However, the losses of HO_x do exist in the cycle such as the reactions of OH with HO_2 and with H_2O_2 to form water, and the heterogeneous losses of H_2O_2 and HO_2NO_2, as discussed in chapter 2. Due to these losses processes, some of the OH radicals reacting with CO are eventually removed from the troposphere.

Besides the direct contribution of CO and its buffer feedback, the reaction between the resulting HO_2 and NO, as shown in reaction (R13), forms NO_2, which photodissociates into NO and ground state oxygen atoms, and the latter further reacts with oxygen molecules to produce O_3. The resulting O_3 will again create $O(^1D)$ and then OH, as shown in fig. 3.9. This process is defined as the oxygen feedback.

As shown fig. 3.10, the reaction between CH_4 and OH initiates a complicated sequence of reactions, which eventually transfers some OH to HO_2 and H_2O_2, and also creates a family of a series of organic compounds, CH_iO_j family, consisting of H_2CO, CH_3, CH_3O, CH_3O_2, CH_3OOH, and HCO. The recycling of the resulting HO_2 and H_2O_2 back to OH is defined as the buffer feedback of the direct contribution of CH_4 to OH, similar to that of CO. Besides, the resulting organics also affect OH directly or indirectly. We call this process the organics feedback, or CH_iO_j feedback. In addition, the resulting HO_2 as well as CH_3O_2 react with NO generating cycles to create O_3 and OH. Similar to CO, we call this process oxygen feedback from CH_4.

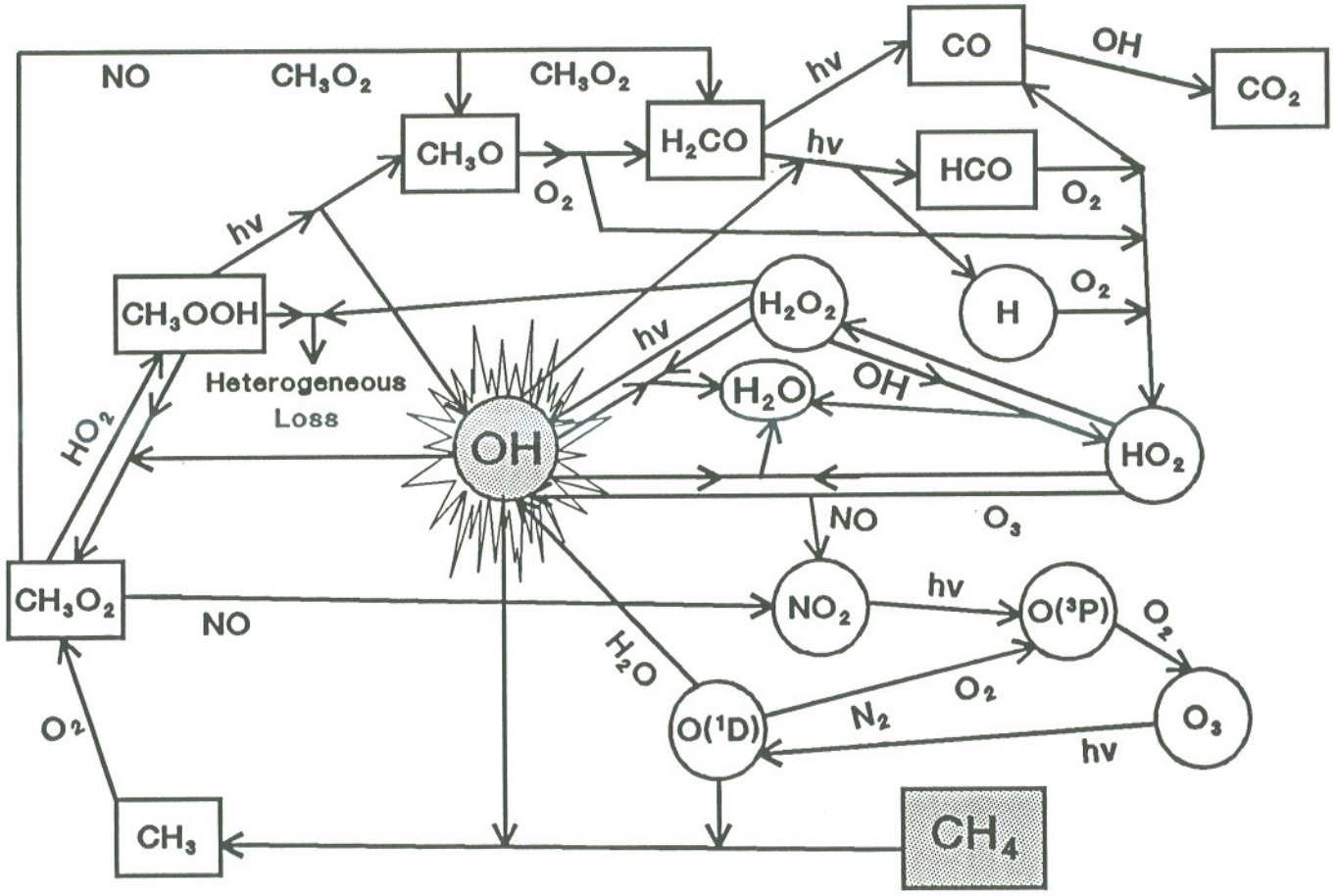

Fig. 3.10 The major reactions and species affecting OH, initialized by CH_4.

3.2.2 Equations and Numerical Method

Based on the chemical mechanisms described in the previous section, the total contribution of CO to OH is the sum of the direct contribution and all its feedback including the buffer feedback and the oxygen feedback, as summarized in fig. 3.11. The mathematical interpretation is shown as follow:

$$TCO_k = DCO_k + FBCO_k + FOCO_k \tag{3.1}$$

where TCO, DCO, FBCO, and FOCO represent the total, direct, buffer feedback, and oxygen feedback contributions of CO, respectively; *k* designates the *k*th time step of a day.

The direct reaction between OH and CO is the only direct contribution of CO to the loss of OH:

$$DCO_k = K_{17}[CO][OH]_k \tag{3.2}$$

where a species with the brackets, [], represents the concentration of the species.

As described in the previous section, HO_2 and H_2O_2, the two buffers of OH, resulting from the reactions initiated by the direct reaction of OH with CO, cycle themselves back to OH by reacting with NO and with O_3, and also by the photodissociation of H_2O_2. Besides, the buffers also consume OH directly. Therefore, the changing rate of OH due to the buffer feedback of CO can be expressed as:

$$\begin{aligned} FBCO_k = {} & \{(K_{10a} + K_{10b})[OH]_k - (K_9[O_3]_k + K_{13}[NO]_k)\} \cdot [HO_2]_k^{CO} \\ & + \{K_{12}[OH]_k - 2J_{37}\} \cdot [H_2O_2]_k^{CO} \end{aligned} \tag{3.3}$$

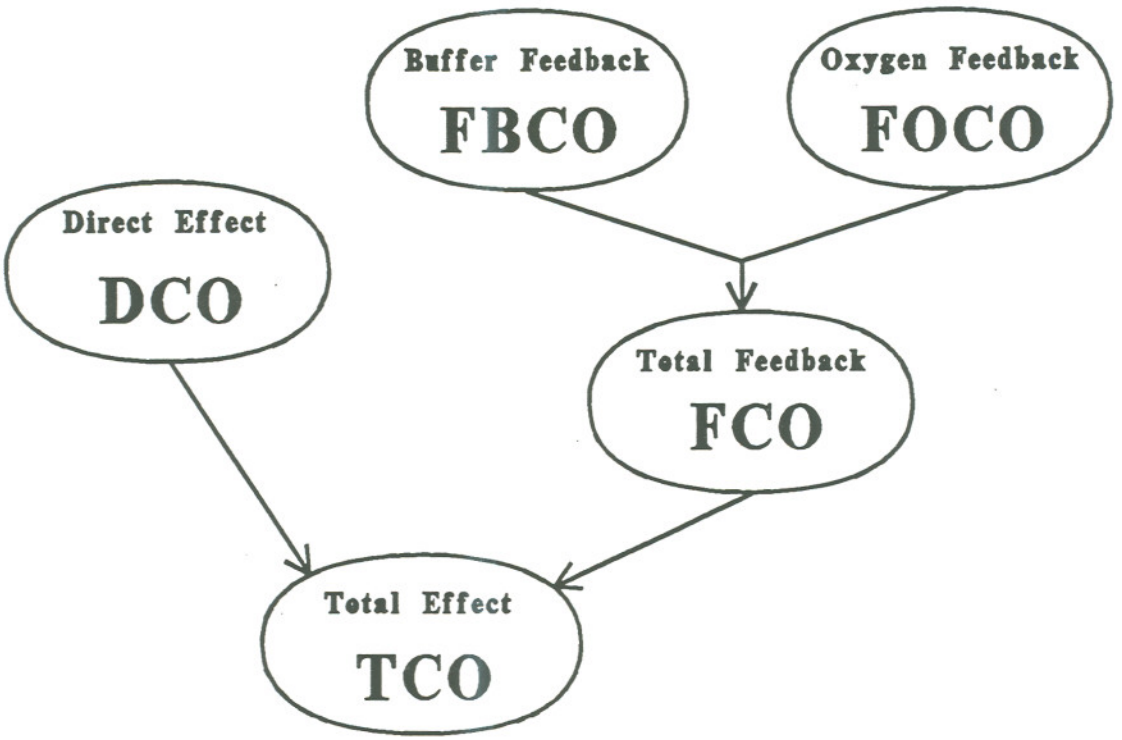

Fig. 3.11 The contributions of CO to OH. DCO (Direct Effect) is the loss rate of OH due to the direct reaction with CO; FBCO (Buffer Feedback) is the production or loss rate of OH due to the effect from HO_2 and H_2O_2; FOCO (Oxygen Feedback) is the production or loss rate of OH due to the effect from a series of resulting oxides (NO_2, $O(^3P)$, and $O(^1D)$); FCO (Total Feedback) is the production or loss rate of OH due to both the buffer feedback and the oxygen feedback; TCO (Total Effect) is the loss rate due to both the direct effect and its total feedback.

Notice that $[HO_2]^{CO}{}_k$ and $[H_2O_2]^{CO}{}_k$ are respectively the amount of HO_2 and H_2O_2 at the *K*th time step, produced by the cycles initiate by the reaction between OH and CO. The values of $[HO_2]^{CO}{}_k$ and $[H_2O_2]^{CO}{}_k$ are never equal to but smaller than the concentrations of HO_2 and H_2O_2, $[HO_2]$ and $[H_2O_2]$.

The contribution of the oxygen feedback to OH is derived from two reactions: the reaction between water vapor and the resulting $O(^1D)$ from the cycle initiated by the reaction of NO and the resulting HO_2, and that between OH and the yielding NO_2 generated in the same cycle. Thus the changing rate of OH due to the oxygen feedback can be expressed as:

$$FOCO_k = K_{30}[OH]_k[NO_2]_k^{CO} - 2K_3[O(^1D)]_k^{CO}[H_2O] \qquad (3.4)$$

where $[NO_2]^{CO}{}_k$ and $[O(^1D)]^{CO}{}_k$ represent the amount of NO_2 and $O(^1D)$ in a unit volume at the *k*th time step, which are produced in the cycles initialized by the direct reaction between OH and CO. A *K* with a subscript corresponds to the rate of a binary or a termolecular reaction and a *J* with a subscript denotes a photodissociation rate. All the chemical reactions included in this study are listed in table 2.1. The concentrations of the series of species shown in eqs. 3.2~3.4 can be obtained by using the information and model results shown in the previous chapter. To obtain the magnitudes of these resulting species due to the processes initialized by the direct reaction between OH and CO, $[X]_k^{CO}$ (X corresponds to HO_2, H_2O_2, etc), one has to solve another set of mass continuity equations, which will be discussed later in this section.

As shown in fig. 3.12, the total contribution of CH_4 to OH (TCH_4), is its direct contribution (DCH_4), plus its three feedbacks: the buffer feedback ($FBCH_4$), the organics (or CH_iO_j) feedback ($FCCH_4$), and the oxygen feedback ($FOCH_4$); i.e.,

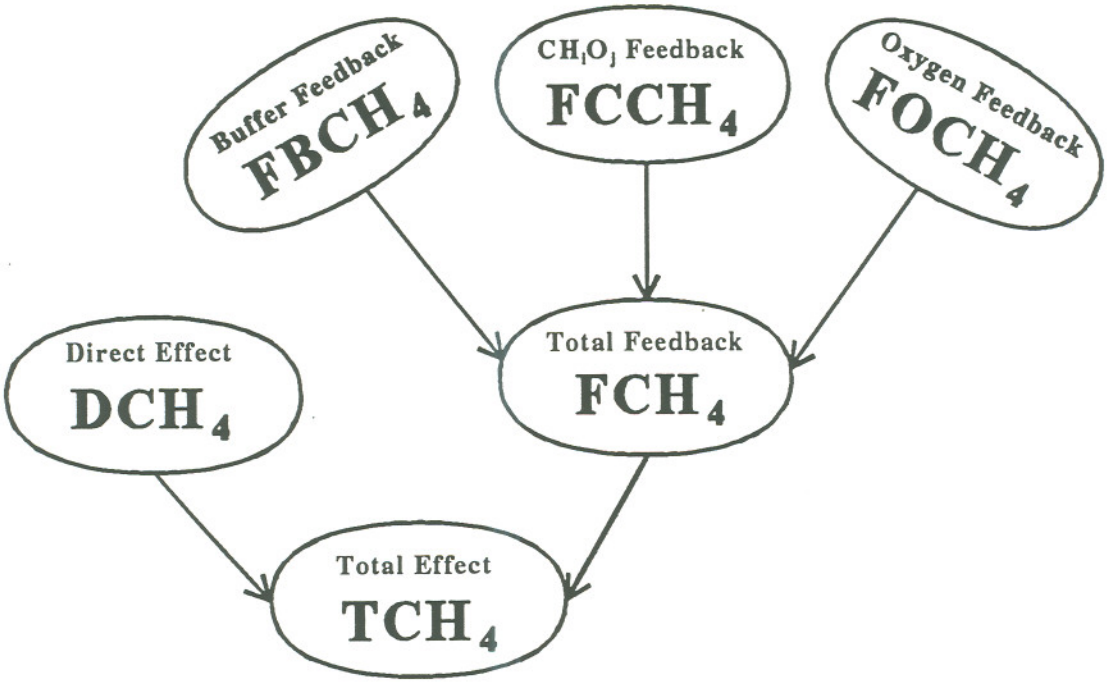

Fig. 3.12 The contributions of CH_4 to OH. DCH_4 (Direct Effect) is the loss rate of OH due to the direct reaction with CH_4; $FBCH_4$ (Buffer Feedback) is the production or loss rate of OH due to the effect from HO_2 and H_2O_2; $FCCH_4$ (CH_iO_j Feedback) is the production or loss rate of OH due to the effect from a series of resulting organic compounds; $FOCH_4$ (Oxygen Feedback) is the production or loss rate of OH due to the effect from a series of resulting oxides (NO_2, $O(^3P)$, and $O(^1D)$); FCH_4 (Total Feedback) is the production or loss rate of OH due to all the three feedbacks of the direct effect; TCH_4 (Total Effect) is the loss rate due to both the direct effect and all its feedbacks.

$$TCH_{4_k} = DCH_{4_k} + FBCH_{4_k} + FOCH_{4_k} + FCCH_{4_k} \tag{3.5}$$

Other than directly consuming OH in the atmosphere, CH_4 also reacts with $O(^1D)$ to produce OH; therefore, the direct contribution of CH_4, or the loss rate of OH due to the direct effect from CH_4 at the *k*th time state is:

$$DCH_{4_k} = K_{18}[CH_4][OH]_k - K_{5a}[O(^1D)]_k[CH_4] \tag{3.6}$$

Among the resulting CH_iO_j species, which are generated from the cycle initiated by CH_4, H_2CO and CH_3OOH have direct influences on OH. On the one hand, H_2CO and CH_3OOH can directly react with OH to remove OH; on the other hand, CH_3OOH can dissociate to OH and CH_3O under solar radiation. Thus the total direct contribution to OH from CH_iO_j family, or the CH_iO_j feedback of the direct contribution of CH_4, at the *k*th time state, is:

$$FCCH_{4_k} = K_{19}[H_2CO]_k[OH]_k + (K_{20}[OH]_k - J_{42}) \cdot [CH_3OOH]_k \tag{3.7}$$

This feedback is a sink of OH for $FCCH_{4_k} > 0$ and a source of OH if $FCCH_{4_k} < 0$.

Similar to CO, the loss or production rate resulting from the buffer feedback of CH_4 can be calculated by the following formula:

$$\begin{aligned} FBCH_{4_k} = {} & \{(K_{10a} + K_{10b})[OH]_k - (K_9[O_3]_k + K_{13}[NO]_k)\} \cdot [HO_2]_k^{CH_4} \\ & + \{K_{12}[OH]_k - 2J_{37}\} \cdot [H_2O_2]_k^{CH_4} \end{aligned} \tag{3.8}$$

where the buffer feedback produces OH if $FBCH_{4_k} < 0$.

The expression of the loss or production rate of OH due to the oxygen feedback of CH_4 is similar to that of CO, although the resulting CH_3O_2, apart from the resulting HO_2, also reacts with NO to eventually form O_3 and OH (also see eqs. 3.21 and 3.28 for a comparison); i.e.,

$$FOCH_{4_k} = K_{30}[OH]_k[NO_2]_k^{CH_4} - 2K_3[O(^1D)]_k^{CH_4}[H_2O] \qquad (3.9)$$

Similarly, $[X]_k^{CH_4}$ (X corresponds to HO_2, H_2O_2, NO_2, $O(^1D)$, etc) represents the amount of species X in a unit volume, which is produced in the cycles initialized only by the direct reaction between OH and CH_4. It should be noted that the number density of either HO_2 or H_2O_2 should be the sum of the numbers of HO_2 or H_2O_2 generated in the cycles initiated by the reactions of OH with CH_4 as well as with CO and with H_2, and with other trace gases. $[X]_k^{CH_4}$ is not equal to but smaller than [X].

The concentrations of a series of species shown in the above equations can be obtained by using the input data shown in the previous chapter or through the model calculations as described in chapter 2. All the chemical reactions, the rates of the reactions, and other input data sets such as the concentrations of trace gases and the eddy diffusivities used in this study were the same as those used in our previous studies (Lu, 1990; Lu and Khalil, 1991 and 1992, and references therein) except the rate of the reaction between OH and CH_4, which was taken from Vaghjiani and Ravishankara (1991). To obtain the magnitudes of these resulting species due to the processes initialized by the direct reaction between OH and species Y (Y corresponding to either CO or CH_4), $[X]_k^Y$ (X corresponds to HO_2, H_2O_2, etc), one has to solve another set of mass continuity equations.

Based on the chemical mechanisms described in this section and the previous one, and the mass continuity equation, the following equations are set up to calculate the amount of product per unit volume in the chemical cycles initiated by the reaction between OH and the species Y:

$$\frac{\partial [X]^Y}{\partial t} = -D_X \cdot [X]^Y + P_X^Y + \frac{\partial}{\partial z} K_z \frac{\partial [X]^Y}{\partial z} \tag{3.10}$$

where $[X]^Y$ (X corresponds to H, HO_2, H_2O_2, NO_2, $O(^3P)$, O_3, or, $O(^1D)$) represents the quantity of species X in a unit volume, which is only generated in the cycles initialized by the direct reaction between OH and Y corresponding to either CO or CH_4; D_X is the loss rate of the species X, in the unit of sec^{-1}; P_X^Y denotes the production rate of the species X in the cycles initiated by the direct reaction between OH and species Y (either CO or CH_4), in the unit of molecules/cm^3/sec.

Whenever a molecule is generated, it always mixes with ambient air and thus gets the same transformation and removal process in the atmosphere no matter what kind of chemical mechanism the molecule is produced by. They are mathematically expressed as follows:

$$D_H = K_{26}[O_2] \tag{3.11}$$

$$D_{HO_2} = K_9[O_3] + (K_{10a} + K_{10b})[OH] + K_{13}[NO] + K_{24}[CH_3O_2] + K_{31}[NO_2] + (K_{11a} + K_{11b})[HO_2] \tag{3.12}$$

$$D_{H_2O_2} = K_{12}[OH] + K_{46} + J_{37} \tag{3.13}$$

$$D_{NO_2} = K_{30}[OH] + K_{31}[HO_2] + K_{32}[NO_3] + K_{33}[CH_3O_2] + J_{38} + K_{16}[O_3] \tag{3.14}$$

$$D_{O(^1P)} = K_{27}[O_2] \tag{3.15}$$

$$D_{O_3} = K_8[OH] + K_9[HO_2] + K_{14}[NO] + K_{10}[NO_2] + J_{36} \quad (3.16)$$

$$D_{O(^1D)} = K_1[N_2] + K_2[O_2] + K_3[H_2O] + K_4[H_2] + (K_{5a} + K_{5b})[CH_4] + K_6[N_2O] \quad (3.17)$$

The production of H due to the chemical cycles, initiated from the reaction between OH and CO, is

$$P_H^{CO} = K_{17}[OH][CO] \quad (3.18)$$

The resulting H atoms are quenched by oxygen molecules to form hydroperoxyl radicals, HO_2, which react with themselves as well as with other ambient HO_2 radicals to generate H_2O_2 molecules, some of which cycle themselves back to HO_2 radicals by reacting with OH. Thus the production rates of the two resulting buffers, HO_2 and H_2O_2, generated in the cycles initiated by the reaction between OH and CO can be expressed as:

$$P_{HO_2}^{CO} = K_{12}[OH][H_2O_2]^{CO} + K_{26}[H]^{CO}[O_2] \quad (3.19)$$

$$P_{H_2O_2}^{CO} = (K_{11a} + K_{11b})[HO_2][HO_2]^{CO} \quad (3.20)$$

The production of NO_2 resulting from the cycles initialized by CO is actually the reaction between the resulting HO_2 and the ambient NO, i.e.,

$$P_{NO_2}^{CO} = K_{13}[NO][HO_2]^{CO} \quad (3.21)$$

The photodissociation of the resulting NO_2 generates the ground state oxygen atoms, which further form O_3 by reacting with atmospheric oxygen molecules. On the other hand, the resulting excited state oxygen atoms, $O(^1D)$, from the photolysis of O_3, are mostly quenched by N_2 and O_2 to reform the ground state oxygen atoms. Thus the production rates of $O(^3P)$, O_3, and $O(^1D)$ in the cycles initiated by CO are expressed

respectively as:

$$P_{O(^3P)} = J_{38}[NO_2]^{CO} + (K_1[N_2] + K_2[O_2])[O(^1D)]^{CO} \quad (3.22)$$

$$P_{O_3}^{CO} = K_{27}[O(^3P)]^{CO}[O_2] \quad (3.23)$$

$$P_{O(^1D)}^{CO} = J_{36}[O_3]^{CO} \quad (3.24)$$

Although the reaction between OH and CH_4 initiated a rather complicated sequence of reactions, the production of the atomic H, generated in the resulting cycles, is actually from the photodissociation of H_2CO; i.e.,

$$P_H^{CH_4} = J_{41a}[H_2CO] \quad (3.25)$$

Besides the chemical mechanisms for producing HO_2, similar to those initialized by CO, the oxygen molecules also react with the resulting CH_3O and HCO to create HO_2; therefore, the total production of HO_2 in the cycles initiated by CH_4 is:

$$P_{HO_2}^{CH_4} = K_{12}[OH][H_2O_2]^{CH_4} + K_{26}[H]^{CH_4}[O_2] + K_{21}[CH_3O][O_2] + K_{22}[HCO][O_2] \quad (3.26)$$

The expression of the resulting H_2O_2 from the cycles initialized by CH_4 is similar to that initialized by CO:

$$P_{H_2O_2}^{CH_4} = (K_{11a} + K_{11b})[HO_2][HO_2]^{CH_4} \quad (3.27)$$

It should be noted that in the cycles initiated by CH_4, the ambient NO reacts not only with the resulting HO_2 but also with the resulting CH_3O_2 to from NO_2 to eventually to create O_3 and $O(^1D)$; i.e.

$$P_{NO_2}^{CH_4} = K_{13}[NO][HO_2]^{CH_4} + K_{25}[CH_3O_2][NO] \quad (3.28)$$

$$P^{CH_4}_{O(^3P)} = J_{38}[NO_2]^{CH_4} + (K_1[N_2] + K_2[O_2])[O(^1D)]^{CH_4} \quad (3.29)$$

$$P^{CH_4}_{O_3} = K_{27}[O(^3P)]^{CH_4}[O_2] \quad (3.30)$$

$$P^{CH_4}_{O(^1D)} = J_{36}[O_3]^{CH_4} \quad (3.31)$$

The numerical method to solve the partial differential equation set, eqs. 3.10 ~ 3.31, is the same as that described in the previous chapter (Also see Lu and Khalil, 1991a). However, before numerically solving the equation set, we first have to solve another series of partial differential equations to obtain the ambient concentrations of a number of species and radicals such as OH, HO_2, and O_3. All the equations, input data set, and numerical method to calculate the ambient concentrations of the species and radicals are provided in the previous chapter (Also see Lu and Khalil, 1991a) with only two exceptions; we included the explicit O_3 calculation in our modified model and the rate constant of the reaction between OH and CH_4 was taken from Vaghjiani and Ravishankara (1991).

3.2.3 Model Results

Fig. 3.13 compares the direct contribution of CO to OH with its feedbacks including the buffer feedback and the oxygen feedback, and with the total contribution of CO to OH for the four latitudes and four seasons. In order to show the importance of each contribution with respect to the direct contribution, the production or loss rates of OH respectively due to direct, feedback, and total contribution are all "normalized" by dividing by that loss rate due to the direct contribution. Bar signs in each legend name correspond to the diurnal and vertical average in the

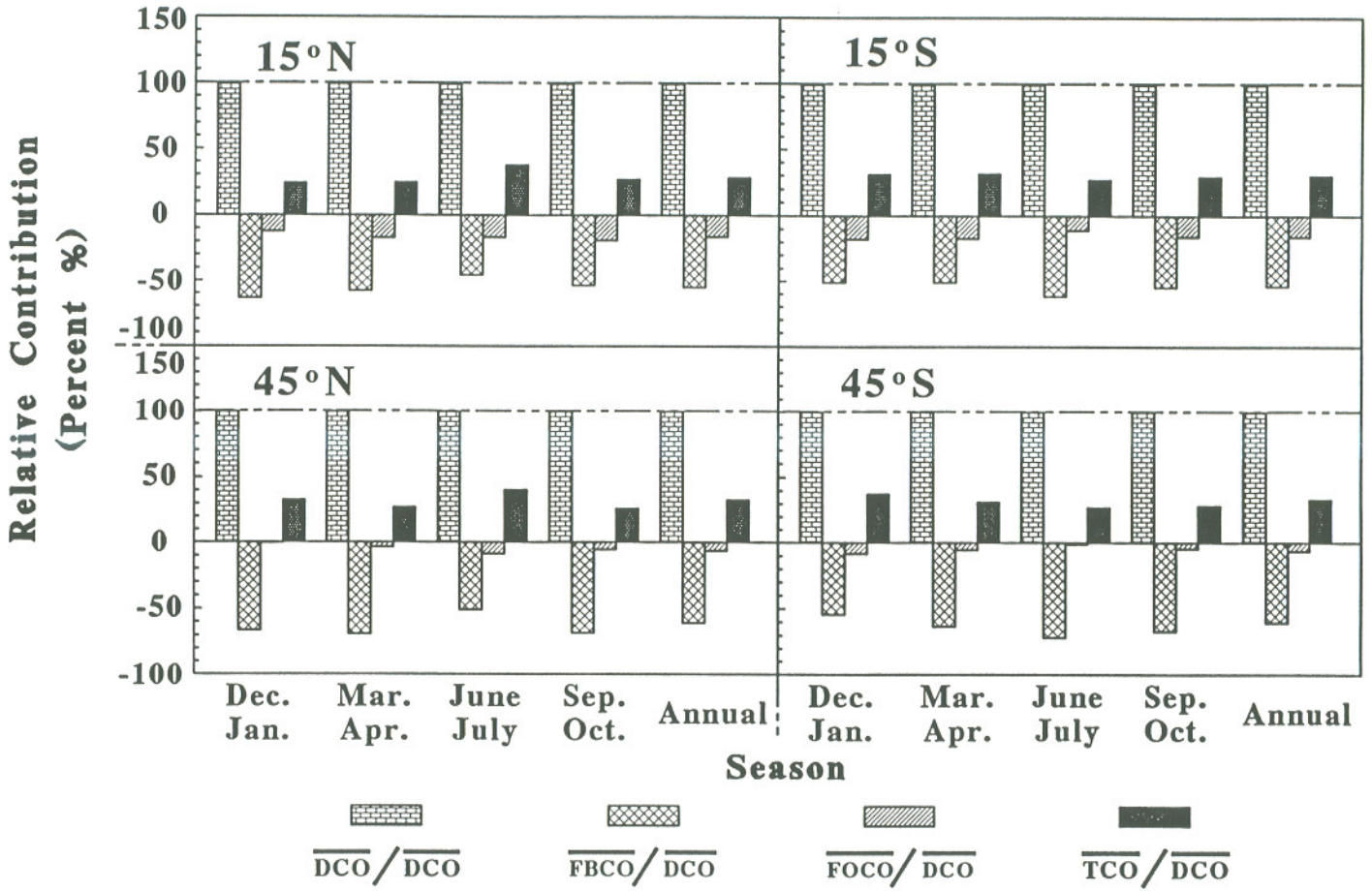

Fig. 3.13 Comparison of the direct, feedback, and total contributions to OH from CO. See text and fig. 3.11 for the definitions of DCO, FBCO, FOCO, and TCO.

troposphere. As shown in this figure, both the buffer feedback and the oxygen feedback are always negative feedbacks of the direct contribution of CO at any latitude in any season, indicating that these two feedbacks recover the hydroxyl radicals, directly consumed by CO. Due to effects of feedbacks, the total contribution of CO, or the total removal rate of OH due to the total contribution of CO, is less than 50% compared to the direct contribution of CO.

It should be noted that the concentration of NO_x has a large influence on the buffer feedback. According to our calculation, the reaction between NO and the resulting HO_2 ($[HO_2]^{CO}$) from the process initiated by the reaction between CO and OH mainly dominates the feedback. Mathematically the product of the concentrations of NO and the resulting HO_2 ($[HO_2]^{CO}$) mainly determines the magnitude of the feedback. A high NO_x simply means a high NO concentration, which tend to cycle more of the resulting HO_2 ($[HO_2]^{CO}$) back to OH. $[HO_2]^{CO}$ is derived from the reaction between OH and CO. A high CO concentration, on the one hand, tends to transfer more OH to H, and then to HO_2; on the other hand, it leads to a relatively low OH concentration, resulting in less OH available for transforming to H, and then to HO_2. On the whole, the effect of the change of CO concentration on $[HO_2]^{CO}$ is reduced, leaving the variation of NO_x concentration as a more important factor for the variation of the buffer feedback. The seasonal variation of the relative intensity of the buffer feedback with respect to the direct contribution in fig. 3.13 shows a maximum value in winter and a minimum value in summer, correlating positively with the NO_x concentration, further illustrates the impact of the NO_x concentration on the buffer feedback.

The NO_x concentration is also essential for the oxygen feedback since the reaction between NO and the resulting HO_2 from the process initialized by the

reaction between OH and CO produce NO_2, which dissociates into $O(^3P)$ under the sunlight, and then to O_3, $O(^1D)$, and OH. However, by contrast to the seasonal variation of NO_x concentrations, the oxygen feedback with respect to the direct contribution of CO generally appears to be largest in summer and smallest in winter, as shown in fig. 3.13. This phenomena indicates that the seasonal variation of the photolysis of the resulting NO_2 and O_3, which is strongest in summer and weakest in winter, is more important for that of the oxygen feedback than that of the NO_x concentration which is highest in winter and lowest in summer.

The magnitudes of seasonal variations of buffer feedback and oxygen feedback with respect to the direct contribution of CO also change with latitude: the seasonal variations of these two feedbacks are more significant in the midlatitudes than in the tropics, corresponding not only to the related changes of seasonal variations of the concentrations of a number of species such as NO and $[HO_2]^{CO}$, but also to those of solar radiation flux.

The comparison of the direct, feedback, and total contributions to OH from CH_4 is shown in fig. 3.14 for the four latitudes and seasons. The buffer feedbacks and oxygen feedbacks, similar to those of CO, always recover the OH directly consumed by CH_4, and they also show seasonal and latitudinal variations. However, the organics feedbacks, on the whole, further remove OH. The phenomena is most significant in summer, when the concentrations of the resulting organic compounds are the highest among the four seasons. Furthermore, the seasonal and latitudinal variations of the organics feedbacks correspond mostly to the related changes of the solar radiation intensity; for example, the seasonal variations of the organics feedback is stronger in the middle latitudes than in the tropics consistent with the larger

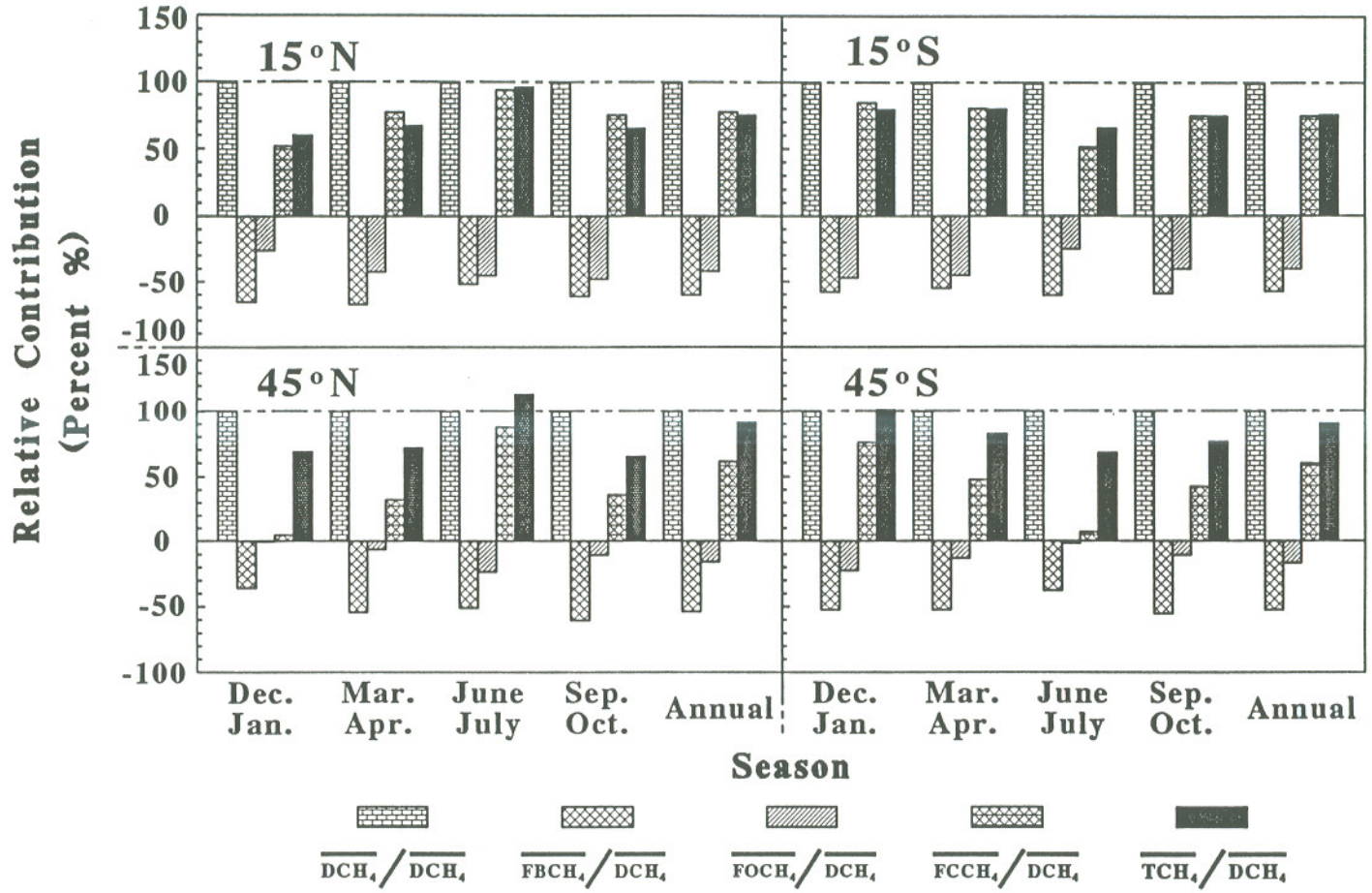

Fig. 3.14 Comparison of the direct, feedback, and total contributions to OH from CH_4. See text and fig. 3.12 for the definitions of DCH_4, $FBCH_4$, $FOCH_4$, $FCCH_4$, and TCH_4.

seasonal variations of solar radiation in the middle latitudes than in the tropics. Combining the direct contribution with its three feedbacks, the total contribution of CH_4 is only a little bit smaller than the direct contribution.

Fig. 3.15a compares the direct contribution of CO with that of CH_4 for the four seasons and latitudes. Methane, on the global scale, directly consumes less than 50% as much OH as CO directly. The variation of the relative difference between the direct contribution of CO and that of CH_4 is due to the seasonal variation of the CO, which is highest in spring in the northern hemisphere corresponding to the biggest relative difference since the seasonal variation of CH_4 was not taken into account in this study.

The total feedback of CH_4, the sum of its buffer feedback, oxygen feedback, and the organics feedback, is also compared with that of CO, the sum of its buffer feedback and oxygen feedback for each season and latitude, as shown in fig. 3.15b. Except in summer at the middle latitudes, the ratio of the total feedback of CH_4 to that of CO is positive, indicating that the total feedback of either CO or CH_4 generally recovers OH. However, the amount of OH recovered by the total feedback of CH_4 is much smaller than that recovered by the total feedback of CO due to the cancellation between the organics feedback of CH_4 and the other two feedbacks of CH_4. The negative values of $\overline{FCH_4}/\overline{FCO}$ in summer in the middle latitudes indicate that the organics feedback of CH_4 is stronger than the sum of the buffer feedback and the oxygen feedback. This phenomena results from the fact that more organic compounds are generated due to strong solar radiation and long daytime as well as lower NO_x and higher organics concentrations in summer compared to in other seasons. The larger negative $\overline{FCH_4}/\overline{FCO}$ at 45 °N compared to that at 45 °S arises from the higher CH_4 concentration at 45 °N than at 45 °S.

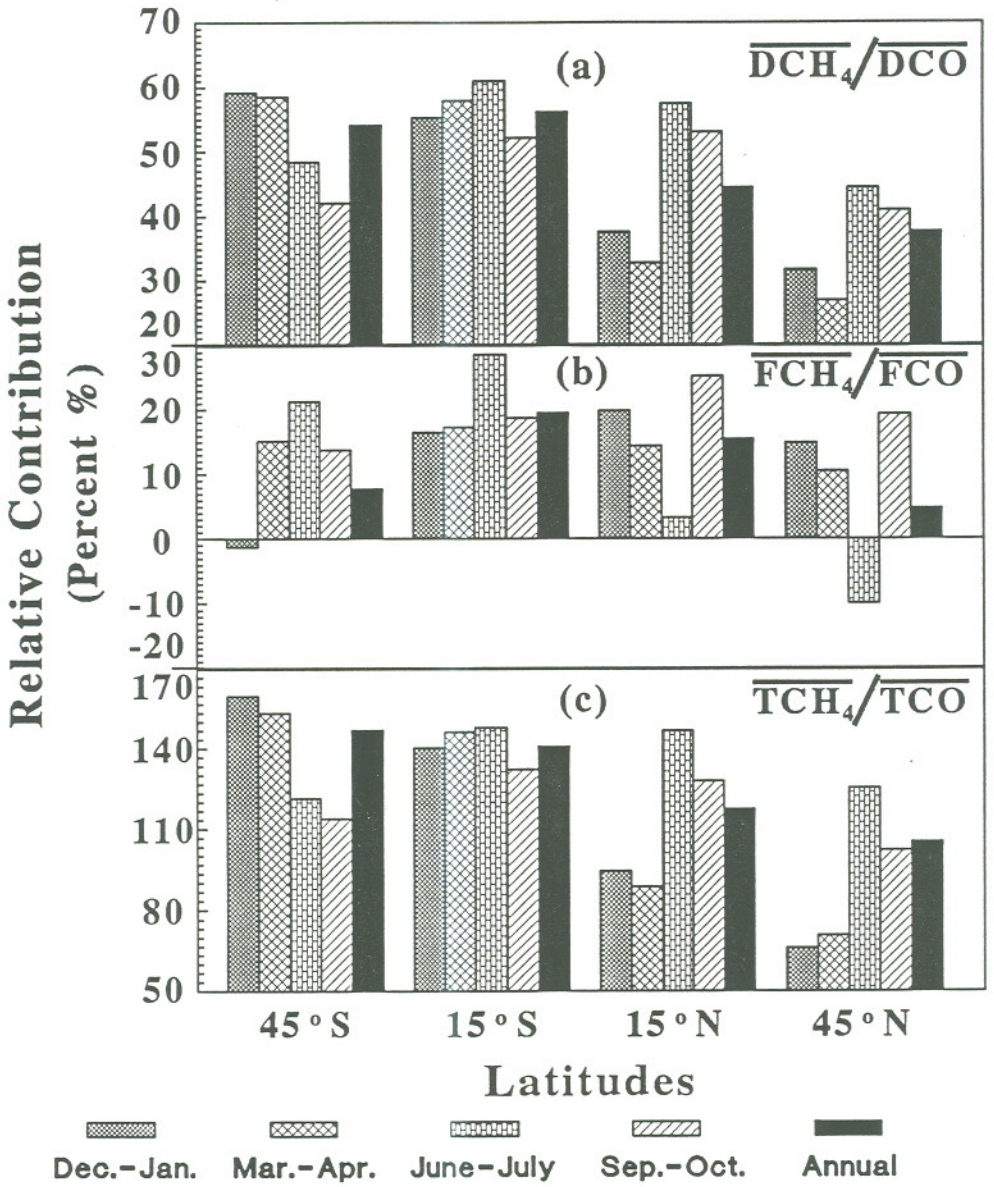

Fig. 3.15 Comparison of the direct contributions to OH from CO and CH_4 (a); Comparison of the total feedback to OH from CO with that from CH_4 (b); Comparison of the total contribution to OH from CO with that from CH_4 (c). See figs. 3.11 and 3.12 for the definitions of DCO, DCH_4, FCO, FCH_4, TCO, and TCH_4. A bar sign corresponds to a diurnal and vertical average in the troposphere.

The comparison of the total contribution of CH_4 to OH, its direct contribution plus all its feedbacks (the total feedback), with that of CO is shown in fig. 3.15c. Due to the compensations and cancellations of the feedbacks, the total contribution of CH_4 to OH, on average, is even larger than that of CO. This phenomena is most significant in summer, when the concentrations of the resulting organic compounds are highest and the levels of NO_x are lowest among the four seasons.

Fig. 3.16 is a summary, comparing the direct, total feedback, and total contributions to OH from CO and CH_4. It shows that on the whole, CH_4 along with its feedbacks removes more OH than CO along with its feedbacks at tropics as well as at middle latitudes although CH_4 directly consumes less than 50% as much OH as CO directly.

3.3 Summary

By comparing all the reactions directly affecting OH and its most important buffer, HO_2, it is concluded that only five reactions directly control the distribution of OH: the reaction of $O(^1D)$ with H_2O and the reactions of HO_2 with NO and with O_3 produce most of OH in the troposphere, while CO and CH_4 consume most of the OH. However, all the six reactions, considered as direct sinks of HO_2 in this study are important during daytime, and variations of some sinks of HO_2 will change the concentration of HO_2, thus resulting in a change in OH concentration. At night only two sinks of HO_2, the reactions of HO_2 with O_3 and with NO_2, are important. The most dominant direct source of HO_2 is the reaction between H and O_2, which on an average provides for more than 60% of HO_2 during the day. The dissociation of HO_2NO_2 is also an important source of HO_2, especially at night when it generates

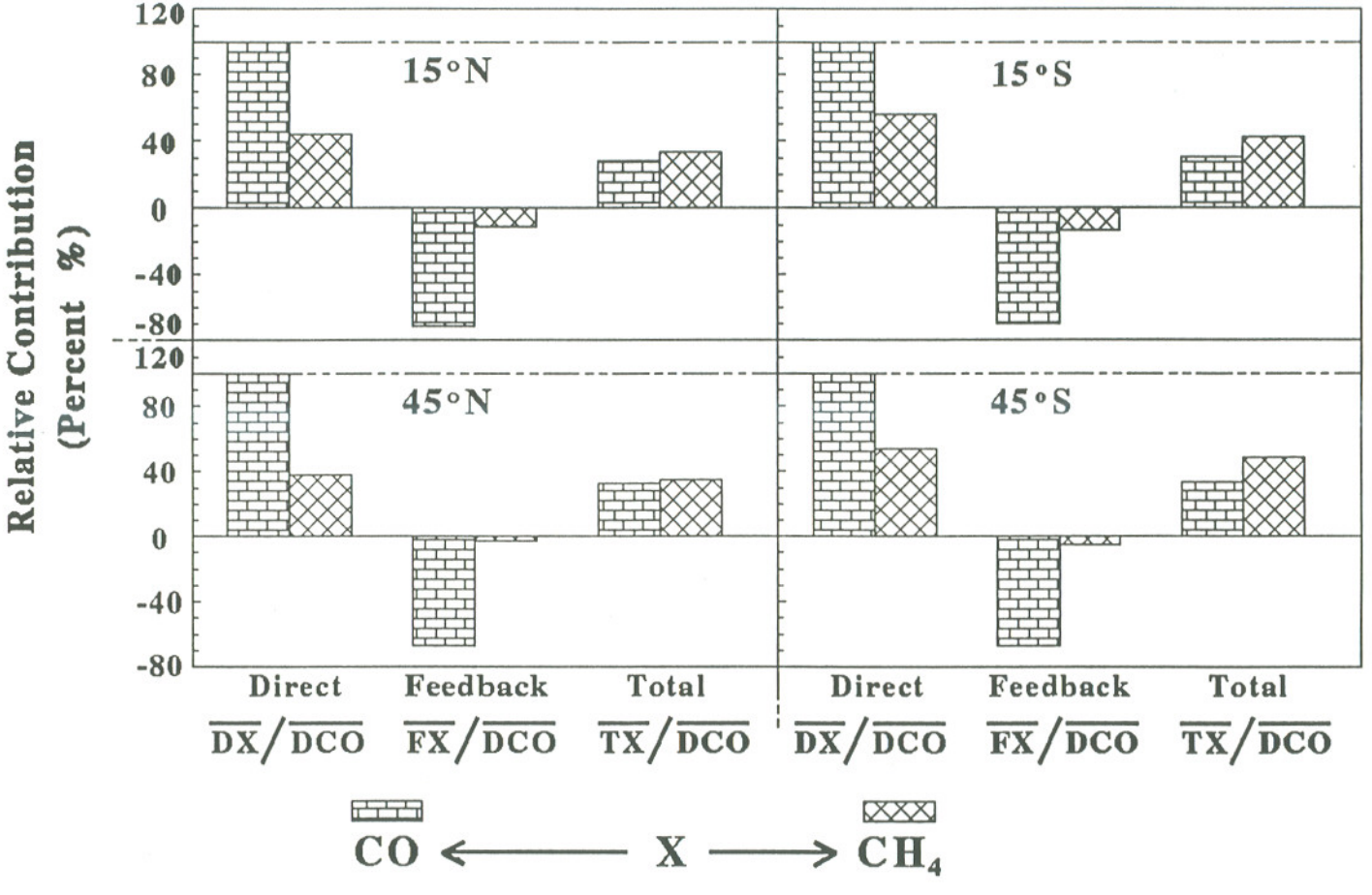

Fig. 3.16 Comparison of the direct, feedback, and total contributions to OH from CO and from CH_4. See figs. 3.11 and 3.12 for the definitions of DCO, DCH_4, FCO, FCH_4, TCO, and TCH_4. A bar sign here corresponds to a diurnal, seasonal, and vertical average in the troposphere.

more than 60% of nighttime HO_2. Since the reaction between O_3 and HO_2 is the only significant source of nighttime OH, it can be further inferred that atmospheric HO_2NO_2 is a dominant source for the nighttime OH.

To study the real contributions of CO and CH_4 to OH, a numerical model was developed to calculate the total contribution to OH from either CO or CH_4, based on the mass conservation law. The method includes the chemical mechanisms of CO, CH_4, and OH by not only considering the direct reactions but also all the feedbacks by tracing a series of reactions and products, which are initiated by the direct reactions.

According to the model results, each feedback of CO and CH_4, especially the buffer feedback or organics feedback, is important even compared to the direct contribution. Specifically, the organics feedbacks of CH_4 further remove OH, while the buffer feedbacks and oxygen feedbacks of both CO and CH_4 recover some of the OH consumed directly by CO and CH_4. It should be noted that NO_x concentration has a large impact on the feedbacks of both CH_4 and CO, especially on the buffer feedbacks. A high background NO_x tends to recover a large amount of OH, directly consumed by CO and CH_4. On the global scale, the higher NO_x region (45 °N) is the higher CO and CH_4 region. A high CO and CH_4 results in a low OH concentration; i.e., the resulting HO_2 concentration is not high. Therefore, even the high NO_x at 45 °N cannot cycle enough of the resulting HO_2 to OH so as to make either CO or CH_4 as a source of OH. However, in regions of low CO or CH_4, where NO_x concentration is high, individually CO or CH_4 might become a source of OH.

On the global scale, the total feedback of CH_4 is much smaller than that of CO due to the cancellation between the organics feedback of CH_4 and the other two feedbacks. Consequently, CH_4 along with its feedbacks may remove even more OH

than CO along with its feedbacks, although on the global scale, CO directly consumes more than twice as much OH as CH_4 directly does. Finally we point out that our calculations do not include the effect of CO production from the oxidation of CH_4. If this aspect is taken into account, the role of CH_4 on OH is even more important than our present calculation.

CHAPTER 4 OPTICAL PROPERTIES OF VARIOUS ATMOSPHERIC COMPONENTS

4.1. General Introduction

Optical properties of various atmospheric components play a significant role in the state and structure of the earth's atmosphere. For example, the absorption of IR radiation by CO_2, O_3, and water vapor, on the one hand, provides a warm surface temperature necessary for life as we know it. On the other hand, the recent increases of CO_2, and other greenhouse trace gases due to human activities causes a trend of global warming and climate change, which some consider to be detrimental. As another example, the strong absorption of solar radiation in ultraviolet wavelengths by ozone protects life from ultraviolet radiation. The optical properties of atmospheric components are also responsible for many spectacular atmospheric scenery, such as colorful sunrises and sunsets, corona, halos, and rainbows. However, the studies of these important optical properties are excluded here since our focus is on atmospheric chemistry.

As described in chapter 2, nearly all the atmospheric chemical reactions are initiated by the solar radiation in the visible and ultraviolet wavelengths. While changing with time of day, season, and latitude due to the relative position between the sun and the earth, the atmospheric radiation field in the visible and ultraviolet wavelengths is also significantly affected by the various atmospheric components such as air molecules, ozone, aerosols, and

cloud droplets. Thus it essential to understand the optical properties of these atmospheric components before the radiation fields are properly modeled. In the remaining chapter, the characteristics of the absorption of O_3, the scattering of air molecules and cloud droplets, the absorption and scattering of aerosols are studied.

4.2 Absorption

The atmospheric absorption of radiation is the essential process to attenuate the intensity of radiation. The attenuation of radiation due to absorption is well described by the famous Beer-Lambert law, which states that the decrease of the radiant intensity traversing a homogeneous medium with a certain path length, *ds* is proportional to the amount of matter in the path and the radiant intensity; i.e.,

$$dI_\lambda = -\sigma_\lambda n I_\lambda ds \tag{4.1}$$

where I with the subscript λ denotes the radiation at wavelength λ; n is the number density of this matter (in units of per volume, i.e., cm^{-3}); and σ is called cross-section of this matter, which is analogous to the geometrical area of this matter, denoting the amount of radiative energy removed from the original beam by the particles. The absorbed energy goes either to some other forms of energy such as heat or to excite chemical reactions.

In radiative transfer problems, the normal optical depth, τ, is an optical property frequently used, which is defined as:

$$\tau = \int_{\infty}^{z} \sigma n dz \tag{4.2a}$$

or $$d\tau = -\sigma n dz \tag{4.2b}$$

where z denotes altitude.

In the clear atmosphere, ozone is the major absorber of ultraviolet radiation. According to eq. 4.2, the normal optical depth for O_3 absorption, τ_a^O, at the height z is expressed as:

$$\tau_a^O = \int_{z}^{\infty} \sigma_a^O(\lambda) N_O(z) dz \tag{4.3a}$$

where σ_a^O is the absorption cross section of O_3 and N_O is the number density of O_3 at height z above the earth's surface. From the above equation, the normal optical depth for O_3 absorption at the altitudinal range form z to $z+\Delta z$ can be expressed as:

$$\Delta\tau_a^O = \int_{z}^{z+\Delta z} \sigma_a^O(\lambda) N_O(z) dz \simeq \sigma_a^O(\lambda) \cdot [N_O(Z) \cdot N_O(z+\Delta z)]^{1/2} \cdot \Delta z \tag{4.3b}$$

4.3 Scattering

Scattering is a fundamental physical process by which a particle in the path of an electromagnetic wave continuously abstracts energy from incident beam and reradiates the

energy in all directions. It is really the interaction of light and matter. It happens at all electromagnetic wavelengths. Most light we perceive with our eyes is indirectly from scattering processes. For example, fair weather clouds look white because of the extensive scattering of the incident light. It is worthwhile to note that scattering is often accompanied by absorption. We see black smoke because it absorbs lights with all colors in visible range. The grass looks green because it scatters green light more effectively than red, yellow, and other different color lights. In other words, the lights with colors other than green on the grass are mostly absorbed. On the other hand, dense rain clouds look dark even though the cloud droplets have negligible absorption because the droplets scattering is so complete that light cannot get through the clouds.

Both scattering and absorption remove energy from an incident light, and the incident light is attenuated as it travels through a medium. The attenuation of incident light is called extinction, which is the sum of absorption and scattering. In a non-absorption medium, scattering is actually equal to extinction.

In the atmosphere, the particles responsible for scattering cover the size from gas molecules ($\sim 10^{-8}$ cm) to large raindrops and hail particles ($\sim$ 1 cm). The relative intensity of scattering pattern depends strongly on the particle size as well as an the wavelength of the incident beam.

4.3.1 Raleigh Scattering

When particles are much smaller than the incident wavelength, the scattering is

called Raleigh scattering. It is often related to molecular scattering. The original formula, derived by Raleigh in 1871, is expressed as:

$$I = \alpha^2 \frac{I_0}{r^2}\left(\frac{2\pi}{\lambda}\right)^4 \frac{1+\cos^2\Theta}{2} \tag{4.4a}$$

where r is the distance between the tiny particle (or the molecule), which scatters the incident light, and the observation point; I and I_0 are intensities of the scattering and incident radiation, respectively; λ is wavelength; Θ is the scattering angle; and α is the polarizability of the small particle, or molecule, and can be expressed as:

$$\alpha = \frac{3}{4\pi N}\cdot\left(\frac{m^2-1}{m^2+2}\right) \doteq \frac{m^2-1}{4\pi N} \tag{4.4b}$$

where m is the non-dimensional refractive index of molecules, which is close to 1; N is the total number of molecules per unit volume, and $N = 1/[\frac{3}{4}\pi r^3]$ by assuming that there is no room left among molecules.

From eq. 4.4a, it is obvious that the scattered energy changes with scattering angle, Θ. To describe the distribution of the scattered energy, it is necessary to define a non-dimensional parameter, the phase function. The phase function, $P(\cos\Theta)$ is normalized with

$$\int_0^{2\pi}\int_0^{\pi} P(\cos\Theta)\sin\Theta d\Theta d\phi = 4\pi \tag{4.5}$$

where ϕ is azimuthal angle.

For Raleigh scattering, the scattered intensity depends on $1+\cos^2\Theta$; thus the phase

function can be expressed as:

$$P(\cos\Theta) = b \cdot (1 + \cos^2\Theta) \tag{4.6a}$$

Substituting the above equation back to eq. 4.5, we obtain $b=3/4$; therefore, the phase function of Raleigh scattering is

$$P(\cos\Theta) = \frac{3}{4} \cdot (1 + \cos^2\Theta) \tag{4.6b}$$

Substituting eq. 4.6b back to eq. 4.4a, then

$$I = I_0 \cdot \frac{P(\cos\Theta)}{4\pi} \cdot \frac{\sigma_s^m}{r^2} \tag{4.4c}$$

where σ_s^m is the cross section (in units of area) for Rayleigh (or molecular) scattering, which can be derived theoretically (for example, see Liou, 1980) and expressed as:

$$\sigma_S^m = \frac{8\pi^3 (m^2-1)^2}{3\lambda^4 N^2} \tag{4.7}$$

For the photochemical problems, an analytic expression of the cross section for Rayleigh scattering, derived by Nicolet (1984) according to the values of the cross section for Rayleigh scattering in air re-evaluated by Bates (1984), is commonly used. It is expressed as:

$$\sigma_S^m(\lambda) = 4.02 \times 10^{-28} \lambda^{(4+x)} \tag{4.8a}$$

where the Rayleigh scattering cross section, σ_s^m, is in cm^{-2} with wavelength λ expressed in

microns (μm), and the parameter χ is given by:

$$\chi = \begin{cases} 0.389\lambda + 0.\dfrac{09426}{\lambda} - 0.3228 & \text{for } 0.20\ \mu \le \lambda \le 0.55\ \mu \\ 0.04 & \text{for } 0.55\ \mu \le \lambda \le 1.0\ \mu \end{cases} \tag{4.8b}$$

According to eq. 4.2, the normal Rayleigh scattering optical depth, τ_s^m, at a height z, above the ground, is given by

$$\tau_s^m = \int_z^{\infty} \sigma_s^m(\lambda) N_m(z) dz \tag{4.9a}$$

where N_m is the number density of atmosphere at the altitude z. The normal Rayleigh scattering optical depth at the altitudinal range form z to $z+\gamma$ can be expressed as:

$$\Delta\tau_s^m = \int_z^{z+\Delta z} \sigma_s^m(\lambda) N_m(z) dz \approx \sigma_s^m(\lambda) \cdot \sqrt{N_m(Z) \cdot N_m(z+\Delta z)} \cdot \Delta z \tag{4.9b}$$

4.3.2 Mie Scattering

When the sizes of particles are comparable to or larger than the incident wavelength as for aerosols and cloud droplets, the scattering is described by Mie theory. This theory was first introduced by Mie (1908), and the derivations of the related equations can be found in many text books of atmospheric radiation (for example, Liou, 1980). Mie scattering is affected by sizes, shapes, and refractive indexes of particles as well as the wavelength of incident wave. The expressions of the scattering and extinction cross sections

and the phase function for Mie scattering are much more complex than those for Rayleigh scattering. By using Mie theory, the scattering and extinction cross sections and the phase function for a single particle with a spherical radius, r, at wavelength, λ can be respectively expressed as:

$$\sigma_s = \pi r^2 Q_s = \frac{\lambda^2}{2\pi} \sum_{n=1}^{\infty} (2n+1)(|a_n|^2 + |b_n|^2) \tag{4.10a}$$

$$\sigma_e = \pi r^2 Q_e = \frac{\lambda^2}{2\pi} \sum_{n=1}^{\infty} (2n+1) Re(a_n + b_n) \tag{4.10b}$$

$$P(r,\Theta) = \frac{\lambda^2}{2\pi \sigma_s(r)} [S_1(\Theta) S_1^*(\Theta) + S_2(\Theta) S_2^*(\Theta)] \tag{4.11}$$

where σ_s and σ_e are the scattering and extinction cross sections; Q_s and Q_e are the scattering and extinction efficiencies; $P(r,\Theta)$ is the phase function; Θ is the scattering angle; $S_1^*(\Theta)$ and $S_2^*(\Theta)$ are the conjugates of the complex functions of $S_1(\Theta)$ and $S_2(\Theta)$, respectively, and $S_1(\Theta)$ and $S_2(\Theta)$ are respectively expressed as follows:

$$S_1(\Theta) = \sum_{n=1}^{\infty} \frac{2n+1}{n(n+1)} [a_n \frac{P_n^1(\cos\Theta)}{\sin\Theta} + b_n \frac{dP_n^1(\cos\Theta)}{d\Theta}] \tag{4.12a}$$

$$S_2(\Theta) = \sum_{n=1}^{\infty} \frac{2n+1}{n(n+1)} [a_n \frac{dP_n^1(\cos\Theta)}{d\Theta} + b_n \frac{P_n^1(\cos\Theta)}{\sin\Theta}] \tag{4.12b}$$

where $P_n^1(\cos\Theta)$ is the associated Legendre polynomial function, and a_n and b_n are Mie coefficients, which are respectively expressed as (van de Hulst, 1957):

$$a_n = \frac{\psi_n'(y)\psi_n(x) - m\psi_n(y)\psi_n'(x)}{\psi_n'(y)\xi_n(x) - m\psi_n(y)\xi_n'(x)} \tag{4.13a}$$

$$b_n = \frac{m\psi_n'(y)\psi_n(x) - \psi_n(y)\psi_n'(x)}{m\psi_n'(y)\xi_n(x) - \psi_n(y)\xi_n'(x)} \tag{4.13b}$$

where $x=2\pi r/\lambda$ is called Mie size parameter; $y=mx$; $m=m_1+i\cdot m_2$ is the complex refractive index (the real part, m_1, related to scattering, and the imaginary part, m_2, related to absorption); and the Ricatti-Bessel functions, $\psi_n(\rho)$ and $\xi_n(\rho)$ (ρ corresponds to either x or y), are respectively given:

$$\psi_n(\rho) = \sqrt{\pi\rho/2}\, J_{n+1/2}(\rho) \tag{4.14a}$$

$$\chi_n(\rho) = -\sqrt{\pi\rho/2}\, N_{n+1/2}(\rho) \tag{4.14b}$$

$$\xi_n(\rho) = \psi_n(\rho) + i\chi_n(\rho) = \sqrt{\pi\rho/2}\, H^{(2)}_{n+1/2}(\rho) \tag{4.14c}$$

where $J_{n+½}(\rho)$ is the Bessel function of the first kind; $N_{n+½}(\rho)$ is the Neumann function; and $H_{n+½}^{(2)}(\rho)$ is the Hankel function of the second kind. Using the definitions of the Bessel, Neumann, and Hankel functions, and their recurrence relations, the Ricatti-Bessel functions can be expressed as a series of sine and cosine functions, which are listed in table 4.1.

Going back to eq. 4.12, if we let $\mu=\cos\theta$, then the first two terms of the associated Legendre polynomial functions are:

Table 4.1. Ricatti-Bessel Functions and Their Recurrence Relations:

Function	Derivative
$\psi_0(\rho) = \sqrt{\frac{\pi\rho}{2}}\, J_{1/2}(\rho) = \sin\rho$	$\psi_0'(\rho) = \cos\rho$
$\psi_1(\rho) = \frac{\sin\rho}{\rho} - \cos\rho$	$\psi_1'(\rho) = -\frac{\sin\rho}{\rho^2} + \frac{\cos\rho}{\rho} + \sin\rho$
...	...
$\psi_n(\rho) = \frac{2n-1}{\rho}\psi_{n-1}(\rho) - \psi_{n-2}(\rho)$	$\psi_n'(\rho) = \psi_{n-1}(\rho) - \frac{n}{\rho}\psi_n(\rho)$
$\chi_0(\rho) = (-1)^0\sqrt{\frac{\pi\rho}{2}}\, J_{-1/2}(\rho) = \cos\rho$	$\chi_0'(\rho) = \cos\rho$
$\chi_1(\rho) = \frac{\cos\rho}{\rho} + \sin\rho$	$\chi_1'(\rho) = -\frac{\cos\rho}{\rho^2} - \frac{\sin\rho}{\rho} + \cos\rho$
...	...
$\chi_n(\rho) = \frac{2n-1}{\rho}\chi_{n-1}(\rho) - \chi_{n-2}(\rho)$	$\chi_n'(\rho) = \chi_{n-1}(\rho) - \frac{n}{\rho}\chi_n(\rho)$
$\xi_0(\rho) = \psi_0(\rho) + i\chi_0(\rho) = \sin\rho + i\cos\rho$	$\xi_0'(\rho) = \psi_0'(\rho) + i\chi_0'(\rho) = \cos\rho - i\sin\rho$
$\xi_1(\rho) = \psi_1(\rho) + i\chi(\rho)$	$\xi_1'(\rho) = \psi_1'(\rho) + i\chi_1'(\rho)$
...	...
$\xi_n(\rho) = \psi_n(\rho) + i\chi_n(\rho)$	$\xi_n'(\rho) = \psi_n'(\rho) + i\chi_n'(\rho)$

$$P_1^1(\cos\Theta) = \sin\Theta = (1-\mu^2)^{1/2} \tag{4.15a}$$

$$P_2^1(\cos\Theta) = 3\cos\Theta\sin\Theta = 3\mu(1-\mu^2) \tag{4.15b}$$

and the recurrence relation of the associated Legendre polynomial functions are:

$$P_n^1(\mu) = \frac{2n-1}{n-1}\mu P_{n-1}^1(\mu) - \frac{n}{n-1}P_{n-2}^1(\mu) \qquad (n>2) \tag{4.15c}$$

By using eqs. 4.15a and 4.15b, and expanding eq. 4.15c, the eq. 4.15 can be further expressed as:

$$\frac{P_n^1(\mu)}{\sin\Theta} = \begin{cases} 1 & n=1 \\ \sum_{j=1}^{p} a_{n,j}\mu^{n+1-2j} & (n\geq 2 \quad \& \quad j \leq \frac{n+1}{2}) \end{cases} \tag{4.16a}$$

$$p = int(\frac{n+1}{2}) = \begin{cases} (n+1)/2 & \text{if n is an odd number} \\ n/2 & \text{if n is an even number} \end{cases} \tag{4.16b}$$

where *int[(n+1)/2]* is the function that converts *(n+1)/2* to integer by truncating the fractional part of *(n+1)/2*. For $n>1$, the coefficients, $a_{n,j}$ can be expressed as:

$$a_{n,j} = \begin{cases} \frac{2n-1}{n-1}a_{n-1,1} & j=1 \\ \frac{2n-1}{n-1}a_{n-1,j} - \frac{n}{n-1}a_{n-2,j-1} & 1<j\leq n/2 \\ -\frac{n}{n-1}a_{n-2,j-1} & j=(n+1)/2 \end{cases} \tag{4.16c}$$

To derive the general polynomial formula for $dP_i^1(cos\Theta)/d\Theta$, one needs to know:

$$\frac{d[c\cdot\sin\Theta\cdot\cos^{j}\Theta]}{d\Theta}=\begin{cases}c[(j+1)\cos^{j+1}\Theta-j\cos^{j-1}\Theta] & (j\geq 1)\\ c\cos\Theta & (j=0)\end{cases}$$

Combining the above equation with eq. 4.16 gives

$$\frac{dP_i^1(\cos\Theta)}{d\Theta}=\sum_{j=1}^{u} b_{n,j}\mu^{n+2-2j} \qquad n,\mu\geq 1 \quad \& \quad \mu\leq n/2+1 \tag{4.17a}$$

$$p=int(\frac{n+2}{2})=\begin{cases}(n+1)/2 & \text{if n is an odd number}\\ n/2+1 & \text{if n is an even number}\end{cases} \tag{4.17b}$$

$$b_{n,j}=\begin{cases}na_{n,1} & j=1\\ a_{n,j}[n-2(j-1)]-a_{n,j-1}[n+1-2(j-1)] & 1<j\leq(n+1)/2\\ -a_{n,j-1} & j=n/2+1\end{cases} \tag{4.17c}$$

Table 4.2 shows the number of terms, the powers of $cos\Theta$, and the coefficient for each term of the first six terms of $P_n^1(cos\Theta)/sin\Theta$ and $dP_n^1(cos\Theta)/d\Theta$. It should be noticed that $dP_n^1/d\Theta$ is the nth order polynomial in $cos\Theta$ and $P_n^1(cos\Theta)/sin\Theta$ is the n-1th order of polynomial in $cos\Theta$. In addition, if n is an odd number, all the terms in the polynomial $P_n^1(cos\Theta)/sin\Theta$ are the even powers in $cos\Theta$ while all the terms of the polynomial $dP_n^1(cos\Theta)/d\Theta$ have odd powers in $cos\Theta$. On the other hand, for an even n, all terms of polynomial $P_n^1(cos\Theta)/sin\Theta$ are of odd powers in $cos\Theta$ while those in the polynomial $dP_n^1(cos\Theta)/d\Theta$ are of even powers of $cos\Theta$. Combining eqs. 4.16a and 4.17a with the characteristics described above, the eqs. 4.12a and 4.12b can be further modified as:

$$S_1(\Theta)=\sum_{n=0}^{\infty} x_{1,n}\cos^n\Theta \tag{4.18a}$$

Table 4.2. Functions of $P_i^1(cos\Theta)/sin\Theta$ and $dP_i^1(cos\Theta)/d\Theta$ [a]

i,j	0	1	2	3	4	5	6	...
1	1.0	***1.0***						
2	***-1.0***	3.0	***6.0***					
3	-1.5	***-16.5***	7.5	***22.5***				
4	***7.5***	-7.5	***-67.5***	17.5	***70.0***			
5	1.875	***54.375***	-26.25	***-236.25***	39.375	***196.875***		
6	***-13.125***	13.125	***262.5***	-78.75	***-748.125***	86.625	***519.75***	
...	...	...	...	...	...	...	...	...

[a] The integers, 0, 1, 2, ···, in the top row of the above the table corresponds to the number of the powers of cosμ; the integers, 1, 2, 3, ···, in the far-left column desiganates the number n in the assciate Legendre function, $P^1_n(\mu)/sin\Theta$, and its derivative, $dP^1_n(\mu)/d\Theta$; the data in the normal fonts inside the internal box are the coefficients of the terms of $P^1_n(\mu)/sin\Theta$, and the data in the bold italic font are the coefficients of the terms of $dP^1_n(\mu)/d\Theta$. For example,

$$\frac{P_5^1(\mu)}{\sin\Theta} = 1.875 - 26.25\,\mu^2 + 39.375\,\mu^4$$

$$\frac{dP_5^1(\mu)}{d\Theta} = 54.375\,\mu - 236.25\,\mu^3 + 196.875\,\mu^5$$

where $\mu = cos\Theta$

$$S_2(\Theta) = \sum_{n=0}^{\infty} x_{2,n}\cos^n\Theta \tag{4.18b}$$

Note complex coefficients $x_{1,n}$ and $x_{2,n}$ are combination of a_k and b_k with various integer k, calculated according to eqs. 4.13a and 4.13b, and of $a_{k,j}$ and $b_{k,j}$ with different integer k and j, calculated by eqs. 4.16c and 4.17c. Furthermore, $x_{1,n}$ and $x_{2,n}$ are the functions of the Mie size parameters, $2\pi r/\lambda$ and $2\pi rm/\lambda$, or the functions of the radius of the particle, r, wavelength, λ, and the refractive index, m. Substituting eqs. 4.18a and 4.18b back to eqs. 4.12a and 4.12b, the phase function for a spherical particle with radius r can be expanded as:

$$P(r,\Theta) = \frac{\lambda^2}{2\pi\sigma_s(r)}\{[\sum_{n=0}^{\infty} Re(x_{1,n})\cos^n\Theta]^2 + [\sum_{n=0}^{\infty} Im(x_{1,n})\cos^n\Theta]^2 + [\sum_{n=0}^{\infty} Re(x_{2,n})\cos^n\Theta]^2 + [\sum_{n=0}^{\infty} Im(x_{2,n})\cos^n\Theta]^2\} \tag{4.19}$$

where $Re(x_{j,n})$ and $Im(x_{j,n})$ are respectively the real part of $x_{j,n}$ and the imaginary part of $x_{j,n}$ ($j=1, 2; n=1, 2, \cdots, \infty$).

4.4 Asymmetry Factor

4.4.1 Forward Scattering, Backward Scattering, and Asymmetry Factor

In dealing with the scattering problems, it is essential to find a quantity which describes the scattering angle, which represents the angle between the incident light and the scattering light. As described in the previous section, the phase function is such a quantity

characterizing the angular distribution of the scattering energy. Instead of calculating the phase function, very often the whole fraction of the light scattered forward or backward by a scatterer is used in dealing with the radiative transfer. For isotropic scattering, the fraction of the scattering energy in the forward direction of the incident beam is equal to that in the backward direction. Thus the fraction of the intensity scattered forward is equal to that of the intensity scattered backward. For anisotropic scattering, the fraction of the intensity scattered forward is no longer equal to that scattered backward. The portion of the backward energy is either strengthened or weakened by the forward scattering energy, and on the average, the fraction of the backward scattering energy is expressed:

$$b_b = \{\int_0^{\pi} \frac{1-\cos\Theta}{2} P(\cos\Theta)\sin\Theta d\Theta\} \Big/ \{\int_0^{\pi} P(\cos\Theta)\sin\Theta d\Theta\} = \frac{1}{2}\int_{-1}^{1} \frac{1-\mu}{2} P(\mu) d\mu \qquad (4.20)$$

where $\mu=cos\Theta$, and Θ is the scattering angle between the incident light and the scattering light; $P(\mu)$ is the phase function, and

$$\int_{-1}^{1} P(\mu) d\mu = 2 \qquad (4.20a)$$

Similarly, the fraction of the forward scattering intensity is given:

$$b_f = \{\int_0^{\pi} \frac{1+\cos\Theta}{2} P(\cos\Theta)\sin\Theta d\Theta\} \Big/ \{\int_0^{\pi} P(\cos\Theta)\sin\Theta d\Theta\} = \frac{1}{2}\int_{-1}^{1} \frac{1+\mu}{2} P(\mu) d\mu \qquad (4.21)$$

Subtracting the fraction of the backward intensity from that of the forward intensity gives:

$$g = b_f - b_b = \{\int_0^{\pi} \cos\Theta P(\cos\Theta)\sin\Theta d\Theta\} \Big/ \{\int_0^{\pi} P(\cos\Theta)\sin\Theta d\Theta\} = \frac{1}{2}\int_{-1}^{1} \mu P(\mu) d\mu \qquad (4.22)$$

where g is called the asymmetry factor. It is the averaged $cos\Theta$, or the first moment of phase function. It actually represents the relative strength of the forward scattering.

4.4.2 Asymmetry Factor for Air Molecules

Substituting eq. 4.6 back to eq. 4.22, a zero asymmetry factor is easily derived. This shows that for Rayleigh scattering the forward scattering intensity and the backward scattering intensity have the same strengths but opposite directions.

4.4.3. Asymmetry Factor of A Single Particle

The asymmetry factor for the scattering of a single particle is rather complicated since the phase function is much more complex than the simple phase function for Rayleigh scattering. By substituting the expression of the phase function of a single particle with the radius *r*, eq. 4.19 back to eq. 4.22, the asymmetry factor of a single spherical particles with a radius *r* can be expressed as:

$$g = \frac{1}{2}\int_{-1}^{1} \frac{\lambda^2}{2\pi\sigma_s(r)} [S_1(\mu)\cdot S_1^*(\mu) + S_2(\mu)\cdot S_2^*(\mu)]\mu d\mu = \sum_{i=1}^{4} \Lambda_i \qquad (4.23a)$$

$$\Lambda_k = \frac{\lambda^2}{4\pi\sigma_s(r)} \int_{-1}^{1} [\sum_{i=0}^{\infty} X_{k,i}\,\mu^i]^2 \mu\, d\mu \qquad k = 1,\ 2,\ 3,\ \text{and}\ 4 \tag{4.23b}$$

$$X_{k,i} = Re(x_{k,i}) \qquad \& \qquad X_{k+2,i} = Im(x_{k,i}) \qquad k = 1\ \&\ 2 \tag{4.23c}$$

where $Re(x_{k,i})$ and $Im(x_{k,i})$ represent the real part and imaginary part of $x_{k,i}$, respectively. It should be mentioned again that $x_{k,i}$ is a function of the radius of the particle, wavelength, and the refractive index.

For any integer, $m \geq 0$,

$$\int_{-1}^{1} \mu^{2m} d\mu = \frac{2}{2m+1} \qquad \text{and} \qquad \int_{-1}^{1} \mu^{2m+1} d\mu = 0$$

Thus expanding the polynomials of μ inside the integral of eq. 4.23b, and then integrating them by using the above formulas, eq. 4.23b finally can be expressed as:

$$\Lambda_k = \frac{\lambda^2}{\pi\sigma_s(r)} \sum_{i=0}^{\infty} X_{k,i} \sum_{j=i+1}^{\infty} \frac{X_{k,j}}{i+j+1} \qquad k = 1,\ 2,\ 3,\ \textit{and}\ 4 \tag{4.23d}$$

$$\text{Or} \quad g = \frac{\lambda^2}{\pi\sigma_s(r)} \sum_{k=1}^{4} \sum_{i=0}^{\infty} X_{k,i} \sum_{j=i+1}^{\infty} \frac{X_{k,j}}{i+j+1}$$

4.4.4 Asymmetry Factor for N_p Particles with the Same Refractive Index

Eq. 4.23 is only suitable for a single spherical particle with a radius *r*, or fit for the radiation field with uniform spherical particles with the same radius *r*. Suppose that there

are N_p spherical particles with different sizes and the same refractive index in a radiation field. The particles follow a size distribution, $n_p(r)$, i.e,

$$N_p = \int_0^{\infty} n_p(r)dr \tag{4.24}$$

where the unit of N_p, is cm^{-3}, and that of the size distribution function, $n_p(r)$, is $\mu m^{-1}cm^{-3}$ if the unit of the radius, r, is μm.

When a bundle of incident light with intensity I_λ travels through an infinitesimal length, Δs, some of the incident energy is transformed into scattering energy due to the scattering of particles. The scattering intensity at wavelength λ within an element range of radius of particles from r to $r+\Delta r$ can be expressed as:

$$\Delta I_\lambda^{ts} = \sigma_s(\lambda,r) I_\lambda \Delta N_p \Delta s = \sigma_s(\lambda,r) I_\lambda n_p(r) \Delta r \Delta s \tag{4.25}$$

Where I_λ^{ts} represents the total intensity due to Mie scattering, and I_λ corresponds to the incident intensity.

The net scattering intensity in the forward direction due to ΔN_p scatterers, or the forward scattering intensity minus the backward scattering intensity, is

$$\Delta I_\lambda^{ns} = \Delta I_\lambda^{ts} \cdot g(r) \Delta s = g(r) \sigma_s(\lambda,r) I_\lambda n_p(r) \Delta r \Delta s \tag{4.26}$$

Where I_λ^{ns} denotes the net scattering intensity in the forward direction, and $g(r)$ corresponds to the asymmetry factor of a spherical particle with the radius r. It should be noted that the net scattering intensity is in the backward direction if ΔI_λ^{ns} is a negative

value.

Integrating the eqs. 4.25 and 4.26 with respect to the radius of particles over the whole radius range, from 0 to infinity, then the total intensity due to Mie scattering and the net scattering intensity for the N_p particles are obtained. According to the definition of the asymmetry factor which denotes the relative strength of the forward scattering, the expression of the asymmetry factor for the N_p particles is expressed as:

$$g_p = \frac{I_\lambda^{ns}}{I_\lambda^{ts}} = \frac{\int_0^\infty g(r)\sigma_s(\lambda,r)n(r)dr}{\int_0^\infty \sigma_s(\lambda,r)n(r)dr} \tag{4.27a}$$

Note that the infinitesimal traversing path, Δs, which appears in eqs. 4.25 and 4.26 is canceled out in eq. 4.27a by assuming that the traversing path is independent of the sizes of particles. Substituting eq. 4.23d to eq. 4.27a, then

$$g_p = \frac{\frac{\lambda^2}{\pi}\sum_{il=1}^{\infty} n(r_{il})\Delta r_{il}\sum_{k=1}^{4}\sum_{i=0}^{\infty} X_{k,i}(\lambda,r_{il})\sum_{j=i+1}^{\infty}\frac{X_{k,j}(\lambda,r_{il})}{i+j+1}}{N_p\sigma_s^p(\lambda)} \tag{4.27b}$$

where σ_s^p is the averaged cross section of the N_p particles, and the averaged cross sections of the N_p particles for scattering, σ_s^p, and extinction, σ_e^p, are expressed as:

$$\sigma_s^p(\lambda) = \frac{1}{N_p}\sum_{il=1}^{\infty}\sigma_s(\lambda,r_{il})n(r_{il})\Delta r_{il} \tag{4.28a}$$

$$\sigma_e^p(\lambda) = \frac{1}{N_p} \sum_{i1=1}^{\infty} \sigma_e(\lambda, r_{i1}) n(r_{i1}) \Delta r_{i1} \qquad (4.28b)$$

4.4.5 Asymmetry Factor for the Real Atmosphere

The real atmosphere consists of suspended particles and drops with different size, shape, and refractive index. Both sizes and shapes of particles affect the scattering pattern. For particles with simple geometrical form, it is possible to extend Mie theory, but generally the problem of scattering by non-spherical particles can be solved only by direct measurements of the primary scattering (Lenoble, 1985). Usually modelers treat irregular scatterers with random orientations as spherical particles. Besides the shapes, the size distributions, the number densities, and the refractive indexes of different types of particles such as drops in clouds and atmospheric aerosols, the number density of air molecules also affects the pattern of scattering in the atmosphere due to Raleigh scattering.

Suppose that there are K types of particles, and each type has a unique size distribution, n_k, refractive index, m_k, due to different chemical composition, and number density, N_k ($k=1, 2, \cdots, K$). The number density of the atmospheric molecules is N_m. The number densities of the particles with various chemical compositions and the atmospheric molecules are functions of height. Consider a vertical cylinder with a unit area of cross section and an infinitesimal vertical length, Δz, at the altitude z in the real atmosphere. The total number of the particles with the kth chemical composition and size distribution in this cylinder is $N_k(z)\Delta z$ ($k=1, 2, \cdots, K$) and that of the atmospheric molecules in the cylinder is $N_m(z)\Delta z$. The total scattering intensity in this element of the cylinder can thus be expressed

as:

$$\Delta I_{\lambda}^{TS} = \sum_{k=1}^{K} I_{\lambda} \sigma_s^k N_k \Delta z + I_{\lambda} \sigma_s^m N_m \Delta z \tag{4.29}$$

where the superscripts k and m respectively correspond to the kth type of particles and the atmospheric molecules; I_{λ} is the averaged incident intensity in the element cylinder; σ_s^k is the scattering cross section of the particles with the kth chemical composition and size distribution, calculated by eq. 4.28a; σ_s^m is the cross section of the atmospheric molecules, calculated either directly from the theory of Raleigh scattering, eq. 4.7, which can be found in text books (e.g. Liou, 1980; Goody and Yung, 1989), or from the analytic expression, eq. 4.8, recommended by WMO Report No. 16 (1985), derived by Nicolet (1984) by using the results of Bates (1984).

From eq. 4.27b, the asymmetry factors for each type of particles, g_k $(k=1, 2, \cdots, K)$ can be obtained. Thus the net scattering intensity in the forward direction in the cylinder due to both K types of particles and the atmospheric molecules can be expressed as:

$$\Delta I_{\lambda}^{TS} = \sum_{k=1}^{K} I_{\lambda} g_k \sigma_s^k N_k \Delta z \tag{4.30}$$

According to the definition of asymmetry factor, which represents the relative strength of the forward scattering, the averaged asymmetry factor in the cylinder in the real atmosphere can be expressed as follows:

$$g = \frac{\Delta I_{NS}}{\Delta I_{TS}} = \frac{\sum_{k=1}^{K} g_k \sigma_s^k N_k \Delta z}{\sum_{k=1}^{K} \sigma_s^k N_k \Delta z + \sigma_s^m N_m \Delta z} \tag{4.31a}$$

When Δz approaches zero, the asymmetry factor at height, z, obtained:

$$g(z) = \frac{\Delta I_{NS}}{\Delta I_{TS}} = \frac{\sum_{k=1}^{K} g_k \sigma_s^k N_k(z)}{\sum_{k=1}^{K} \sigma_s^k N_k(z) + \sigma_s^m N_m(z)} \tag{4.31b}$$

If we assume that the particles are horizontally uniform, from eq. 4.31a, the averaged asymmetry factor for Δz at height z can be further expressed as:

$$\overline{g} = \frac{\Delta I_{NS}}{\Delta I_{TS}} = \frac{\sum_{k=1}^{K} g_k \Delta \tau_s^k}{\sum_{k=1}^{K} \Delta \tau_s^k + \Delta \tau_s^m} \tag{4.31c}$$

where the normal optical thickness for the scattering by the kth type of particles, τ_s^k, and by the atmospheric molecules, τ_s^m, can be expressed as:

$$\tau_s^k = \sigma_s^k N_k \Delta z \quad (k = 1,\ 2,\ \cdots,\ K) \qquad \tau_s^m = \sigma_s^m N_m \Delta z \tag{4.32}$$

To avoid heavy computation, the atmospheric scatterers can be divided into three categories: atmospheric molecules, atmospheric aerosols, and drops in clouds. To see the vertical change of the asymmetry factor by using the eq. 4.31, one needs to divide the whole atmosphere into a series of thin layers. Suppose the atmosphere is divided into N layers,

as shown in fig. 4.1. From eq. 4.31b, the asymmetry factor at the *i*th level can be expressed as:

$$g_i = \frac{g_a N_a(z_i)\sigma_s^a + g_c N_c(z_i)\sigma_s^c}{N_m(z_i)\sigma_s^m + N_a(z_i)\sigma_s^a + g_c N_c(z_i)\sigma_s^c} \tag{4.33a}$$

Using eq. 4.31c, the averaged asymmetry factor in the *i*th layer (between levels *i-1* and *i*) can be written as:

$$\overline{g_i} = \frac{g_a \tau_{s,i}^a + g_c \tau_{s,i}^c}{\tau_{s,i}^m + \tau_{s,i}^a + \tau_{s,i}^c} \tag{4.33b}$$

where the superscript *m*, *a*, and *c* respectively correspond to the scattering of the atmospheric molecules, aerosols, and drops in clouds; the subscript *s* denotes the scattering; and the subscript *i* represents the *i*th layer. g_a and g_c are respectively the asymmetry factors of aerosols and cloud drops in the atmosphere, calculated according to eq. 4.27b. The asymmetry factor, *g*, is actually a composite of the asymmetry factors of several types of the atmospheric scatterers: air molecules, atmospheric aerosols, and cloud drops, as shown in eqs. 4.33a and 4.33b. For distinction from the asymmetry factors of aerosols and cloud drops, this composite asymmetry factor is thereafter refer to as the atmospheric asymmetry factor. The atmospheric asymmetry factor is what we need in dealing with the radiative transfer problems in the real atmosphere. $\tau_{s,i}^m$, $\tau_{s,i}^a$, and $\tau_{s,i}^c$ in the above equation are respectively the normal optical depths in the *i*th layer due to the scattering of the atmospheric molecules, aerosols, and drops in clouds. The normal optical depth can be expressed as:

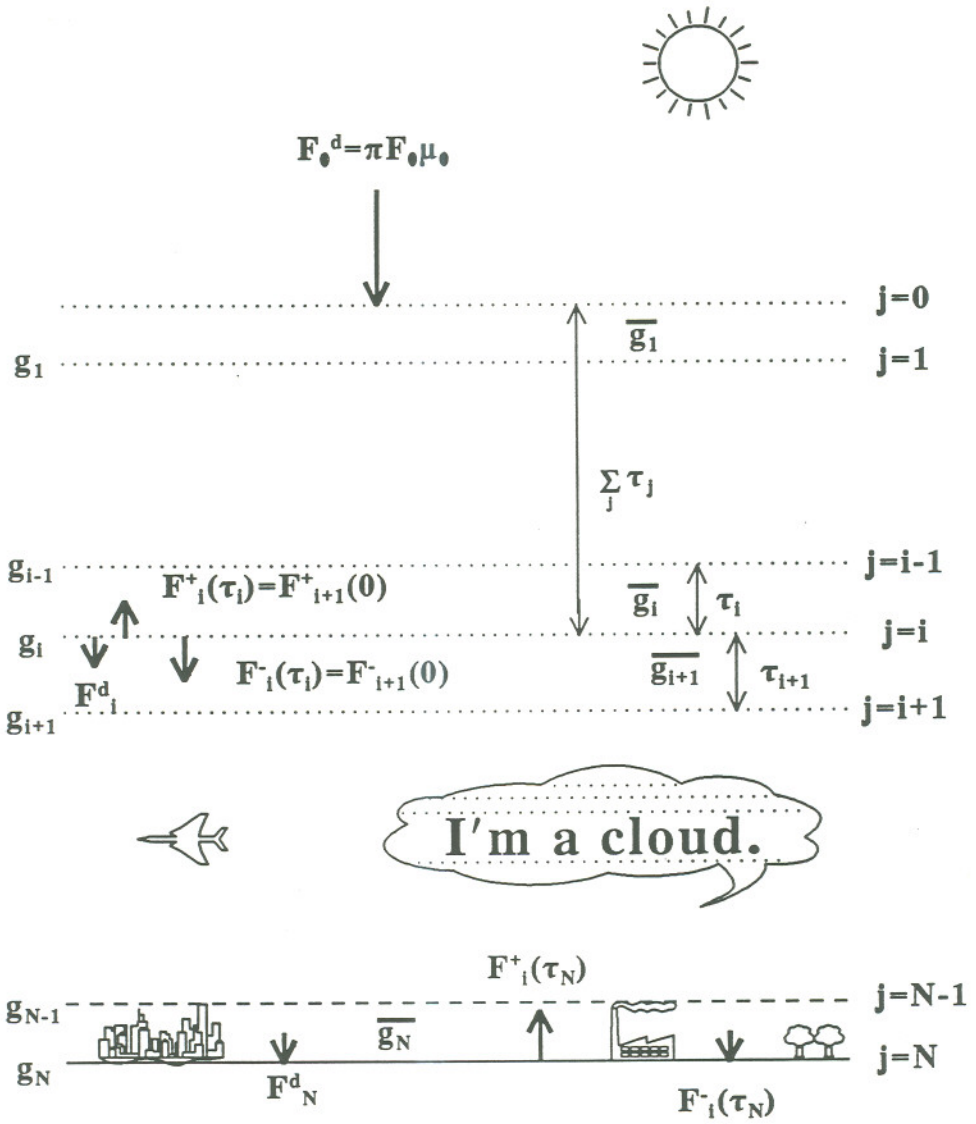

Fig. 4.1 The radiative transfer chart (after Lu and Khalil, 1992b).

$$\tau^{y}_{s,i} = \int_{z_{i-1}}^{z_i} \sigma^{y}_{s,i} N_y dz = \sigma^{y}_{s,i} [N_y(z_i) \cdot N_y(z_{i-1})]^{1/2} \cdot (z_{i-1} - z_i) \tag{4.34}$$

where the s in the subscript s,i represents scattering; the superscript or the subscript y corresponds to m, a, or c, denoting air molecules, aerosol, or drops in clouds; σ_s^y is the scattering cross section of the above atmospheric components; N_y is the number density of the y component in the atmosphere.

4.5 Model Results

In order to study the optical properties of various atmospheric components so that the effects of these components on the radiative transfer can be properly modeled, we considered four atmospheric conditions: 1) clear and clean air including only ozone absorption and Rayleigh or molecular scattering, 2) urban atmosphere (the previous conditions plus aerosol absorption and scattering), 3) urban air with a dense stratus cloud (case 2 plus a stratus at 1.5 ~ 2.5 km), and 4) urban air with a dense altostratus (case 2 plus an altostratus cloud at 5.5~6.5 km) (Lu and Khalil, 1992b and 1992c). The scattering pattern of the first case is clear: a zero asymmetry factor for all heights since there is no Mie scattering involved in this case. Therefore our focus is mainly on the latter three cases.

The vertical profiles of the ozone concentration and the number density of aerosols are taken from Demerjian et al. (1980). The vertical profile of the number density of air molecules is taken from U.S. standard atmosphere (1976). The cross sections for Rayleigh

scattering are taken from WMO-Report No. 16 (1985). The extraterrestrial solar flux, the surface albedos, and ozone absorption coefficients are taken from Demerjian et al. (1980). Aerosol particles and cloud drops are assumed to be spherical in this study. For atmospheric aerosols, a complex refractive index of m=1.5-0.1i, taken from Demerjian et al. (1980), was used in our major radiative transfer model (Lu and Khalil, 1992b). The optical effects of various imaginary parts, from -1 to 0, which correspond to feature of aerosol absorption, are also tested in this study. For clouds a real index of refraction of 1.33 is chosen by assuming only water drops in the cloud, implying that water drops are complete scatterers. The size distribution of aerosols is also taken from (Demerjian et al., 1980), which is expressed as:

$$n_a = a r^2 \exp(-b r^{0.5}) \tag{4.35a}$$

$$b = 15.12 \quad \text{and} \quad a = \frac{N_a(z) \cdot b^6}{2 \times 5!} \tag{4.35b}$$

where r represents the radius of aerosols in units of μm; $N_a(z)$ denotes the number density of aerosols at altitude z in units of cm^{-3}; the unit of the size distribution function of the atmospheric aerosols is thus $cm^{-3}\mu m^{-1}$. The size distribution of drops in clouds are assumed as the following modified gamma distribution:

$$n_c(r) = a_1 r^{n_1} \exp(-b_1 r) \tag{4.36a}$$

Using the above equation to fit the cloud model drop distribution parameters employed by Stephens (1979), we obtain n_1 and b_1 respectively for the stratus and altostratus, as shown

in table 4.3, and

$$a_1 = \frac{N_c(z) b_1^{n_1+1}}{n!} \tag{4.36b}$$

here $N_c(z)$ is the number density of drops at altitude z in the cloud.

Fig. 4.2 shows the size distributions of aerosols and drops in the clouds. The mode radius as well as the spectrum of radius ranges of the drops in the clouds are much larger than that of the atmospheric aerosols, indicating that clouds scatter much more solar radiation than aerosols. It also means that much more computation time is required to calculate the optical features of clouds than those of aerosols (Lu and Khalil, 1992b).

For convenience of comparison, our model resolutions in altitude and wavelength are the same as those of Demerjian et al. (1980) for clear atmospheric conditions; thirty-four layers from the earth's surface up to 70 km above the surface and 48 wavelength ranges from 290 nm to 700 nm are chosen. For cloudy condition, a dense one-km cloud in sub-divided into 100 sub-layers with 10 m of the vertical resolution.

Fig. 4.3 shows the normal optical thickness of ozone absorption, Rayleigh scattering, aerosol scattering and extinction, and the scattering of drops in the stratus and altostratus clouds. In the clear atmosphere, the ultraviolet and visible wavelengths from 290 nm to 700 nm, where most atmospheric chemical reactions take place, can be roughly divided into several regions. When wavelength $\lambda < 305$ nm, the O_3 absorption dominates the radiative transfer. The effect of ozone absorption declines sharply as wavelength increases, and the effect of the molecular scattering becomes important for wavelengths between 310 nm and

Table 4.3. The Coefficients for the Size Distributions of Clouds in This Study[1].

Cloud Type	ND (cm^{-3})	LWC (g/m^3)	MR (μm)	n_1	b_1
Stratus	440	0.22	3.5	5	10/7
Altostratus	430	0.28	4.5	10	20/9

[1] The above table is taken from Lu and Khalil (1992b) and the data in the first three columns are taken from Stephens (1979). Here ND represents the number density of the drops in a cloud; LWC denotes the liquid water content in the cloud; amd MR is the mode radius, corresponding to the maximum number of drops.

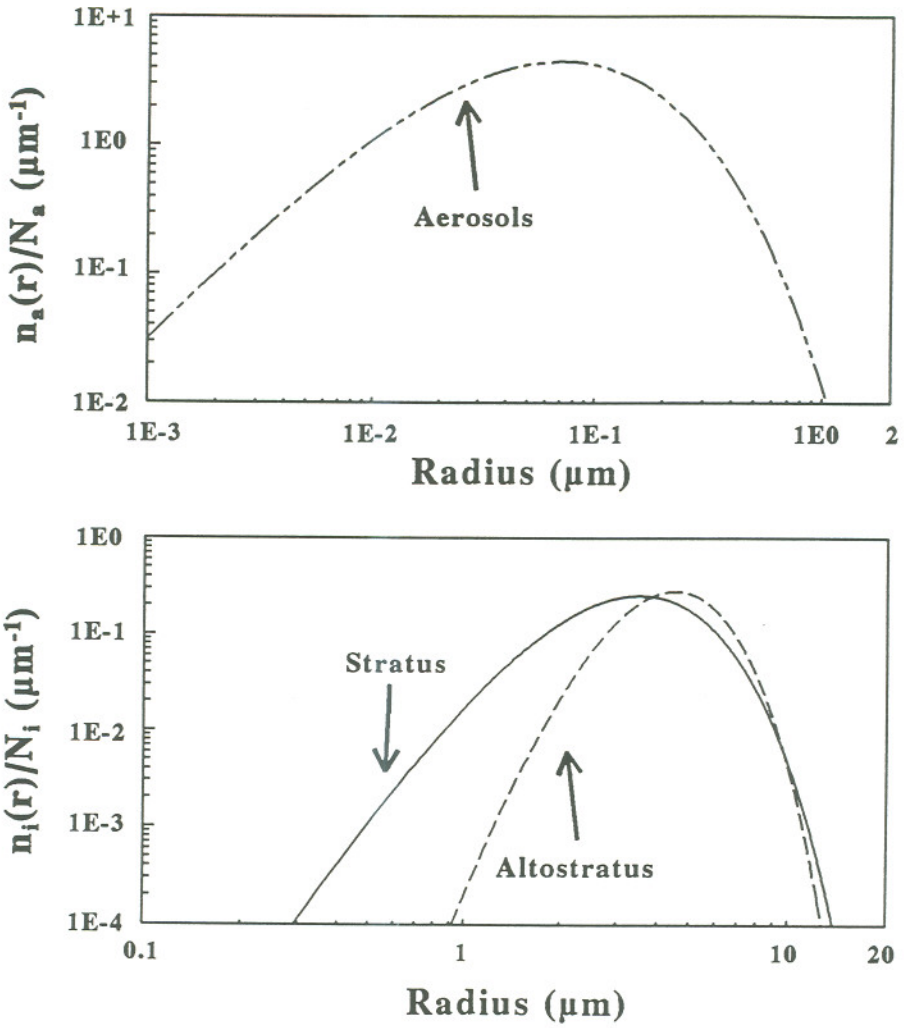

Fig. 4.2 Size distribution of aerosols and drops in clouds, where $n_a(r)$ and $n_i(r)$ are the size distributions of atmospheric aerosols and drops inside clouds; r denotes the radius of aerosols or drops; $i=1$ and 2 corresponds to stratus and altostratus; N_a and N_i represent the total numbers of aerosols and drops inside a stratus for $i=1$ or drops inside an altostratus for $i=2$.

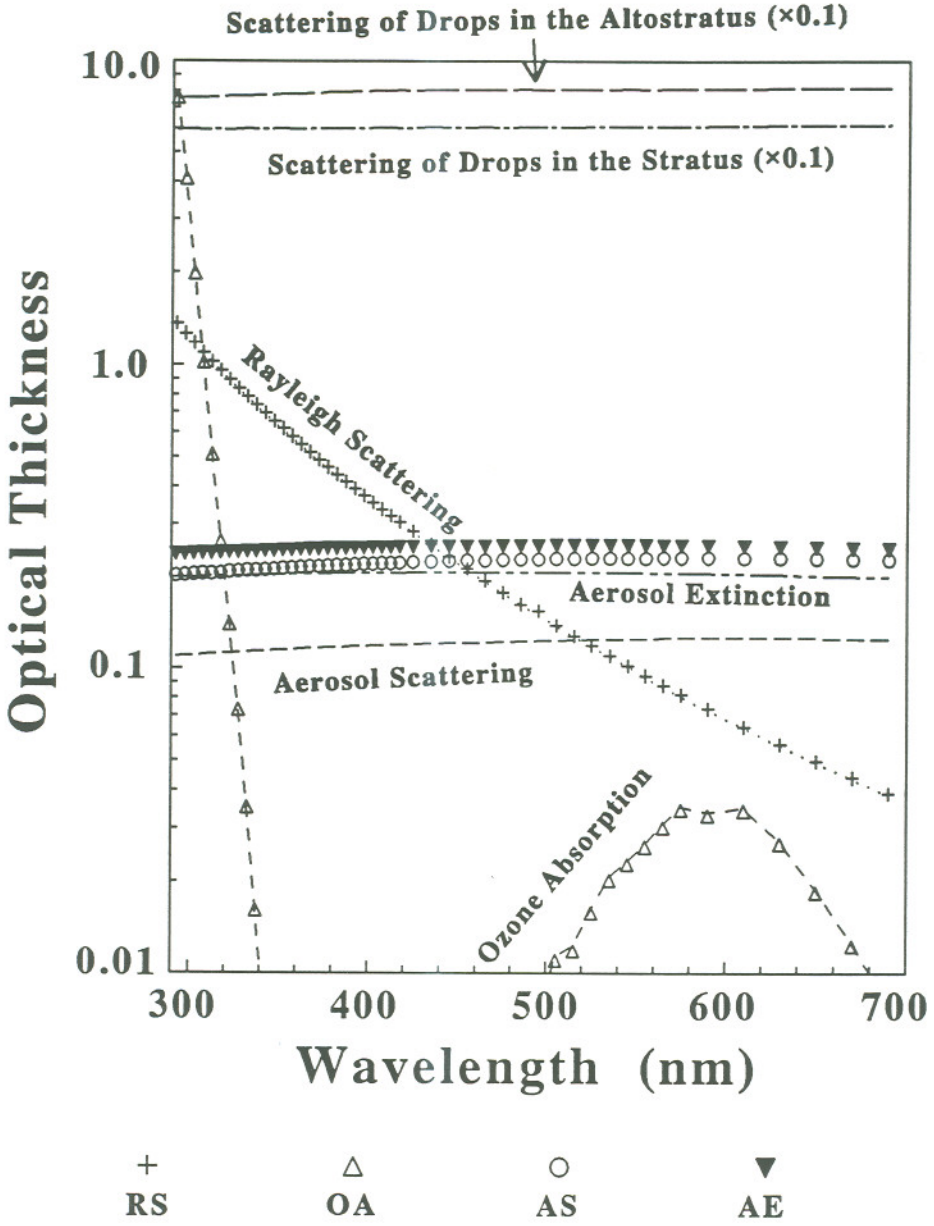

Fig. 4.3 Normal optical thickness of ozone absorption, Raleigh scattering, aerosol scattering and extinction, and the scattering of drops in the stratus and altostratus clouds. All the lines shown in this figure are our model results, while all the symbols correspond to the model results calculated by Demerjian et al. (1980), where the legend names, *RS, OA, AS,* and *AE* respectively correspond to the normal optical thickness of Raleigh scattering, ozone absorption, and aerosol scattering and extinction.

450 nm. The effect aerosol scattering is important when $\lambda > 450$ nm and the effect becomes dominant for $\lambda > 600$ nm. The influence of clouds on the radiative transfer is obvious. The optical thickness of a one-km heavy stratus is more than 6 times as large as the sum of the thickness of Rayleigh scattering, aerosol extinction, and O_3 absorption for the whole atmosphere within the strong O_3 absorption wavelength, 290~295 nm, and more than 4.33 times within the weak O_3 absorption and molecular scattering region, 680~700 nm.

Comparing our model results with the results calculated by Demerjian et al. (1980), one can see that the thickness of both O_3 absorption and molecular scattering, calculated in the two models agrees very well. There is a small difference between the two model results in the normal thickness of aerosol extinction; however, the two model results have a big difference in the aerosol scattering thickness. As shown in fig. 4.3, the model results of Demerjian et al. (1980) indicate that about 90% of aerosol optical thickness is due to the scattering process and only about 10% of that is due to the absorption. In contrast, our model shows that aerosol absorption contributes more than 40% to the total aerosol effect.

The normal thickness of aerosol scattering or extinction is defined as the integral of the product of the number density of aerosols and the cross section of either aerosol scattering or extinction over the entire height of the atmosphere. Thus the major reason for the difference between the aerosol scattering and extinction depths should be the calculation of the cross sections since the size distribution and the vertical profile of the number density of the atmospheric aerosols for calculating the optical thickness of both aerosol scattering and extinction are the same in both models.

Fig. 4.4 shows the model calculated scattering and extinction efficiencies (Q_s and Q_e) as functions of the size parameter, $x=2\pi r/\lambda$, for various refractive indexes with the same real part, *1.5,* but different imaginary parts from *-1* to *0*. From eq. 4.35, one can quickly calculate that the mode radius of the atmospheric aerosols, which corresponds to the maximum number of aerosol particles, is 0.07 μm. Since the size distribution changes sharply around the mode radius, most of the atmospheric aerosol particles have radius close to 0.07 μm according to the size distribution of the atmospheric aerosols (Demerjian, 1980); i.e. the effect from the whole atmospheric aerosols can be roughly seen as the effect from aerosol particles with radius near 0.07 μm. Thus the range of the size parameter from 0.1 to 10, shown in fig. 4.4, covers the ultraviolet and visible wavelengths from 290 nm to 700 nm as well as most of the contribution of the atmospheric aerosols to the radiative transfer in the ultraviolet and visible wavelengths since $x\sim1.5$ corresponds to the aerosols with radius close to *0.07* nm at the wavelength $\lambda\sim290$ nm and $x\sim0.6$ corresponds to the same size aerosols at the wavelength $\lambda\sim700$ nm. As we can see, for zero imaginary part of the refractive index, there is no difference between the scattering and extinction efficiency, indicating that the particle with zero imaginary part of the refractive index is a perfect reflector. As the imaginary part increases, the difference between the scattering and extinction efficiencies increase, indicating that more incident light is absorbed.

Fig. 4.5 shows the ratio of scattering efficiency to extinction efficiency as a function of the size parameter from 0.1 to 10, where most of the influence of the atmospheric aerosols occurs on the radiative transfer within wavelength from 290 nm to 700 nm (i.e., $x \sim 1$). The ratio for the aerosol particles with zero imaginary part of the refractive index is

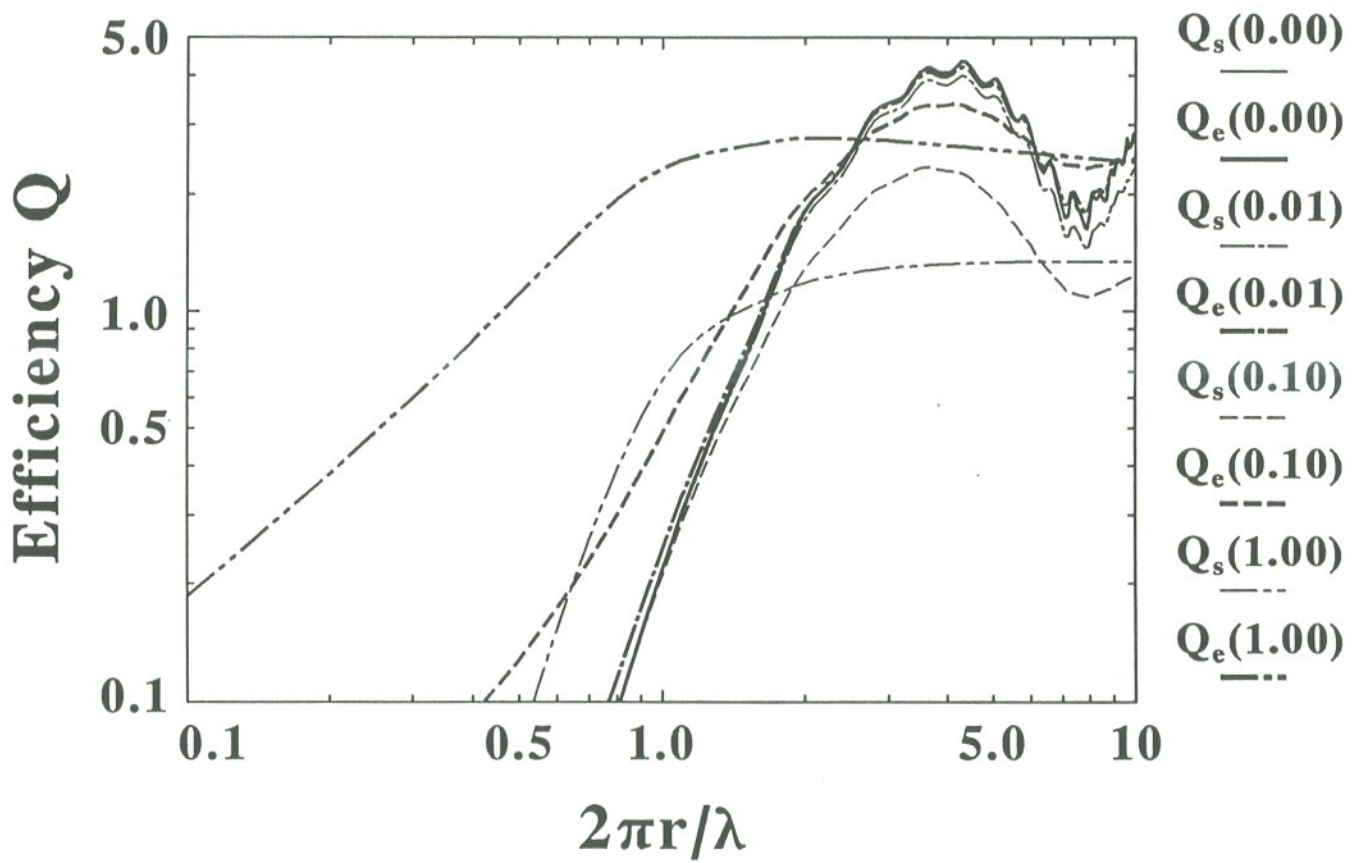

Fig. 4.4 Model calculated scattering and extinction efficiencies, $Q_s(n_i)$ and $Q_e(n_i)$, as functions of the size parameter, $x=2\pi r/\lambda$, for various refractive indexes, $n_r - i\,n_i$, with the same real part, *1.5,* but different imaginary parts from *-1* to *0*.

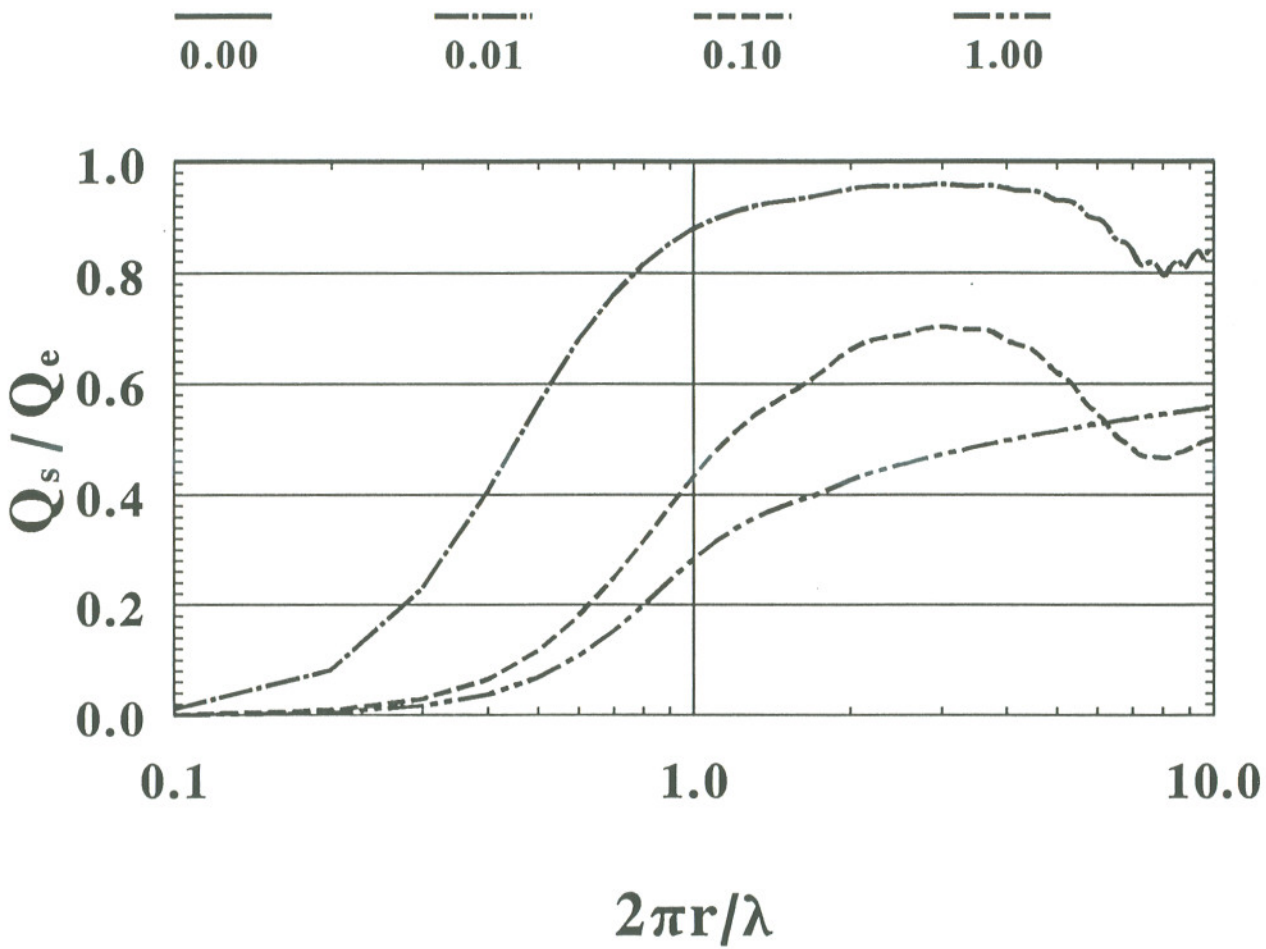

Fig. 4.5 Ratio of scattering efficiency to extinction efficiency as a function of the size parameter from *0.1* to *10* for different imaginary parts of the refractive indexes. Each legend name in this figure corresponds to n_i of the complex index of the refraction, $n_r - i\,n_i$, where n_r is *1.5* for all cases.

one, indicating that no difference between scattering and extinction efficiencies for a complete reflector. The ratios are very small at small size parameters for the refractive indexes with non-zero imaginary parts, m_i; e.g., 0.011 for m_i=-0.01, 0.0012 for m_i=-0.1, and 6.68×10^{-4} for m_i=-1.0 when x=0.1, indicating that absorption rather than scattering is dominant optical effect for small particles ($x\sim0.1$) with non-zero imaginary parts for the refractive index. The ratios increase quickly with the increase of the size parameter when x<1, and they reach their maximum values at about x=3 for m_i=-0.01 and -0.1. By definition, the exact values of scattering and extinction efficiencies, the difference between the two efficiencies, and the size distribution of aerosol particles controls the difference between the normal optical depths between aerosol scattering and extinction. As shown in fig. 4.4, the Q values at x<1 are very small compared to those at x>1, thus making less of a contribution to optical depths for aerosol scattering and absorption. For particles with x>10, the contribution to the optical depths are also small since the maximum number of particles appears at x~1 and the number of particles with x>10 is very small. Thus the normal optical depths for the aerosol scattering and absorption are mainly controlled by the aerosol particles with x value between 1 and 10. Since the maximum number densities of particles and the maximum values of exact efficiencies are respectively at x approximately equal to 1 and x approximately equal or larger than 4 while the maximum values of the ratios of O_s to Q_e appear at x approximately equal to or larger than 3, the ratio of the normal optical depth of the aerosol scattering to that of the aerosol extinction must be less than the maximum value of the ratio of Q_s to Q_e, which appears about 70% for m_i=-0.1 and about 95% for m_i=-0.01 at x~3.0, as shown in fig. 4.5.

From our calculation, as shown in figs. 4.4 and 4.5, it is impossible to conclude about 90% of aerosol extinction due to the scattering process for atmospheric aerosols with an imaginary part m_i=*-0.1* of the complex imaginary index. The effects of various refractive indexes with different real and imaginary parts were also tested in this study to compare with previous studies. Generally our model results agree very well with others (e.g. Deirmendjian et al., 1961; Hansen and Travis, 1974). It is interesting that the normal optical thickness of the atmospheric aerosol scattering and extinction, calculated in this study, agree well with those calculated by Demerjian et al. (1980) when we replaced the imaginary refractive index m_i=*-0.1* with m_i=*-0.01*. The computational rounding errors in Mie scattering calculation might also be another reason for the difference between the two model results. In this study, computation, double precision was used dealing with problems of Mie theory.

Fig. 4.6 shows the efficiencies of extinction and scattering as functions of the size parameters for various refractive indexes with the same real part, *1.5*, and different imaginary parts from *-1* to *0*. For small imaginary refractive index, i.e., the absolute value of imaginary refractive index less than 0.01, there are a series of major maxima, minima, and ripples in Q_e and Q_s, resulting from interference of light diffracted, reflected, and refracted by the particle. As the size parameter increases, all extinction efficiencies eventually converge to a value of two no matter how big the differences of the imaginary parts of the refractive indexes are. This implies that a large particle removes from the incident beam exactly twice the amount of light it can intercept (Hansen and Travis, 1974; Liou, 1980). As the imaginary refractive index increases, the maxima, minima, and ripples of both Q_e and Q_s are damped out.

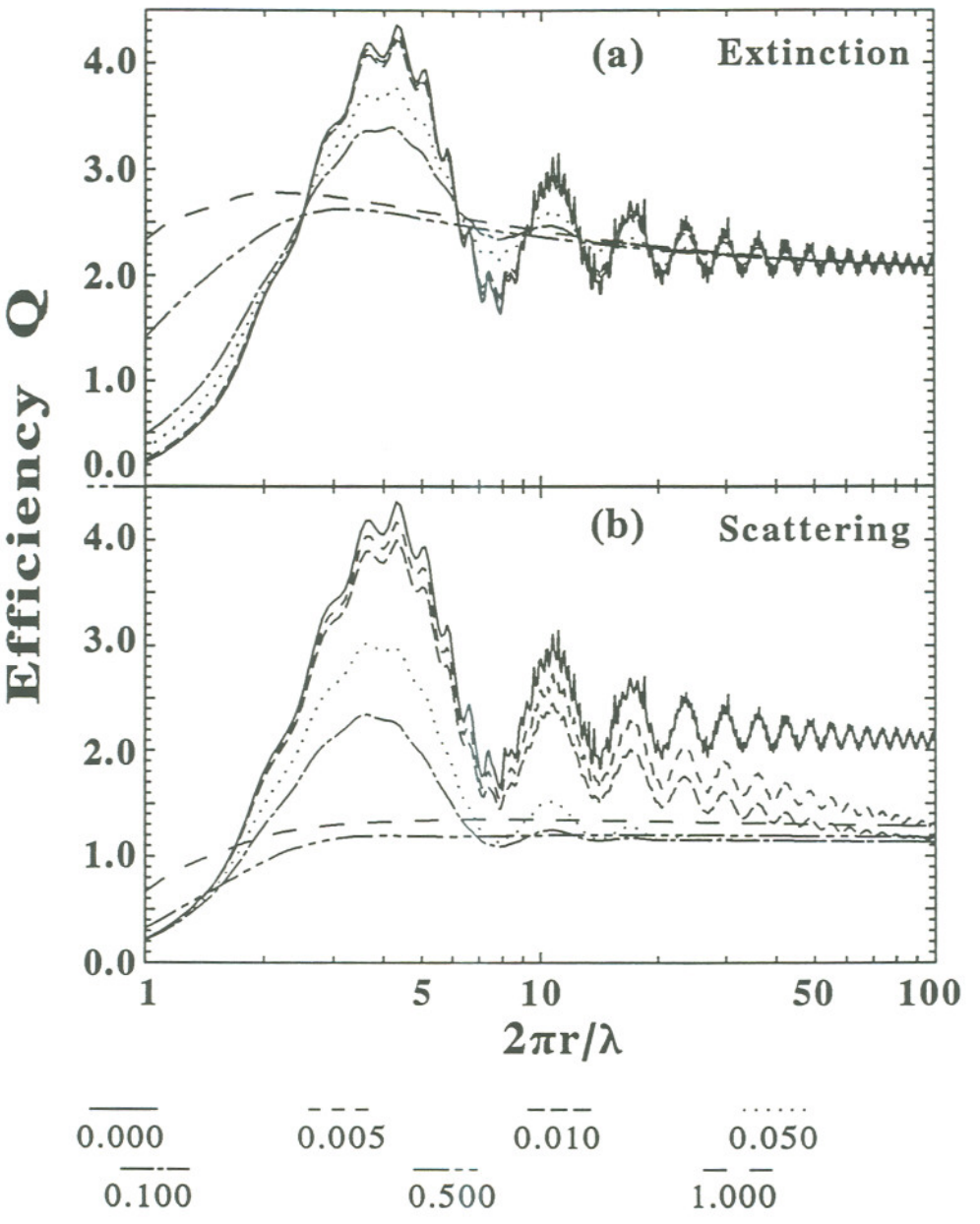

Fig. 4.6 Efficiencies of extinction and scattering as functions of the size parameters for various refractive indexes with the same real part, *1.5*, and different imaginary parts from *-1* to *0*. Each legend name in this figure corresponds to n_i of the complex index of the refraction, $n_r - i\,n_i$, where n_r is *1.5* for all cases.

Fig. 4.7 shows the vertical profiles of the atmospheric asymmetry factors for four different wavelength ranges: 295~300 nm, 395~400 nm, 510~520 nm, and 680~700 nm in the clear urban atmosphere. As one can see, the vertical structures of the asymmetry factors for all the wavelength ranges in ultraviolet and visible wavelengths generally follow a typical pattern: the asymmetry factor first decreases rapidly with height from the earth's surface, reaching a minimum value at around 8 km above the earth's surface, and then increases with height reaching a peak value around 22 km, and finally decreases with height. This kind of the vertical structure of the asymmetry factor results from the vertical distributions of the aerosols and the air molecules, or more precisely from the vertical profile of the ratio of the product of the aerosol scattering cross section and the number density of aerosols to that of the molecular scattering cross section and the number density of molecules, as shown in eq. 4.33a. In the lower and middle troposphere, on the one hand, the rapid rate of the decrease of the number of aerosol particles with height (Braslau and Dave, 1973; Demerjian et al., 1980) compared to the declining rate of the number of air molecules with height (US Standard Atmosphere, 1976) is key reason for the fast decrease of the asymmetry factor with height. On the other hand, a relatively small increase of the atmospheric aerosols with height from 8 km above the earth's surface and a relatively large increase of the aerosols with height in the lower stratosphere due to the stratospheric sources such as the accumulation of the volcanic aerosols and the aerosols from the injection of airplanes versus the decrease of the air molecules with height result in the minimum and maximum asymmetry factors appearing in the upper troposphere and lower stratosphere. Similarly, the different rates of the decreases of the numbers of the aerosols

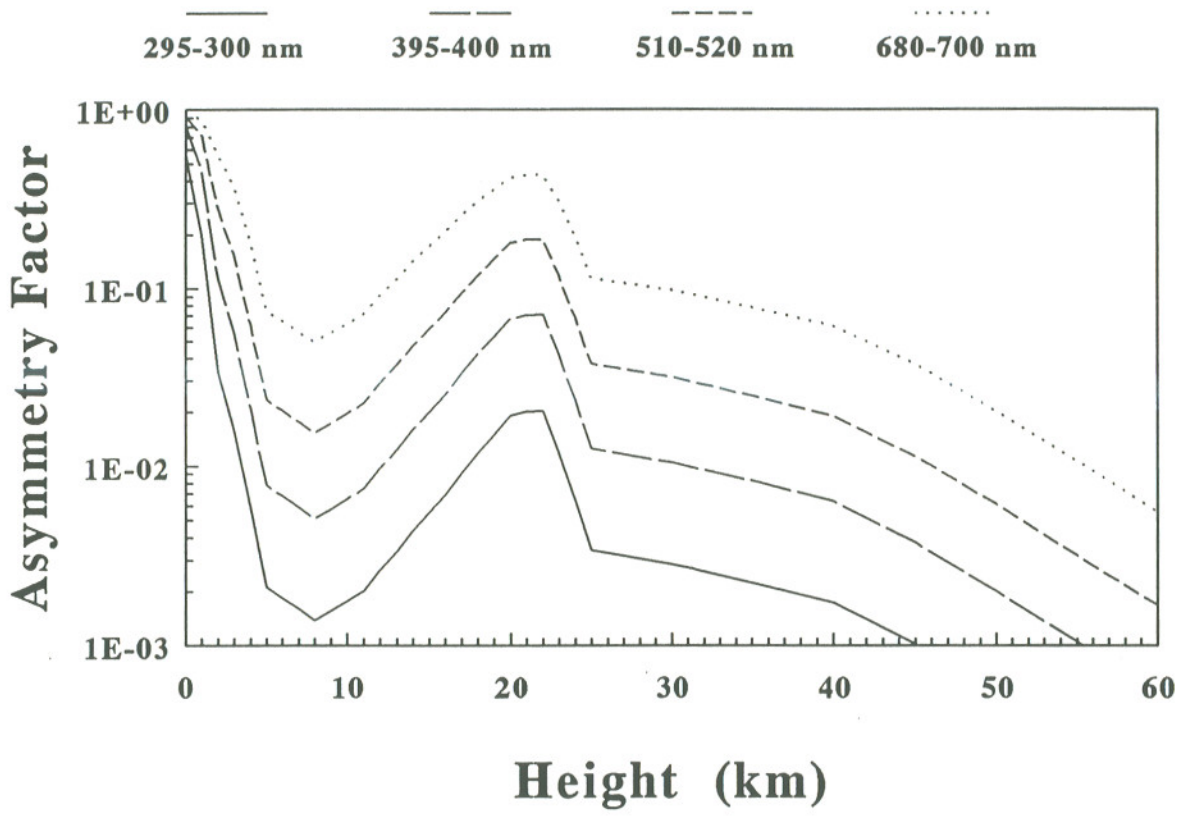

Fig. 4.7 Vertical profiles of the asymmetry factors for four different wavelength ranges: *295~300* nm, *395~400* nm, *510~520* nm, and *680~700* nm in the clear urban atmosphere.

and the air molecules with heights in the middle and upper atmosphere determine the vertical pattern of the asymmetry factor there.

Another significant feature of the atmospheric asymmetry factor, clearly shown in fig. 4.7, is that at any height the asymmetry factor increases with wavelength, mainly resulting from the rapid decrease of the molecular scattering cross section with the increase of wavelength since the aerosol scattering cross section only increases slightly with wavelength. As shown in fig. 4.3, the importance of aerosol scattering increases with wavelength while the influence of molecular scattering becomes weak as wavelength increases, resulting in the increase of the asymmetry factor with wavelength, as shown in fig. 4.7. Since aerosols are heavier than air molecules, it can be argued that the number of the atmospheric aerosols would decrease with height faster than the air molecules in the upper atmosphere where there is no any source of aerosols, leading to an asymptotic limit of 0, as shown in fig. 4.7.

Fig. 4.8 compares the asymmetry factors of the atmospheric aerosols, calculated with eq. 4.27b, with the atmospheric asymmetry factors, calculated with eq. 4.33a, for different heights in the ultraviolet and visible wavelengths from 290 nm to 700 nm. Same as fig. 4.7, this figure shows the asymmetry factor increases with wavelength. It is interesting that the curves of the asymmetry factor versus wavelength at two different heights are almost parallel above the atmospheric boundary. Above the atmospheric boundary, the effect of molecular scattering is dominant over the aerosol scattering; i.e., $N_m \sigma_s^m \gg N_a \sigma_s^a$. Thus eq. 4.33a can be modified for the clear urban atmosphere above the boundary layer as follows:

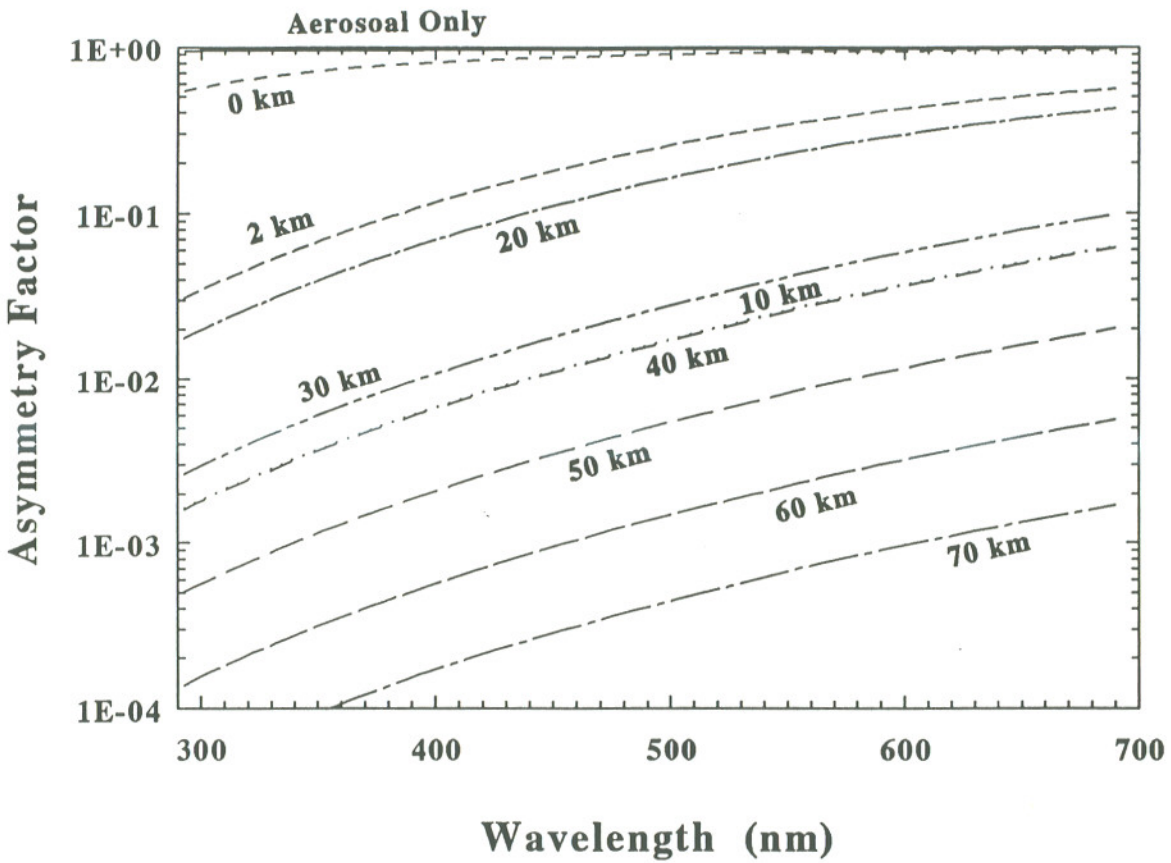

Fig. 4.8 Comparisons of the asymmetry factors of the atmospheric aerosols, calculated with eq. 4.27b, with the atmospheric asymmetry factors, calculated with eq. 4.33aa, for different heights in the ultraviolet and visible wavelengths from *290* nm to *700* nm.

$$g_i \propto \frac{g_a N_a(z_i)\sigma_s^a}{N_m(z_i)\sigma_s^m} \qquad z > 2 \text{ km} \qquad (4.33d)$$

where the superscripts or subscripts m and a respectively correspond to the scattering of the atmospheric molecules and aerosols; the subscript s denotes the scattering; and the subscript i represents the ith level; g_a is the asymmetry factors of aerosols in the atmosphere, calculated according to eq. 4.27b. Therefore the ratio of the asymmetry factors at two different heights can be approximated as:

$$\frac{g(z_i)}{g(z_j)} \propto \frac{\dfrac{g_a N_a(z_i)\sigma_s^a}{N_m(z_i)\sigma_s^m}}{\dfrac{g_a N_a(z_j)\sigma_s^a}{N_m(z_j)\sigma_s^m}} = \frac{N_a(z_i)N_m(z_j)}{N_m(z_i)N_a(z_j)} \qquad z_i,\ z_j > 2 \text{ km} \quad \text{and} \quad z_i \neq z_j$$

From the above equation, one can see that the ratio of the asymmetry factors at two different heights above 2 km is mainly controlled by the number densities of aerosols and air molecules, independent of wavelength, which is why the curves of the asymmetry factors versus wavelength are parallel at different heights.

From fig. 4.8, one can also see that the asymmetry factor decreases with height very rapidly in the lower and middle troposphere. Due to the accumulation of stratospheric aerosols, the asymmetry factors are higher at 20 km and 30 km above the earth's surface than at 10 km, and the latter is even close to that at 40 km. In addition, the asymmetry factor increases with wavelength. These features can be seen from fig. 4.7 and the physical reason for them were discussed earlier.

Probably the most important portion of fig. 4.8 is the distinction between the asymmetry of the aerosol particles and the atmospheric asymmetry factor. The former is never equal to the latter even at the earth's surface, especially for the ozone strong absorptions wavelength. For example, in the wavelength 290~295 nm the asymmetry factor of the aerosols, g_a, is 0.948, while the atmospheric asymmetry factor at the earth's surface for the urban atmosphere, g_{sur}, is 0.545; there is more than 70% relative difference ($(g_a-g_{sur})/g_{sur}=0.739$)!! In contrast, in the wavelength range 680~700 nm at the earth's surface, there is only a 2% difference between the two asymmetry factors. At 75 km above the earth's surface, there are more than four orders of magnitude of difference between the two asymmetry factors in 290~300 nm and more than two orders of magnitude of difference in 680~700 nm.

In order to see the importance of the asymmetry factor for the precise calculation of the radiation field, or actinic flux, the actinic fluxes were calculated and compared for different wavelengths, altitudes and solar zenith angles, by substituting the atmospheric asymmetry factors with eq. 4.33b as well as the asymmetry factors of the atmospheric aerosols with eq. 4.27b and zero asymmetry factor into our radiative model (Lu and Khalil, 1993b). Fig. 4.9 shows the vertical profiles of the relative errors of the actinic fluxes with the asymmetry factor of the atmospheric aerosols and with zero asymmetry factor in 295~300 nm at zenith angles 0° and 86°. The relative error is defined as the difference between the two actinic fluxes calculated respectively with either the asymmetry factor of the aerosols or zero asymmetry factor and with the atmospheric asymmetry factor, divided by the actinic flux with the atmospheric asymmetry factor; i.e.,

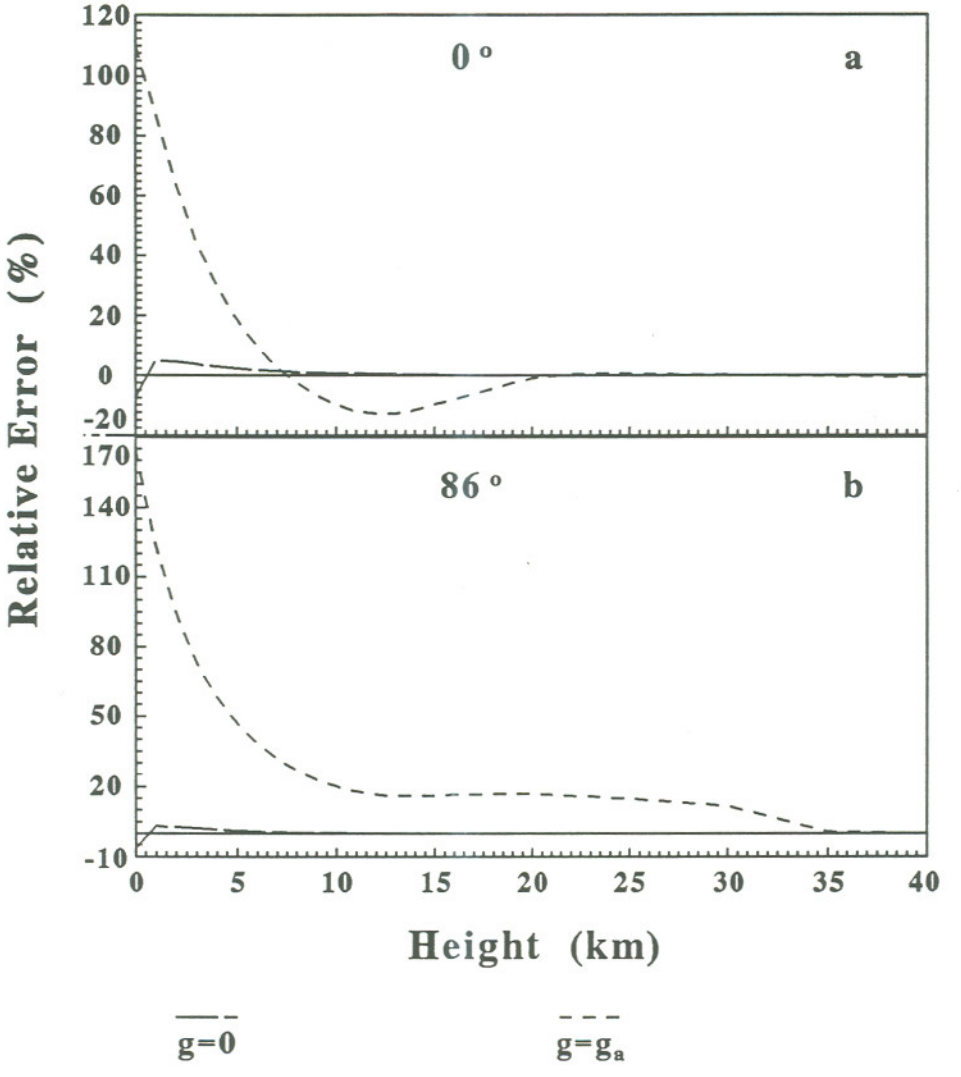

Fig. 4.9 Vertical profiles of the relative errors of the actinic fluxes with the asymmetry factor of the atmospheric aerosols, g_a, and those with zero asymmetry factor in *295~300* nm at zenith angles *0°* and *86°*.

$$\varepsilon = \frac{J(g_x) - J(g)}{J(g)}$$

where $J(g)$ is the actual actinic flux calculated with the atmospheric asymmetry factor, g; g_x is either g_a, the asymmetry factor of the aerosols calculated with eq. 4.27b, or zero asymmetry factor; $J(g_x)$ is the actinic flux, calculated with the asymmetry factor, g_x. For convenience, ε, is referred to as the relative error of the actinic flux with either g_a or zero asymmetry factor.

The relative error of the acinic flux with g_a within 295~300 nm wavelength is significant, especially in the lower atmosphere, where most of the atmospheric aerosols and air molecules reside. At zero zenith angle, the relative error, as shown in fig. 4.9a, first decreases rapidly from about 110% at the earth's surface to about -13%, at 12~13 km above the earth's surface, then it gradually increases back to a small positive value, 0.5%, at 22 km, above which the absolute relative error is limited to less than 1%. With two-stream technique, the magnitude of the actinic flux at a certain height can be determined from three parts: the direct radiative flux, the upward diffuse flux, and the downward flux (e.g. Lu and Khalil, 1992b; also see the next chapter). The direct flux only depends on the extraterrestrial flux, the total normal optical depth, and solar zenith angle; therefore, the variation of the asymmetry factor only affects the upward and downward diffuse fluxes since the asymmetry factor represents the relative strength of the forward scattering. At small zenith angle, the downward diffuse flux is larger than the upward diffuse flux in the lower and middle troposphere due to the forward scattering which is stronger than the backscattering since almost all the atmospheric aerosols reside in this region. Due to the

accumulation of the backscattering, the upward diffuse flux increases with height, and it becomes dominant over the downward diffuse flux in the upper troposphere and in the lower stratosphere, as shown in fig. 4.10a (For detailed address of the effects of diffuse fluxes on the radiation field, see Lu and Khalil, 1992b). Replacing the atmospheric asymmetry factor, g, by the asymmetry factor of aerosol, g_a, would mistakenly increase the portion of the forward scattering energy, thus increasing the downward diffuse flux but decreasing the upward diffuse flux, resulting in a significantly large positive relative error in the lower troposphere and a large negative relative error in the lower stratosphere, as shown in fig 4.9a.

At a large solar zenith angle of *86°*, as shown in fig. 4.10b, in the same wavelength range, due to the larger traversing path and strong ozone absorption, the downward diffuse flux is always larger than the upward diffuse flux for all the heights in and below the middle stratosphere (Also see Lu and Khalil, 1992b). Thus substituting g_a to g for a large zenith angle would incorrectly enlarge the downward diffuse flux, resulting in large positive errors in the whole troposphere and in the low and middle stratosphere, as shown in fig. 4.9b.

Fig. 4.9 also shows the vertical profiles of the relative error of the actinic flux with zero asymmetry factor. Using zero asymmetry factor actually underestimates the forward scattering but overestimates the backscattering, resulting in 8% of a negative relative error at the earth's surface and 5% of a positive relative error at the top of the atmospheric boundary layer, *2* km above the earth's surface, for zero zenith angle, and -6% and +3% of relative errors at the related heights for 86° zenith angle. The rapid change of the relative error from negative value to positive value is due to the quick reduction of g value

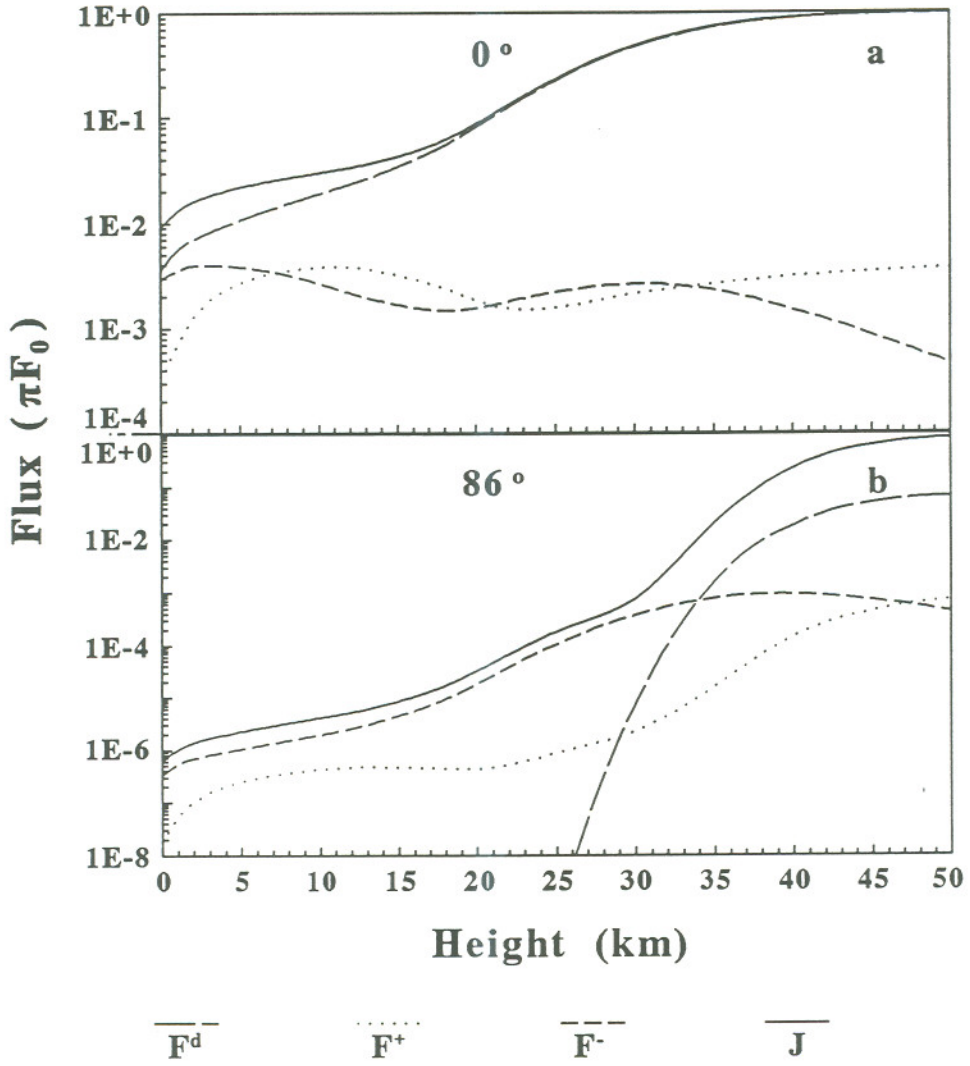

Fig. 4.10 Vertical profiles of the direct radiative flux, F^d, the upward diffuse flux, F^+, the downward diffuse flux, F^-, and the actinic flux, J, at $0°$ and $86°$ zenith angles within the wavelength range, *295~300* nm, for the clear urban atmosphere.

with height toward zero, which also make the relative error less 1% for all heights above the middle troposphere. This implies that a zero asymmetry factor can be used for the calculation of radiation field in the upper troposphere and the atmosphere above.

Fig. 4.11 shows the relative errors of the actinic fluxes with g_a and with zero asymmetry factor for the wavelength range from 290 nm to 700 nm at the earth's surface. Generally the relative error of the actinic fluxes with g_a decreases with wavelength from about 110% at 300 nm to about 4% at 700 nm for zero zenith angle and from about 190% from 300 nm to about 2% at 700 nm for 86° zenith angle, resulting from the decrease of the difference between g_a and g with wavelength, as shown in fig. 4.8. There is a small peak of the relative error at 297.5 nm at zero zenith angle while no such peak appears for the large zenith angle, 86°. As shown in fig. 4.3, the ozone absorption dominates over the aerosol scattering and absorption as well as the molecular scattering at wavelength less than 310 nm and the strength of O_3 absorption increases rapidly with decreasing wavelength. The scattered radiative energy is absorbed by ozone in the strong O_3 absorption wavelength, thus reducing the accumulation of the diffuse radiative energy (Lu and Khalil, 1992). On the one hand, if one mistakenly replaced g with g_a for a small zenith angle in the wavelength greater than 297.5 nm, the portion of the diffuse radiative energy, especially the multiple scattering energy, absorbed by O_3, would be too large to compensate for the portion of the increase of the diffuse energy due to the first forward scattering process caused by the increase of the difference between g and g_a with decreasing wavelength, as shown in fig. 4.8, resulting in the decrease of the relative error with decreasing wavelength, as shown in fig. 4.11a. On the other hand, for the large zenith angle, *86*°, a large portion of the diffuse

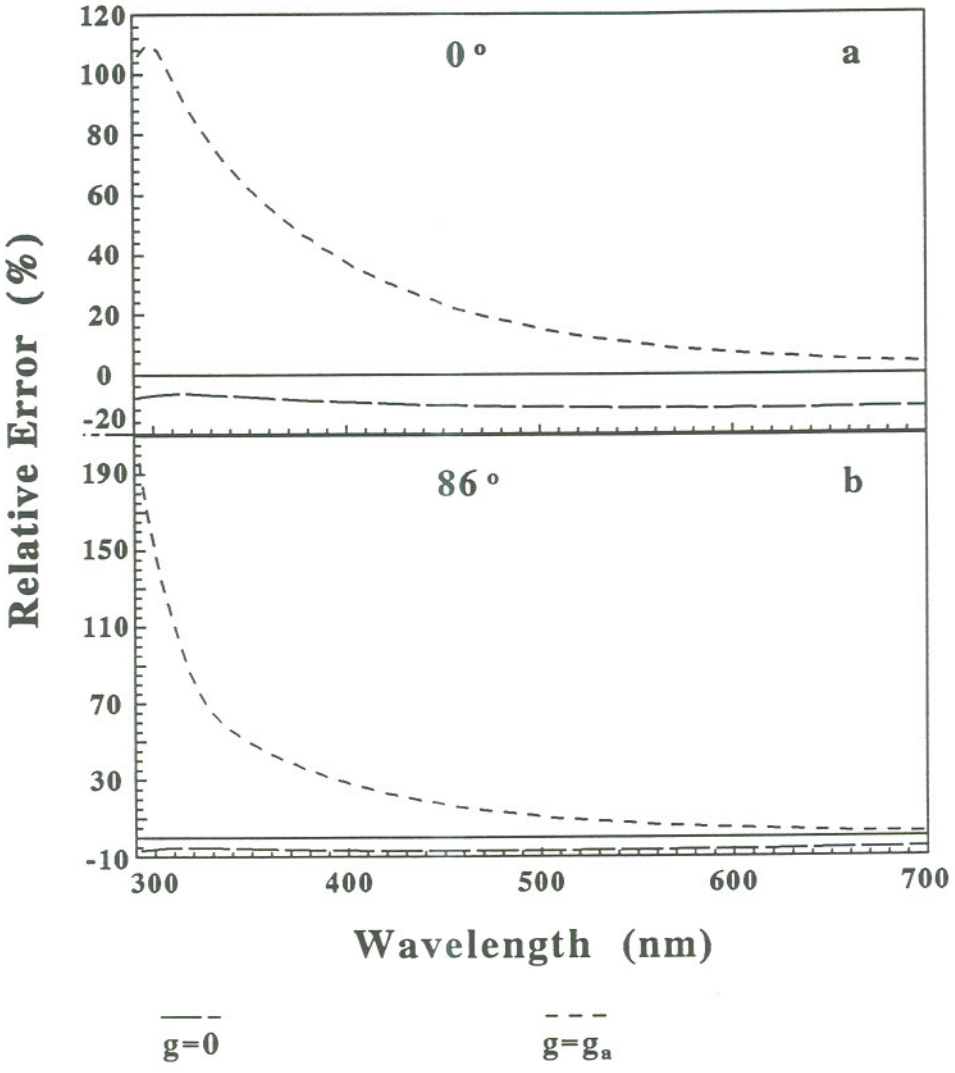

Fig. 4.11 Relative errors of the actinic fluxes with the asymmetry factor of the atmospheric aerosols, g_a, and those with zero asymmetry factor for the wavelength range from *290* nm to *700* nm at the earth's surface.

energy results from the first scattering process since the multiple scattering energy is greatly reduced due to the long traversing path and the strong O_3 absorption (Lu and Khalil, 1992). Therefore, if g were mistakenly replaced by g_a for a large zenith angle, the relative error would simply decrease with wavelength, as shown in fig. 4.11b, since the difference of g_a and g increase with wavelength.

Fig. 4.11 also compares the relative error of the actinic fluxes calculated with zero asymmetry factor. The relative error, on the whole, increases slightly with wavelength for in the wavelength range from 290 nm to 700 nm corresponding to the increase of the difference between two asymmetry factors, g and 0, with wavelength. Consequently, using zero asymmetry factor, on the average, causes about a 10% underestimate of the actinic flux for the zero zenith angle and about a 6% underestimate for $86°$ zenith angle.

As shown in fig. 4.3, the optical depth of a one-km dense cloud (τ_s^c), either the stratus or the altostratus, is much larger than the sum of the optical depths of the aerosol scattering and the molecular scattering for the whole atmosphere ($\tau_s^a + \tau_s^m$). Thus according to eq. 4.33b, the asymmetry factor of cloud droplets, g_c, calculated with eq. 4.27b, can be used as a good approximation for the atmospheric asymmetry factor inside cloud, g; i.e.,

$$g = \frac{g_a \tau_s^a + g_c \tau_s^c}{\tau_s^m + \tau_s^a + \tau_s^c} \approx g_c \qquad \text{for } \tau_s^c \gg \tau_s^m, \tau_s^a \qquad 25c$$

It should be noted that eq. 4.33c is not necessary suitable for all the locations in the cloud except for the vertically uniform cloud, because the scattering of drops at any location inside the vertically uniform cloud is equally dominant over the molecular and aerosol scattering

processes. In reality, the vertically uniform cloud dose not exist. Naturally the number of drops and the liquid water content at the edge of cloud is much smaller than those in the middle of the cloud. Pruppacher (1980) pointed out that the liquid water content increases with height above the cloud base, reaches a maximum value some where in the upper half of the cloud, and decreases rather rapidly toward the cloud top.

In order to see the influence of vertical structures of clouds on the asymmetry factor and radiation field, five hypothetical vertical cloud structures were constructed (Lu and Khalil, 1992). For convenience, these five vertical structures of clouds are labelled as: 1) *uni* corresponding to the vertically uniform cloud, whose liquid water content is all the same anywhere inside the cloud; 2) *ma6*, whose maximum water liquid content is equal to the mean liquid water content of the *uni* and is located at 60% of the whole cloud thickness from the cloud bottom; 3) *av6*, whose maximum liquid water content is located at the same height as the *ma6* and whose vertically averaged liquid water content is equal to that of the *uni*; 4) *ma8*, whose maximum water liquid content, located at 80% of the whole cloud thickness from the cloud bottom, is equal to the mean liquid water content of the *uni*; and 5) *av8*, whose maximum liquid water content is located at the same height as the *ma8* and whose vertically averaged liquid water content is equal to that of the *uni*. As shown in fig. 4.12, the liquid water contents of the four vertically non-uniform clouds are assumed to be zero at the cloud bottoms, and increase with height until the maximum values are reached at some heights in the upper half of the clouds, and then decrease relatively rapidly with height to zero at the cloud tops.

Fig. 4.13 shows the vertical profiles of the atmospheric asymmetry factors in the five

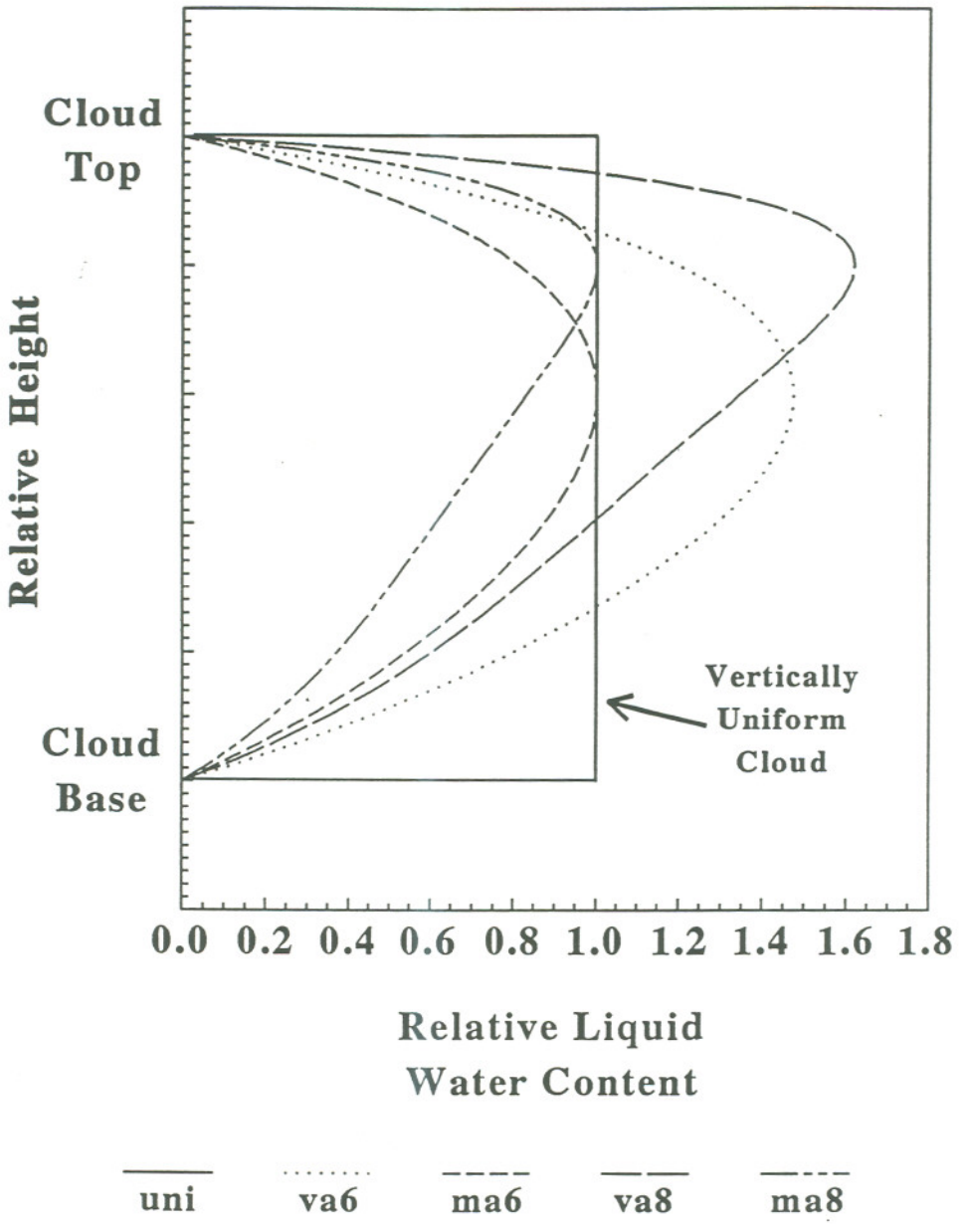

Fig. 4.12 The vertical profiles of the liquid water contents for five hypothetical vertical cloud structures. The relative liquid water content is defined as the liquid water content of a cloud at a height divided by that of the vertically uniform cloud. See the text for the definitions of the legend names for different clouds (after Lu and Khalil, 1992b).

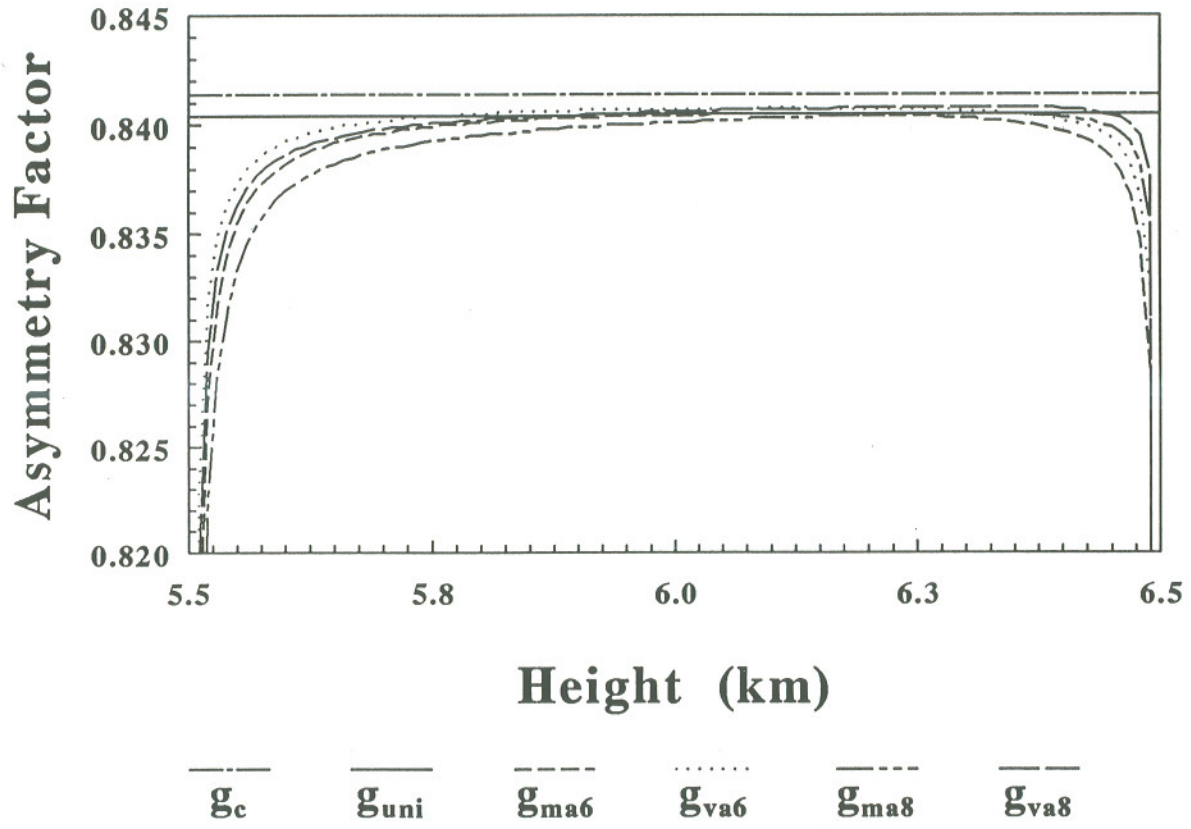

Fig. 4.13 Vertical profiles of the atmospheric asymmetry factors (g_{uni}, g_{ma6}, g_{va6}, g_{ma8}, g_{va8}) and the asymmetry factor of the cloud drops (g_c) inside the five different vertical structures of the altostratus (*5.5~6.5* km) within wavelength *295~300* nm, where the subscripts *uni, va6, ma6, va8,* and *ma8* correspond to the five different vertical structures of the altostratus.

different vertical structures of the altostratus (5.5~6.5 km) within wavelength 295~300 nm. As a comparison, the vertical profile of the asymmetry factor of cloud droplets, calculated from eq. 4.27b according to the size distribution of drops shown in table 4.3, is also shown in fig 4.13. The asymmetry factor outside a cloud, though not shown in fig. 4.13, is the same as in a clear atmosphere, as shown in fig. 4.7, since a cloud does not change the atmospheric components outside it. As shown in fig. 4.13, the asymmetry factors inside the vertically uniform cloud, calculated with eq. 4.33a, are only 0.1% less than those of the drops of the cloud, calculated with eq. 4.27b, since the scattering due to cloud drops is much stronger than the scattering processes due to air molecules and atmospheric aerosols, as shown in fig. 4.3. The 0.1% lower asymmetry factor of the vertically uniform cloud compared to the asymmetry of cloud drops is mostly due to the Raleigh scattering, which is dominant over the aerosol scattering inside the cloud.

For the vertically non-uniform clouds, as shown in fig. 4.13, the atmospheric asymmetry factors increase very rapidly with height from the cloud bottoms to the value close to the asymmetry factor of drops, and they drop very fast with height near the cloud tops. The change of the asymmetry factor with height results from the variation of the liquid water content, or the number of drops, with height. Specifically, the rate of the decrease of the asymmetry factor near the cloud top is larger than that of the increase of the asymmetry factor near the cloud bottom due to the faster decreasing rate of the liquid water content near the cloud top compared to the increasing rate of the liquid water content near the cloud bottom. From fig. 4.13, one can also find that the asymmetry factor inside the cloud correlates well with the liquid water content by comparing the water liquid

contents and the asymmetry factors near the edges of the four different vertically non-uniform clouds; for example, the liquid water content increases faster in the *ma6* than the *ma8* near the bottom of the cloud, corresponding to the faster increase of the asymmetry factor with height in the *ma6* compared to the *ma8*, and near the cloud top the faster decreasing rate of the water liquid content in the *ma8* than in the *ma6* results in more rapidly decreasing rate of the asymmetry factor in the *ma8* in the *ma6*.

To show the effects of the different vertical structures of clouds on the field of actinic fluxes, the relative difference between the actinic fluxes in the atmosphere with a vertically non-uniform cloud and with a vertically uniform cloud is defined as:

$$\eta_i = \frac{J_i - J_{uni}}{J_{uni}}$$

where J_{uni} is the actinic flux for the vertically uniform cloud, and J_i is the actinic flux for one of the four different vertically non-uniform the altostratus (5.5 ~ 6.5 km); i=1, 2, 3, and 4 corresponds to four different vertically non-uniform altostratus clouds. Fig. 4.14 shows the vertical profiles of the reactive differences of the actinic fluxes in the atmosphere with the vertically non-uniform altostratus and the vertically uniform altostratus at 0° (fig. 4.14a) and 86° (fig. 4.14b) within 295~300 nm wavelength. For convenience, we thereafter refer η_i to be the relative difference for the *i*th vertically non-uniform cloud (e.g., the relative difference for the cloud *ma6*). The actinic flux outside a cloud is greatly affected by the total liquid water content of the cloud, while the local variation of the liquid water content inside a cloud has a weak influence on the actinic fluxes outside a cloud. This is true for both small and large zenith angles, as shown in fig. 4.14a and 4.14b. Within the wavelength

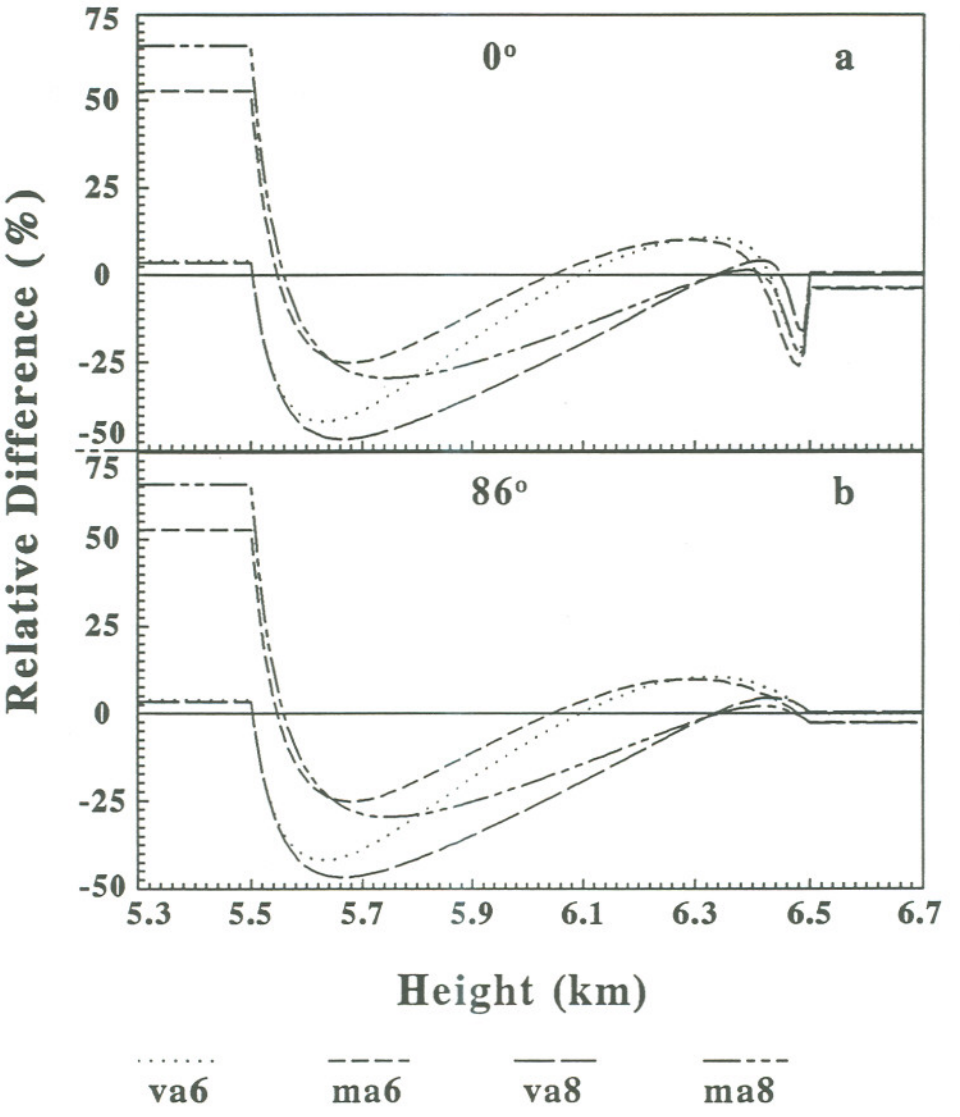

Fig. 4.14 Vertical profiles of the relative differences between the actinic fluxes in the atmosphere with the vertically non-uniform altostratus and the vertically uniform altostratus at *0°* (fig. 13a) and *86°* (fig. 13b) within *295~300* nm wavelength.

range 295~300 nm, the relative difference for the cloud *va6* or the cloud *va8* is about 4% at the bottom of the cloud and less than 1% at the cloud top, corresponding to the same amount of total liquid water content for the three different vertical structures of clouds. In contrast, since the total liquid water contents of the clouds *ma6* and *ma8* are respectively 68% and 62% of that of the cloud *uni*, the relative differences between the actinic fluxes within the same wavelengths are about 65% for the clouds *ma8* and *uni*, and about 53% for *ma6* and *uni* at the bottom of the cloud, and less than 4% between *ma8* or *ma6* and *uni* at the top of the cloud.

The relative differences among the actinic fluxes inside the vertically uniform cloud and the vertically non-uniform clouds are obvious. For zero zenith angle and 295~300 nm wavelength, the relative difference for all the vertically non-uniform clouds first drops with height quickly from the cloud bottom to a negative minimum value in the lower part of the cloud, and then increases with height until a maximum value is reached in the upper part of the cloud, and then decreases with height again to another minimum, and finally increases rapidly again to the relative differences at the cloud top. The vertical profiles of the relative differences in the same wavelength range, *295~300* nm, at the large zenith angle, *86°* is similar to those at zero zenith angle except that there are no rapid reductions from the cloud tops to minimum values close to the cloud tops. Such vertical profiles of the relative differences result from the differences of the vertical structures of liquid water contents in the clouds. Near the top of the cloud, the number of drops is much larger in the vertically uniform cloud than in the non-uniform cloud. On the one hand, more drops means more solar radiation is transferred into diffuse energy by Mie scattering processes, and the diffuse

energy is scattered back and forth, and is thus accumulated. On the other hand, more drops implies that more radiative energy is confined locally and less radiative energy transfers downward. For a small zenith angle, the accumulation of the diffuse energy is stronger than the effect of blocking transfers downward due to the large number of drops in the very upper part of the vertically uniform cloud compared to the vertically non-uniform cloud, resulting in relative higher actinic flux in the very upper part for the vertically uniform cloud compared to the vertically non-uniform cloud. While the very upper part of the vertically uniform cloud traps and conserves more energy than that of the non-uniform cloud, it also blocks more energy to transfer downward, leading to the increase of relative difference of the actinic fluxes with decreasing height immediately after the first dip. For a large zenith angle in the upper part of the cloud, however, more radiative energy is blocked by the large number of drops near the top of the vertically uniform cloud due to the long traversing path compared to the vertically non-uniform cloud, resulting in the increase of the relative difference with decreasing height in the upper part of the cloud. The relative differences for both the small and large zenith angles keep increasing with decreasing height until maximum values are reached, where the sum of the diffuse energy produced by the local scattering processes and the accumulation of the diffuse energy produced at different heights, especially by the accumulation of the energy due to the backscattering, or "reflected", by drops at the height where the maximum liquid water content is, appears a maximum value, compared to that for the vertically uniform cloud. Near the bottom of the cloud, again the number of drops in the vertically uniform cloud is much higher than that of the vertically non-uniform cloud, preventing more diffuse energy from transporting downward through the cloud bottom, leading to a smaller actinic flux below the cloud base

of the vertically uniform cloud compared to that below the vertically non-uniform cloud. The more drops of the vertically uniform cloud near the bottom also reflects more diffuse energy upward, resulting in larger increase of the actinic flux with height in the lower part of the vertically uniform cloud than in the vertically non-uniform cloud. For more information about the influence of the vertical structure of a cloud on the radiation field, see Lu and Khalil (1992b).

As emphasized before, the variation of the asymmetry factor only affects the distributions of the upward and downward diffuse fluxes since the asymmetry factor represents the relative strength of forward scattering. Thus one needs to understand the effects of the diffuse fluxes, both in upward and downward directions, on the actinic flux before going through the effect of the asymmetry factor on the actinic flux. As an example, fig. 4.15 shows the direct flux, the diffuse fluxes, and the actinic flux within wavelength range 295~300 nm at 0° and 86° zenith angles in the vertically uniform altostratus cloud (*uni*). At zero zenith angle, the direct radiative flux drops to almost zero once the solar beam travels into the cloud since almost all the direct insolation is converted into the diffuse energy by the scattering processes of the cloud drops. Thus near the cloud top inside the cloud, the radiative energy is scattered back and forth, and thus accumulated by drops, resulting in maximum values for both the upward and downward diffuse fluxes close to the cloud top. The cloud drops, on the other hand, block more energy transferring downward, leading to decreasing the diffuse fluxes, both upward and downward, with decreasing height. At the large zenith angle, 86°, within the same wavelength, almost all the direct radiative energy is converted into the diffuse energy before the solar beam even enters the cloud due

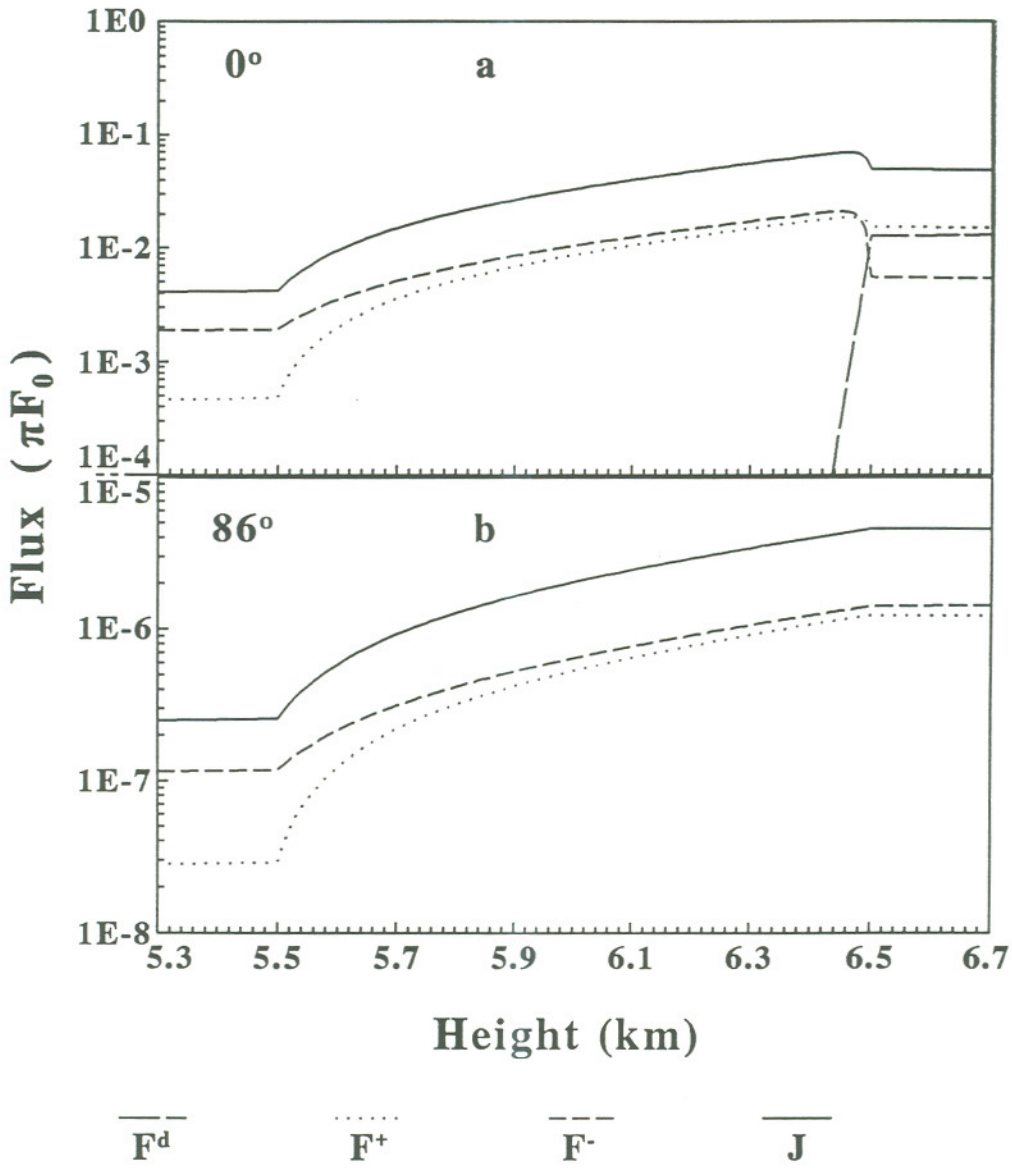

Fig. 4.15 Vertical profiles of the direct flux, F^d, the upward and downward diffuse fluxes, F^+ and F^-, and the actinic flux, J, within wavelength range *295~300* nm at *0°* (fig. 4.15a) and *86°* (fig. 4.15b) in the vertically uniform altostratus cloud (*uni*). It should be noted that all the fluxes in this figure are normalized by dividing by the extraterrestrial flux, πF_0.

to the long traversing path and strong ozone absorption (Lu and Khalil, 1992b). The long traversing path and the strong ozone absorption also reduce the effect of the accumulation of the diffuse energy; therefore, there is no maximum of either the upward diffuse flux or the downward diffuse flux appearing near the cloud top, as shown for a small zenith angle. The vertical profiles of the diffuse fluxes of the non-uniform clouds have similar features as those of the uniform cloud, as shown in fig. 4.15, although the vertical changes of the diffuse fluxes near the edges of the clouds are smoother in the non-uniform clouds than in the uniform cloud (Lu and Khalil, 1992b). It should be mentioned that the actinic flux is the integral of the radiative intensity over the whole sphere, which is equal to the direct radiative flux divided by the cosine of the solar zenith angle plus the sum of the upward and downward diffuse fluxes divided by a integral weight factor, which is different for various two-stream scheme techniques such as Eddington, quadrature, Delta function, etc (For more information, see Meador and Weaver, 1980; Madronich, 1987; Toon et al., 1990; Lu and Khalil, 1992b).

Replacing the atmospheric asymmetry factor with the asymmetry factor of cloud droplets inside the cloud and with the asymmetry factor of aerosols outside the cloud (referred hereafter as the overestimated asymmetry factors) would overestimate the relative strength of the forward scattering for all heights both inside and outside the cloud since the asymmetry factors of both cloud drops and aerosols are larger than the atmospheric asymmetry factor at the same height. However, this overestimate of the asymmetry factor would not result in the higher downward fluxes and lower upward fluxes for all heights. It should be kept in mind that the diffuse flux at a given height is equal to the diffuse energy

produced at the height due to the scattering processes and the diffuse energy arriving at the height but resulting from the scattering processes not at that height. For example, for the vertically uniform cloud within 295~300 nm at 0° zenith angle, on the one hand, the overestimated asymmetry factor outside the cloud causes more diffuse radiative energy sent forward into cloud, resulting in more diffuse energy scattered back and forth, and accumulated, thus higher upward and downward fluxes compared to those calculated with the atmospheric asymmetry factor for most of the heights inside the cloud (the diffuse fluxes calculated with the atmospheric asymmetry factor are referred hereafter as the actual, or the correct, diffuse fluxes). On the other hand, the overestimate of the asymmetry factor below the bottom of the cloud and inside the cloud would also cause more diffuse energy transferring forward out of the cloud and less scattered back into cloud. In other words, the overestimate of the asymmetry factor would let more diffuse energy "leaking" out of the cloud, leading to the lower diffuse fluxes in the very lower part of the cloud compared to the actual diffuse fluxes at the same heights, as shown in fig. 4.16a and fig. 4.16b.

Similarly, replacing the atmospheric asymmetry factor with zero asymmetry factor for all heights both inside and outside the cloud would underestimate the relative strength of the forward scattering for all heights. The zero asymmetry factor would strengthen the backscattering, and the resulting upward diffuse flux would be higher than the correct upward diffuse flux in the very upper part of the cloud because of the accumulation of the strong backscattering. Also the accumulation of the backscattering of the upward diffuse energy would result in the higher downward diffuse flux in the very upper part of the cloud for the same wavelength and zero zenith angle. However, the zero asymmetry factor also

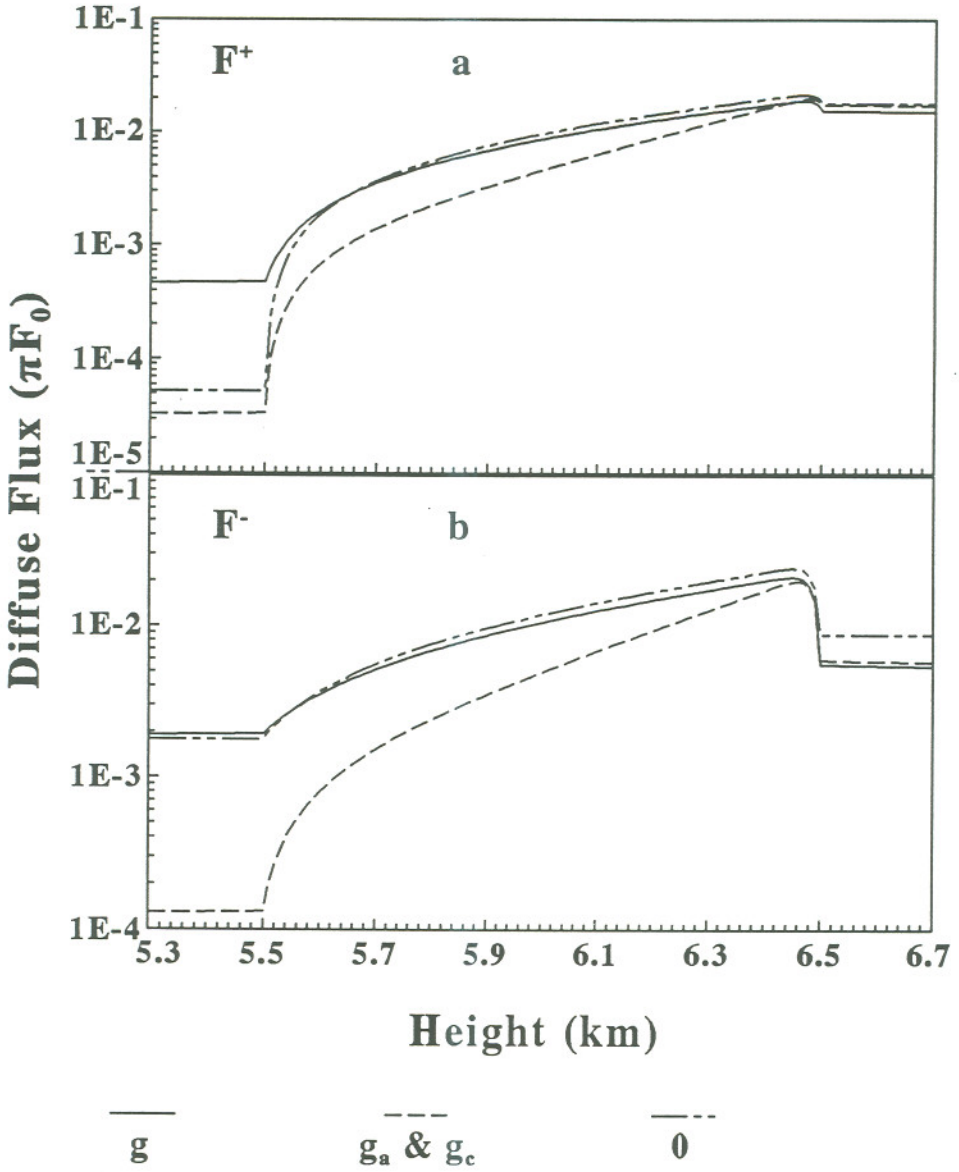

Fig. 4.16 Comparison of the diffuse fluxes, F^+ and F^- (units relative to the extraterrestrial flux, πF_0), calculated by using the atmospheric asymmetry factor, g, with those calculated by using the asymmetry factor of the atmospheric aerosols, g_a, outside the vertically uniform altostratus cloud and the asymmetry factor of the cloud drops, g_c, inside the cloud, as well as with those calculated by using zero asymmetry factor for all heights both inside and outside the cloud within *295~300* nm at *0°*.

causes less radiative energy transferring downward, leading to lower diffuse fluxes appearing at all heights below the very upper part of the cloud compared to the actual diffuse fluxes, as shown in figs. 4.16a and 4.16b.

For the large zenith angle, 86°, as shown in fig. 4.17, using the overestimated asymmetry factor would increase the downward diffuse flux within 295~300 nm wavelength compared to the actual downward diffuse flux for all heights inside cloud due to the long traversing path. The higher downward diffuse flux also increases the upward diffuse flux due to multiple scattering of the droplets of a vertically uniform cloud compared to the actual upward diffuse flux for almost all the heights inside the cloud except the very lower part of the cloud, where the upward diffuse flux would be smaller than the actual upward diffuse flux due to the weak backscattering. For the similar reason for those at 0° zenith angle, the diffuse fluxes, both upward and downward, calculated with zero asymmetry factors, would be lower than those calculated with the actual asymmetry factor for the almost all heights except at the very upper part of the atmosphere, where the diffuse fluxes calculated with zero asymmetry factor are higher than the actual diffuse fluxes, as shown in figs. 4.17a and 4.17b.

After discussing the effects of the diffuse fluxes on the actinic fluxes (fig. 4.15) and the influences of the variation of the asymmetry factors on the diffuse fluxes (figs. 4.16 and 4.17), we can now answer the question about how large the error would be in the calculation of the radiation field for a cloud if the correct asymmetry factor is not used. In this study, the actinic fluxes were calculated by using five types of the asymmetry factors for examining the effect of the asymmetry factor on the radiation field. It is convenient to label

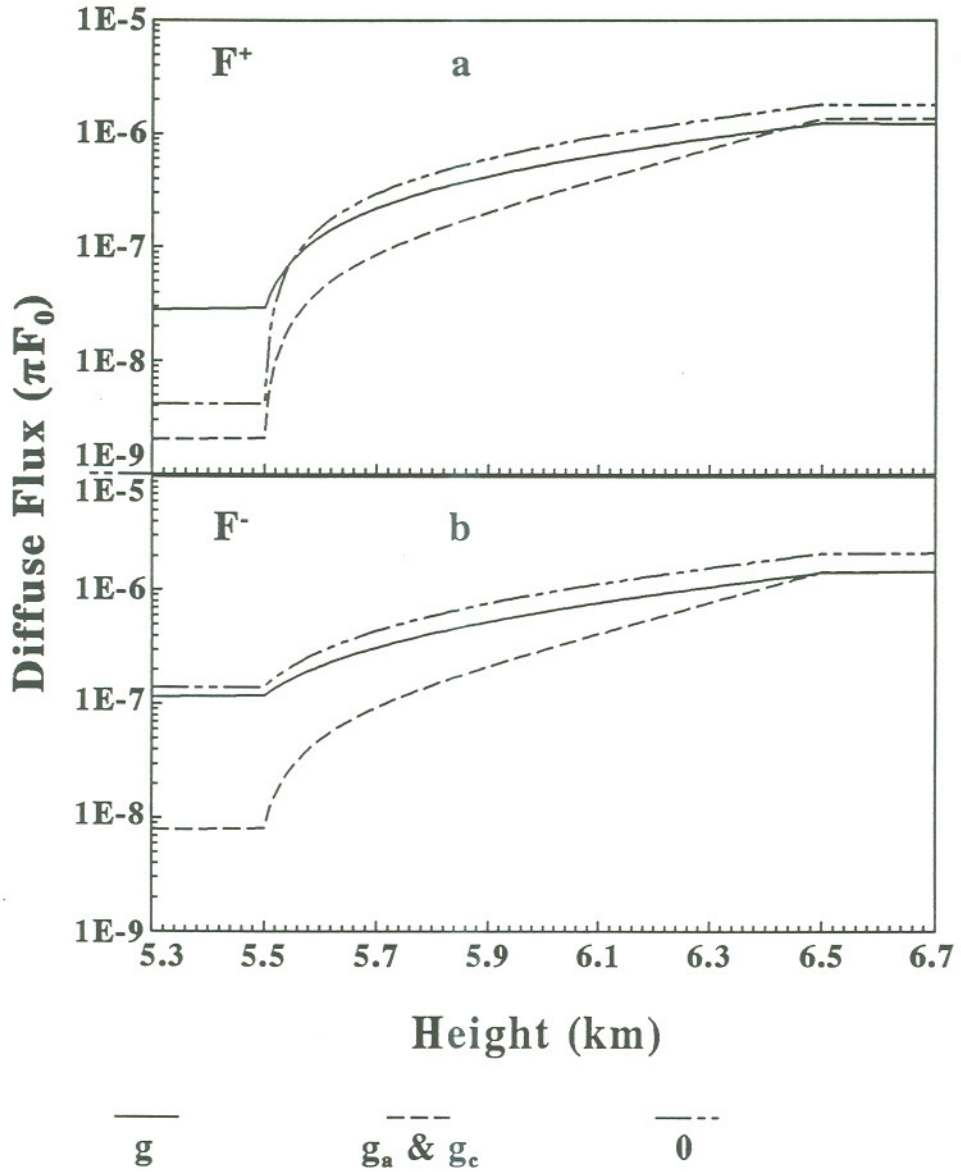

Fig. 4.17 Comparison of the diffuse fluxes, F^+ and F^- (units relative to the extraterrestrial flux, πF_0), calculated by using the atmospheric asymmetry factor, g, with those calculated by using the asymmetry factor of the atmospheric aerosols, g_a, outside the vertically uniform altostratus cloud and the asymmetry factor of the cloud drops, g_c, inside the cloud, as well as with those calculated by using zero asymmetry factor for all heights both inside and outside the cloud within *295~300* nm at *86°*.

the actinic fluxes calculated with different types of the asymmetry factors as: 1) J, the correct actinic flux calculated with the correct asymmetry factor, the atmospheric asymmetry factor, for both inside clouds and outside clouds; 2) J_0, the actinic fluxes calculated by replacing only the atmospheric asymmetry factor inside a cloud with zero asymmetry factor; 3) J_{00}, the actinic fluxes calculated with zero asymmetry factor both inside and outside the cloud; 4) J_g, the actinic fluxes calculated by replacing only the atmospheric asymmetry factor inside the cloud with the asymmetry factor of the cloud droplets; 5) J_{gg}, the calculated actinic fluxes by replacing the atmospheric asymmetry factor with the asymmetry factor of the cloud droplets inside the cloud and with the asymmetry factor of the atmospheric aerosols outside the cloud. It should be noted that the asymmetry factors of drops and aerosols are calculated from eq. 4.27b and are independent of height, while the atmospheric asymmetry factors, calculated from eq. 4.33b, depends on height, as shown in figs. fig. 4.7 and 4.13. For easy recognition the magnitude of the error in estimate of the actinic flux with the incorrect asymmetry factor, the relative error is defined as:

$$\varepsilon_x = \frac{J_x - J}{J}$$

where ε_x represents the relative error of J_x; x designates 0, or 00, or g, or gg; J_x corresponds to J_0, J_{00}, J_g, and J_{gg}.

Fig. 4.18 shows the vertical profiles of the relative errors for three different hypothetical altostratus clouds, *uni*, *va6*, and *va8*, with the same amount of the total liquid water content inside clouds but different vertical structures for zenith angles equal to 0° and 86° within 295~300 nm. The relative error of J_g is less than or about 1%, for all types of

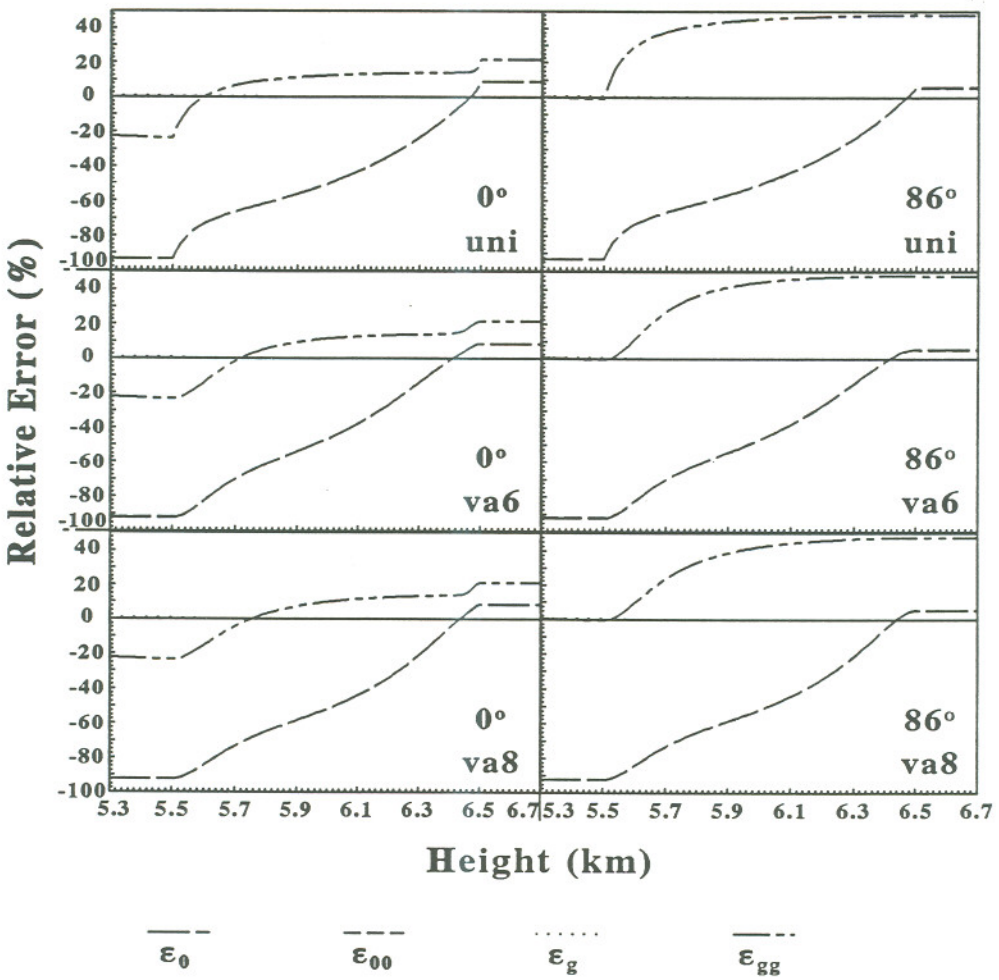

Fig. 4.18 Vertical profiles of the relative errors for three different hypothetical altostratus clouds, *uni*, *va6*, and *va8*, with the same amount total liquid water content inside clouds but different vertical structures for zenith angles equal to *0°* and *86°* within *295~300* nm. See the text for the definitions of the legend names.

clouds and zenith angles, indicating that replacing the atmospheric asymmetry factor inside a cloud with the asymmetry factor of cloud drops and keeping the atmospheric asymmetry factor outside the cloud results in little error in estimate of the actinic flux. This is understandable since the difference between the atmospheric asymmetry factor and the asymmetry factor of drops inside cloud is very small for all heights inside the uniform cloud and for almost all heights inside the non-uniform cloud, as shown in fig. 4.13. Although the difference between the atmospheric asymmetry factor and the asymmetry factor of drops at the edges of the non-uniform cloud is very large, as shown in fig. 4.13, the relative error of J_g near the cloud edges is very small since the radiative fluxes at the cloud edges are controlled by the accumulation of radiative energy produced around the edges. However, the relative errors of J_{gg}, J_0, and J_{00} (J_0 and J_{00} are overlapped one another in the fig. 4.18) are significant. The relative error of J_{gg} decreases from more than +20% at the cloud top to less than -20% at the cloud bottom at 0° zenith angle, and it decreases from about 50% at the cloud top to almost zero value at the cloud bottom, while the relative errors of J_0 and J_{00} decrease from less than +10% from the cloud top to less than -90% at the cloud bottom for both small and large zenith angles, as shown in fig. 4.18. Comparing fig. 4.18 with figs. 4.15~4.17, one can easily conclude that the vertical large variations of the relative errors result from the related changes of diffuse fluxes due to the variation of the asymmetry factor. It should be noted that the vertical profiles of the relative errors for both the vertically uniform cloud and the vertically non-uniform cloud are basically the same although one can see that the relative errors change more smoothly around the cloud edges for the vertically non-uniform cloud than for the vertically uniform cloud.

4.6 Summary

The optical properties of air molecules, aerosols, and cloud droplets have been studied in detail. Generally, in the ultraviolet and visible wavelengths (290~700 nm), the effect of O_3 absorption dominates that of molecular scattering for wavelength less than 310 nm, and the influence of molecular scattering is larger than that of O_3 absorption for wavelength larger than 310 nm. The effect of aerosol scattering becomes important for $\lambda \geq 500$ nm. The influence of clouds is substantially larger. For example, the effects of the optical thickness of one-km dense stratus is much larger than total thickness of molecular scattering, aerosol scattering and absorption, and O_3 absorption for the whole atmosphere.

The asymmetry factor, one of the highlights of this study, along with other important quantities dealing with Mie scattering problems, has been studied in detail for various atmospheric conditions. All the complex functions including Legendre functions and Ricatti-Bessel functions are expanded into a series of sine and cosine functions. The expression of the atmospheric asymmetry factor have been theoretically derived based on the definition of the asymmetry factor and Mie theory, and numerical scheme to calculate the asymmetry factor has been described in detail. The distinction between the atmospheric asymmetry factor and the asymmetry factor of various types of atmospheric scatterers was shown in this study. The asymmetry factor of a certain type of scatterers, which represents the relative strength of the forward scattering for this type of scatterers, relies on the size distribution, the number density, and the optical properties of this type of scatterers. In contrast, the atmospheric asymmetry factor at a given height, which corresponds to the relative intensity

of the forward scattering of all types of scatterers at this height, depends on the physical states and optical properties of all kinds of the atmospheric scatterers, and it changes not only with wavelength but also with height.

According to the computation, the atmospheric asymmetry factor for a clear urban atmosphere increases with wavelength in the ultraviolet and visible range due to the slight increase of the strength of Mie scattering and the decrease of the strength of Raleigh scattering with wavelength. Unlike the asymmetry factor of the atmospheric aerosols, the atmospheric asymmetry factor for a clear urban atmosphere changes significantly with height, especially in the troposphere and lower stratosphere below 25 km above the earth's atmosphere, resulting from the different vertical profiles of two major scatterers in atmosphere, air molecules and atmospheric aerosols. Specifically the atmospheric asymmetry factor decreases rapidly with height in the lower and middle troposphere corresponding to the quicker decrease of the number density of atmospheric aerosols with height compared to that of the air molecules, and it increases with height around tropopause and in lower stratosphere resulting from the accumulation of the atmospheric aerosols due to the volcanic eruptions and airplane injections. The atmospheric asymmetry inside various types of clouds with different macro-structures are also studied. The asymmetry factors near the cloud edges inside the vertically non-uniform clouds also change greatly with height resulting from the relative strengths among the scattering processes of air molecules, atmospheric aerosols, and drops inside the cloud.

It should be emphasized again that the atmospheric asymmetry factor is never equal to the asymmetry factor of the atmospheric aerosols or that of cloud droplets, even at the

earth's surface where the atmospheric asymmetry factor in a clear urban atmosphere, for example, is equal to 0.545 in the wavelength 290~295 while the asymmetry factor of the atmospheric aerosols is 0.948, which is 74% larger than the atmospheric asymmetry factor! Assuming that the actual asymmetry factor is equal to the asymmetry factor of any type of scatterers of the atmosphere (such as aerosols) can lead to large error in estimating the radiation field for photochemical model calculation. For example, the replacement of the atmospheric asymmetry factor with the asymmetry factor of the aerosol particles would lead to more than 100% overestimate of the actinic flux at the earth's surface around 300 nm for a clear urban atmosphere. For a cloudy condition, inappropriate replacement of the atmospheric asymmetry factor with the asymmetry factor of atmospheric aerosols outside a cloud and with the asymmetry factor of cloud drops inside the cloud would also result in significantly large error in the estimates of the actinic fluxes at different heights, especially near the cloud top and base.

CHAPTER 5 RADIATIVE TRANSFER UNDER VARIOUS ATMOSPHERIC CONDITIONS

After discussions of the optical properties such as the cross sections, the asymmetry factors, and the normal optical properties of various atmospheric components including air molecules, ozone gas, atmospheric aerosol particles, and cloud droplets for different atmospheric conditions, it is time for me to address the radiative transfer in various atmospheric conditions. The focus in this study is on how the radiation field affects the atmospheric chemistry. Only the radiation within ultraviolet and visible wavelength will be discussed in this chapter since almost all the atmospheric chemical reactions are initiated by the radiation in these wavelengths. Thus the topic of the radiative transfer at infrared wavelength is not included here.

This chapter begins with a general introduction to the sun, which is our primary source of radiation, and basic concepts of radiative transfer. Then the radiative transfer model developed in this study is described in detail so that readers may reproduce or modify the method. In the next, the variations of the radiation fields for various atmospheric conditions, calculated by using the radiative transfer model, are discussed. Finally the important points will be summarized.

5.1 General Introduction and Basic Concepts

The sun, formed almost 4.6 billion years ago, is a gaseous sphere with a radius about 6.95×10^{35} g. It mainly contains hydrogen ($\sim$ 75% of its total mass) and helium ($\sim$ 25%) plus a small amount of heavier elements such as iron, silicon, neon, and carbon. The temperature of the sun decreases from about 5×10^{6} °K at the center to 5800 °K at the surface. The source of solar energy comes from the fusion conversion from four hydrogen atoms to one helium.

Located 1.5×10^{8} km from the earth's surface, the sun is about 3×10^{5} times closer to us than the next nearest star. Virtually all the energy that reaches the earth from space is in the form of solar electromagnetic radiation. The intensity of solar radiation in the earth's atmosphere depends on the solar surface activities such as sunspots, the rotation of the earth, and the earth's atmospheric constituents.

Outside the earth's atmosphere, the solar radiation can be approximated as blackbody emission at 6000 °K. Inside the atmosphere, the solar radiation intensity changes with times of day, latitude, and season, and is also greatly affected and reduced by absorption, scattering, and reflection processes of various atmospheric constituents including O_3, air molecules density, aerosols, and water drops in clouds, and the optical properties of these compositions such as the refractive indexes and size distributions of aerosols and drops, and the locations and macro-structures of clouds. Fig. 5.1 compares the spectral irradiance distributions at the top of the atmosphere and sea level for a clear atmosphere, illustrating the attenuation of the absorption and scattering processes by various atmospheric

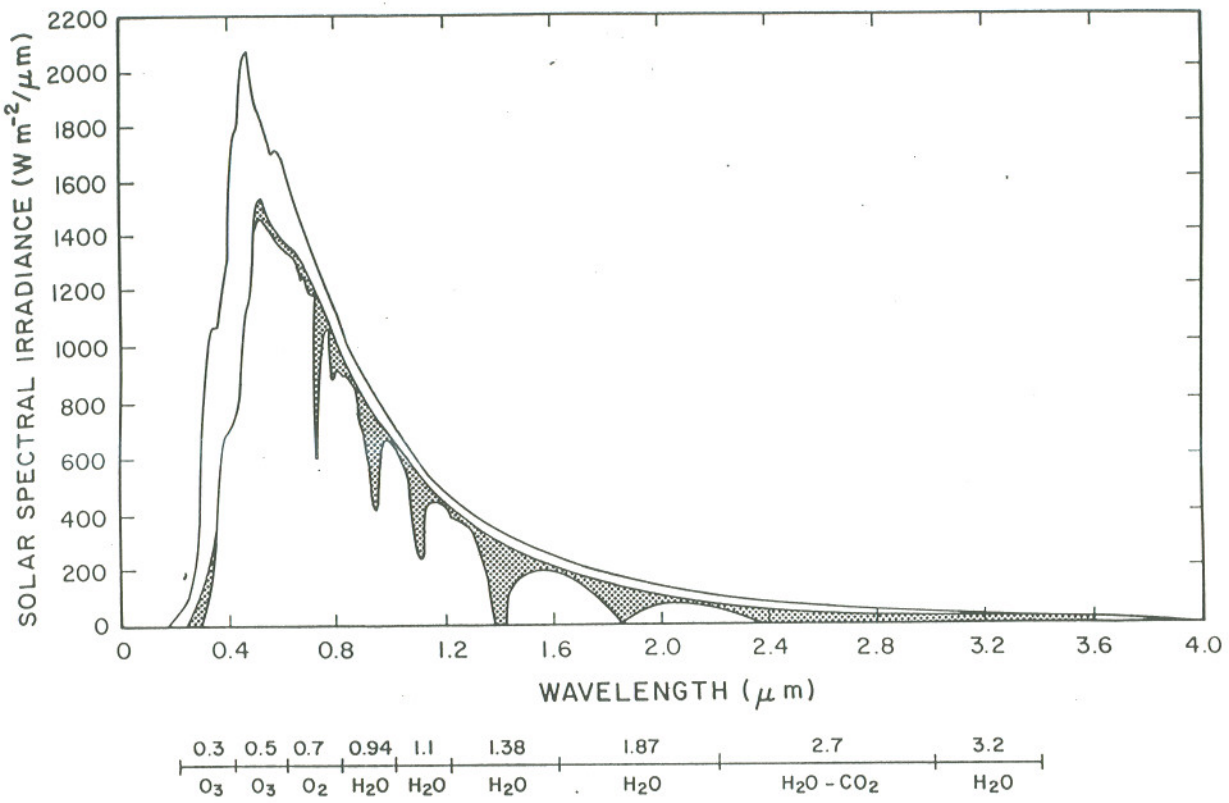

Fig. 5.1 The spectral irradiance distributions at the top of the atmosphere (the top curve) and at the sea level (the bottom curve) for a clear atmosphere, adapted from Liou (1980). The shaded areas represent absorption due to various gases in the clear atmosphere, and the outer envelope of the shaded areas denotes the reduction of solar irradiance due to scattering.

components.

The radiative transfer in the atmosphere is a very complicated process. On the one hand, the direct solar insolation is attenuated by absorption and scattering of various atmospheric components in the path through which the solar beam passes down to the earth's surface, and by reflection of the earth's surface. On the other hand, the intensity of radiative energy may be strengthened by emission as well as multiple scattering from other particles and directions. In addition, the intensity of radiative energy is greatly affected by relative position between the sun and the earth, or the observation point of the earth, precisely. Mathematically, the radiative transfer in the earth's atmosphere can be seen as that in a plane parallel scattering atmosphere, which is described by the general equation of radiative transfer:

$$\mu \frac{dI_\lambda(\tau,\theta,\phi)}{d\tau} = I_\lambda(\tau,\theta,\phi) - J_\lambda(\tau,\theta,\phi) \tag{5.1}$$

where λ denotes wavelength λ; $\mu = cos\theta$, and θ and ϕ are zenith and azimuth angles, which identify the direction of propagation of radiative intensity; τ is the normal optical depth; I_λ is the radiation intensity, or radiance at wavelength λ (erg cm^{-2} sec^{-1} sr^{-1}); J_λ is called the source function, which can be further expressed as:

$$\begin{aligned} J_\lambda(\tau,\mu,\phi) = {} & \frac{\omega_0}{4\pi}\int_0^{2\pi}\int_{-1}^{1} I_\lambda(\tau,\mu',\phi')P(\mu,\phi,\mu',\phi')d\mu'd\phi' \\ & + \frac{\omega_0}{4\pi}\pi F_0 P(\mu,\phi,-\mu_0,\phi_0)e^{-\tau/\mu_0} \end{aligned} \tag{5.2}$$

Note a negative (positive) sign before μ designates the radiation traveling in the downward

(upward) direction. A subscript *0* for μ and ϕ represents the direction of propagation of the incident radiative beam; $P(\mu,\phi,\mu',\phi')$ is the phase function for the radiative energy scattered from the direction (μ',ϕ') into the direction (μ,ϕ); ω_0 is the single-scattering albedo.

For most atmospheric problems representing the real atmosphere, an exact equation of radiative transfer is not possible. A number of numerical techniques have been developed to calculate the radiation field with sufficient accuracy for most purposes (For an overview of various methods, see Lenoble, 1985). Methods have also been developed to determine the radiation field to study atmospheric chemistry (e.g., Leighton, 1961; Braslau and Dave, 1973; Lacis and Hansen, 1974; Liou, 1974; Turco, 1975; Yung, 1976; Isaksen et al., 1977; Wiscombe, 1977; Fiocco et al., 1978; Meier et al., 1978, 1982; Mugnai et al., 1979; Anderson and Meier, 1979; Demerjian et al., 1980; Luther, 1980; Meador and Weaver, 1980; Pitari and Visconti, 1980; Nicolet et al., 1982; Thompson, 1984; Madronich, 1987; Stamnes et al., 1988; Hough, 1988; Toon et al., 1989; and references therein). Despite the complicated radiative transfer process, schemes for fast computation of radiative transfer have been reported by many researchers for the modeling of the atmospheric chemistry (e.g. Thompson, 1984; Madronich, 1987; Hough, 1988; Toon et al., 1989; and references therein).

However, the previous studies were either limited to a particular situation of radiative transfer [e.g. Luther and Gelinas (1976) for Rayleigh scattering; Fiocco et al. (1978) for aerosols; Madronich (1978) for clouds] or used a very complicated model with heavy time consuming calculation that is difficult for others to use (e.g. Demerjian et al.,

1980). We have developed a detailed radiative transfer model to calculate the field of actinic fluxes for different time, location, and various atmospheric conditions including the effects of aerosols and different types of clouds (Lu and Khalil, 1992b). The numerical technique of our model is built upon the rapid multiple two-stream model described by Toon et al. (1989). Thus the first purpose of this chapter is to clearly address the topics not only on the numerical solution to the general equation of radiative transfer, eq. 5.1, but also on how to use the fast computation technique effectively to estimate the radiative transfer for various realistic atmospheric problems, and the latter is rarely concerned in the previous studies. Furthermore, how to incorporate the key elements such as the normal optical depths, single scattering albedos, and the asymmetry factors, as described in the previous chapter (Also see Lu and Khalil, 1992b and 1993b), into the radiative transfer model is a focus of this study, and the methods to calculate the irradiances and the actinic fluxes for different locations, times, and scenarios are described in detail for readers to reproduce or modify the calculation for their own researches.

Another major purpose of this study is to give a full explanation of physical meaning of all fluxes in the UV and visible wavelengths from 290 to 700 nm in terms of effects of the ozone absorption, aerosol scattering and absorption, and the scattering of cloud droplets, with special focus on the strong and zero ozone absorption ranges (e.g. 290~300 & 395~400 nm) as well as the weak Rayleigh scattering and O_3 absorption wavelength (e.g. 680~700 nm). Previous publications lack the interpretation of the physical meaning of the variations of the actinic fluxes. One of the purposes in this chapter is to distinguish between the irradiance and actinic flux for all heights, and different wavelengths and zenith angles.

There were some previous papers discussing the difference between the irradiance and actinic flux (e.g. Demerjian et al., 1980; Madronich, 1987), but none of them showed the magnitude of the difference in the atmosphere in terms of the variations of wavelength, zenith angle, altitude, and various atmospheric conditions. As one highlight of this chapter, the effects of clouds on the radiation field are studied in detail. The feedbacks of the physical states of clouds including cloud locations and types, size distributions and number densities of cloud drops, and the macro-structures of clouds on actinic fluxes are calculated, analyzed, and tested.

5.2 Numerical Method

Although exact analytic solutions to eq. 5.1 for practical or realistic atmospheric problems are not known, a number of techniques have been developed and derived from the general equation of radiative transfer to calculate the radiation field with sufficiently high accuracy. Among these physical and numerical approaches, the two-stream approximation has been commonly used. The technique is to determine the radiative transfer by simply converting the radiative field into two stream with opposite direction: downward and upward. It provides a rapid computational scheme with a relatively high accuracy for the most of the radiative problems. Due to different numerical treatments and applications, there have been different forms of two-stream techniques such as the quadrature, Eddington, and Delta function. Meador and Weaver (1980) showed that all existing two-stream approximations can be represented by identical forms of coupled differential equations by integrating the radiative intensity over hemispheres. Toon et al.

(1989) developed an algorithm suitable for computing radiative field in inhomogeneous multiple scattering atmospheres by deriving a tri-diagonal matrix solution for multiple layers based on a number of the generalized two-stream solutions (Meador and Weaver, 1980).

As shown in fig. 4.1 in the previous chapter, the atmosphere is divided into N layers. Based on Beer's law, the direct radiative flux, F_i^d, which is in the downward direction, can be expressed as:

$$F_i^d = \pi F_0 \mu_0 \exp[-\sum_{j=1}^{i} \tau_j/\mu_0] \qquad i = 0,\ 1,\ 2,\ \cdots,\ N \tag{5.3}$$

where πF_0 is the extraterrestrial flux, or the solar flux at the top of the atmosphere. At the top of the atmosphere, there is no downward diffuse flux; i.e.,

$$F_1^-(0) = 0 \tag{5.4a}$$

At the bottom of the atmosphere, or at the earth's surface, the upward diffuse flux is equal to the reflected downward flux including both the direct flux and the diffuse flux:

$$F_N^+(\tau_N) = r_s\{F_N^-(\tau) + F_N^d\} = r_s\{F_N^-(\tau_N) + \pi F_0 \mu_0 \exp[-\sum_{j=1}^{N} \tau_j/\mu_0]\} \tag{5.4b}$$

where r_s is the reflectivity at the earth's surface. The diffuse flux at each level in each layer within the atmosphere should satisfy the condition of flux continuity:

$$F_i^+(\tau_i) = F_{i+1}^+(0)$$
$$F_i^-(\tau_i) = F_{i+1}^-(0) \qquad i = 1,\ 2,\ \cdots,\ N-1 \qquad (5.4c)$$

where superscript + represents the direction of the diffuse flux is upward and superscript - denotes the direction of the diffuse flux is downward.

Within each of the N homogeneous layers, the diffuse flux can be expressed by the two-stream approximation (Meador and Weaver, 1980; Toon et al., 1989). Generally within the ith layer (the layer between level i-1 and level i), the two-stream approximations are:

$$\frac{\partial F_i^+}{\partial \tau_{ia}} = \gamma_{1i} F_i^+ - \gamma_{2i} F_i^- - S_i^+$$
$$\frac{\partial F_i^-}{\partial \tau_{ia}} = \gamma_{2i} F_i^+ - \gamma_{1i} F_i^- + S_i^- \qquad i = 1,\ 2,\ \cdots,\ N \qquad (5.5a)$$

where τ_{ia} is the normal optical depth at any point within the ith layer and $0 \le \tau_{ia} \le \tau_i$, where τ_i is the total optical depth of the ith layer. Using the quadrature technique (Meador and Weaver, 1980; Toon et al., 1989), then

$$\gamma_{1i} = 3^{1/2}[2 - \omega_{0i}(1 + g_i)]/2$$
$$\gamma_{2i} = 3^{1/2}\omega_{0i}(1 - g_i)/2$$
$$\gamma_{3i} = [1 - 3^{1/2} g_i \mu_0]/2$$
$$\gamma_{4i} = 1 - \gamma_{3i} \qquad i = 1,\ 2,\ \cdots,\ N \qquad (5.5b)$$
$$S_i^+ = \gamma_{3i} \pi F_0 \omega_{0i} \exp[-(\sum_{j=1}^{i-1} \tau_j + \tau_{ia})/\mu_0]$$
$$S_i^- = \gamma_{4i} \pi F_0 \omega_{0i} \exp[-(\sum_{j=1}^{i-1} \tau_j + \tau_{ia})/\mu_0]$$

where ω_{0i} is the averaged single scattering albedo, and g_i is the averaged asymmetry factor in the ith layer.

Toon et al. (1989) derived a set of stable expressions of diffuse fluxes by modifying the general solution of the two-stream equations, eq. 5.5a:

$$\begin{aligned} F_i^+(\tau_{ia}) &= Y_{1,i}\{\exp[-\alpha_i(\tau_i-\tau_{ia})]+\beta_i\exp(-\alpha_i\tau_{ia})\} \\ &\quad +Y_{2,i}\{\exp[-\alpha_i(\tau_i-\tau_{ia})]-\beta_i\exp(-\alpha_i\tau_{ia})\}+C_i^+(\tau_{ia}) \\ F_i^-(\tau_{ia}) &= Y_{1,i}\{\beta_i\exp[-\alpha_i(\tau_i-\tau_{ia})]+\exp(-\alpha_i\tau_{ia})\} \\ &\quad +Y_{2,i}\{\beta_i\exp[-\alpha_i(\tau_i-\tau_{ia})]-\exp(-\alpha_i\tau_{ia})\}+C_i^-(\tau_{ia}) \end{aligned} \tag{5.6a}$$

where the coefficients, α_i, β_i, and $C^{\pm}{}_i(\tau_{ia})$ are expressed as follows:

$$\begin{aligned} \alpha_i &= (\gamma_{1i}^2-\gamma_{2i}^2)^{1/2} \\ \beta_i &= \frac{\gamma_{2i}}{\gamma_{1i}+\alpha_i} = \frac{\gamma_{1i}-\alpha_i}{\gamma_{2i}} \\ C^+(\tau_{ia}) &= \frac{\omega_{0i}\pi F_0\exp[-(\sum_{j=0}^{i-1}\tau_j+\tau_{ia})/\mu_0][(\gamma_{1i}-1/\mu_0)\gamma_{3i}+\gamma_{4i}\gamma_{2i}]}{\alpha_i^2-1/\mu_0^2} \\ C^-(\tau_{ia}) &= \frac{\omega_{0i}\pi F_0\exp[-(\sum_{j=0}^{i-1}\tau_j+\tau_{ia})/\mu_0][(\gamma_{1i}+1/\mu_0)\gamma_{4i}+\gamma_{3i}\gamma_{2i}]}{\alpha_i^2-1/\mu_0^2} \end{aligned} \tag{5.6b}$$

Substituting the above equations back to *2N* boundary conditions, eqs. 5.4a~c, a set of *2N* linear equations are formed. After some algebraic combinations and eliminations, the set of equations are converted into a set of linear equations with a tri-diagonal matrix (Toon et al., 1989), which can be expressed as follows:

$$\begin{bmatrix} B_{1,1} & C_{1,1} & & & & & & & & \\ A_{2,1} & B_{2,1} & C_{2,1} & & & & & & & \\ & \cdots & & \cdots & & & & & & \\ & & & A_{1,i} & B_{1,i} & C_{1,i} & & & & \\ & & & & A_{2,i} & B_{2,i} & C_{2,i} & & & \\ & & & & & \cdots & & \cdots & & \\ & & & & & & & A_{1,N} & B_{1,N} & C_{1,N} \\ & & & & & & & & A_{2,N} & B_{2,N} \end{bmatrix} \begin{bmatrix} Y_{1,1} \\ Y_{2,1} \\ \cdots \\ Y_{1,i} \\ Y_{2,i} \\ \cdots \\ Y_{1,N} \\ Y_{2,N} \end{bmatrix} = \begin{bmatrix} D_{1,1} \\ D_{2,1} \\ \cdots \\ D_{1,i} \\ D_{2,i} \\ \cdots \\ D_{1,N} \\ D_{2,N} \end{bmatrix} \tag{5.7a}$$

where the coefficients can be expressed as follows:

$$\begin{aligned} &B_{1,1} = e_1^+; \qquad C_{1,1} = -e_1^-; \qquad D_{1,1} = -C_1^-(0); \\ &A_{1,i} = e_i^- f_i^+ - e_i^+ f_i^-; \qquad B_{1,i} = e_i^+ e_{i+1}^+ - f_i^+ f_{i+1}^+; \qquad C_{1,i} = f_i^+ f_{i+1}^- - e_i^+ e_{i+1}^-; \\ &D_{1,i} = f_i^+ [C_{i+1}^+(0) - C_i^+(\tau_i)] + e_i^+ [C_i^-(\tau_i) - C_{i+1}^-(0)]; \qquad i = 2,\ 3,\ \cdots,\ N \end{aligned} \tag{5.7b}$$

$$\begin{aligned} &A_{2,N} = e_N^+ - r_s f_N^+; \qquad B_{2,N} = e_N^- - r_s f_N^-; \qquad D_{2,N} = r_s F_N^d - C_N^+(\tau_N) + r_s C_N^-(\tau_N) \\ &A_{2,i} = e_i^+ e_{i+1}^- - f_i^+ f_{i+1}^-; \qquad B_{2,i} = e_i^- e_{i+1}^- - f_i^- f_{i+1}^-; \qquad C_{2,i} = e_{i+1}^+ f_{i+1}^- - e_{i+1}^- f_{i+1}^+ \\ &D_{2,i} = e_{i+1}^- [C_{i+1}^+(0) - C_i^+(\tau_i)] + f_{i+1}^- [C_i^-(\tau_i) - C_{i+1}^-(0)] \qquad i = 1,\ 2,\ \cdots,\ N-1 \end{aligned} \tag{5.7c}$$

$$\begin{aligned} e_i^\pm &= 1 \pm \beta_i \exp(-\alpha_i \tau_i) \\ f_i^\pm &= \beta_i \pm \exp(-\alpha_i \tau_i) \end{aligned} \tag{5.7d}$$

By solving the equation set, eqs. 5.7a~d, a set of $Y_{1,i}$ and $Y_{2,i}$ are obtained. Thus the diffuse fluxes upward and downward at each level can be expressed as:

$$\begin{aligned} F_i^+(\tau_i) &= Y_{1,i} e_i^+ + Y_{2,i} e_i^- + C_i^+(\tau_i) \\ F_i^-(\tau_i) &= Y_{1,i} f_i^+ + Y_{2,i} f_i^- + C_i^-(\tau_i) \end{aligned} \tag{5.8}$$

and the total radiative flux (irradiance) in the downward direction and actinic flux at each

level are:

$$F_{net}(\tau_i) = \int \mu I d\Omega = F_i^d - F_i^+(\tau_i) + F_i^-(\tau_i)$$
$$J_i(\tau_i) = \int I d\Omega = [F_i^+(\tau_i) + F_i^-(\tau_i)]/\mu_1 + F_i^d/\mu_0 \quad (5.9)$$

where μ_1 is a weighed factor for the integral, and $\mu_1 = 3^{-1/3}$ (Toon et al., 1989). Instead of simply using $sec\theta$, a formula of air mass, μ_0, is taken from Liu and Liu (1990) to take into account the effect of atmospheric curvature and refraction of atmosphere; i.e.,

$$m = \mu_0^{-1} = [\cos\theta_0 + 0.15(93.885 - \theta_0)^{-1.253}]^{-1} \quad (5.10)$$

where θ_0 is the solar zenith angle, which can be further expressed as the functions of some known angles: the solar inclination, the latitude, and the hour angle, as shown in eq. 2.32. Fig. 5.2 shows the values of μ_0, calculated from $sec\theta_0$, and calculated from eq. 5.10, and their relative difference, and related values are listed in table 5.1. From the figure, one can see that the μ values corrected based on the atmospheric curvature and refraction are not much different from those using simple cosine of zenith angle for the zenith angles less than 80°; however, the relative difference between the two μ values becomes significant for the zenith angles larger than 80°. This indicates that using of corrected μ values is very important to estimate the radiative transfer at sunrise and sunset.

It seems straight-forward that the actinic flux and radiative flux can be obtained by just solving the above equations. There are complications, however. In order to use the two-stream approximation, one has to know the parameters: the normal optical depth, the single scattering albedo, and the asymmetry factor. These parameters change with time, location, composition, and volume of the atmosphere, and the physical state and optical

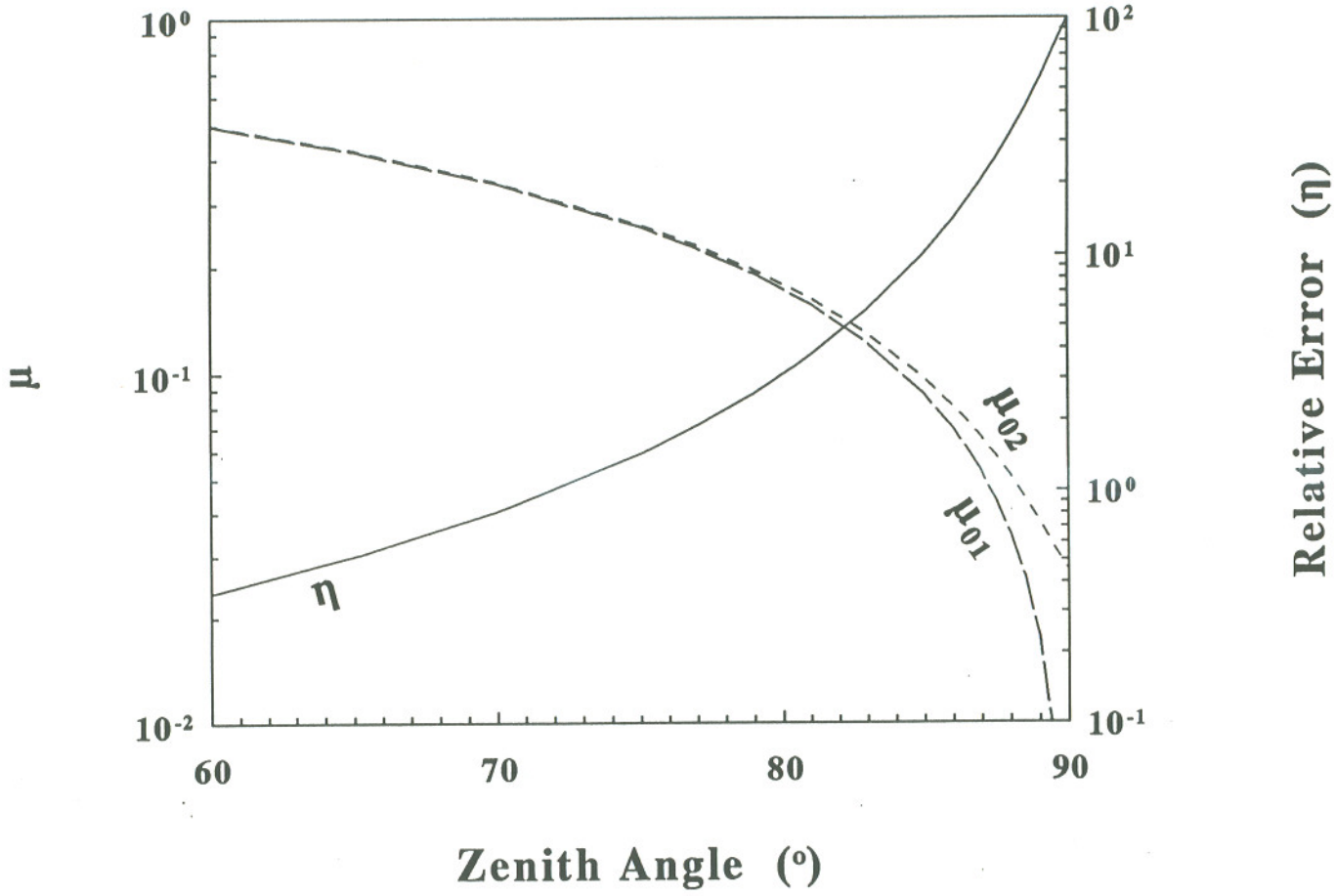

Fig. 5.2 Variations of μ_0 with zenith angle, where $\mu_{01}=\cos\theta_0$; $\mu_{02}=\cos\theta_0+0.15(93.885-\theta_0)^{-1.253}$; $\eta=(\mu_{02}-\mu_{01})/\mu_{02}$. See eq. 5.10 and text for more information.

Table 5.1 μ_0 Values for Various Zenith Angles: (a) Calculated from $cos\theta_0$ and (b) Calculated from eq. 5.10, and Relative Difference between the Two μ_0 Values:

Zenith Angle θ	μ_{01} [a]	μ_{02} [b]	η [c]
0	1.000	1.000	0.051
10	0.985	0.985	0.059
20	0.940	0.940	0.073
30	0.866	0.867	0.095
40	0.766	0.767	0.13
50	0.643	0.644	0.20
60	0.500	0.502	0.36
70	0.342	0.345	0.82
80	0.174	0.179	3.1
90	0.000	0.0274	100

where θ_0 is the solar zenith angle; μ_{01} and μ_{02} are μ values calculated respectively form the cosine of the zenith angle and from eq. 5.10, as shown in the following notes; η is the relative error of μ values without correction for atmospheric curvature and refraction.

---

[a] $\mu_{01} = \cos\theta_0$

[b] $\mu_{02} = \cos\theta_0 + 0.15(93.885 - \theta_0)^{-1.253}$ (5.10)

[c] $\eta = \dfrac{|\mu_{01} - \mu_{02}|}{\mu_{02}} \times 100$

characteristics of the different constituents of the atmosphere. Specifically the normal optical depth in the *i*th layer is the sum of the normal optical depths from the absorption of O_3 ($\tau_{a,i}^{o}$), the molecular scattering ($\tau_{s,i}^{m}$), the absorption and scattering of aerosols ($\tau_{a,i}^{a}$) and ($\tau_{s,i}^{a}$), and scattering of drops of clouds ($\tau_{s,i}^{c}$); i.e.,

$$\tau_i = \tau_{a,i}^{o} + \tau_{s,i}^{m} + \tau_{a,i}^{a} + \tau_{s,i}^{a} + \tau_{s,i}^{c} \tag{5.11a}$$

$$\tau_{x,i}^{y} = \int_{z_{i-1}}^{z_i} \sigma_{x,i}^{y} N_y dz = \sigma_{x,i}^{y} [N_y(Z_i) \cdot N_y(Z_{i-1})]^{1/2} \cdot (Z_{i-1} - Z_i) \tag{5.11b}$$

where the x in the subscript x,i is either a or s, representing absorption or scattering; the superscript or the subscript y corresponds to m, o, a, or c, denoting air molecules, ozone, aerosol, or drops in clouds; σ is the cross section of the above atmospheric components for either absorption or scattering; N_y is the number density of the atmospheric component y. Here the cross section for Raleigh (molecular) scattering and O_3 absorption are respectively taken from WMO (1985) and Demerjian et al. (1980); the cross sections for aerosol absorption and scattering, and for the scattering of drops in clouds were calculated by following the numerical method described in detail in the previous chapter, based on Mie theory.

The single-scattering albedo is defined as the ratio of the scattering coefficient to extinction (scattering plus absorption) coefficient (Liou, 1980). In the *i*th layer (between the *i-1*th and *i* levels), the averaged single scattering albedo can be further expressed as the ratio of the total scattering normal optical depth ($\tau_{s,i}$) to the total extinction normal optical

depth in this layer (τ_i):

$$\omega_{0i} = \frac{\tau_{s,i}}{\tau_i} = \frac{\tau_{s,i}^m + \tau_{s,i}^a + \tau_{s,i}^c}{\tau_{a,i}^o + \tau_{s,i}^m + \tau_{a,i}^a + \tau_{s,i}^a + \tau_{s,i}^c} \tag{5.12}$$

The asymmetry factor is also an important parameter to determine the radiation field. It is defined as the first moment of the phase function, and from eq. 4.22

$$g = \frac{1}{2}\int_{-1}^{1} P(\cos\Theta)\cos\Theta d\cos\Theta \tag{5.13a}$$

where $P(\cos\Theta)$ is the phase function, and Θ corresponds to the scattering angle, which is the angle between the incident beam and the scattering beam. Although the physical meaning and mathematical form of the asymmetry factor has been known for a long time, there is not a publication that clearly addresses the calculation of asymmetry factor under realistic atmospheric considerations taking into account the variations of air density, aerosols, and drops in clouds. There has been further confusion between the averaged asymmetry factor of a certain component such as aerosols and drops of clouds in the atmosphere and the averaged asymmetry factor of all components in the atmosphere (Lu and Khalil, 1993b). The former can be obtained by using the relevant theory, as addressed in the previous chapter; for instance, the asymmetry factor for molecules in the atmosphere is equal to zero, and that for aerosols and drops can be calculated by using Mie theory and eq. 5.13a (see sections 4.4.3 and 4.4.4. The latter, the atmospheric asymmetry factor, on the other hand, is a composite of the asymmetry factors of several types of the atmospheric scatterers such

as air molecules, atmospheric aerosols, and cloud droplets. It should be emphasized that the averaged asymmetry factor for a specific atmospheric component is not what one should use in the two stream approximation in dealing with radiative transfer in ultraviolet wavelengths. Instead the atmospheric asymmetry factor of all the components in the atmosphere is required. The detailed numerical calculation of asymmetry factor are addressed in detail in the previous chapter (Also see Lu and Khalil, 1993b). In short, the numerical form of the atmospheric asymmetry factor in the *i*th layer (between levels *i-1* and *i*, according to eq. 4.33b, can be expressed as:

$$\overline{g_i} = \frac{g_a \tau_{s,i}^a + g_c \tau_{s,i}^c}{\tau_{s,i}^m + \tau_{s,i}^a + \tau_{s,i}^c} \tag{5.13b}$$

where the superscript m, a, and c respectively correspond to the scattering of the atmospheric molecules, aerosols, and drops in clouds; the subscript s denotes the scattering; and the subscript i represents the ith layer. g_a and g_c are respectively the asymmetry factors of aerosols and cloud drops in the atmosphere, calculated according to eq. 4.27b. It should be noted that outside a cloud $\tau_{s,i}^c = 0$; thus the atmospheric asymmetry factor is entirely controlled by the asymmetry factor of aerosols and the normal scattering optical depths of aerosols and air molecules.

In summary, in order to precisely calculate the actinic flux in different altitudes and time, three parts of work needs to be done. First, the atmospheric conditions must be specified; different weather and atmospheric characteristics in different locations and time lead to different radiation fields. The input data sets required in this study are vertical profiles of number densities of air molecules, ozone, and aerosols; the size distributions of

aerosols and cloud droplets; the refractive indexes of aerosols and cloud droplets; the heights, depths, liquid water contents, and macro-structures of clouds. Secondly, by using these input data, all the parameters characterizing the optical properties including the normal depths, single scattering albedos, and the asymmetry factors are calculated with the numerical methods described in the previous and this chapters. Finally all the radiative fluxes including the direct radiative flux, the upward and downward diffuse fluxes, the net radiative flux (or the irradiance), and actinic flux are obtained incorporated the optical parameters into the radiative transfer model described in this chapter.

5.3 Model Results

In this study the same four atmospheric conditions are used as in the studies of optical properties in the previous chapter: 1) clear and clean air including only ozone absorption and Rayleigh or molecular scattering, 2) urban atmosphere (the previous conditions plus aerosol absorption and scattering), 3) urban air with a stratus cloud (case 2 plus a stratus at 1.5 ~ 2.5 km), and 4) urban air with an altostratus (case 2 plus an altostratus cloud at 5.5~6.5 km). These four atmospheric conditions were chosen to compare the effects of clouds, aerosols, atmospheric molecules, and O_3 on the radiation field. The vertical profiles of the ozone concentration and the number density of aerosols are taken from Demerjian et al. (1980). The vertical profile of the number density of air molecules is taken from U.S. standard atmosphere (1976). The cross sections for Rayleigh scattering are taken from WMO-Report No. 16 (1985). The extraterrestrial solar flux, the surface albedos, and ozone absorption coefficients are taken from Demerjian et al. (1980).

Aerosol particles and cloud drops are assumed to be spherical in this study. A complex index of refractive of m=1.5-0.1i (Demerjian et al., 1980) represents the part absorption of radiation by aerosols. The size distribution of aerosols and cloud droplets are assumed to be modified gamma distributions, as shown in eqs. 4.35 and 4.36 as well as in table 4.3 and fig. 4.2 in the previous chapter. For convenience of comparison, our model resolutions in altitude and spectrum are the same as those of Demerjian et al. (1980) for clear atmospheric conditions; thirty-four layers from the earth's surface up to 70 km above the surface and 48 wavelength ranges from 290 nm to 700 nm are chosen. For cloudy condition, a heavy 1 km cloud in sub-divided into 100 sub-layers with 10 m of the vertical resolution.

5.3.1 Direct and Diffuse Fluxes, Irradiances, and Actinic Fluxes

The vertical profiles of the direct radiative flux, F^d, the upward diffuse flux, F^+, the downward diffuse flux, F^-, the net irradiance, F_{net}, and the actinic flux, J, at zero zenith angle in the wavelength range, 295~300 nm for the four different scenarios, as described in the beginning of this section, are shown in fig. 5.3. For the convenience of the comparison, all the fluxes in this figure are normalized by dividing by the extraterrestrial radiative flux, πF_0. In the clear atmosphere, as shown in fig. 5.3a and 5.3b, the direct radiative fluxes decrease significantly with decreasing height in this wavelength region. Mainly due to the strong ozone absorption in this wavelength range, the direct radiative flux decreases with decreasing height, which is especially apparent in the ozone layer, between 15 and 30 km above the earth's surface. Besides the strong ozone absorption, the air molecules also affect the direct radiative flux by blocking the incident beam and scattering it in different

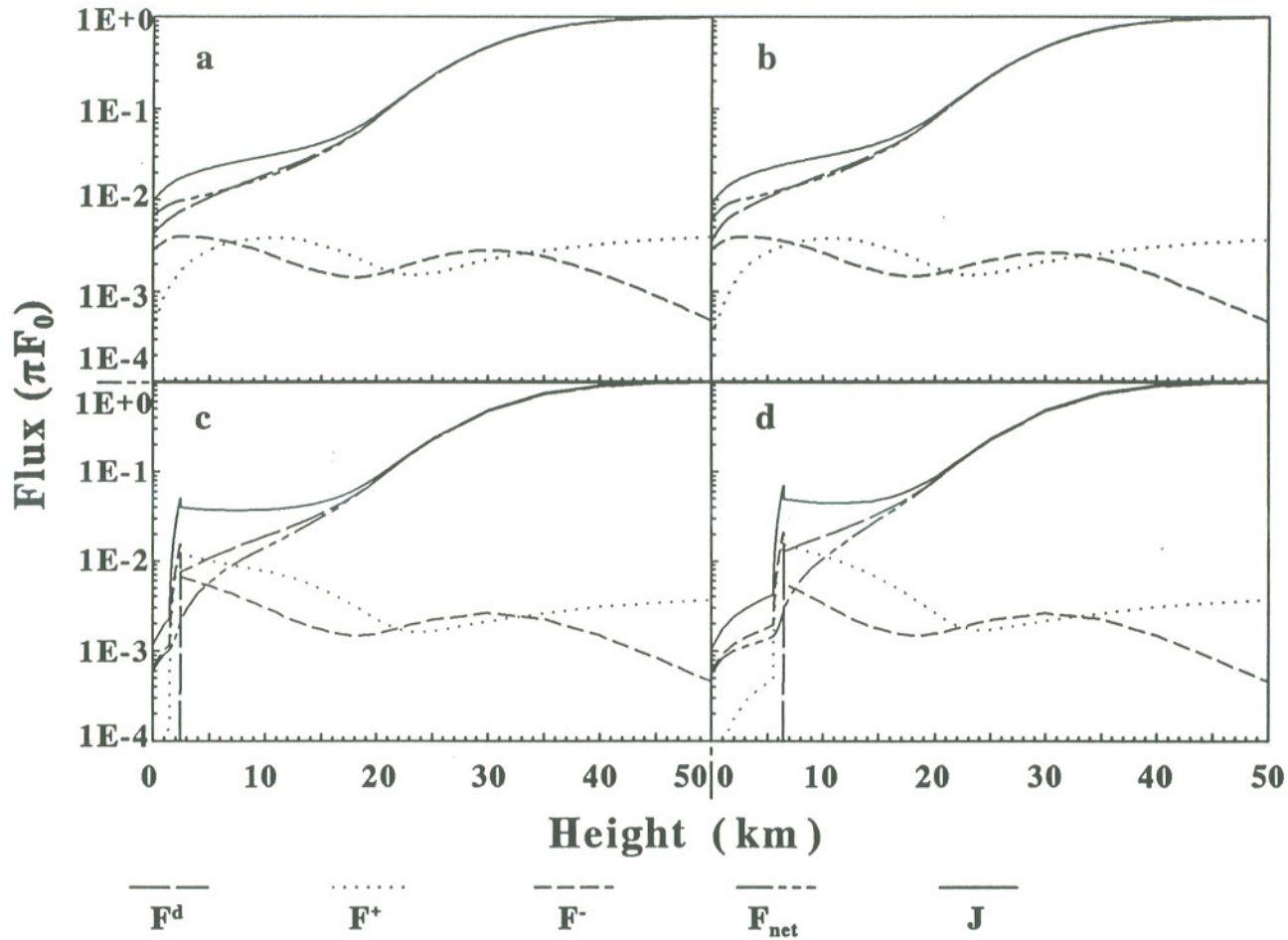

Fig. 5.3 The vertical profiles of the direct radiative flux, F^d, the upward diffuse flux, F^+, the downward diffuse flux, F^-, the net irradiance, F_{net}, and the actinic flux, J, at zero zenith angle within the wavelength range, *295~300* nm for the four different scenarios: the clear and clean atmosphere (fig. 5.3a), the urban atmosphere (fig. 5.3b), the urban atmosphere with a stratus (*1.5~2.5* km) (fig. 5.3c), and the urban atmosphere with an altostratus (*5.5~6.5* km) (fig. 5.3d).

directions. As shown in fig. 5.3a, the effect of Rayleigh scattering on the direct radiative flux is evident in the lower atmosphere, where large percentages of air molecules appear. Atmospheric aerosols in the urban atmosphere also affect the direct radiative flux by scattering and absorption. The effect, though small compared to the ozone absorption, decreases the direct radiative flux especially in the atmospheric boundary layer, as shown in fig. 5.3b, since most of aerosol particles reside in the boundary layer.

The vertical profile of the diffuse flux, either upward or downward, in the clear and clean atmosphere is similar to that in the urban atmosphere. On the one hand, the upward diffuse flux first increases with height from the earth's surface to reach a maximum at the top of troposphere, then decreases with height to a minimum at about 23 km above the earth's surface, and then increases again with height but the slope of increase gradually decrease to zero at the top of the atmosphere. On the other hand, the downward diffuse flux first increases with height from the surface to a maximum value at the top of the atmospheric boundary layer, around 2 km above the earth's surface, and then decreases with height, reaching a minimum value at about 18 km, and then increases again with height to another maximum at around 30 km, and finally decrease monotonously with height to a zero value at the top of the atmosphere. The diffuse flux at a given altitude originally results from scattering processes; however, the magnitudes of the diffuse fluxes, both in the upward and in the downward directions, not only depend on the first scattering processes at this height resulting from the number densities of air molecules and aerosol particles at this altitude, but also on the whole radiation field, and the atmospheric components and their number densities below and above this height. Strictly the upward (or downward) diffuse

flux at a certain height of the atmosphere is equal to the diffuse flux upward (or downward) due to all scattering processes happening at this height plus the sum of all radiative energies reaching this height resulting from all the scattering processes from the whole atmosphere below (or above) this point. At the top of the atmosphere, where the number densities of air molecules and aerosols are very small and thus the scattering processes at this height are negligible, both the downward and the upward diffuse fluxes occurring at this height due to the scattering processes are close to zero. As the solar radiation enters the atmosphere, scattering processes occur and convert the direct solar radiation into the diffuse energy and send it in all directions. The deeper through the atmosphere the solar beam travels, the more direct solar energy is transformed into the diffuse energy by air molecules and aerosols, which exist in the traversing path of the radiation, and thus greater the diffuse downward flux is produced. As a result of the combination of the scattering processes occurring at a given height and the accumulation of downward diffuse energies from the atmosphere above the height, the total downward diffuse flux increases with the decrease of the height in the upper atmosphere. Ozone absorption is also accompanied by scattering processes, and the scattered radiation is absorbed by O_3, which trends to reduce the accumulation of the diffuse energy. Due to the ozone absorption, the downward diffuse flux decreases with decreasing height to a minimum value at around 18 km above the earth's surface. In the boundary the combination of the large numbers of O_3 molecules, air molecules, and aerosols make the downward diffuse flux increase with height. The increase of the upward diffuse flux with height in the troposphere mainly results from the accumulation of back scattering of direct solar insolation by a large number of air molecules and aerosols in the lower atmosphere, while the strong ozone absorption in the ozone layer

reduces this accumulation and results in a minimum upward diffuse flux at about 23 km above the earth's surface. At the upper atmosphere, as the number of air molecules, ozone molecules, and aerosol particles becomes less and less, the scattering and absorption processes occurring become weaker and weaker; therefore all the upward diffuse energies produced in the lower and middle atmosphere and reaching the upper atmosphere do not change much, leading to an almost constant total upward diffuse flux in the upper atmosphere.

It is interesting that either the upward or downward diffuse flux has a minimum value in the ozone layer; however, the minimum upward diffuse flux is always located above the minimum downward diffuse flux, as shown in fig. 5.3a~d. This phenomena is due to the vertical structure of O_3. The maximum ozone concentration is around 21 and 22 km above the earth's surface (McClatchey, 1972; Demerjian et al., 1980). On the one hand, the region around maximum O_3 concentration absorbs a large percentage of the downward diffuse energy above it to prevent the energy from penetrating downward through and accumulating below the region. On the other hand, by absorbing the energy upward from the atmosphere below the region, the region filters out a large percentage of energy upward through it. Consequently the region absorbs most of the upward and downward diffuse energies, leading to the height of the minimum downward diffuse flux below the altitude of the maximum O_3 concentration and the height of the minimum upward diffuse flux above the height with the maximum ozone concentration. As shown in figs. 5.3a and 5.3b, the direct radiative flux, the net radiative flux (or the irradiance), and the actinic flux are almost identical in the middle and upper atmosphere since the diffuse flux there is much smaller than direct radiative flux.

It should, nonetheless, be emphasized that the actinic flux at the top of the atmosphere is always larger than the extraterrestrial solar flux because of the non-zero upward diffuse flux due to the scattering processes in the atmosphere below, as shown in table 5.2. The diffuse fluxes begin to be important at about 20 km above the earth's surface for the actinic flux, but their contributions to the net radiative flux are noticeable only in the low and middle troposphere, beyond which the contribution to the net radiative flux from the downward diffuse flux almost cancels out that from the upward diffuse flux. The reason that the effects on the actinic flux are distinct in the troposphere and low stratosphere is the integral weighed factor, $\mu_1^{-1}=3^{1/2}$, as shown in eq. 5.9. On the whole, the relative difference between the actinic flux and the net radiative flux, about 50%, at the earth's surface, is much larger than that at 65 km, only about 1%.

The effects of clouds on radiative field are significant, as clearly shown in figs. 5.3c and 5.3d. The direct radiative fluxes, similar to those in figs. 5.3a and 5.3b, decrease with decreasing height due to the ozone absorption, the scattering of air molecules and aerosols above the tops of clouds; however, the direct radiative flux drops to almost zero once the solar beam travels into clouds because almost all the direct insolation is converted into the diffuse energy by the scattering processes by cloud drops. Thus the magnitudes of both the net radiative flux and the actinic flux inside and below the clouds depend only on the diffuse flux. On the one hand, the actinic flux and net irradiance below clouds are greatly reduced by clouds, as shown in fig 5.3. One the other hand, because of the accumulation of diffuse energy due to scattering, particularly back scattering, of the direct solar insolation by cloud droplets, both downward and upward diffuse fluxes reach their maximum values very close

Table 5.2. The Direct Radiative Flux (F^d), The Upward Diffuse Flux (F^+), The Downward Diffuse Flux (F^-), The Net Flux (The Irradiance F_{net}), and The Actinic Flux (J) at the Earth's Surface and at 65 km above the Earth's Surface for Four Scenarios, Three Wavelength Ranges, and Two Zenith Angles.

W (nm)	H (km)	S	0° of the Solar Zenith Angle					86° of the Solar Zenith Angle				
			F^d	F^+	F^-	F_{net}	J	F^d	F^+	F^-	F_{net}	J
295 . . . 300	65	CC	1.00	4.31E-3	3.77E-5	1.00	1.01	0.0805	1.17E-3	3.74E-5	0.0794	1.00
		UR	1.00	4.05E-3	3.57E-5	1.00	1.01	0.0805	1.11E-3	3.54E-5	0.0794	1.00
		ST	1.00	4.05E-3	3.57E-5	1.00	1.01	0.0805	1.11E-3	3.54E-5	0.0794	1.00
		AL	1.00	4.07E-3	3.57E-4	1.00	1.07	0.0805	1.11E-3	3.54E-5	0.0794	1.00
	0	CC	4.29E-3	3.57E-4	2.85E-3	6.79E-3	9.85E-3	4.79E-31	2.07E-8	4.14E-7	3.93E-7	7.53E-7
		UR	3.54E-3	3.21E-4	2.87E-3	6.09E-3	9.07E-3	4.47E-32	1.67E-8	3.34E-7	3.18E-7	6.08E-7
		ST	5.36E-29	3.17E-5	6.33E-4	6.02E-4	1.15E-3	0.00	1.73E-9	3.45E-8	3.28E-8	6.28E-8
		AL	5.02E-36	2.90E-5	5.81E-3	5.52E-3	1.06E-3	0.00	1.78E-9	3.55E-8	3.38E-8	6.46E-8
395 . . . 400	65	CC	1.00	0.189	1.61E-5	0.811	1.33	0.0810	0.0471	1.19E-5	0.0339	1.08
		UR	1.00	0.163	1.32E-5	0.838	1.28	0.0810	0.0459	1.12E-5	0.0352	1.08
		ST	1.00	0.824	2.52E-5	0.177	2.43	0.0810	0.0736	1.17E-5	7.38E-3	1.13
		AL	1.00	0.868	2.59E-5	0.133	2.50	0.0810	0.0753	1.17E-5	5.70E-3	1.13
	0	CC	0.691	0.0427	0.163	0.811	1.047	8.39E-4	1.79E-3	0.0349	0.0339	0.0738
		UR	0.565	0.0394	0.223	0.749	1.02	7.02E-5	1.48E-3	2.96E-2	0.0282	0.0546
		ST	5.75E-27	7.11E-3	0.142	0.135	0.259	0.00	2.36E-4	4.72E-3	4.48E-3	8.58E-3
		AL	1.45E-35	5.67E-3	0.114	0.108	0.206	0.00	1.89E-4	3.78E-3	3.59E-3	6.87E-3
680 . . . 700	65	CC	1.00	0.159	1.45E-5	0.841	1.28	0.0810	0.0226	1.20E-6	0.0584	1.04
		UR	1.00	0.103	1.35E-6	0.897	1.18	0.0810	0.0274	1.14E-6	0.0537	1.05
		ST	1.00	0.787	2.81E-6	0.214	2.36	0.0810	0.0646	1.22E-6	0.0165	1.11
		AL	1.00	0.883	3.31E-6	0.118	2.53	0.0810	0.0689	1.22E-6	0.0122	1.12
	0	CC	0.955	0.147	0.0237	0.832	1.25	0.0454	8.97E-3	0.0144	0.0508	0.607
		UR	0.785	0.141	0.154	0.797	1.29	4.03E-3	4.48E-3	0.0258	0.0254	0.102
		ST	1.51E-26	0.0272	0.181	0.154	0.361	0.00	8.17E-4	5.44E-3	4.63E-3	0.0108
		AL	3.35E-35	0.0142	0.0944	0.0823	0.188	0.00	4.34E-4	2.89E-3	2.46E-3	5.76E-3

where *W* represents the wavelength range; *H* denotes the altitude; S specifies the scenarios, and *CC, UR, ST,* and *AL* correspond to the clear and clean atmosphere, the urban atmosphere, the urban atmosphere with a stratus (1.5~2.5 km), and the urban atmosphere with an altostratus (5.5~6.5 km).

to the cloud top, and the actinic flux is higher at any height above the cloud top, compared to that at the same height without a cloud.

Fig. 5.4 shows the vertical profiles of all the five fluxes within the same wavelength range as the previous figure but at the zenith angle $\theta=86°$. A bigger zenith angle means a longer path for the solar radiation to travel and more molecules and aerosols for it to encounter. Thus most of the direct solar energy is converted into the diffuse energy by air molecules before the solar beam even enters the ozone layer. A longer traversing path also means more radiative energy is absorbed by O_3. By comparing fig. 5.4 with fig. 5.3, it is clear that all the five fluxes at a large zenith angle drop much faster than those at zero zenith angle. Similar to fig. 5.3, for a large zenith angle a cloud further blocks the direct radiative energy above to penetrate through and reflects it back to upper atmosphere due to the scattering processes by cloud droplets, resulting in even lower net radiative flux and actinic flux below the cloud than those in a clear atmosphere. It should be mentioned that there is a big difference between the actinic flux and the irradiance at the upper atmosphere although both parameters are highly dependent on the direct radiative flux there, or the extraterrestrial flux, and the contribution of diffuse flux is negligible there. The difference results from their definitions, i.e., a spherical integral for the actinic flux and an integral in the vertical direction for the irradiance, as shown in eq. 5.9 in the last section (also see Madronich, 1987). In the strong ozone absorption band, e.g. in the wavelength 295~300 nm, the diffuse radiative energy upward is almost all absorbed by ozone before it reaches the top of the atmosphere. Therefore, at the top of the atmosphere, the actinic flux is close to the extraterrestrial flux, while the irradiance there is close to the direct downward flux,

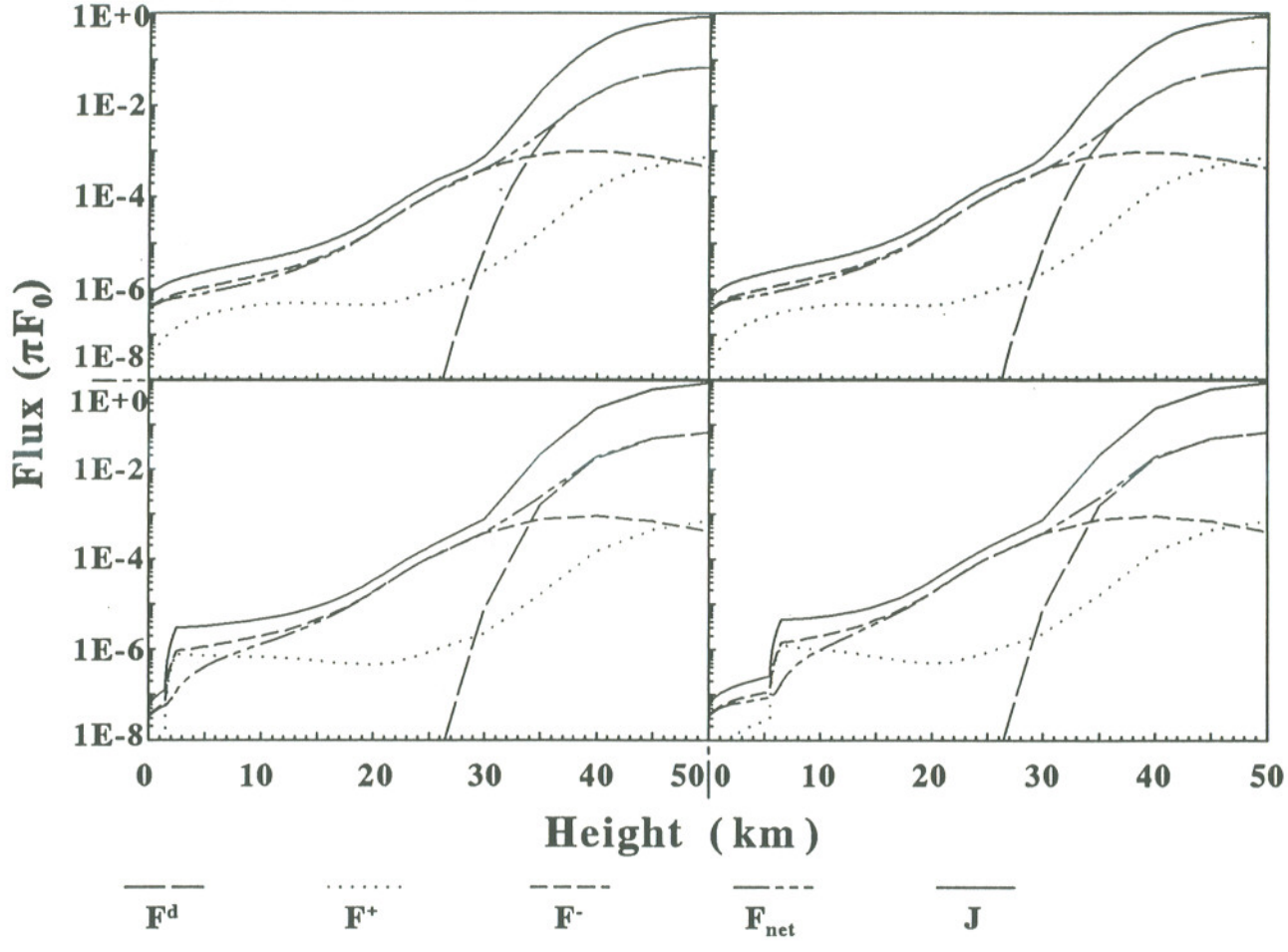

Fig. 5.4 The vertical profiles of all the five fluxes within the same wavelength range as previous figure but at the zenith angle θ=*86°*. See fig. 5.3 for more information about the scenarios and the legend names.

which is equal to the extraterrestrial flux times cosine of solar zenith angle, or alternatively, the ratio of the actinic flux to the irradiance in the upper atmosphere is close to secθ in the strong ozone absorption wavelength.

The vertical profiles of actinic fluxes at 10 different zenith angles in the four scenarios with the strong O_3 absorption wavelength, 295~300 nm, are illustrated in fig. 5.5. It is obvious that the actinic flux decreases greatly with decreasing height and with increasing zenith angle, mostly due to the strong O_3 absorption. A cloud reduces significantly the actinic flux below it, while increasing the actinic flux above it.

The five fluxes, compared in fig. 5.3, are also compared in the zero O_3 absorption range, 395~400 nm, as an example, shown in fig. 5.6. Unlike fig. 5.3, the direct radiative flux decreases slowly with decreasing height in the whole atmosphere since there is no O_3 absorption. In a clear and clean atmosphere, as shown in fig. 5.6, the downward diffuse flux increases with decreasing height due to two reasons. First, there are more air molecules in the lower atmosphere than in the upper atmosphere, leading to more molecular scattering processes, and thus more downward fluxes produced, accordingly. Secondly, or more importantly, the accumulation of the downward diffuse energy sent from the atmosphere above increases with the decrease of the height. On the contrary, the upward diffuse flux increases with height only arising from the accumulation of the upward fluxes from the atmosphere below. In the urban atmosphere, the diffuse fluxes are also affected by the scattering of aerosols, especially in the boundary layer where the strong scattering processes occur by most of the atmospheric aerosols, leading to not only a significant increase of the downward diffuse flux with decreasing height but also a decrease of the upward diffuse flux

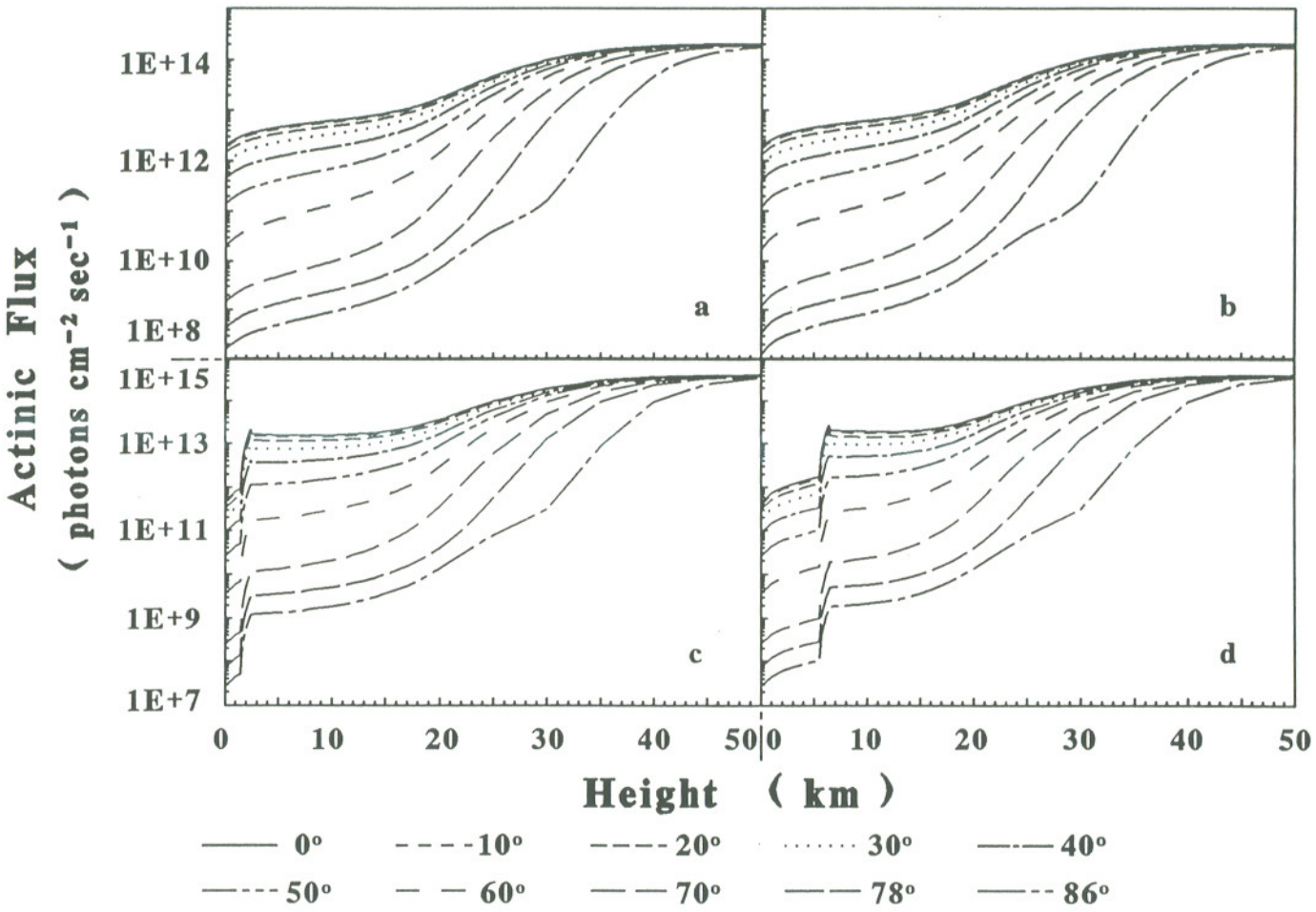

Fig. 5.5 The vertical profiles of the actinic fluxes at 10 different zenith angles in the four scenarios within the strong O_3 absorption wavelength, *295~300* nm. See fig. 5.3 for more information about the scenarios and legend names.

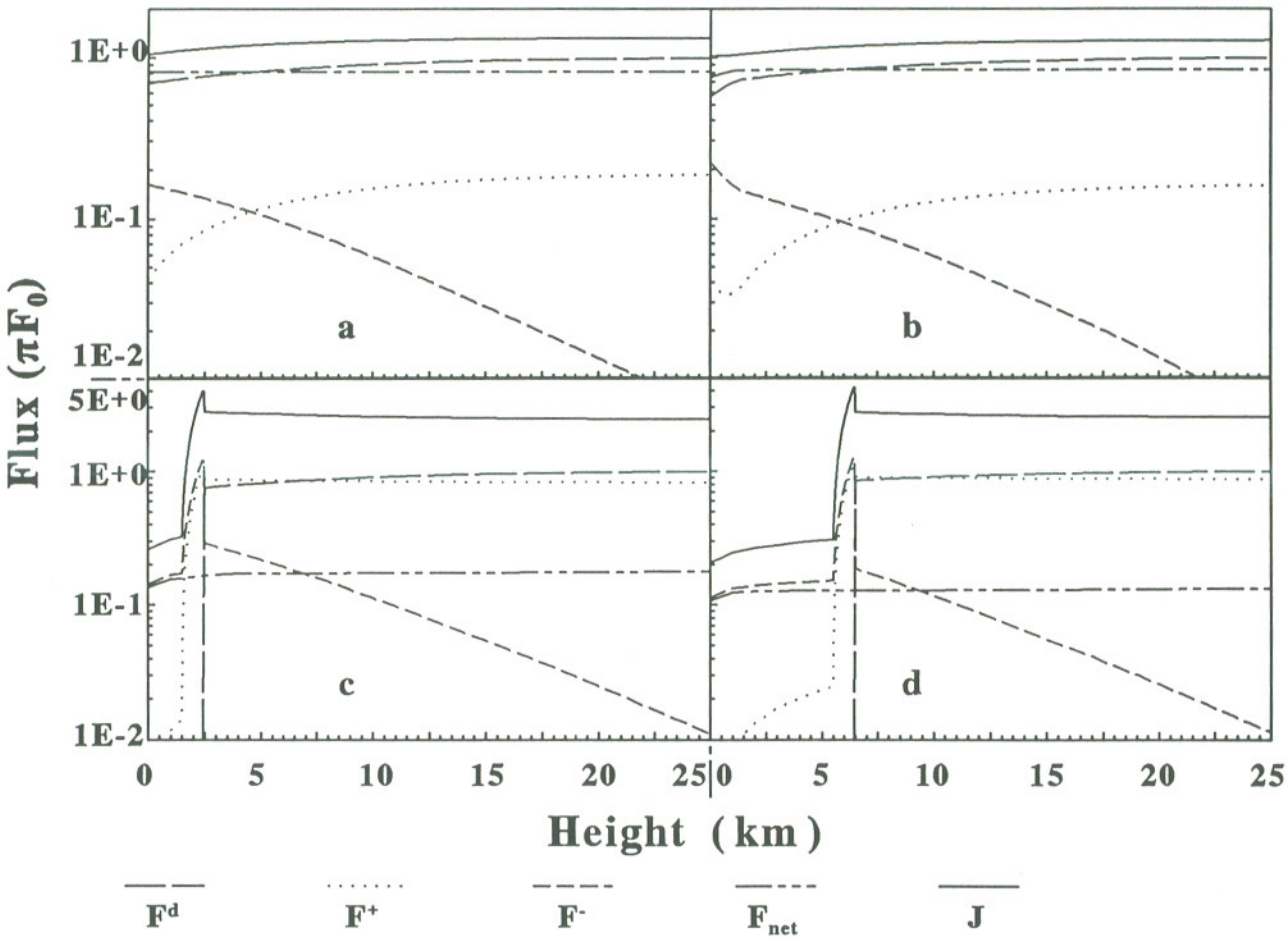

Fig. 5.6. The vertical profiles of all the five fluxes within the wavelength *395~400* nm at the zenith angle $\theta=0°$. See fig. 5.3 for more information about the scenarios and the legend names.

with height in the boundary layer. It should be noted that in a clean and clear air all the direct radiative energy lost within the zero ozone absorption wavelength is indeed converted into diffuse energy, and is thus conserved, resulting in no vertical change of the irradiance, as shown in fig. 5.6a. The decreases of the net radiative flux with decreasing height in an urban atmosphere either with a cloud or without a cloud, as shown in fig 5.6b~d, are due to aerosol absorption, which are apparent in the boundary layer. Lacking O_3 absorption, the actinic fluxes in the clear atmosphere are greater than the extraterrestrial flux for the whole atmosphere, as shown in figs. 5.6a and 5.6b. Even at the earth's surface, the actinic fluxes for the urban atmosphere and for the clean atmosphere are respectively about 2% and 5% greater than the extraterrestrial flux. At 65 km above the surface, the actinic fluxes are about 30% more than the extraterrestrial flux, as shown in table 5.2. When a heavy cloud, either a stratus or an altostratus, appears, it blocks the radiative energy passing though it and reflects the energy back by the multiple scattering processes from cloud droplets, as shown in figs. 5.6c and 5.6d, as well as table 5.2. We emphasize that there is two conflicted effects of Mie scatterers on in situ diffuse radiative field. On the one hand, more scatterers can generate more local scattering energy from the direct radiative energy as well as the other diffuse energy outside. On the other hand, more scatterers block more outside diffuse energy through, thus decreasing the total local diffuse radiative energy. Combing these two effects leads to peaks of the diffuse fluxes, both upward and downward, that appear close to a cloud top, resulting in a maximum actinic flux there, which is about 4 times the extraterrestrial flux.

The vertical profiles of the five fluxes for the four scenarios within wavelength

395~400 nm at a large solar zenith angle, 86°, are shown in fig. 5.7. A large zenith angle means that more direct energy is converted into the diffuse energy and diluted by more scatterers, as the solar beam travels a longer path through the atmosphere to the earth's surface. Similar to the previous figure, the net flux remains a constant in the whole atmosphere in a clear and clean atmosphere due to the lack of the O_3 absorption, while the decrease of the irradiance with decreasing height in the boundary layer in the urban air results from the absorption of aerosols. When a cloud appears at a large zenith angle, there is no a peak actinic flux near the cloud top inside the cloud, as shown at zero zenith angle in fig. 5.6. Instead, there is a drop from the cloud top right outside a cloud to the cloud top inside the cloud due to the sudden conversion from the direct radiation to the diffuse energy. It indicates that for a large zenith angle, drops inside a cloud block the accumulation of the local diffuse radiative energy and prevent any peak of the actinic flux inside a cloud, although a tiny peak of the downward diffuse flux can still be visible. Due to the blockage by the scatterers, there is less upward diffuse energy reaching the top of the atmosphere, resulting in less actinic flux there compared to that at zero zenith angle, as also shown in table 5.2.

The vertical profiles of the actinic flux for the four scenarios and ten zenith angles within the zero ozone absorption wavelength, 395~400 nm, are summarized in fig. 5.8. As discussed in two previous figures, the actinic flux decreases with decreasing height and increasing zenith angle mostly due to scattering except in the boundary layer where the absorption of aerosols also affects the radiation field. By balancing the energy produced by scattering in a given height inside a cloud and the accumulation of the diffuse energy not

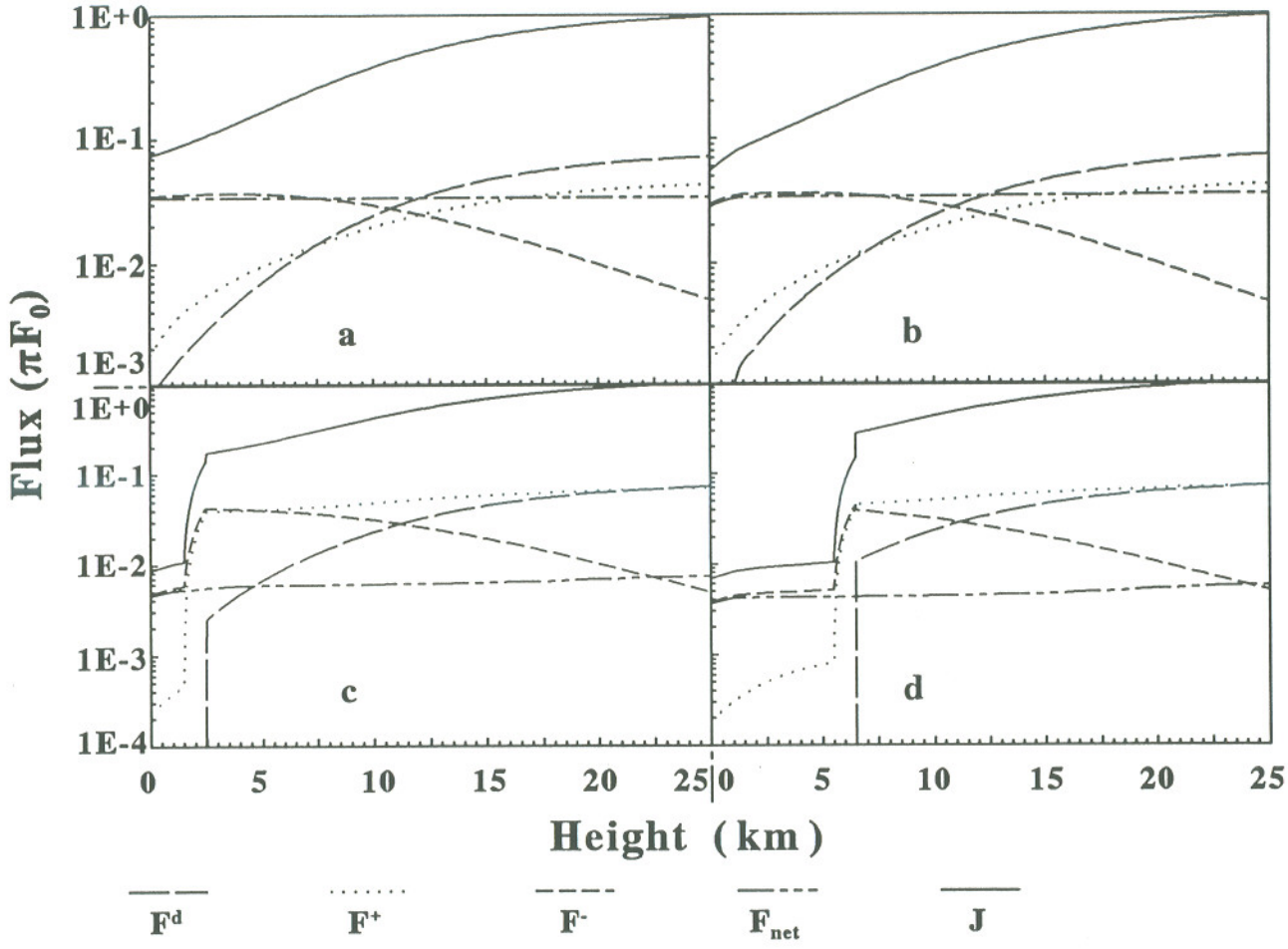

Fig. 5.7 The vertical profiles of all the five fluxes within the wavelength *395~400* nm at the zenith angle θ=*86°*. See fig. 5.3 for more information about the scenarios and the legend names.

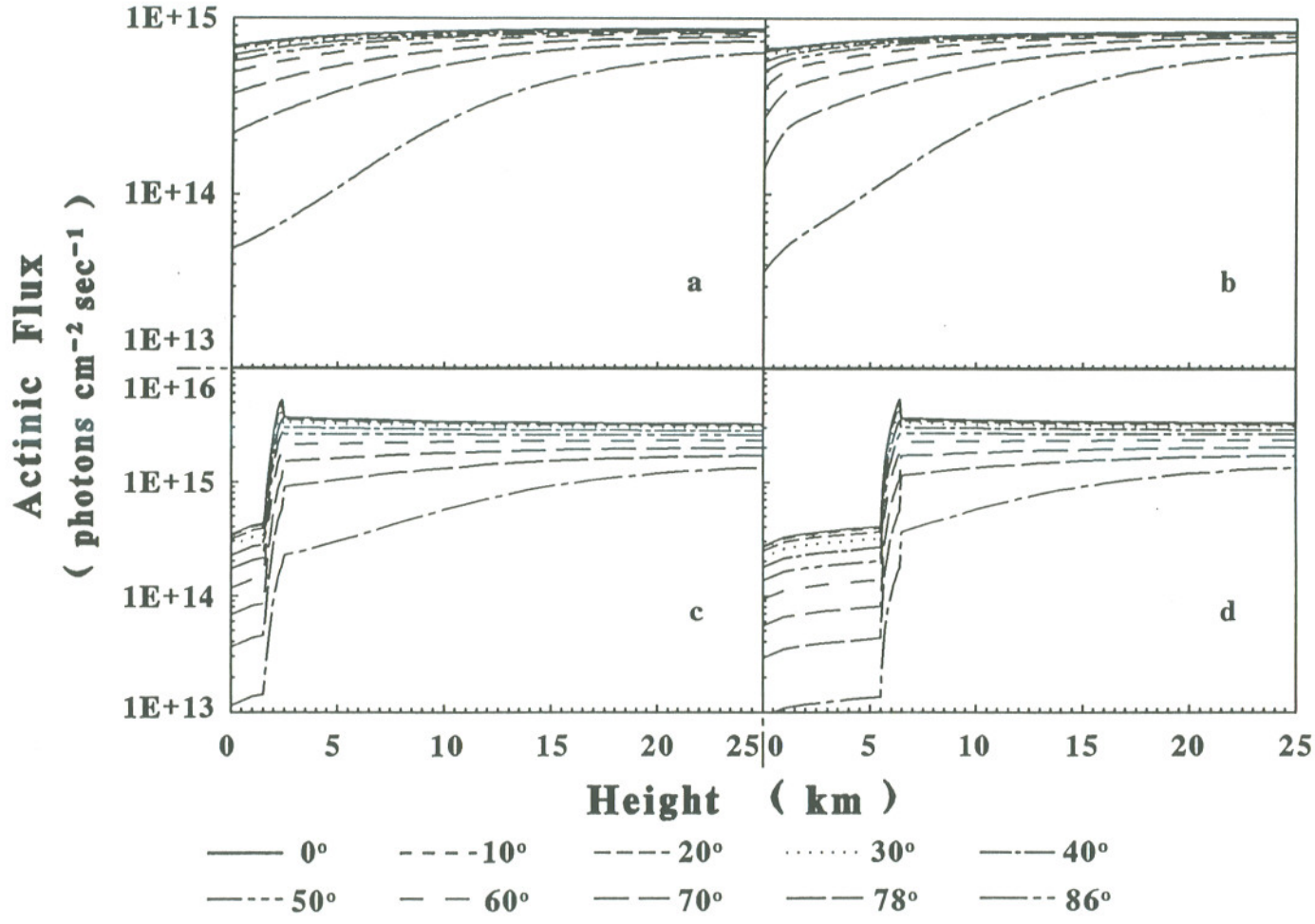

Fig. 5.8 The vertical profiles of the actinic fluxes at 10 different zenith angles in the four scenarios within zero O_3 absorption wavelength, *395~400* nm. See fig. 5.3 for more information about the scenarios and legend names.

produced but reached that height, it is obvious that the peak actinic flux inside a cloud appears near the cloud top for a small zenith angle, while the actinic flux above the top of the cloud is larger than that below the top for a large zenith angle. The actinic flux at the top of the atmosphere is significantly larger than the extraterrestrial flux when a heavy cloud appears due to the strong scattering of drops inside the cloud and none efficient absorbers in this wavelength range.

Fig. 5.9 compares the direct radiative fluxes, the diffuse fluxes, the irradiances, and the actinic fluxes with the extraterrestrial flux for different height at zero of the zenith angle within 680~700 nm. According to our calculation, the effect of Rayleigh scattering is much weaker in this wavelength than in the wavelength 295~300 nm and 395~400 nm, while the effect of O_3 absorption is even weaker compared to that of Rayleigh scattering. Thus there is a little direct radiative energy transferring to the diffuse energy and absorbed by O_3, leading to an even lower slope of the decrease of the direct radiative flux than that in the wavelength 395~300 nm. Due to weak Rayleigh scattering and O_3 absorption, and a higher surface albedo, 0.15, in this wavelength range, compared to 0.05 in 295~300 nm or 395~300 nm, the upward diffuse flux is always higher than the downward flux for the whole atmosphere, even in the lower atmosphere, as shown in fig. 5.9a. The effect of aerosol is dominant in this wavelength range in the urban atmosphere, as shown in fig. 5.9b. The diffuse fluxes increase significantly in the lower troposphere due to much stronger forward scattering processes of aerosols compared to O_3 absorption and Raleigh scattering, as well as due to the high surface albedo. The cloud effect is also apparent. Almost all the direct radiative energy are virtually converted into the diffuse energy due to scattering processes

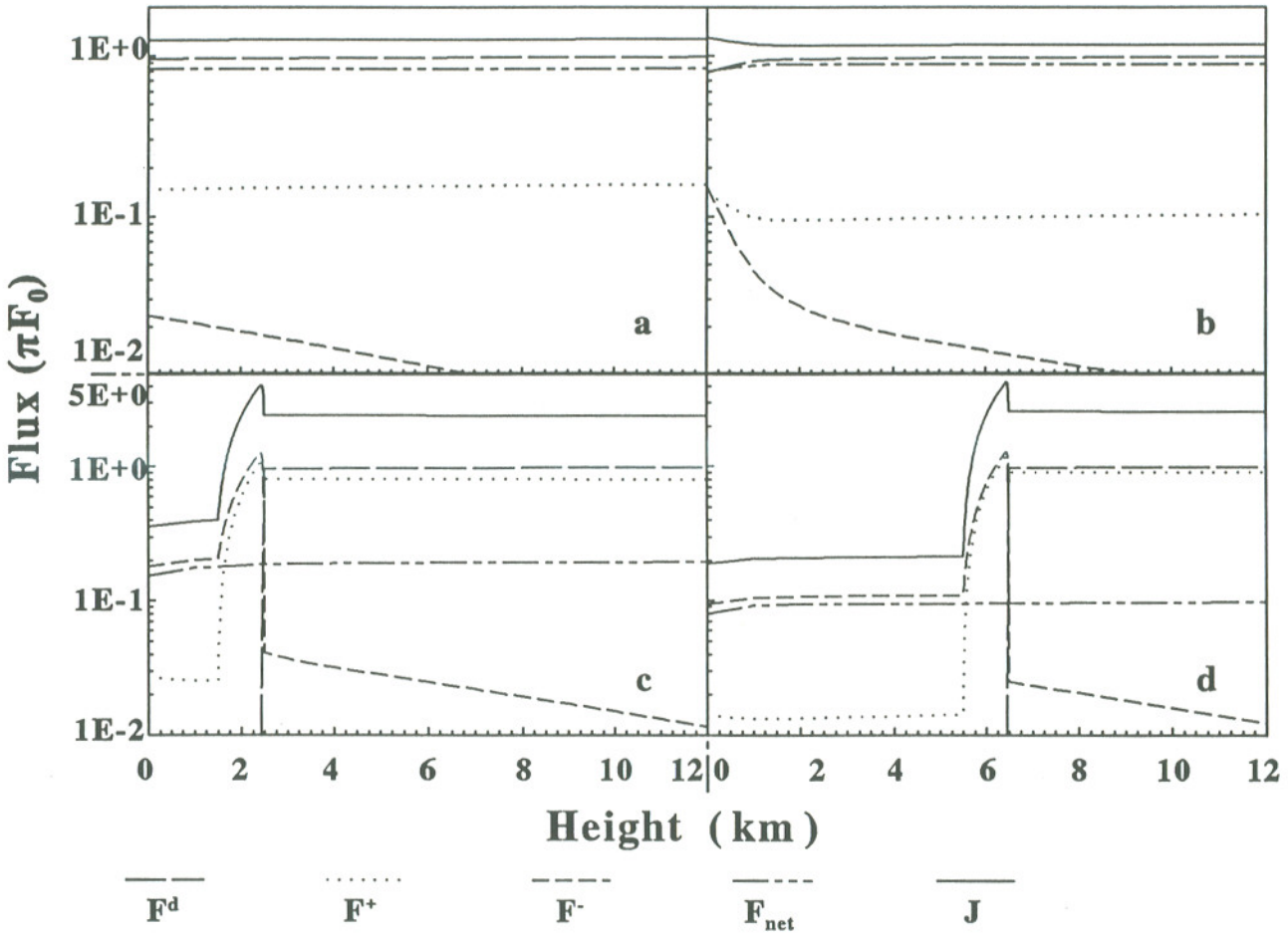

Fig. 5.9 The vertical profiles of all the five fluxes within the wavelength *680~700* nm at the zenith angle $\theta=0°$. See fig. 5.3 for more information about the scenarios and the legend names.

by drops once the solar radiation enters a cloud, either a heavy stratus or a heavy altostratus cloud. Since the forward scattering of the drops in a cloud is larger than the backward scattering ($g>0$, and $g \sim 0.88$ for the stratus and 0.81 for the altostratus in this wavelength range according to our model results), the downward diffuse flux is much higher than the upward flux below the cloud. On the contrary, due to the accumulation of the backscattering of the direct radiative energy, the backward flux is always higher than the forward flux above the cloud. For the same reason in figs. 5.3 and 5.6, the peak of the actinic flux appears near the cloud top inside the cloud. Due to the strong forward scattering, the forward diffuse flux is always higher than the backward flux inside a cloud.

All the five fluxes for different heights and scenarios are also compared for the large solar zenith angle, 86°, as shown in fig. 5.10. More solar energy is diluted by air molecules, aerosols, and drops in the cloud through larger traversing path, leading to a relatively larger decrease of the direct radiative flux with decreasing height compared to that at a small zenith angle. Unlike those shown in the previous figure, the downward diffuse fluxes are larger than the upward fluxes at a large zenith angle in the atmospheric boundary layer, as shown in figs. 5.10a and 5.10b, because of the accumulation of the strong forward scattering processes there and the blockage of the accumulation of the backward scattering energy due to a long path of traversal as well as due to more air molecules and aerosols in the path. As shown in figs 5.10c and 5.10d, the effect of clouds in this wavelength is more apparent than in the wavelength ranges 295~300 nm and 395~400 nm. Above a cloud top, the magnitude of the direct radiative flux does not decrease much compared to that in wavelength range 395~400 nm due to weak Rayleigh scattering and O_3 absorption, resulting

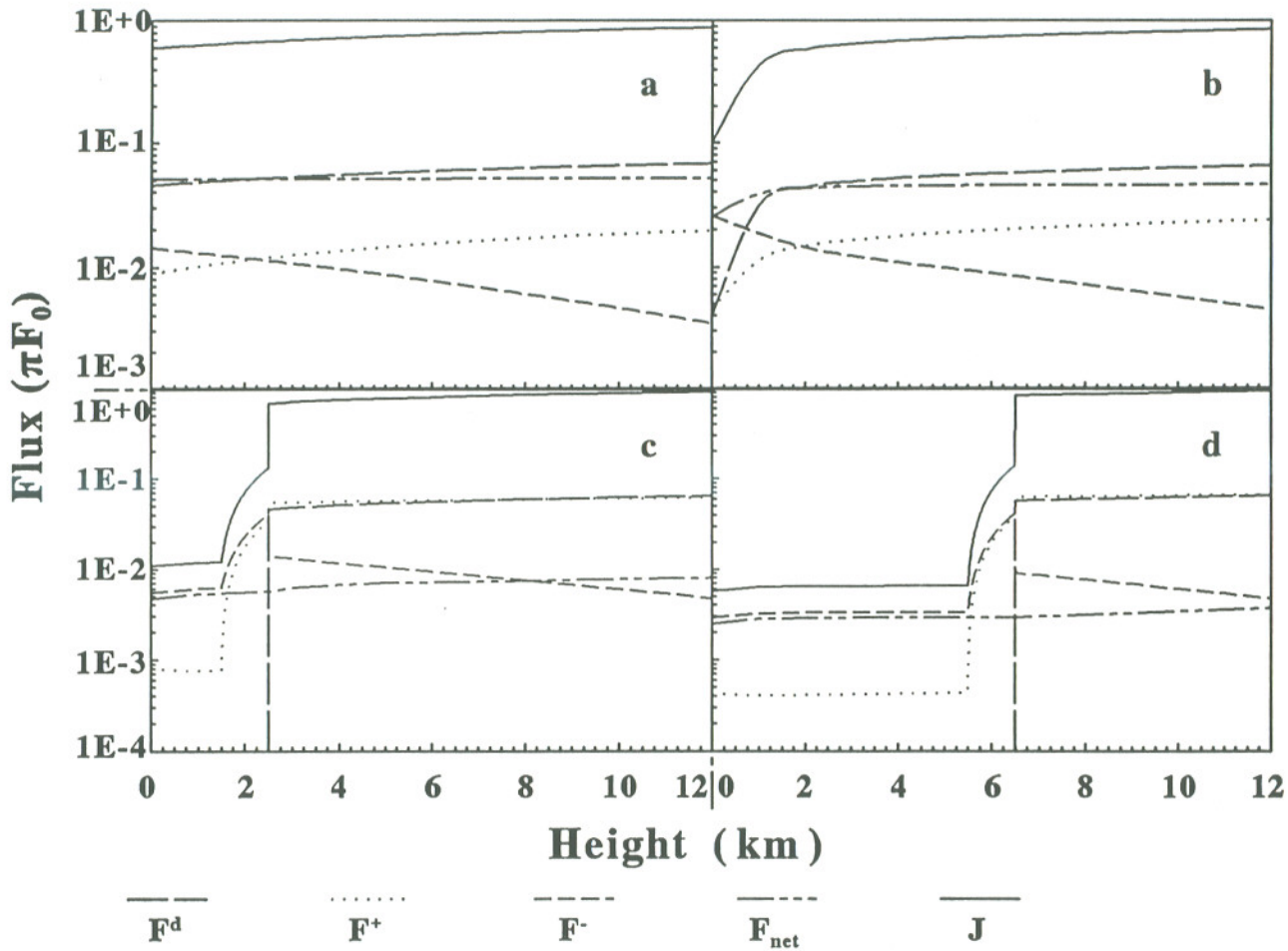

Fig. 5.10 The vertical profiles of all the five fluxes within the wavelength *680~700* nm at the zenith angle θ=*86°*. See fig. 5.3 for more information about the scenarios and the legend names.

in very little diffuse energy, both upward and backward, produced from the direct radiative energy there. Once the solar beam travels into the cloud, nearly all the direct radiative energy is immediately transferred into diffuse energy, leading to a peak of the downward diffuse flux near the cloud top inside the cloud. Due to the backscattering and the accumulation of the upward diffuse energy, the upward diffuse flux is larger above the top of the cloud than that inside the cloud. Since the direct flux at the top of the cloud is almost equal to the upward diffuse flux, the contribution of the direct flux there to the actinic flux there is much larger than those of diffuse fluxes ($1/\mu_1=3^{1/2}\sim1.73$ v.s. $1/\cos86°\sim14.3$). However, there is virtually no direct radiative flux inside the cloud; therefore, a big jump appears at the top of a cloud between the actinic flux inside and outside the cloud, as shown in figs. 5.10c and 5.10d.

Fig. 5.11 shows the vertical profiles of the actinic fluxes for ten zenith angles and four scenarios within 680~700 nm in the troposphere. As discussed in previous figures, the actinic flux decreases with decreasing height and with increasing zenith mostly due to the scattering processes. Due to the strong forward Mie scattering, the actinic flux increases with decreasing height in the boundary layer for small zenith angles, while it decreases with decreasing height for large zenith angles in the urban condition since a long traversing path dilutes more solar energy than a short one and prevents from the accumulation of the diffuse energy at any height. Similar to those shown in figs. 5.5 and 5.8, a cloud decreases the actinic flux significantly below it and increases that above it. Similar to those shown in fig. 5.8, a big jump of the actinic flux between inside and outside a cloud top for a small zenith angle and a large reduction for a large zenith angle result form the conflicted

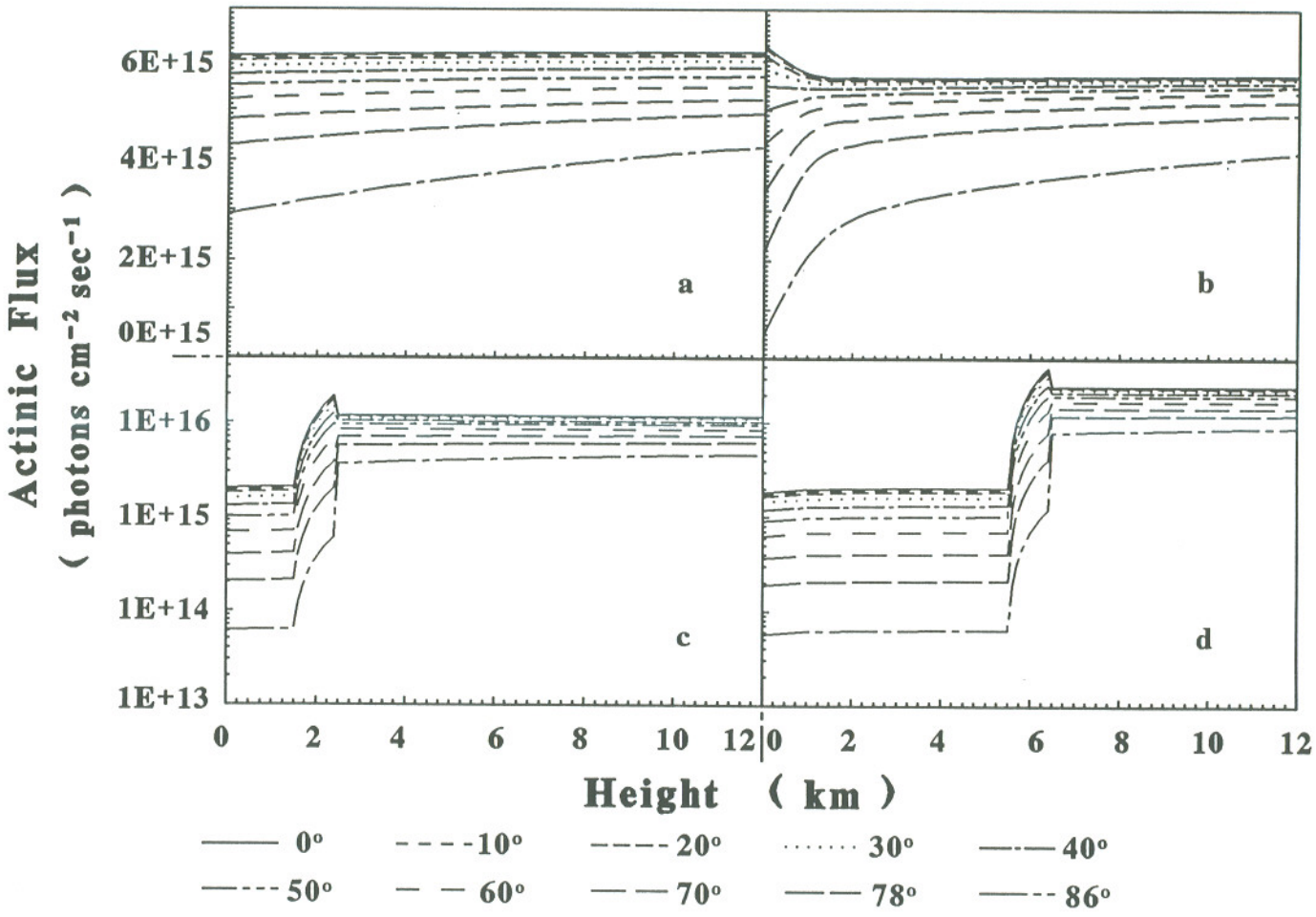

Fig. 5.11 The vertical profiles of the actinic fluxes at 10 different zenith angles in the four scenarios within wavelength range *680~700* nm. See fig. 5.3 for more information about the scenarios and legend names.

functions, i.e., the blockage and enhancement of the accumulation of the diffuse energy due to the scattering processes of the drops of the cloud.

Fig. 5.12 compares the irradiances and the actinic fluxes for two heights: 0 and 65 km, two zenith angles: 0° and 86°, three wavelength ranges, and four different scenarios. To show the distinction between the actinic flux and the irradiance, the irradiance and the actinic flux for every scenario within a wavelength range in the upper atmosphere are all divided by the extraterrestrial flux within the wavelength range. At the earth's surface, the actinic flux and the irradiance for each scenario within a wavelength is divided by the irradiance at the earth's surface in the clear and clean atmospheric condition in that wavelength range at 0° zenith angle. Comparing fig. 5.12a with 5.12b., one can see several big differences between the actinic fluxes and the irradiances in the upper atmosphere. First, the actinic fluxes are always greater than or equal to the extraterrestrial flux, which is always greater than or equal to the irradiances there. The irradiance is equal to or close to the extraterrestrial flux only in the strong O_3 absorption wavelength range at zero zenith angle, while the actinic flux is equal to or close to the extraterrestrial flux at any zenith angle in that wavelength range. It can be further inferred that at 90° zenith angle the actinic flux at the top of the atmosphere for any wavelength and scenario is equal to the extraterrestrial flux, while the irradiance is close to zero. Secondly, the feature of the lower atmosphere such as aerosols and clouds greatly affects the radiation strength of upper atmosphere in the none and weak O_3 absorption wavelengths, i.e., 395~400 nm and 680~700 nm, as shown in figs. 5.12a and 5.12b. For example, compared the irradiance and the actinic flux at 65 km and zero zenith angle in a clear and clean atmosphere with those

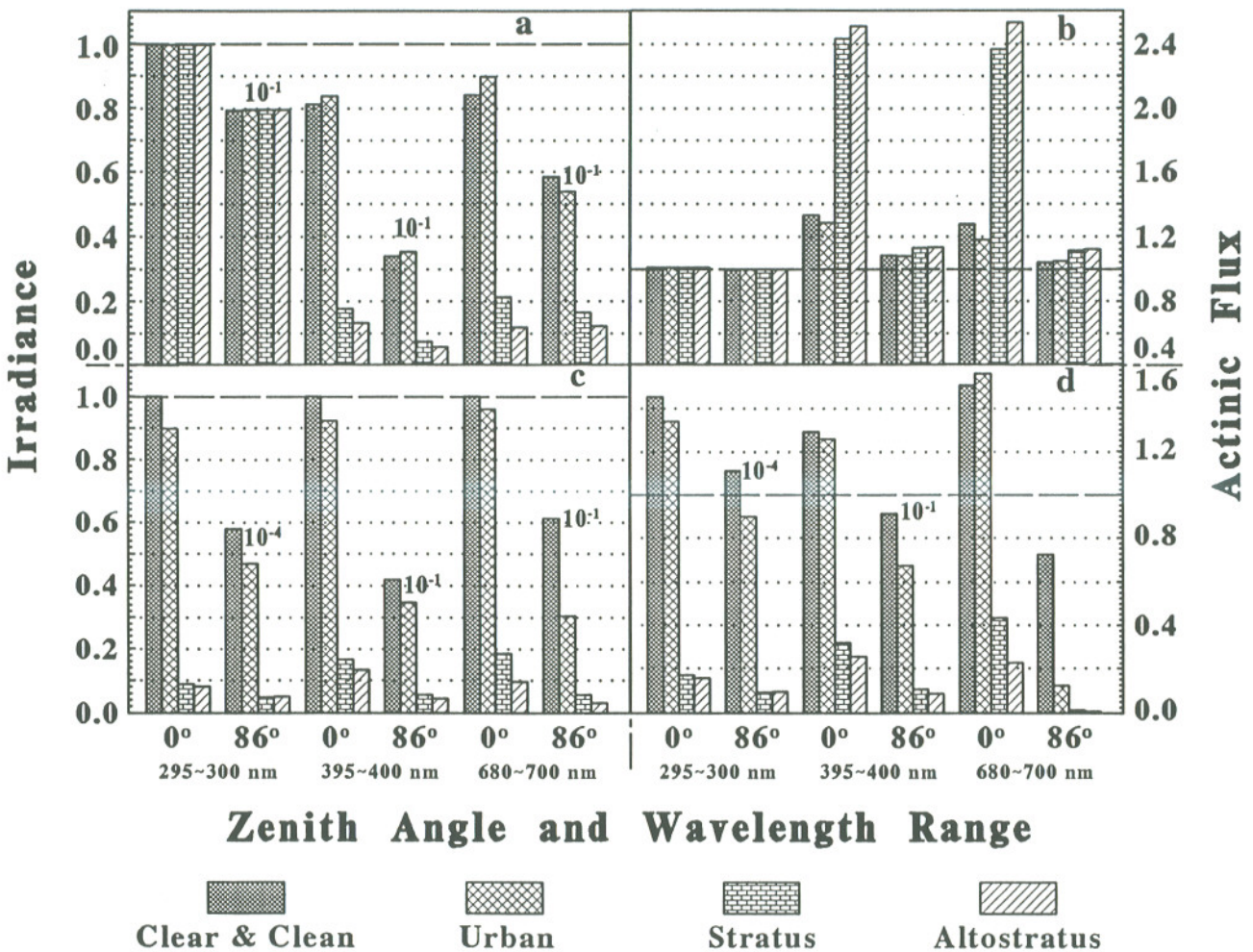

Fig. 5.12 Comparison of the irradiances and the actinic fluxes for the four different scenarios, three wavelength ranges, and two zenith angles: *0°* and *86°*; comparison of the actinic fluxes at the earth's surface (fig. 12d) and at *65* km above the earth's surface (fig. 12b); comparison of the irradiances at the earth's surface (fig. 12c) and at 65 km (fig. 12a).

at the same height and zenith angle in the rest 3 conditions, the irradiance, in the urban atmosphere within 680~700 nm, increases by about 6.5% without a cloud and decreases by 85% with the altostratus, corresponding to a 8% of decrease and an about 100% of increase of the actinic fluxes. It is noteworthy that the maximum actinic flux always corresponds to the minimum irradiance in the upper atmosphere in any wavelength among the four different scenarios. Furthermore, in any two scenarios, the bigger actinic fluxes corresponds to the smaller irradiance. This feature of the upper atmospheric radiation field results from the upward diffuse flux, which decreases the strength of the radiative flux in the downward direction (i.e., the direction of the irradiance) but increases the total radiative flux received from all the directions in the upper atmosphere, as clearly shown in eq. 5.9. Finally, the irradiance is more sensitive to solar zenith than the actinic flux. The irradiance is more than 20 times greater at 0° zenith angle than at 86° for the zero O_3 absorption wavelength, 395~400 nm, and it is more than 10 times over that for the strong O_3 absorption wavelength, 295~300 nm, in the upper atmosphere. There is only about 1% of difference between the actinic fluxes at 0° and 86° in 295~300 nm, and the actinic flux at 0° doubles that at 86° in 395~400 nm in the upper atmosphere.

Same as those in the upper atmosphere, the actinic fluxes at the earth's surface are always greater than the irradiances there. However, the actinic flux correlates positively with the irradiance there, as shown in figs. 5.12c and 5.12d, resulting from the downward diffuse flux, which increases the strength of the radiative flux in the downward direction as well as the total radiative flux in all the directions. The variation of both the actinic flux and the irradiance with the variation of zenith angle is much larger than that in the upper

atmosphere is more than four magnitudes larger at 0° zenith angle than at 86° at the earth's surface. It should be mentioned that the surface actinic fluxes in the urban air, scenario 2, calculated with our model in this study, generally agree well with those computed by Demerjian et al. (1981) with less than 10% of the relative errors between the results with the two totally different models since the similar input data set were used.

5.3.2. The Effect of the Macro-structure of Clouds

In the previous discussion, the liquid water content in a cloud is assumed to be vertically uniform; i.e., the liquid water content, the number density of droplets, and the size distribution of droplets inside the cloud are vertically the same everywhere. On the macroscale, the cloud water content increases with height above the cloud base, reaches a maximum somewhere in the upper half of the cloud, and decreases rather rapidly toward the cloud top (Pruppacher, 1981). In order to see the influence of vertical structures of clouds on radiation field, five hypothetical vertical cloud structures were made in this study. The vertical structures of liquid water contents and the names of these five clouds are the same as used in the studies of optical properties in the previous studies, as shown in fig. 4.13. The optical properties of these five clouds are discussed in detailed in the previous chapter and interested readers can refer to chapter 4 for more information.

The vertical profiles of the actinic fluxes for the five different vertical structures of the stratus (1.5 km ~ 2.5 km) at zero of the zenith angle with the wavelengths 295~300 nm, 395~400 nm, and 680~700 nm are shown in figs. 5.13b, 5.13d, and 5.13f. Here again the

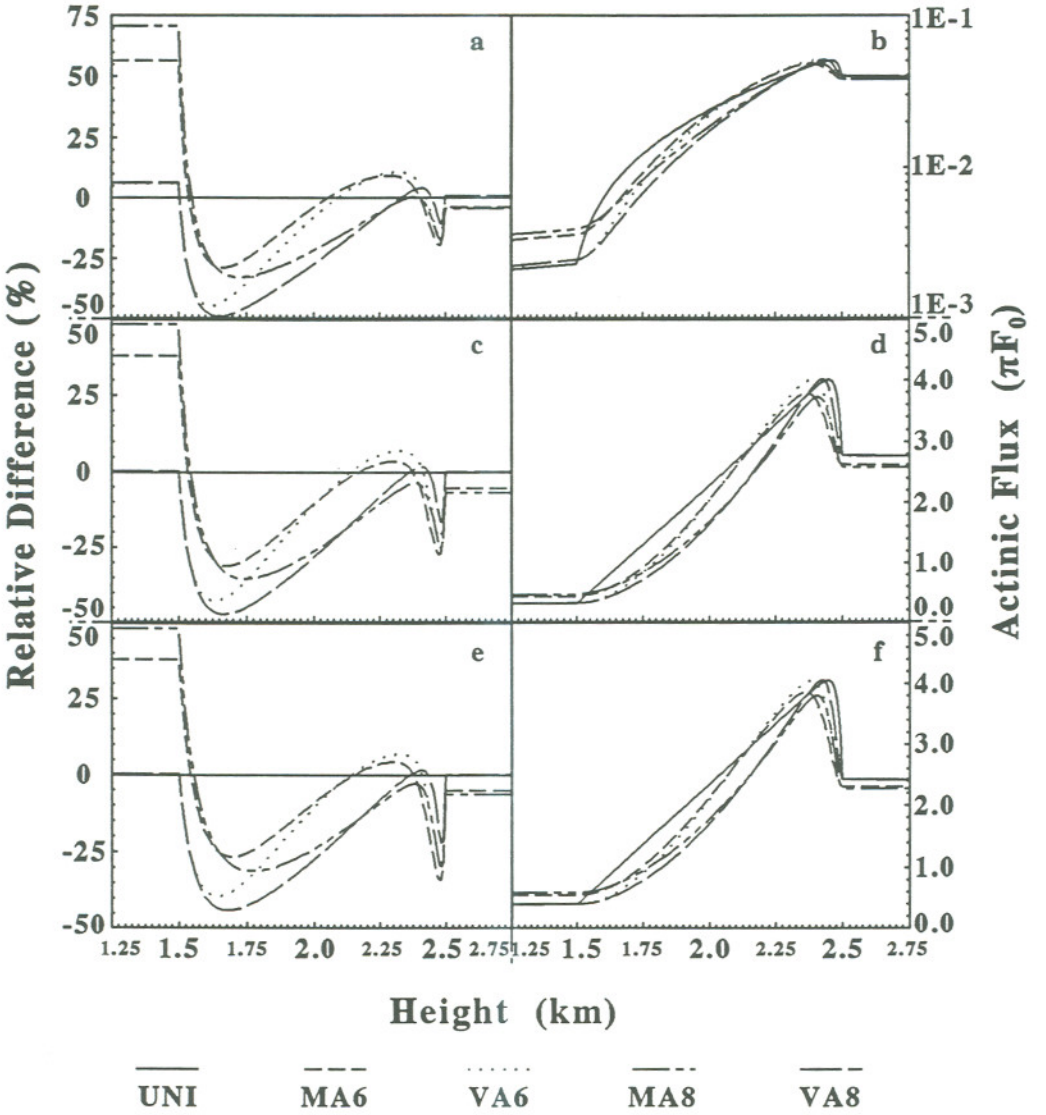

Fig. 5.13 The vertical profiles of the actinic fluxes and the relative difference between the actinic fluxes in any cloud of the five different vertical structures of the stratus (*1.5 ~ 2.5* km) and the vertically uniform cloud at zero zenith angle with wavelength range *295~300* nm (figs. 14b and 14a), *395~400* nm (figs. 14d and 14c), and *680~700* nm (figs. 14f and 14e). The relative difference is defined as:

$$\eta = \frac{J_i - J_{uni}}{J_{uni}}$$

where J_{uni} is the actinic flux for the vertically uniform cloud, and J_i is the actinic flux for any cloud of the five different vertical structures of the stratus (*1.5 ~ 2.5* km); i=1, 2, 3, 4, 5 correspond to five different vertical structures of the stratus cloud.

actinic fluxes are all normalized by dividing by the extraterrestrial flux, πF. The relative difference between the actinic fluxes in a vertically uniform cloud and vertically non-uniform clouds are also shown in figs. 5.13a, 5.13c, and 5.13e. Two major results can be seen in this figure. First the actinic flux outside a cloud is greatly affected by the total liquid water content of a cloud, while the local variation of the liquid water content inside a cloud has a weak influence on the actinic fluxes outside a cloud. For example, within the wavelength 295~300 nm, the relative difference of the actinic fluxes between the cloud *va6* or the cloud *va8* and the cloud *uni* is about 5% at the bottom of the cloud and less than 1% at the cloud top, corresponding to the same total liquid water content for the three different types of clouds. In contrast, since the total liquid water contents of the clouds *ma6* and *ma8* are respectively 68% and 62% of that of the cloud *uni*, the relative differences of the actinic fluxes within the same wavelengths are more than 70% between the clouds *ma8* and *uni*, and more than 55% between *ma6* and *uni* at the bottom of the cloud, and more than 5% between *ma8* or *ma6* and *uni* at the top of the cloud.

Secondly, the relative differences of the actinic fluxes inside the clouds among the vertically uniform cloud and the vertically non-uniform clouds are obvious. The vertical profiles of the relative differences of the actinic fluxes inside the clouds generally follow a typical shape: the relative difference first droplets with height quickly from a big positive difference for the clouds *ma6* or *ma8*, or from a small positive difference or virtually none difference for the clouds *va6* or *va8* at the cloud bottom to a negative minimum in the lower part of the cloud, and increases with height until a maximum in the upper part of the cloud, and then decreases to a minimum, and finally increases again to the relative differences at

the cloud top. The variation of the relative difference with height results from the difference of vertical structure of liquid water contents in the clouds. Near the top of cloud, the number of droplets are much larger in the vertically uniform cloud than in the non-uniform cloud,and thus more solar radiation is transferred into diffuse energy by Mie scattering processes at the top of the cloud *uni*. The diffuse energy is scattered back and forth, and is thus accumulated in the very upper cloud, resulting in relative higher actinic flux there in the vertically uniform cloud than in the vertically non-uniform cloud. As the very upper part of the vertically uniform cloud traps and conserves more energy than that of the vertically non-uniform cloud, it also blocks more energy to transfer downward, leading to the increase of relative difference of the actinic fluxes with decreasing height immediately after the first dip. The relative difference keeps increasing with decreasing height until a maximum is reached, where the sum of the diffuse energy produced by the local scattering processes and accumulation of the diffuse energy produced at different heights, especially reflected by droplets at the height where the maximum liquid water content is, appears a maximum value. Near the bottom of the cloud, the number of droplets in the vertically uniform cloud is much higher than that of the vertically non-uniform cloud, preventing more diffuse energy from transporting downward through the cloud, leading to a smaller actinic flux below the cloud base compared to that below the vertically non-uniform cloud. The more droplets of the vertically uniform cloud at the bottom also reflects more diffuse energy upward, resulting in larger actinic flux in the lower part of the vertically uniform cloud than in the vertically non-uniform cloud.

5.4 Summary

A detailed radiative transfer model has been developed in this study based on the two-stream technique and Mie theory to study the fields of the irradiance and the actinic flux in the spectrum where most atmospheric chemical reactions take place, or the ultraviolet wavelengths from 290 to 700 nm. The radiative transfer in the atmosphere is complicated; the irradiance and the actinic flux changes not only with time of day, season, and latitude due to the relative location of the sun and the observed point, but also with the local constituents of the atmosphere such as the number densities of the air molecules, ozone, aerosols, cloud droplets, and their optical properties such as cross sections and refractive indexes.

To find the effects of O_3, air molecules, aerosols, and cloud droplets on the radiation field, the fields of the actinic fluxes and the irradiances were computed by simulating four different scenarios: the clear and clean atmosphere, the urban clear atmosphere, the urban atmosphere with a stratus (1.5~2.5 km), and the urban atmosphere with an altostratus (5.5~6.5 km). To fully understand the complicated radiative transfer processes and recognize the difference between the irradiances and the actinic fluxes, the direct and the diffuse fluxes, which determine the values of the actinic fluxes and the irradiances, are analyzed, discussed, and addressed in detail for three wavelengths: the strong O_3 absorption wavelengths (e.g. 295~300 nm), the zero O_3 absorption range (e.g. 395~400 nm), and the weak molecular scattering and O_3 absorption range (e.g. 680~700 nm). According to our model results, due to the strong O_3 absorption, both the actinic flux and the irradiance decrease more significantly with decreasing height and increasing zenith angle in the strong

O_3 absorption wavelength than in the none or weak O_3 absorption range. The effect of aerosols becomes important in the atmospheric boundary layer, where most of the aerosols reside. It is apparent that a heavy cloud, either a lower stratus or a high altostratus, has a significant influence on the radiation field. A cloud decreases greatly the actinic flux below it while increasing the actinic flux above it. For example, at 0° zenith angle the surface actinic flux in a heavy altostratus condition could be only about 10% of the surface actinic flux for the strong O_3 absorption range and about 20% of the surface actinic flux for the none ozone absorption range in the clear and clean atmosphere, while the actinic flux within the none or weak ozone absorption range at the top of the atmosphere doubles compared to that in the clear atmospheric condition . However, within the strong O_3 absorption range the actinic flux at the top of the atmosphere is not affected by the physical and synoptic state of the lower atmosphere since the energy reflected and scattered upward by the earth's surface, air molecules, aerosols, and droplets of clouds has been almost absorbed by O_3 molecules before it can reach outer space.

The effect of different vertical structures of liquid water content on the radiation field was also invested in this study. Five hypothetical vertical cloud structures were made and their influences were compared. It is concluded that the radiation field outside a cloud is mainly controlled by the total number of droplets inside the cloud; the effect of local variation of the liquid water content inside a cloud on the actinic flux outside the cloud is not that significant. However, the actinic flux inside a cloud changes significantly with the variation of local water liquid content inside the cloud.

CHAPTER 6 EFFECTS OF AEROSOLS AND CLOUDS ON TROPOSPHERIC CHEMISTRY

The fields of the actinic fluxes are one of the most dominant factors defining the strengths (or rates) of atmospheric chemical reactions, as discussed in chapter 2. The diurnal variations of OH and the rates of the photodissociations associated with OH are such examples. The seasonal and latitudinal variations of radiation fields are also a major driving force for the related variations of trace gases and free radicals in the atmosphere, apart from the variations of emissions of trace gases. Besides its diurnal, seasonal, and latitudinal variations due to the relative position between the sun and the observation point in the earth's atmosphere, the field of radiation (or actinic fluxes for the atmospheric chemistry, precisely) is greatly affected by various atmospheric components, which either scatter or absorb the incident light. The atmospheric aerosols and clouds are two common atmospheric phenomena causing a great deal of change in the local radiation field, as described in the previous chapter. The purpose of this chapter is to estimate the effects of aerosols and clouds on the tropospheric chemistry.

This chapter starts with a demonstration of the response of photolysis processes to variation of radiation field by showing the temporal and spatial variations of photolysis rates of a number of photochemically reactive species for different atmospheric conditions. Then the tropospheric OH will be examined for a number of scenarios including the clean and

clean atmosphere, urban atmospheric condition, the variations of stratospheric O_3, and cloudy conditions to identify the importance of clouds and atmospheric aerosols for the atmospheric chemistry.

6.1. Variations of Photolysis Rates

A chemical reaction takes place only if stimulated by the addition of energy. In a laboratory the major source of energy is heat. Other forms of energy such as radiative energy, electric discharge, and ionizing radiation are used less frequently. In contrast, almost all the atmospheric chemical reactions are initiated by solar insolation since the heat content of ambient air is not sufficient for thermal activation, and lightning discharges and cosmic ionizing radiation are not globally significant in stimulating chemical reactions.

Although photolysis results from the radiative energy striking molecules and free radicals, the mere interaction between light and matter such as scattering processes are insufficient to stimulate a chemical reaction. For the theory of photochemistry, radiative energy can become photochemically effective only if the energy is absorbed by molecules or free radicals. Furthermore, the energy must be incorporated into a molecule or free radical. Such a equivalent unit of radiative energy is photon. The absorption of radiative energy by molecules or free radicals, however, is not necessary to produce a certain photochemical reaction since the excited molecules or free radicals due to absorption of radiative energy may simply give off the energy as radiation, transfer it into heat, dissipate it by collision, utilize the energy for chemical transformation, transfer all or part of the

energy to other molecules or free radicals that then react further, or enter into some chemical reactions directly. The fate of the excited molecules and free radicals depend not only on the photochemical nature of the molecules and free radicals and the amount of energy they receive, but also on the availability of other molecules and free radicals in the environment to interact these excited species.

The mathematical formula for the rate of the photolysis of a molecule or free radical have been shown in eq. 2.31 in chapter 2; i.e.,

$$k_m = \int_{\lambda_1}^{\lambda_2} \sigma_m(\lambda,T)\Phi_m(\lambda,T)j(\lambda,\theta)d\lambda = \Sigma_j \overline{\sigma_m(\lambda_j,T)} \cdot \overline{\Phi_m(\lambda_j,T)} \cdot \overline{J(\lambda_j,\theta)} \qquad (6.1)$$

where σ_m is the absorption cross section of species m at wavelength λ and temperature T, denoting the amount of incident energy removed by the species; Φ_m is called quantum yield of species m, which define the final outcome of the excited species. It actually reflects the ability of a photochemically reactive species to participate in a certain photolysis process after it absorbs radiative energy. Suppose that $m1$ out of $n1$ ($m1 \leq n1$) excited species m would proceed a certain photolysis i. Then the quantum yield of species m involving in the ith photolysis can simply expressed as:

$$\Phi_m = \frac{\text{number of excited molecules } m \text{ involved in the photolysis } i}{\text{total number of photons absorbed (or excited molecules)}} = \frac{m1}{n1} \qquad (6.2)$$

j in eq. 6.1 is the monochromatic actinic flux, which is the integral of monochromatic intensity (or radiance) over the whole sphere, 4π. J is the total actinic flux within the wavelength range from λ to $\lambda+\Delta\lambda$, i.e.,

$$\overline{J(\lambda_j,\theta)} = \int_{\lambda_j}^{\lambda_j+\Delta\lambda} j(\lambda,\theta)d\lambda \approx j(\lambda_j,\theta)\Delta\lambda \tag{6.3}$$

It should be noted that all the actinic fluxes calculated in the previous section are the *J* rather than j values.

Combining the actinic fluxes calculated in the previous chapter with the cross sections and quantum yields of a number of photochemically active species, which are taken from DeMore, et al. (1985), the rates of these photodissociations can be calculated. Fig. 6.1 shows the vertical profiles of the rates of 12 photolysis at *0°* solar zenith angle for the clear and clean atmospheric condition, which neglects all the effects of aerosols and clouds. Almost all the photolysis rates increase apparently with height, except for the photodissociations of NO_3, which only increase slightly with height. As described in the previous chapter, the actinic flux decreases rapidly with decreasing height in the strong O_3 absorption wavelength, while the actinic flux only increases slightly with height in the wavelengths greater than 410 nm since the effects of Rayleigh scattering and O_3 absorption are very weak in these wavelengths. Thus it is understood that the feature, which photolysis rates generally increases with height, results from the increase of actinic flux with height.

However, the field of the actinic flux is not the only factor causing the variation of photodissociation rates, the variations of the cross sections and quantum yields with wavelength also largely affect the values of the rates. Based on eq. 6.1, each photochemically reactive species has a so-called photochemically reactive wavelength range, and the integral of the product of the cross section, the quantum yield, and the actinic flux

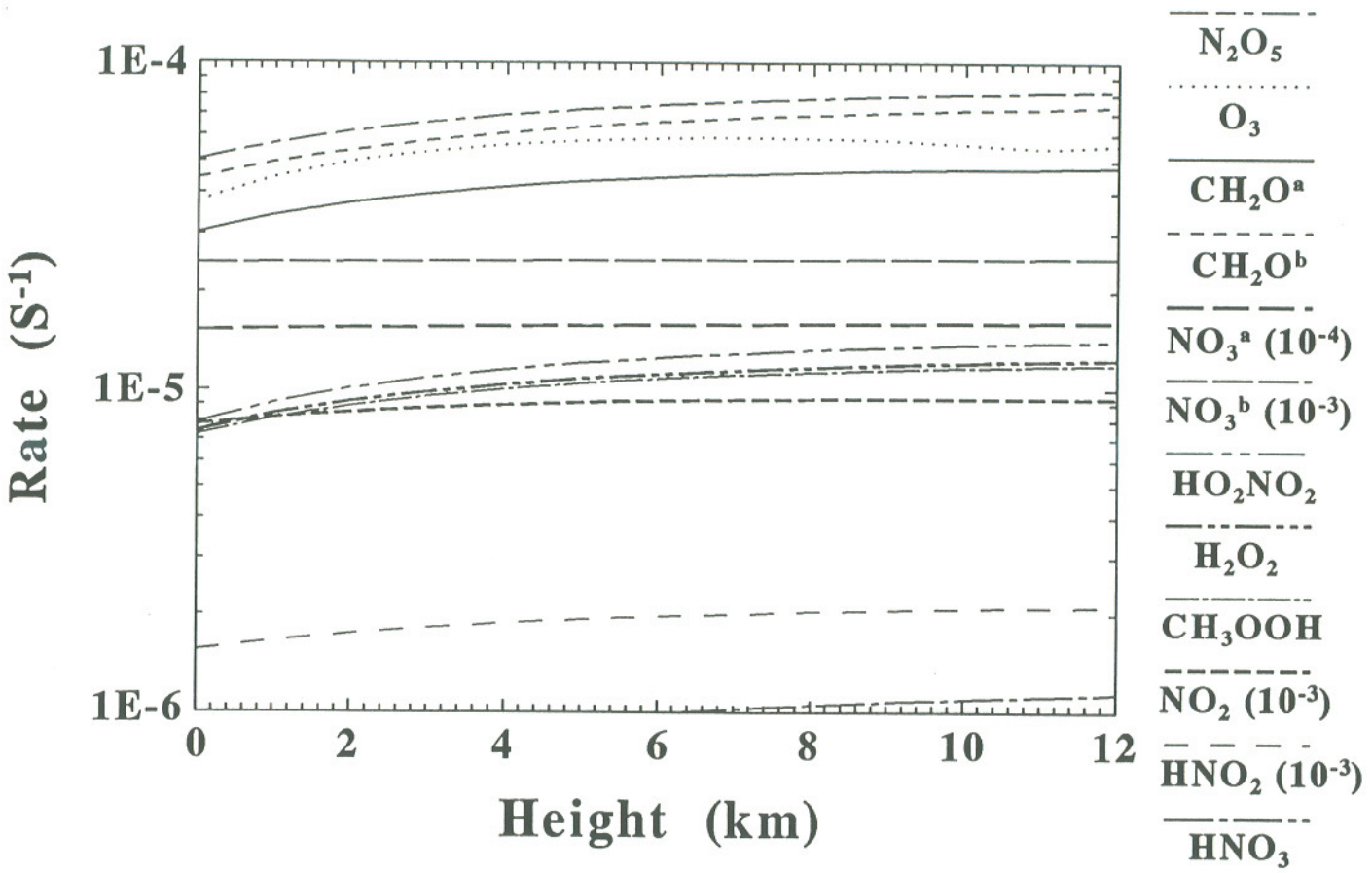

Fig. 6.1 Vertical profiles of the rates of 12 photodissociations at *0°* solar zenith angle for the clear and clean atmospheric condition, where the products of all the photodissociations are listed in table 2.1a, and $CH_2O^a + h\nu \rightarrow H + HCO$; $CH_2O^b + h\nu \rightarrow H_2 + CO$; $NO_3^a + h\nu \rightarrow NO_2 + O$; $NO_3^b + h\nu \rightarrow NO_2 + O$.

over the wavelength range is much larger than the integral of the product over the wavelength outside the range. The photolysis rates of the species with reactive wavelength range below 350 nm, such as HO_2NO_2, CH_3OOH, and HNO_3, increase more rapidly with height than those with the reactive wavelength extending to beyond 350 nm, like those of NO_2 and HNO_2, since the actinic flux increases with wavelength and the increase of the actinic flux with height actually decreases with wavelength. The activated wavelength for the photolysis of NO_3 extends up to about 700 nm (DeMore et al., 1985), resulting in slightly vertical increases of photolysis of NO_3 at $0°$ zenith angle since the vertical variation of actinic flux is negligible in the troposphere for small zenith angle and wavelength greater than 400 nm.

For some photochemically reactive species, the quantum yields and cross sections also change with height, leading to some vertical variations of photolysis rates although the variations of quantum yields and cross sections with temperature or pressure are small compared to the vertical variations of the actinic flux for the activated wavelength ranges. For example, as shown in fig. 6.2b, the quantum yield of O_3 decreases with height for the wavelength greater than 300 nm due to its temperature-dependent relationship (DeMore et al., 1985). The quantum yield, however, does not decrease with height around the tropopause, from 11 to 12 km, where the temperature is constant according to the U.S. Standard Atmosphere (U.S. Standard Atmosphere, 1976). The decrease of the quantum yield of O_3 with height tend to reduce the increase of the photolysis rate of O_3 with height, resulting from the increase of the actinic flux with height in the related wavelength range. On the other hand, as shown in fig. 6.2a, the cross section of O_3 decreases with wavelength

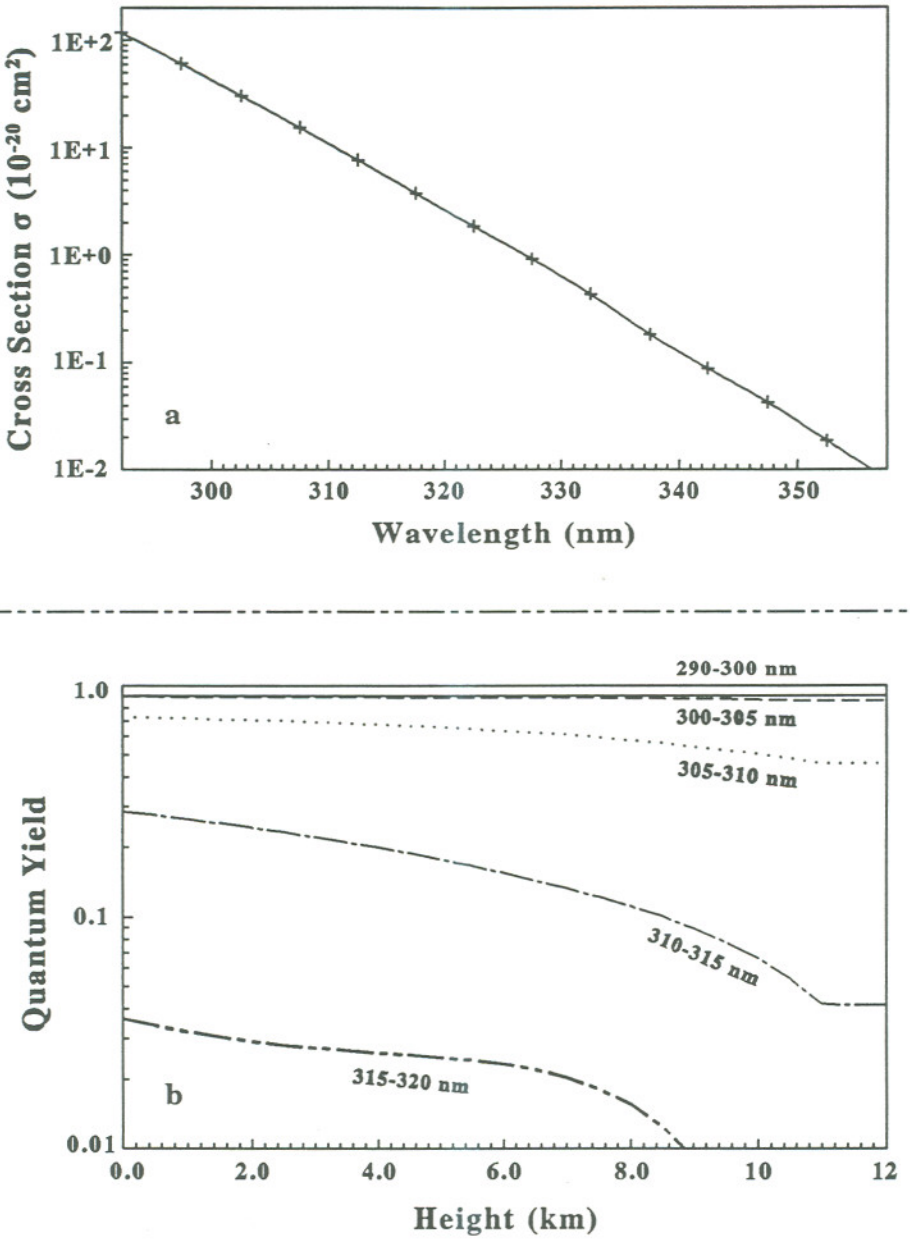

Fig. 6.2 Absorption cross section (*fig. 6.2a*) and quantum yield (*fig. 6.2b*) of the O_3.

within the reactive wavelength range, where the actinic flux increases with height. Thus the decrease of cross section of O_3 and the increase of the actinic flux also offset each other. The combination of the decrease of the quantum yield and the increases of the actinic flux with height and wavelength, and decrease of the cross section with wavelength make the photolysis rate of O_3 have a unique vertical profile, as shown in fig. 6.1.

Fig. 6.3 shows the vertical profiles of the photolysis rates of the photochemically active species, shown in fig. 6.1 but at a larger zenith angle, *86°*. For the large zenith angle, the magnitudes of photolysis rates of all species are smaller than those at zero zenith angle in response to a large reduction of the actinic flux from zero zenith angle to the large zenith angle, as described in the previous section. Compared fig. 6.3 with fig. 6.1, the degree of the decreases of the photolysis rates with decreasing height at the large zenith angle is larger than that at zero zenith angle, resulting from a larger decrease of the actinic flux with height at the large zenith angle than at zero zenith angle. In addition, the decrease of the quantum yield of O_3 with height and wavelength, along with the decrease of the cross section with wavelength and increase of the actinic flux with height and wavelength, results in the non-monotonously increase of the photolysis rate of O_3 with height.

In this study, the photolysis rates of a series of photochemically reactive species were also calculated and compared for the four different atmospheric conditions: the clear and clean atmosphere, the urban atmosphere, the urban air with a one-km dense stratus located at 1.5 km above the earth's surface, and the urban air with a one-km dense altostratus at 5.5 km above the surface (for the detailed information about the four conditions, see two previous chapter). Fig. 6.4 compares the vertical profiles of the photodissociation rates of

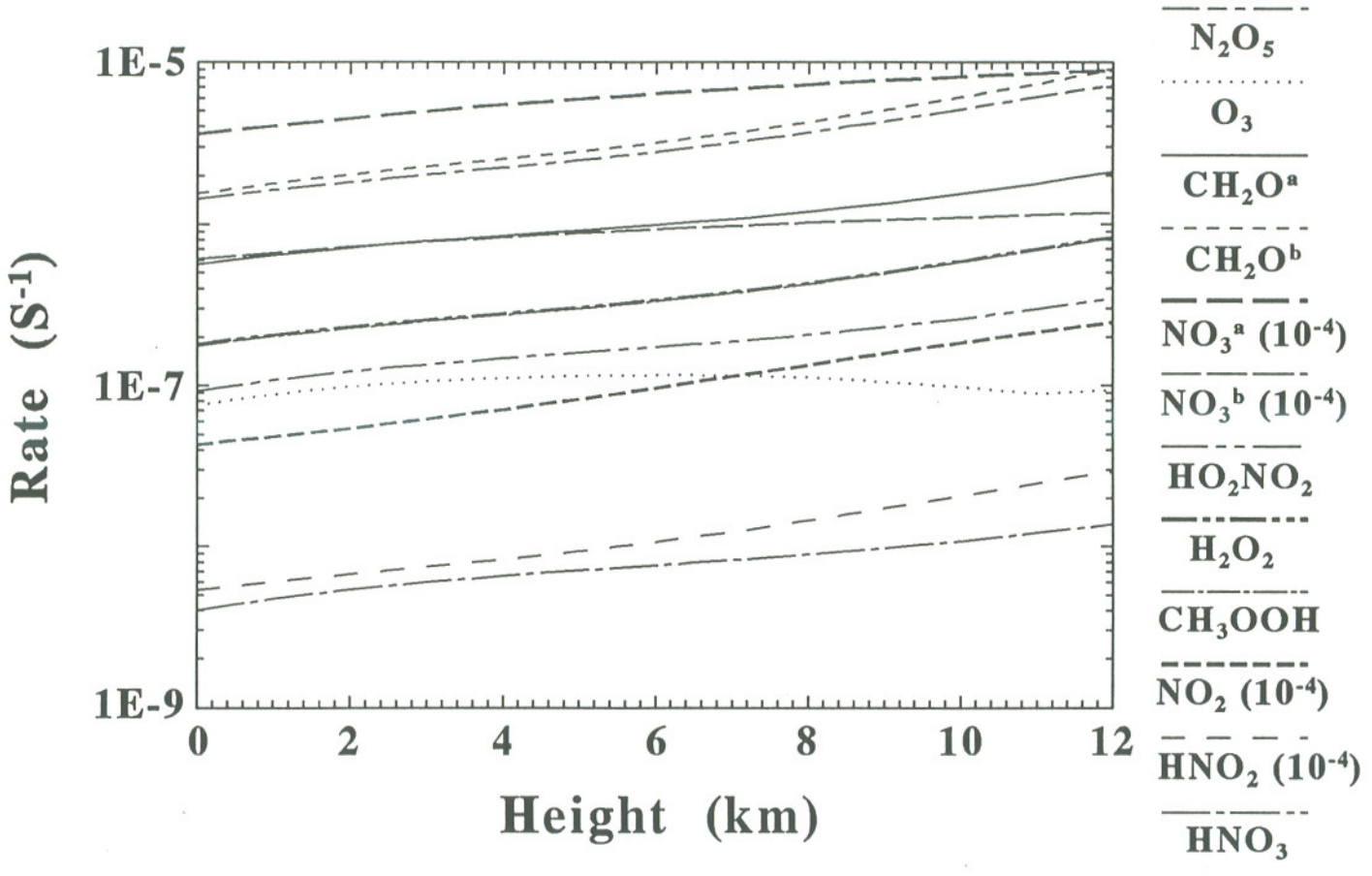

Fig. 6.3 Vertical profiles of the rates of 12 photodissociations at *86°* solar zenith angle for the clear and clean atmospheric condition, where the products of all the photodissociations are listed in table 2.1a, and $CH_2O^a + h\nu \rightarrow H + HCO$; $CH_2O^b + h\nu \rightarrow H_2 + CO$; $NO_3^a + h\nu \rightarrow NO_2 + O$; $NO_3^b + h\nu \rightarrow NO_2 + O$.

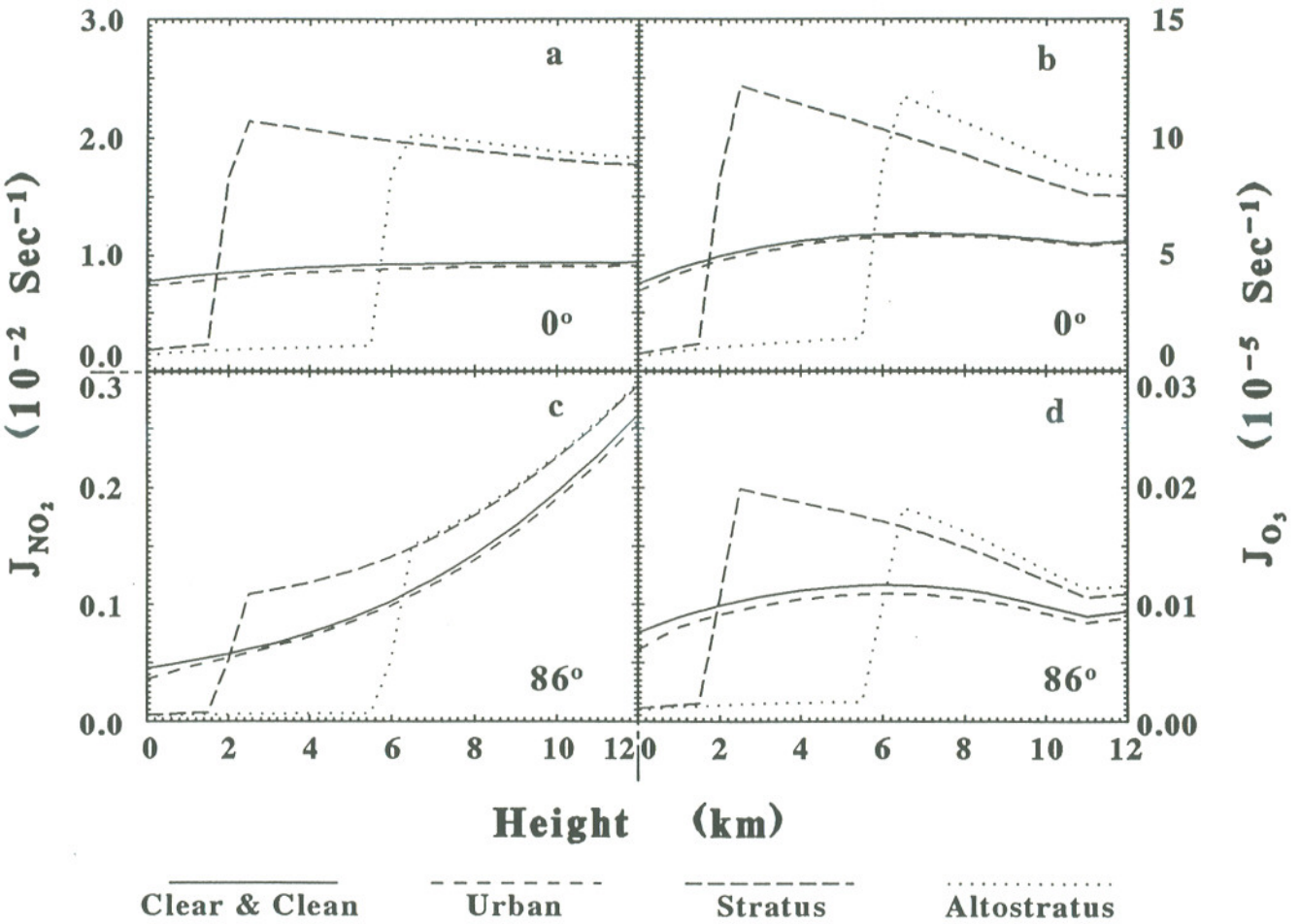

Fig. 6.4 Vertical profiles of the photodissociation rates of NO_2 and O_3 at 0° and 86° zenith angles for four different atmospheric conditions. See text for more information on four atmospheric conditions.

NO_2 and O_3 at 0° and 86° zenith angles for the four different atmospheric conditions. As shown in the previous chapter, the actinic flux is smaller in the clear urban atmosphere than in the clear and clean atmosphere due to the aerosol absorption and scattering, resulting in smaller photolysis rates of both O_3 and NO_3 in the clear urban atmosphere than in the clear and clean atmosphere. Due to the strong scattering of cloud droplets, the actinic fluxes above the one-km dense stratus or altostratus cloud are much larger than those at the same height in the cloud-free condition, while the actinic fluxes below the cloud are significantly smaller than those at the same height in the clear sky. As the result, the photolysis rates of both NO_2 and O_3 above the cloud are much larger than those in the clear atmosphere, and those below the cloud are much smaller than those in the clear condition.

It is interesting that the photolysis rates of NO_2 above both the stratus and altostratus clouds decrease with height at *0°* zenith angle but increase with height at the larger zenith angle, *86°*, while those of O_3 above the clouds decrease with height for both small and large zenith angles for almost all the heights in the troposphere except around tropopause. As discussed in the previous chapter, the actinic fluxes above the clouds decrease with height for small zenith angles, while the actinic fluxes increase with height for larger zenith angles. Thus the variations of the vertical profiles of the photodissociation of NO_2 above the clouds are mainly caused by those of the actinic fluxes. In contrast, the decreases of the photolysis rates of O_3 arise largely from the decreases of the quantum yields of O_3 with height, as shown in fig. 6.2. In the top of the troposphere, the quantum yield of O_3 does not decrease with height, as shown in fig. 6.2b. Accordingly, the photolysis rate of O_3 around the tropopause increases slightly with height due to the distribution of

the actinic flux there.

The variations of the photolysis rates of O_3 and NO_2 with various zenith angles from 0° to 90° at the earth's surface as well as at the tropopause, 12 km above the earth's surface are shown in fig. 6.5. As shown in figs. 6.5a and 6.5b, the photodissociation rates of both O_3 and NO_2 are much larger for clear atmosphere than for the cloudy air at the earth's surface, corresponding to the larger actinic fluxes at the earth's surface in the atmosphere without clouds than those with clouds, as discussed in the previous chapter. In contrast, for almost all zenith angles except for the large zenith angle close to 90°, or near sunrise or sunset, the actinic fluxes at 12 km above the earth's surface with a dense cloud underneath are larger than those without a cloud because of the accumulation of strong backscattering of the incident radiative energy by the cloud droplets. For a large zenith angle close to 90° zenith angle, most of the diffuse radiative energy scattered backward by the cloud droplets is either absorbed or blocked by O_3 or air molecules on the way to 12 km above the earth's surface due to the long traversing path, as described in the previous chapter. Accordingly the photolysis rates of NO_2 and O_3 around the tropopause are larger with a cloud underneath than those without a cloud and the differences among the photolysis rates in the four atmospheric conditions decrease with zenith angle to be almost negligible around 90° zenith angle, as shown in figs. 6.5c and 6.5d.

It should be noted that the photolysis rate of any photochemically reactive species is very small but not zero at 90° zenith angle, or at exact sunrise or sunset, when the actinic flux is not zero due to the effects of the curvature and refraction of the earth's atmosphere. Intuitively, it is not completely dark just before the sunrise or after sunset.

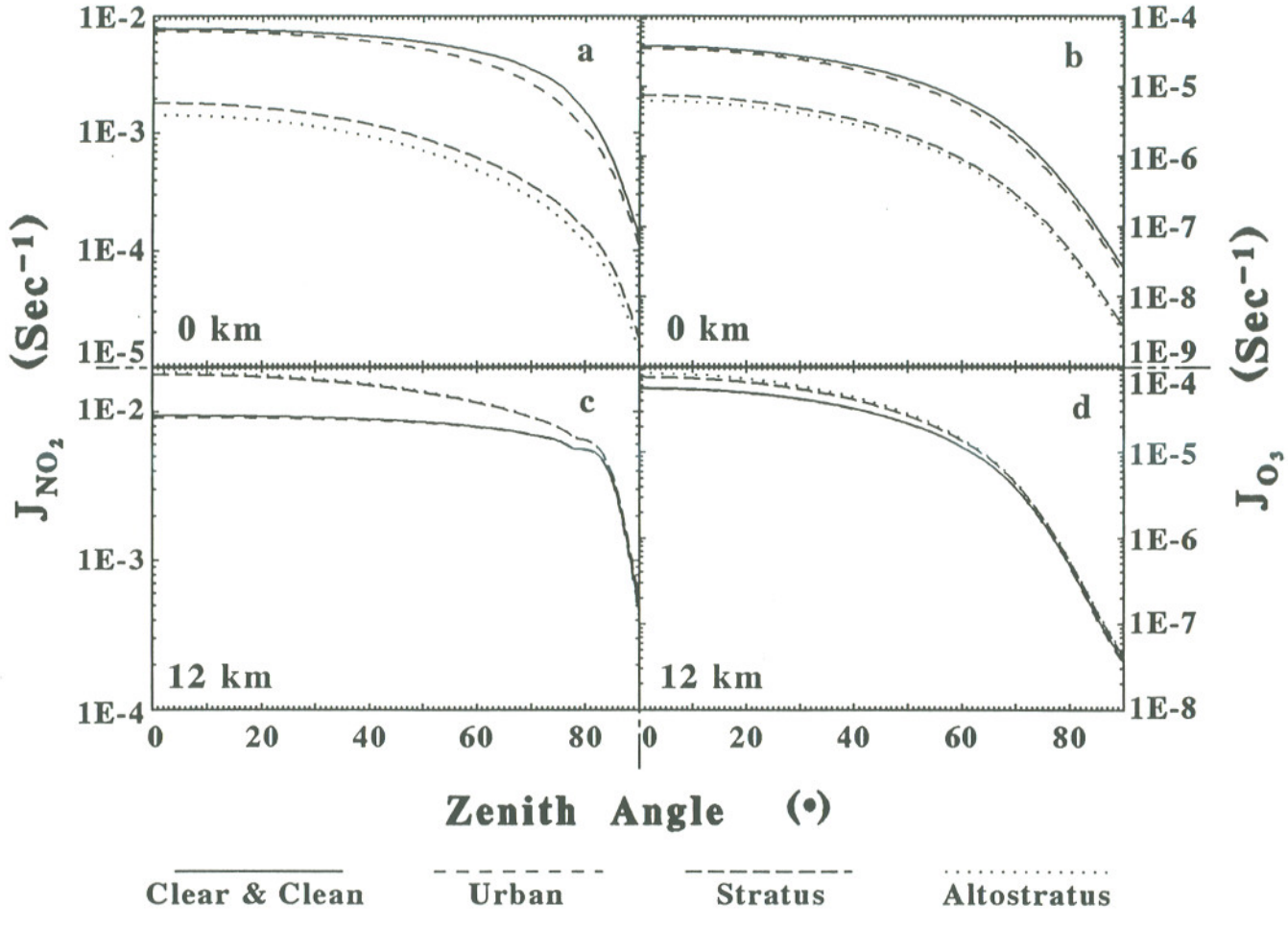

Fig. 6.5 Variations of the photolysis rates of O_3 and NO_2 with various zenith angles from 0° to 90° at the earth's surface as well as at the tropopause, 12 km above the earth's surface, for four atmospheric conditions.

6.2 Effects of Clouds and Aerosols on Tropospheric OH

With the photochemical model described in chapter 2, the optical model addressed in chapter 3, the radiative model depicted in the previous chapter, and the method to calculated the photolysis rates described in the previous section, the effects of clouds and aerosols on any photochemically reactive species in the troposphere can be estimated (Lu and Khalil, 1992c, 1993b and c). In this study OH is chosen as such a species, for it plays a significant role in tropospheric chemistry.

There are seven scenarios created to study the possible variation of tropospheric OH. The first four scenarios are the four atmospheric conditions, described in the previous chapters and section. They are *CA* (clear and clean atmosphere), *UA* (clear urban atmosphere), *ST* (urban air with a one-km dense stratus cloud at 1.5 km above the earth's surface), and *AT* (urban air with a one-km dense altostratus cloud at 5.5 km above the surface). The fifth scenario, namely *2AE*, is set by only doubling the concentration of atmospheric aerosol at each height without changing other conditions of the clear urban atmosphere. The last two scenarios, i.e., $1.25O_3$ and $0.75O_3$ are chosen respectively by increasing and decreasing the current stratospheric O_3 level by 25%. These scenarios are chosen to study the effects of clouds and aerosols on tropospheric chemistry as well as to compare the effects with the possible changes of tropospheric chemistry due to the variation of stratospheric O_3.

Fig. 6.6 shows the vertical profiles of diurnally averaged OH concentrations for the seven different scenarios. It is obvious that the effects of atmospheric aerosols are mainly

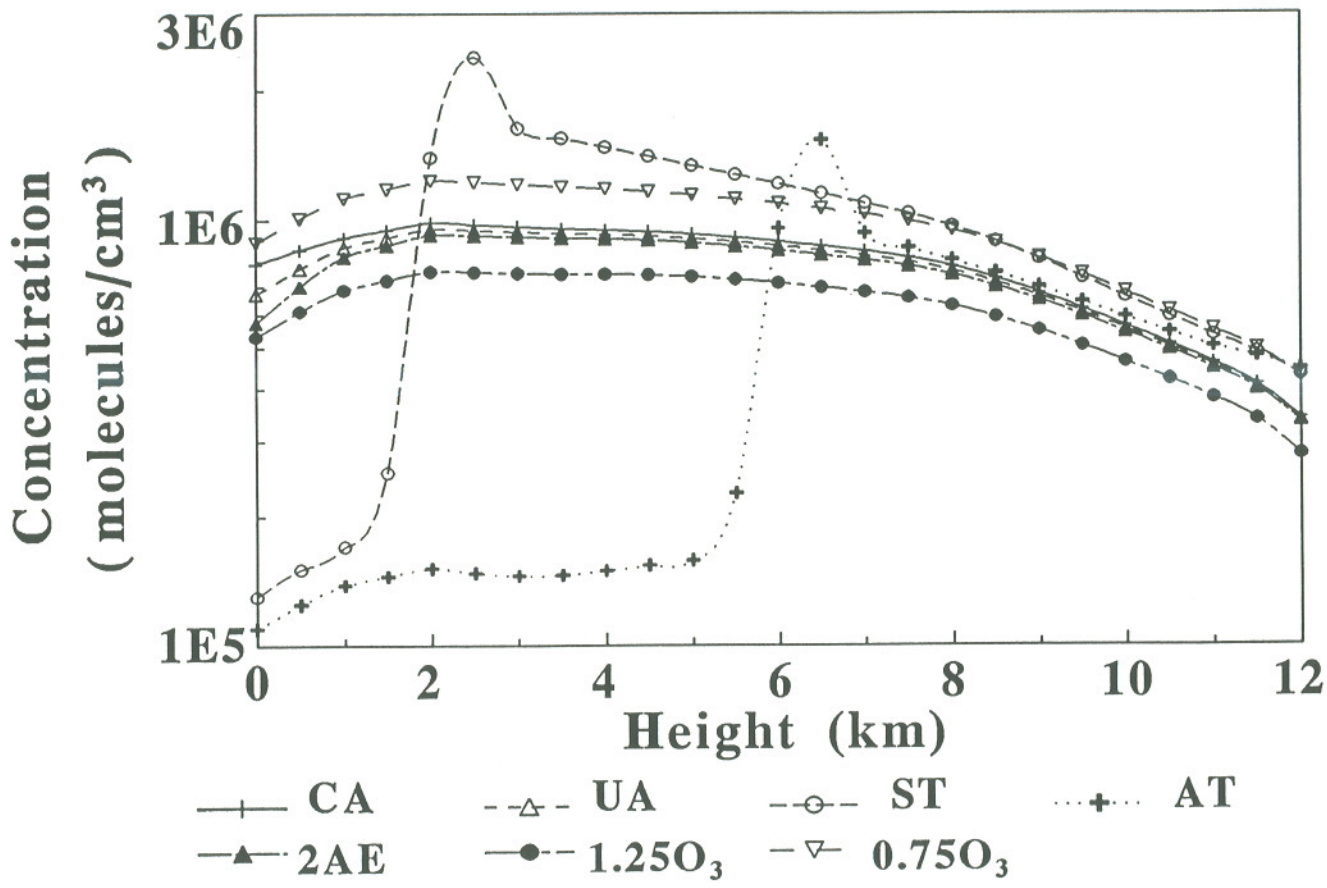

Fig. 6.6 Vertical profiles of diurnally averaged OH concentrations for the seven different scenarios. See text for the definitions of legend names corresponding to seven scenarios.

limited in the atmospheric boundary layer, or within the lowest 1.5 km, even for the case where the aerosol concentrations are doubled for all heights, as shown in this figure. However, the effects of clouds are substantially large on the tropospheric OH. Below the cloud, either the low dense stratus or the high heavy altostratus, the OH concentrations are much smaller in a cloudy sky than in a clear atmosphere. The reason for such a feature is that a cloud blocks the radiative energy to pass through it, resulting in smaller actinic fluxes and thus the lower photolysis rate of O_3 below the cloud compared to those without the cloud since the photodissociation of O_3 is the primary source of OH. In contrast, the OH concentration above a cloud is higher in a cloudy air than in a clear sky, resulting from the higher actinic fluxes above the cloud due to the backscattering of the incident light by cloud droplets.

Inside a cloud, the diurnally averaged OH concentrations increase significantly with height, as shown in fig. 6.6. The quick increase of actinic flux with height inside the cloud, as discussed in the previous chapter, is the prevailing reason for this feature. It should be mentioned that in order to fit better the chemistry inside the cloud, two aspects of the photochemical model was modified in this study. First, instead of adapting the H_2O vapor data set of Logan et al. (1981), a 0.77 of relative humidity, recommended by Manabe and Wetherwald (1967), was chosen to calculate the vertical profiles of water molecules in a clear air and outside the cloud in a cloudy sky, while the relative humidity inside the cloud is assumed to be 1. Thus according to the definition of the relative humidity and Clausius-Clapeyron equation, the water vapor pressure can be expressed as:

$$e = \begin{cases} 0.77 E_0 \exp\left\{\dfrac{L}{R_w}\left(\dfrac{1}{273} - \dfrac{1}{T}\right)\right\} & \text{outside clouds} \\ E_0 \exp\left\{\dfrac{L}{R_w}\left(\dfrac{1}{273} - \dfrac{1}{T}\right)\right\} & \text{inside clouds} \end{cases} \tag{6.4}$$

where E_0=6.11 mbar is the saturation vapor pressure of H_2O at 273°K; R_w=0.287/0.622=0.461 $Jg^{-1}°K^{-1}$) is the gas constant for water vapor; L is the latent heat of the vaporization, which can be computed from the expression for a perfect gas (Stone and Carlson, 1979):

$$L = 2510 - 2.38 \cdot (T - 273) \tag{6.5}$$

Incorporating eq. 6.4 into the ideal gas law, the number density of water molecules at different heights can be calculated from the following expression:

$$n_w = \frac{e \cdot M}{P} = \begin{cases} 0.77 \cdot \dfrac{E_0 \cdot M}{P} \cdot \exp\left\{\dfrac{L}{R_w} \cdot \left(\dfrac{1}{273} - \dfrac{1}{T}\right)\right\} & \text{outside clouds} \\ \dfrac{E_0 \cdot M}{P} \cdot \exp\left\{\dfrac{L}{R_w} \cdot \left(\dfrac{1}{273} - \dfrac{1}{T}\right)\right\} & \text{inside clouds} \end{cases} \tag{6.7}$$

where P is the atmospheric pressure; T is the atmospheric temperature; M is the number density of the atmosphere.

Besides using the above formula to calculate the number density of water molecules inside and outside the clouds, the heterogeneous loss rates for the water-soluble species

included in the photochemical model such as nitrogen-containing acids, H_2CO, CH_3OOH are increased by one order of magnitude at a given height inside clouds relative to those at the same height in a clear atmosphere to take into account the enhancement of wet removal processes inside clouds. From fig. 6.6, it is apparent that the negative feedback of clouds on tropospheric OH due to the increases of heterogeneous processes inside clouds cannot offset the positive feedbacks of clouds on tropospheric chemistry due to the increases of H_2O molecules as well as the actinic fluxes inside clouds.

The tropospheric OH level is sensitive to the stratospheric O_3 level. When the stratospheric O_3 decreases, more incident radiative energy reaches troposphere, resulting in an increase of photodissociation of O_3, which causes higher OH level in the troposphere. In contrast, the tropospheric OH concentration decreases when field of the actinic fluxes becomes weak due to an increase of the stratospheric O_3 level. As shown in fig. 6.6, the vertical profiles of OH concentrations corresponding to the positive and negative 25% of variations of the current stratospheric O_3 level are respectively located below and above the vertical profile of OH in the clear urban atmosphere, defining a upper and a lower limits of tropospheric OH concentration due to the variation of the stratospheric O_3. If the aerosol concentration is doubled in the urban air, the surface OH concentration is very close to that when the stratospheric O_3 level were increased by 25%. This indicates that the polluted urban air with high aerosol concentration will be slow the atmospheric chemical process at the earth's surface. When a cloud, either low dense stratus or high heavy altostratus, appears, the OH concentration below the cloud base is much smaller than the lower limit of OH level caused by a 25% increase of the current stratospheric O_3, while OH

level above the cloud is close or even larger than the upper limit of the OH concentration due to a 25% decrease of the current stratospheric O_3, as shown in fig. 6.6.

By averaging the diurnally averaged OH concentrations over the whole height from the earth's surface to the tropopause, the vertically and diurnally averaged OH concentrations for different scenarios were calculated. Fig. 6.7 shows these vertically averaged OH levels as well as the diurnally averaged OH concentrations at the earth's surface and at 12 km above the surface. By comparing the OH concentrations for the clear and clean air, the urban air, and the polluted urban air with the doubled current aerosol concentration, there are apparent differences among the surface OH concentrations among these three situations; however, there are very small variations among the OH concentrations at the tropopause as well as among the vertically averaged OH levels for the three scenarios. This indicates that the effect of the atmospheric aerosols on tropospheric chemistry are mostly limited in the lower troposphere.

The effects of clouds are substantially larger compared to those of the atmospheric aerosols. When a cloud appears in the troposphere, it reduces the surface OH concentration while increasing the OH level at the tropopause. As to the situation where the dense stratus or the altostratus appears, the surface OH level is much lower than the lower OH limit due to a 25% increase of the current stratospheric O_3 concentration, while the OH concentration at the tropopause is approximately equal to or even larger than that resulting from a 25% depletion of the current stratospheric O_3 level. The location of a cloud also affects the tropospheric chemistry. On the whole, the low dense stratus results in a vertically averaged OH concentration larger than that in clear air, while the high

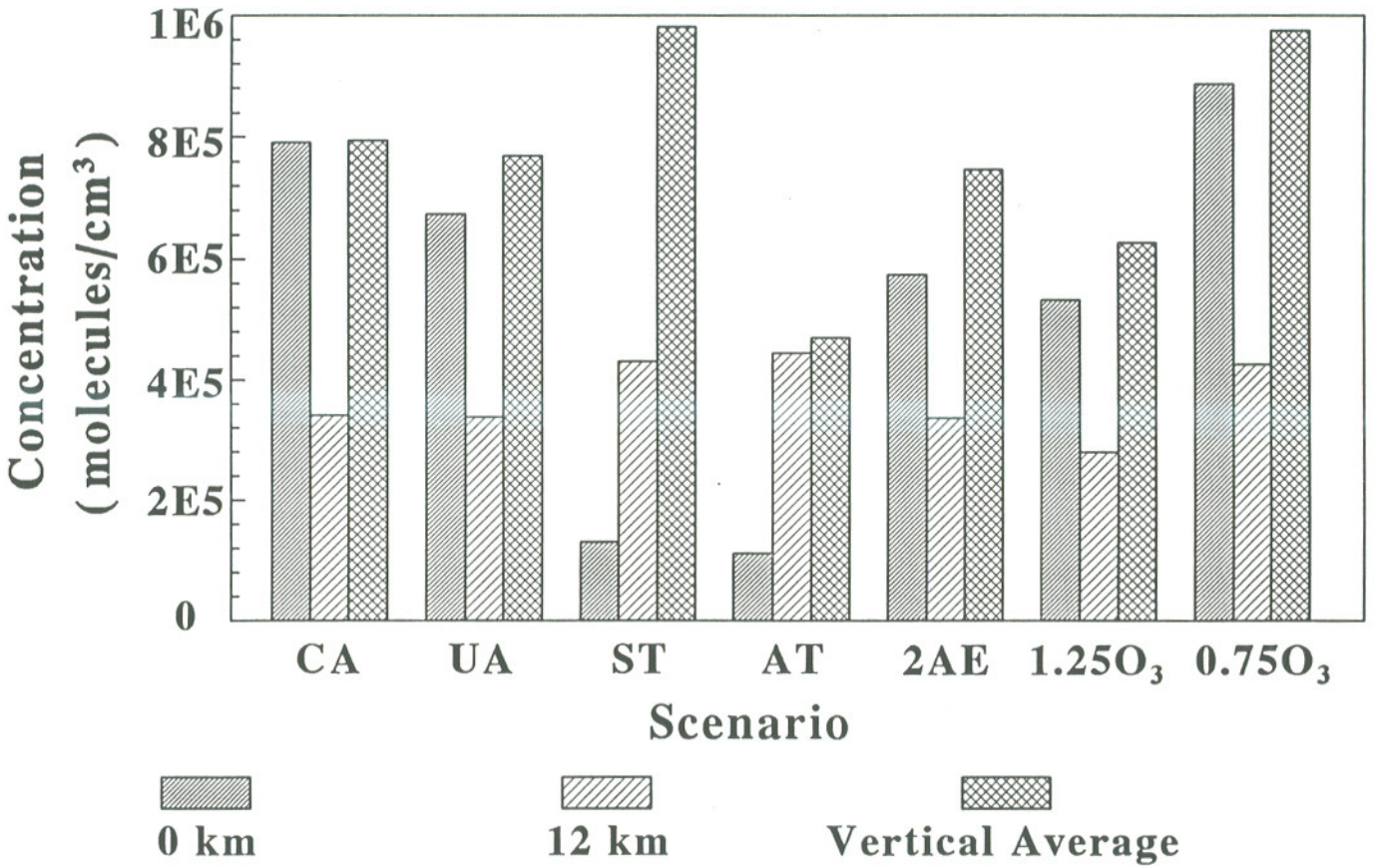

Fig. 6.7 Vertically and diurnally averaged OH concentrations as well as the diurnally averaged OH concentrations at the earth's surface and at 12 km above the surface for seven different scenarios.

altostratus cloud leads to a vertically averaged OH level smaller than that in clear atmosphere. Furthermore, the averaged OH level in the situation where the low dense stratus appears is even slightly larger than that when the stratospheric O_3 level depletes by 25% of the current level, while the whole tropospheric OH level in the high dense altostratus cloud is apparently lower than that when the stratospheric O_3 concentration increases by 25% of the current level. Consequently, the contribution of clouds to tropospheric chemistry could be comparable or even larger than the effects of significant change of the stratospheric O_3 such as depletion of the stratospheric O_3, as clearly shown in fig. 6.7.

6.3 Summary

By coupling the optical model and the radiative transfer model with the photochemical model, the effects of clouds and atmospheric aerosols on tropospheric chemistry were compared. The effect of aerosols on OH chemistry is only limited in the atmospheric boundary layer, while clouds affect the radiation in the whole troposphere. Specifically, the OH concentrations below a cloud could be reduced significantly by a dense cloud and those above the cloud would increase compared to the OH levels in a clear atmosphere. The tropospheric OH level, on the whole, could be increased by low clouds but decreased by high clouds, and the deviation of the tropospheric OH concentration caused by the appearances of clouds could be comparable to or even larger than those resulting from large variations of the stratospheric O_3 level. For example, the effect of low clouds such as a low dense stratus on tropospheric chemistry could be even greater than the

effects of stratospheric O_3 depletion.

The physics and chemistry inside clouds are very complicated and the parameterization considered in this study may not represent the real heterogeneous interactions inside the cloud. Nonetheless the effects of clouds on the tropospheric chemistry outside clouds are significant. It should be mentioned that the urban condition frequently used in this study does not consider the effects of pollution with high concentrations NO_x and NMHC although high concentration of aerosols is taken into account.

CHAPTER 7 CONCLUSIONS AND DISCUSSION

In this dissertation, a detailed time-dependent multiple one-dimensional photochemical model (M1DPCM) has been developed to study tropospheric chemistry and the distributions of a series of reactive species with special focus on the strongest oxidant in the global atmosphere, OH. The model, based on the mass continuity theory, includes the physical characteristics of the atmosphere such as temperature, pressure, solar intensity, and the turbulent transfer, as well as the chemical production and removal processes of HO_x, NO_x, O_x, and CH_iO_j, and heterogenous processes.

The OH concentration calculated with M1DPCM shows a strong diurnal variation as well as apparent changes with altitude, season, and latitude. The large diurnal variation of OH results from the corresponding variation of the actinic flux due to the natural day-night exchange, while the altitudinal, latitudinal, and seasonal variations of OH are caused by both the related changes of the actinic flux and distributions of a number of trace gases. On the whole, the globally, seasonally, and diurnally averaged OH concentration is 8.2×10^5 molecules/cm^3 with about 10% greater abundance of OH in the northern hemisphere than in the southern hemisphere, corresponding to more O_3 and NO_x in the northern hemisphere.

The characteristics of nighttime OH was one of major interests in this study. The model results indicate that although, on the whole, the globally averaged nighttime OH

concentration, $1.3\times10^{+4}$ molecules/cm^3, is two orders of magnitude smaller than the daytime OH concentration, $1.6\times10^{+6}$ molecules/cm^3. Nighttime OH is important in the mid-latitudes and mid-troposphere, where about 10% of removal processes resulting from OH takes place during the nighttime.

The possible secular variation of OH concentration over a wide range of climatic conditions from ice ages to the present were also studied with the M1DPCM. It is concluded that the OH concentration, on the whole, decreases slightly from ice ages to the present, resulting from the compensation of the concurrent increases of sinks and sources of OH. However, the averaged nighttime OH concentration in ice ages, calculated with the model, is about three times as large as that at the present, arising mainly from the significant increase of the two major sinks of OH, CO and CH_4, because the nighttime OH is insensitive to the major source of daytime OH, O_3.

Consequently the current OH concentrations, calculated with M1DPCM, are generally consistent with various measurements and other model results (For more information on measurements and model results, see Altshuller, 1989; Thompson, 1992); however, the differences among the past OH levels calculated with various photochemical model are relatively large, mainly resulting from differences of the input data sets used by different model.

The concentrations of seventeen other reactive species calculated along with OH were discussed this dissertation and our model results agree with other model results (e.g. Logan et al., 1980; Thompson and Cicerone, 1982). Generally, the features of these

species are linked with the features of OH since each of these species influences OH, directly or indirectly. Among these species, the hydroperoxyl radical, HO_2, was studied in detail since it acts as a buffer of OH. Similar to OH, HO_2 concentration also shows a strong diurnal variation as well as obvious seasonal, latitudinal, and altitudinal changes. Like OH, vertically the maximum daytime HO_2 concentration appears at the earth's surface or in the lower troposphere but the maximum nighttime OH is in the middle troposphere.

In order to find the most important chemical reactions affecting tropospheric OH, all the reactions directly affecting OH and its most important buffer, HO_2, were compared. it is concluded that only five reactions directly control the tropospheric OH concentration: the reaction of $O(^1D)$ with H_2O and the reactions of HO_2 with NO and with O_3 produce most of the tropospheric OH, while CO and CH_4 consume most of the OH. However, all the six direct sinks of HO_2 included in this model are approximately equally important during daytime, and variations of these sinks will lead to changes of OH concentration since HO_2 is the most important buffer of OH. At night the reactions of HO_2 with O_3 and with NO_2 are dominant over other direct sinks of HO_2. The most dominant direct source of HO_2 is the reaction between H and O_2, and the dissociation of HO_2NO_2 is also an important source of HO_2, especially at night when it generates even more HO_2 than 60% of nighttime HO_2. Since the reaction between O_2 and HO_2 is the only significant source of nighttime OH, it can be further inferred that atmospheric HO_2NO_2 is a dominant source for the nighttime OH.

To further understand the mechanism of removal processes of the tropospheric OH, another multiple one-dimensional photochemical feedback model has been developed to

evaluate the total contributions to tropospheric OH from CO and CH_4, which are the largest and the second largest direct sinks of OH. Based on the mass conservation law, this model is created by tracing a series of reactions and products, which are initiated by the direct reactions of OH with CO or CH_4. With this method, not only the direct contributions of CO and CH_4 but also all the feedbacks of the direct contributions are taken into account. By using this method, it is concluded that each feedback of CO and CH_4, especially the buffer feedback or organics feedback, is important even compared to the direct contribution. Specifically, the organics feedbacks of CH_4 further remove OH, while the buffer feedbacks and oxygen feedbacks of both CO and CH_4 recover some of the OH consumed directly by CO and CH_4. On the global scale, the total feedbacks of both CH_4 and CO are negative feedbacks of the direct effects, recovering the OH directly consumed by the two species. However, the total feedback of CH_4 is much smaller than that of CO due to the cancellation between the organics feedback and the other two feedbacks of CH_4. Consequently, CH_4 along with its feedbacks may remove even more OH than CO along with its feedbacks, although on the global scale, CO directly consumes more than twice as much OH as CH_4 directly does.

Almost all atmospheric chemical reactions are initiated by solar radiation. Thus it is essential to know the radiation field in order to better understand the chemical processes in the atmosphere. In order to understand the radiative transfer processes, one must know the optical properties of atmospheric components. In this study, the numerical method to calculate the absorption and scattering cross sections and the asymmetry factors of the atmospheric aerosols and droplets has been presented. By calculating and comparing the

optical thickness of various atmospheric components, it is concluded that in the ultraviolet and visible wavelengths (290~700 nm), the effect of O_3 absorption dominates that of molecular scattering for wavelength less than 310 nm, and the effect of aerosol scattering becomes important for $\lambda \geq 500$ nm, while the influence of molecular scattering is large inbetween. However, the optical effect of a cloud may be substantially larger than all the effects of O_3, air molecules, and the atmospheric aerosols.

As one important part of this study, the detailed numerical scheme to calculate the atmospheric asymmetry factor have been described in detail in this dissertation. Furthermore, the distinction between the atmospheric asymmetry factor and the asymmetry factors of various types of atmospheric scatters such as cloud droplets and aerosol particles was presented and illustrated. Basically the asymmetry factor of a certain type of scatterers, which represents the relative strength of the forward scattering for this type of scatterers, relies on the size distribution, the number density, and the optical properties of this type of scatterers. In contrast, the atmospheric asymmetry factor at a given height, which corresponds to the relative intensity of the forward scattering of all types of scatterers at this height, depends on the physical states and optical properties of all kinds of the atmospheric scatterers, and it changes not only with wavelength but also with height. Assuming that the actual asymmetry factor is equal to the asymmetry factor of any kind of scatters can lead to a large error in estimate of the radiation field for photochemical model calculation.

Based on conservation of radiative energy and the two-stream technique, a detailed radiative transfer model has been developed to study the fields of the irradiance and the actinic flux in the ultraviolet and visible wavelengths for various atmospheric conditions

including the clear and clean air, clear urban atmosphere, and cloudy urban air with different types of clouds. The magnitude of variation of the actinic flux depends ont only on zenith angle, which is caused by the relative position between the sun and the earth, but also on wavelength and altitude, which mainly result from the optical properties and vertical distributions of various atmospheric components. For example, the actinic flux increases significantly with height in the strong O_3 absorption wavelengths around 300 nm, while it increases slightly with height in the zero-ozone absorption wavelengths. The effect of the atmospheric aerosols becomes important only in the atmospheric boundary layer, where most of the aerosols reside, while the effects of clouds on radiative fields can be substantially large. A cloud decreases greatly the actinic flux below it while increasing the actinic flux above it.

In this dissertation, the distinction between the irradiance and actinic flux are illustrated. The former is used for the climate modeling and the latter is for atmospheric chemistry modeling. Mistakenly replacing the actinic flux with the irradiance would lead to a significant error in calculation of photolysis rates. As another highlight of this study, the effect of different vertical structures of liquid water content of clouds on the radiation field was also explored. It is concluded that the effect of a cloud on the radiation field outside a cloud is mainly controlled by the total number of droplets inside the cloud; the effect of local variation of the liquid water content inside a cloud on the actinic flux outside the cloud is not that significant. However, the actinic flux inside a cloud changes significantly with the variation of local water liquid content inside the cloud.

Finally, by incorporating the optical model and the radiative transfer model with the

photochemical model, the effects of clouds and atmospheric aerosols on tropospheric chemistry were studied. It is concluded that the effect of aerosols on OH chemistry is only limited in the atmospheric boundary layer, while clouds affect the radiation in the whole troposphere. Specifically, the OH concentrations below a cloud could be reduced significantly by a dense cloud and those above the cloud would increase compared to the OH levels in a clear atmosphere. The tropospheric OH level, on the whole, could be increased by low clouds but decreased by high clouds, and the deviation of the tropospheric OH concentration caused by the appearances of clouds could be comparable to or even larger than those resulting from large variations of the stratospheric O_3 level. For example, the impact of low clouds such as a low dense stratus on tropospheric chemistry could be even greater than the effects of stratospheric O_3 depletion.

The micro and macro features of aerosols are complicated and variable, and heterogeneous processes in clouds and aerosols such as gas-aqueous equilibria, aqueous phase reactions inside clouds, transformation of urban aerosols, and heterogeneous reactions occurring on the surfaces of the polar stratospheric ice crystals (e.g. nitric acid trihydrate ice particles) and possibly on background sulfate particles in the lower stratosphere directly affect atmospheric chemical processes (e.g. Chameides, 1984; Jacob, 1986; Lelieveld and Crutzen, 1990; Anderson et al., 1991; Brasseur, 1991; Granier and Brasseur, 1991; Turpin et al., 1991). The effects of clouds and aerosols are significant and their mechanisms are very complex and variable. In addition, dry deposition and precipitation scavenging of trace gases and free radicals are important processes (e.g., Slinn, 1984; Sehmel, 1984; Sickles et al., 1989), which are connected with clouds and atmospheric chemistry. As future work, it

is desirable to directly model these important processes instead of parameterizing them.

REFERENCES

Altshuller, A. P., 1989, Ambient air hydroxyl radical concentrations: measurements and model predictions, *J. Air Poll. Asso. 39,* 704-708.

Anderson, D. E., Jr., and R. R. Meier, 1979, Effects of anisotropic multiple scattering on solar radiation in the troposphere and stratosphere, *Appl. Opt., 18,* 1955-1960.

Anderson, J. G., D. W. Toohey, and W. H. Brune, 1991, Free radicals within the Antarctic vortex: the role of CFCs in Antarctic ozone loss, *Science 251,* 39-46.

Atkinson, R. and A. C. Lloyd, 1984, Evaluation of kinetic and mechanistic data for modeling of photochemical smog, *J. Phys. Chem. Ref. Data 13,* 315-444.

Bates, D. R., 1984, Raleigh scattering by air, *lanet. Space Sci., 32*, 785-790.

Braslau, N., and J. V. Dave, 1973, Effect of aerosols on the transfer of solar energy through realistic model atmospheres. Part II: Partly-absorbing aerosols, *J. Appl. Meteo., 12,* 616-619.

Brasseur, G. P., 1991, Ozone depletion: a deepening, broadening trend, *Nature 352*, 668-669.

Campbell, M. J., J. C. Sheppard, F. J. Hopper, and R. Hardy, 1982, Measurements of tropospheric hydroxyl radical concentrations by ^{14}C tracer method, paper presented at the 2nd Symposium on the composition of the Nonurban Troposphere. AM. Meteorol. Soc., AGU, and NASA, Williamsburg, Va., May 25-28.

Campbell, M. J., J. C. Farmer, C. A. Fitzner, M. N. Henry, J. C. Sheppard, F. J. Hopper, R. Hardy, and V. Muralidhar, 1986, Radiocarbon tracer measurements of atmospheric hydroxyl radical concentrations, *J. Atoms. Chemi. 4*, 413-427.

Chameides, W. L. and A. Tan, 1981, The two dimensional diagnostic model for tropospheric OH: an uncertainty analysis, *J. Geophys. Res. 86,* 5209-5223.

Chameides, W. L., 1984, The photochemistry of a remote marine stratiform cloud, *J. Geophys. Res., 89*, 4739-4755.

Chan, C. Y., T. M. Hard, A. A. Mehrabzadeh, L. A. George, and R. J. O'Brien, Third-Generation FAGE instrument for tropospheric hydroxyl radical measurement, *J. Geophys. Res. 95,* 18,569-18,576.

Cicerone, R. J. and R. S. Oremland, 1988, Biogeochemical aspects of atmospheric methane, *Global Biochemical Cycles 2*, 299-327.

Crutzen, P. J. and L. T. Gidel, 1983, A two-dimensional photochemical model of the atmosphere, 2: the tropospheric budgets of the anthropogenic chlorocarbons CO, CH_4, CH_3Cl and the effect of various NO_x sources on tropospheric ozone, *J. Geophys. Res. 88,* 6641-6661.

Crutzen, P. J., 1991, Methane's sinks and sources, *Nature 350,* 380-381.

Crutzen, P. J. and P. H. Zimmermann, 1991, The changing photochemistry of the troposphere, *Tellus 43AB*, 136-151.

Davis, L. I., C. C. Wang, X. Tang, H. Niki, and B. Weinstock, 1982, Fluorescence measurements of OH at Niwot Ridge, paper presented at the 2nd Symposium on the composition of the Nonurban Troposphere. AM. Meteorol. Soc., AGU, and NASA. Williamsburg, Va., May 25-28.

Demerjian, K. L., K. L. Schere, and J. T. Peterson, 1980, Theoretical estimates of actinic (spherically integrated) flux and photolytic rate constants of atmospheric species in the lower troposphere, *Adv. Environ. Sci. Technol., 10*, 369-459.

Deirmendjian, D., R. Clasen, and W. Viezee, 1961, Mie scattering with complex index of refraction, *J. Opt. Soc. Am., 51*, 620.

DeMore, W. B., J. J. Margltan, M. J. Molina, R. T. Watson, D. M. Golden, R. F. Hampson, M. J. Kurylo, C. J. Howard, and A. R. Ravishankara, 1985, Chemical kinetics and photochemical data for use in stratospheric modeling, *JPL Publication 85-87,* NASA, JPL, Pasadena, California.

Donahue, N. M., and R. G. Prinn, 1990, Nonmethane hydrocarbon chemistry in the remote marine boundary layer, *J. Geophys. Res. 95,* 18,387-18,411.

Eisele, F. L., and D. J. Tanner, 1991, Ion-assisted tropospheric OH distributions, *J. Geophys. Res. 96,* 9295-9308.

Felton, C.C., J. C. Sheppard, and M. J. Campbell, 1988, Measurements of the diurnal OH cycle by a ^{14}C-tracer method, *Nature, 225,* 53-55.

Finlayson-Pitts, B. J. and J. N. Pitts, Jr., 1986, *Atmospheric Chemistry: Fundamentals and Experimental Techniques,* John Wiley & Sons, Inc, New York.

Fiocco, G., A. Mugnai, and W. Forlizzi, 1978, Effects of radiation scattered by aerosols on the photodissociation of ozone, *J. Atmos. Terr. Phys., 40,* 949-961.

Fishman, J. and P. J. Crutzen, 1977, A numerical study of tropospheric photochemistry using a one-dimensional model, *J. Geophys. Res. 82,* 5897-5906.

Fishman, J. and P. J. Crutzen, 1978, The distribution of the hydroxyl radical in the troposphere, *Atmospheric Science, Paper No. 284,* Dept. of Atmos. Science, Colorado State Univ., Fort Collins, Colorado.

Fung, I, J. John, J. Lerner, E. Matthews, M. Prather, L. P. Steele, and P. J. Fraser, 1991, Threee-dimensional model synthesis of the global methane cycle, *J. Geophys. Res. 96,* 13,033-13,065.

Goody, R. M., and Y. L. Yung, 1989, *Atmospheric Radiation, Theoretical Basis*, Oxford University Press, New York.

Granier, C. and G. Brasseur, 1992, Ozone and other trace gases in the arctic and Antarctic

regions: three-dimensional model simulations, *J. Geophys. Res., 96*, 2995-3011.

Hansen, J. E., and L. D. Travis, 1974, Light scattering in planetary atmospheres, *Space Sci. Rev., 16*, 527-610.

Hard, T. M., C. Y. Chan, A. A. Mehrabzadeh, W. H. Pan, and R. J. O'Brien, 1986, Diurnal cycle of tropospheric OH, *Nature, 322,* 617-620.

Hard, T. M., A. A. Mehrabzadeh, C. Y. Chan, and R. J. O'Brien, 1992, FAGE measurements of tropospheric HO with measurements and model of interferences, *J. Geophys. Res. 97*, 9795-9817.

Hough, A. M., 1988, The calculation of photolysis rates for use in global tropospheric modelling studies, *AERE Rept. R-13259*, 52 pp., Her Majesty's Stationery Office, London.

Hough, A. M., 1991, Development of a two-dimensional global tropospheric model: model chemistry, *J. Geophys. Res. 96,* 7325-7361.

Hubler, G., D. Perner, U. Platt, A. Tonnissen, and D. H. Ehhalt, 1984, Groundlevel OH radical concentration: new measurements by optical absorption, *J. Geophys. Res., 89,* 1309-1319.

Isaksen, I. S. A., K. H. Midtbo, J. Sunde, and P. J. Crutzen, 1977, A simplified method to include molecular scattering and reflection in calculations of photon fluxes and photodissociation rates, *Geophys. Norv., 31*, 11-26.

Jacob, J. D., 1986, Chemistry of OH in remote clouds and its role in the production of formic acid and peroxymonosufate, *J. Geophys. Res. 91,* 9807-9826.

Kanakidou, M. and P. J. Crutzen, 1993, Scale problems in global tropospheric chemistry modeling: comparison of results obtained with a three-dimensional model, adopting longitudinally uniform and varying emissions of NO_x and NMHC, *Chemosphere 26,* 787-802.

Kasting, J. F. and H. B. Singh, 1986, Nonmethane hydrocarbons in the troposphere: Impact on the odd hydrogen and odd nitrogen chemistry, *J. Geophys. Res. 91,* 13,239-13,256.

Khalil, M. A. K., and R. A. Rasmussen, 1983a, Sources, sinks, and seasonal cycles of atmospheric methane, *J. Geophys. Res. 88,* 5131-5144.

Khalil, M. A. K., and R. A. Rasmussen, 1983b, Increase and seasonal cycles of nitrous oxide in the earth's atmosphere, *Tellus, 35B,* 161-169.

Khalil, M. A. and R. A. Rasmussen, 1984a, Lifetime of methylchloroform (CH_3CCl_3), *Tellus, 36B,* 317-332.

Khalil, M. A. K. and R. A. Rasmussen, 1984b, Modeling chemical transport and mass balances in the atmosphere, Environmental Exposure from Chemicals, Editors: W. B. Neely and G. E. Blau, CRC Press, Inc, Boca Raton, Florida, 22-54.

Khalil, M. A. and R. A. Rasmussen, 1984c, Carbon monoxide in the earth's atmosphere: increasing trend, *Science 224,* 54-56.

Khalil, M. A., and R. A. Rasmussen, 1985, Causes of increasing methane: depletion of hydroxyl radicals and the rise of emissions, *Atmos. Env. 19*, 397-407.

Khalil, M. A. and R. A. Rasmussen, 1990a, Constrains on the global sources of methane and an analysis of recent budgets, *Tellus, 42B*, 229-236.

Khalil, M. A. K. and R. A. Rasmussen, 1990b, The global cycle of carbon monoxide: trends and mass balance, *Chemosphere 20,* 227-242.

Khalil, M. A. K. and R. A. Rasmussen, 1992, The global sources of nirtrous oxide, *J. Geophy. Res. 97*, 14,651-14,660.

Lacis, A. A., and J. E. Hansen, 1974, A parameterization for the absorption of solar radiation in the earth's atmosphere, *J. Atmos. Sci., 31*, 118-133.

Law and Pyle, 1991, Modeling the response of tropospheric trace species to changing source gas concentrations, *Atmos. Environ. 25A*, 1863-1871.

Leighton, P. A., 1961, *Photochemistry of air pollution,* Academic Press, Inc, New York.

Lelieveld, J. and P. J. Crutzen, 1990, Influences of cloud photochemical processes on tropospheric ozone, *Nature 343*, 227-233.

Lenoble, J, 1985, *Radiative Transfer in Scattering and Absorbing Atmospheres: Standard Computational Procedures,* A. Deepak, Hampton, Va.

Levine J., S., 1985, *The photochemistry of atmospheres - Earth, the other planets, and comets,* Academic Press, Inc, New York.

Levine, J. S., C. P. Rsinsland, and G. M. Tenille, 1985, The photochemistry of methane and carbon monoxide in the troposphere in 1950 and 1985, *Nature 318*, 254-257.

Levy, H., 1971, Normal atmosphere: Large radical and formaldehyde concentrations predicted, *Science, 173,* 141-143.

Liou, K. N., 1974, Analytic two-stream and four stream solutions for radiative transfer, *J. Atmos. Sci., 31,* 1473-1475.

Liou, K. N., 1980, *An Introduction to Atmospheric Radiation,* Academic, New York.

Liu, C. S. and W. B. Liu, 1990, *Atmospheric Radiation*, Nanjian University Press, Nanjian, China

Liu, S. C., J. R. McAfee, and R. J. Cicerone, 1984, Radon 222 and tropospheric vertical transport, *J. Geophys. Res. 89,* 7,291-7,297

Liu, S. C. and M. Trainer, 1988, Responses of the tropospheric ozone and odd hydrogen radicals to column ozone change, *J. Atmos. Chem. 6,* 221-233.

Logan, J. A., M. J. Prather, S. C. Wofsy, and M. B. McElroy, 1981, Tropospheric chemistry: a global perspective, *J Geophys. Res. 86,* 7210-7254.

Logan, J. A., 1983, Nitrogen oxides in the troposphere: global and regional budgets, *J. Geophys. Res. 88,* 10,785-10,807.

Lu, Y., 1990, *Modeling tropospheric OH chemistry,* M.S. Thesis, *pp245* (OGI/ESE/CAS, Beaverton, Oregon).

Lu, Y., and M. A. K. Khalil, 1990, Model calculations of nighttime OH, *EOS Transactions 71,* 1232-1233.

Lu, Y. and M. A. K. Khalil, 1991a, Tropospheric OH: Model calculations of spatial, temporal, and secular variations, *Chemosphere 23,* 397-444.

Lu, Y., and M. A. K. Khalil, 1991b, The real roles of CO and CH_4 in OH chemistry, *EOS, Transactions 72 (44),* 100.

Lu, Y. and M. A. K. Khalil, 1992a, Model calculations of nighttime OH, *Tellus 44B*, 106-113.

Lu, Y., and M. A. K. Khalil, 1992b, Radiative and active fluxes for atmospheric chemistry: calculations for various atmospheric conditions, *J. Geophys. Res. (submitted), pp49.*

Lu, Y., and M. A. K. Khalil, 1992c, Radiative transfer and tropospheric chemistry, *EOS, Transactions 73 (25),* 26.

Lu, Y., and M. A. K. Khalil, 1993a, Methane and carbon monoxide in OH chemistry: the effects of feedbacks and reservoirs generated by the reactive products, *Chemosphere 26*, 641-656.

Lu, Y., and M. A. K. Khalil, 1993b, Theoretical simulation of the asymmetry factor for various atmospheric conditions, *J. Atmos. Sci. (to be submitted), pp52.*

Luther, F. M., 1980, Annual report of Lawrence Livermore Laboratory to the FAA on the High Altitude Pollution Program-1980, *Publ. UCLA-50042-80,* Lawrence Livermore Lab., livermore, Calif.

Madronich, S., 1987, Photodissociation in the atmosphere 1. Actinic flux and the effects of ground reflections and clouds, *J. Geophys. Res., 92,* 9740-9752.

Manabe, S. and R. T. Wetherald, 1967, Thermal equilibrium of the atmosphere with a

convective adjustment, *J. Atmos. Sci. 21*, 361-385.

McClatchey, R. A., R. W. Fenn, J. E. A. Selby, F. E. Volz, and J. S. Garing, 1972, Optical Properties of the Atmosphere, *3rd ed., Tech. Rept. AFCRL-72-0497,* Air Force Cambridge Res. Labs., Bedford, Massachusetts.

McElory, M. B., 1989, Studies of polar ice: insights for atmospheric chemistry, In *The Environmental Record in Glaciers and Ice Sheets*, H. Oeschger and C. C. Langway, Jr., Eds., Wiley, London, 363-377.

Meador, W. E., and W. R. Weaver, 1980, Two-stream approximations to radiative transfer in planetary atmosphere: A unified description of existing methods and a new improvement, *J. Atmos. Sci., 37,* 630-643.

Meier, R. R., J. S. Lee, and D. E. Anderson, 1978, Atmospheric scattering of middle uv radiation from an internal source, *Appl. Opt., 17,* 3216-3225.

Meier, R. R., D. E. Anderson, Jr., and M. Nicolet, 1982, Radiation field in the troposphere and stratosphere from 240-1000 nm, I General analysis, *Planet. Space Sci., 30,* 923-933

Mugnai, A., P. Petroncelli, and G. Fiocco, 1979, Sensitivity of the photodissociation of NO_2, NO_3, HNO_2, and H_2O_2 to the solar radiation diffused by the ground and by atmospheric particles, *J. Atmos. Terr. Phys., 41,* 351-359.

Nicolet, M., R. R. Meier, and D. E. Anderson, Jr., 1982, Radiation field in the troposphere and stratosphere, II, Numerical analysis, *Planet. Space Sci., 30,* 935-983.

Nicolet, M., 1984, On the molecular scattering in the terrestrial atmosphere: An empirical formula for its calculation in the homosphere, *Planet. Space Sci., 32*, 1467-1468.

Perner, D., U. Platt, M. Trainer, G. Hubler, J. Drummond, W. Junkermann, J. Rudolph, B. Schubert, A. Volz, D. H. Ehhalt, K. J. Rumpel, and G. Helas, 1987, Measurements of tropospheric OH concentrations: A comparison of field data with model predictions, *J. Atmos. Chem., 5,* 185-216.

Pitari, G. and G. Visconti, 1979, A simple method to account for Rayleigh effects on

photodissociation rates, *J. Atmos. Sci., 36,* 1803-1811

Platt, U., M. Rateike, W. Junkermann, J. Rudolph, and D. H. Ehhalt, 1988, New tropospheric OH measurements, *J. Geophys. Res., 93,* 5159-5166.

Pinto, J. P., Y. L. Yung, D. Rind, G. L. Russell, J. A. Lerner, J. E. Hansen, and S. Hameed, 1983, A general circulation model study of atmospheric carbon monoxide, *J. Geophys. Res. 88,* 3691-3702.

Pinto, J. P. and M. A. K. Khalil, 1991, The stability of tropospheric OH during ice ages, interglacial epochs, and modern times, *Tellus 43B,* 347-352.

Prather, M., and C. M. Spivakovsky, 1990, Tropospheric OH and the lifetimes of Hydrochlorofluorocarbons, *J. Geophys. Res. 95,* 18,723-18,729.

Prinn, R., D. Cunnold, R. Rasmussen, P. Simmonds, F. Alyea, A. Crawford, P. Fraser, and R. Rosen, 1987, Atmospheric trends in methychloroform and the global average for hydroxyl radical, *Science 238*, 945-950.

Prinn, R., D. Cunnold, P. Simmonds, F. Alyea, R. Boldi, A. Crawford, P. Fraser, D. Gutzler, D. Hartley, R. Rosen, and R. Rasmussen, 1992, Global average concentration and trend for hydroxyl radicals deduced from ALE/GAGE trichloroethene (methyl chloroform) data for 1978-1990, *J. Geophys. Res. 20*, 2445-2461.

Pruppacher, H. R. 1981, The microstructure of atmospheric clouds and precipitation, In: *Clouds Their Formation, Optical properties, and Effects*, P. V. Hobbs and A. Deepak, Eds., Academic.

Rodgers, M. O., J. D. Bradshaw, S. T. Sandholm, S. Kesheng, and D. D. Davis, 1985, A 2-λ laser-induced fluorescence field instrument for ground-based and airborne measurements of atmospheric OH, *J. Geophys. Res.90*, 12,819-12,834.

Rotmans, J., R. J. Swart, and O. J. Vrieze, 1990, The role of the CH_4-CO-OH cycle in the greenhouse problem, *The Sci. of the Total Environ. 94,* 233-252.

Rasmussen, R. A. and M. A. K. Khalil, 1986, Atmospheric trace gases: trends and

distributions over the last decade, *Science 232,* 1623.

Sehmel, G. A., 1984, Deposition and resuspension, In D. Randerson (ed.), *Atmospheric Science and Power Production*, Technical Information Center, USA, 533-583.

Seinfeld, J. H., 1986, *Atmospheric Chemistry and Physics of Air Pollution,* John Wiley & Sons, Inc, New York.

Shirinzadeh, B., C. C. Wang, and D. Q. Deng, 1987, Diurnal variation of the OH concentration in ambient air, *Geophys. Res. let. 14,* 123-126.

Sickles, II, J.E., L.L. Hodson, W.A. McClenny, R.J. Paur, T.G. Ellestad, and J.D. Mulik, K.G. Anlauf, H.I. Schiff, and D.K. Bubacz, 1989, Field comparison of methods for the measurement of gaseous and particulate contributors to acidic dry deposition, *Atmos. Environ. 24A*, 155-165.

Slinn, W. G. N, 1984, Precipitation scavenging, In D. Randerson (ed.), *Atmospheric Science and Power Production*, Technical Information Center, USA, 466-532.

Singh, H. B., 1977a, Atmospheric holocarbons: evidence in favor of reduced hydroxyl radical concentrations in the troposphere, *Geophys. Res. Lett. 3,* 101-104.

Singh, H. B., 1977b, Preliminary estimation of average tropospheric HO concentrations in the northern and southern hemisphere. *Geophys. Res. Lett. 4*, 453-456.

Spivakovsky, C. M., R. Yevich, A. J. Logan, S. C. Wofsy, M. B. McElroy, and M. J. Prather, 1990, Tropospheric OH in a three-dimensional chemical tracer model: An assessment Based on observations of Cl_3CCl_3, *J. Geophys. Res. 95*, 18,441-18,471.

Stamnes, K., S. Tsay, W. Wiscombe, and K. Jayaweera, 1988, Numerically stable algorithm for discrete-ordinate-method radiative transfer in multiple scattering and emitting layered media, *Appl. Opt., 27,* 2502-2509.

Stephens, G. L., 1979, Optical properties of eight water cloud types, *CSIRO Aust. Div. Atmos. Phys. Tech. Pap. No. 36,* 1-35.

Stone, P. H. and J. H. Carlson, 1979, Atmospheric lapse rate regions and their parameterization, *J. Atmos. Sci. 36,* 415-423.

Thompson, A. M. and R. J. Cicerone, 1982, Clouds and wet removal as causes of variability in trace-gas composition of the marine troposphere, *J. Geophys. Res. 87,* 8,811-8,826.

Thompson, A. M., 1984, The effects of clouds on photolysis rates and ozone formation rates in the unpolluted troposphere, *J. Geophys. Res., 89*, 1341-1349.

Thompson, A. M. and R. J. Cicerone, 1986, Possible perturbations to atmospheric CO, CH_4, and OH, *J. Geophys. Res. 91,* 10,853-10,864.

Thompson, A. M., M. A. Huntley, and R. W. Stewart, 1990, Perturbations to tropospheric oxidants, 1985-2035 1. calculations of ozone and OH in chemically coherent regions, *J. Geophys. Res. 91,* 10,853-10,846.

Thompson, A. M., M. A. Huntley, and R. W. Stewart, 1991, Perturbations to tropospheric oxidants, 1985-2035 2. Calculations of hydrogen peroxide in chemically coherent regions, *Atmos. Environ. 25A,* 1837-1850.

Thompson, A. M., 1992, The oxidizing capacity of the Earth's atmosphere: probable past and future changes, *Science 256,* 1157-1165.

Tie, X., F. N. Alyea, D. M. Cunnold, and C.-Y. J. Kao, 1991, Atmospheric methane: a global three-dimensional model study, *J. Geophys. Res. 96,* 17,339-17,348.

Toon, O. B., C. P. Mckay, and T. P. Ackerman, and K. Santhanam, 1989, Rapid calculation of radiative heating rates and photodissociation rates in inhomogeneous multiple scattering atmospheres, *J. Geophys. Res., 94,* 16,287-16,301.

Turco, R. P., Photodissociation rates in the atmosphere below 100 km, *Geophys. Surv., 2,* 153-192, 1975.

Turpin, B. J., J. J. Huntzicker, S. M. Larson, G. R. Cass, 1991, Los Angeles summer midday particulate carbon: primary and secondary aerosol, *Environ. Sci. Tech. 23,* 281-289.

Vaghjiani, G. L. and A. R. Ravishankara, 1991, New measurement of the rate coefficient for the reaction of OH with methane, *Nature 350*, 406-409.

Valentin, K. M., 1990, *Numerical modeling of the climatological and anthropogenic influences on the chemical composition of the troposphere since the last glacial maximum,* Ph.D. Thesis, *238pp*, University of Mainz, Germany, Dec., 1990.

van de Hulst, H. C., 1957, *Light Scattering by Small Particles*, John Wiley, New York.

Volz, A., D. H. Ehhalt, and R. G. Derwent, 1981, Seasonal and latitudinal variation of ^{14}CO and the tropospheric concentration of OH radicals, *J. Geophys. Res. 86,* 5163-5171.

Wang, C. C., L. I. Davis, P. M. Selzer, and R. Munoz, 1981, Improved airborne measurements of OH in the atmosphere using the technique of laser-induced fluorescence, *J. Geophys. Res. 86,* 1181-1186.

Watanabe, T., M. Yoshida, S. Fujiwara, K. Abe, O. Onoe, M. Hirota, and S. Igarashi, 1982, Spin trapping of hydroxyl radical in the troposphere for determination by electron spin resonance and gas chromatography/mass spectrography, *Anal. Chem. 54,* 2470-2474.

Weinstock, B., 1969, Carbon monoxide: residence time in the atmosphere, *Science 166,* 224-225.

Weiss, R. F., 1981, The temporal and spatial distribution of tropospheric nitrous oxide, *J. Geophys. Res. 86,* 7185-7195.

Wiscombe, W. J., 1977, The delta-Eddington approximation for a vertically inhomogeneous atmosphere, *Tech. Note TN-121 + STR,* Natl. Cent. for Atmos. Res., Boulder, Colo.

WMO, 1985, *Atmospheirc Ozone 1986, WMO Global Ozone Research and Monitoring Project - Report NO. 16*, NASA, Washington, D.C., 1985.

Wofsy, S. C., 1978, Temporal and latitudinal variations of stratospheric trace gases: a critical comparison between theory and experiment, *J Geophys. Res. 83,* 364-3785.

Yao, F., I. Wilson, and H. Johnston, 1982, Temperature-dependent ultraviolet absorption spectrum for dinitrogen pentoxide, *J. Phys. Chem. 86,* 3611.

Yung, Y. L., 1976, A numerical method for calculating the mean intensity in an inhomogeneous Raleigh scattering atmosphere, *J. Quant. Spectrosc. Radiat. Transfer, 16*, 755-761.

VITA

The author was born on October 23, 1960 in Nanjing, China. In 1983, he received his B.S. in the field of atmospheric science at Nanjing University, one of the most famous universities in China. He obtained his M.S. in the field of environmental science and engineering at Oregon Graduate Institute of Science and Technology in 1990. The author will further pursue his research interests at Atmospheric Research and Exposure Assessment Laboratory of USEPA with the National Research Council Fellowship.